Chaotic advection, mixing, and property exchange in three-dimensional ocean eddies and gyres

by

Genevieve Jay Brett

Submitted to the Joint Program in Applied Ocean Science & Engineering
in partial fulfillment of the requirements for the degree of

Doctor of Philosophy

at the

MASSACHUSETTS INSTITUTE OF TECHNOLOGY

and the

WOODS HOLE OCEANOGRAPHIC INSTITUTION

June 2018

Author . . . .
Joint Program in Physical Oceanography
Massachusetts Institute of Technology
& Woods Hole Oceanographic Institution
May 11, 2018

Certified by . . . .
Larry Pratt
Senior Scientist
Woods Hole Oceanographic Institution
Thesis Supervisor

Certified by . . . .
Irina Rypina
Associate Scientist
Woods Hole Oceanographic Institution
Thesis Supervisor

Accepted by . . . .
Larry Pratt
Chairman, Joint Committee for Physical Oceanography
Woods Hole Oceanographic Institution

Chaotic advection, mixing, and property exchange in three-dimensional ocean eddies and gyres

by

Genevieve Jay Brett

Submitted to the Joint Program in Physical Oceanography
Massachusetts Institute of Technology
& Woods Hole Oceanographic Institution
on May 11, 2018, in partial fulfillment of the
requirements for the degree of
Doctor of Philosophy

Abstract

This work investigates how a Lagrangian perspective applies to models of two oceanographic flows: an overturning submesoscale eddy and the Western Alboran Gyre. In the first case, I focus on the importance of diffusion as compared to chaotic advection for tracers in this system. Three methods are used to quantify the relative contributions: scaling arguments including a Lagrangian Batchelor scale, statistical analysis of ensembles of trajectories, and Nakamura effective diffusivity from numerical simulations of dye release. Through these complementary methods, I find that chaotic advection dominates over turbulent diffusion in the widest chaotic regions, which always occur near the center and outer rim of the cylinder and sometimes occur in interior regions for Ekman numbers near 0.01. In thin chaotic regions, diffusion is at least as important as chaotic advection. From this analysis, it is clear that identified Lagrangian coherent structures will be barriers to transport for long times if they are much larger than the Batchelor scale. The second case is a model of the Western Alboran Gyre with realistic forcing and bathymetry. I examine its transport properties from both an Eulerian and Lagrangian perspective. I find that advection is most often the dominant term in Eulerian budgets for volume, salt, and heat in the gyre, with diffusion and surface fluxes playing a smaller role. In the vorticity budget, advection is as large as the effects of wind and viscous diffusion, but not dominant. For the Lagrangian analysis, I construct a moving gyre boundary from segments of the stable and unstable manifolds emanating from two persistent hyperbolic trajectories on the coast at the eastern and western extent of the gyre. These manifolds are computed on several isopycnals and stacked vertically to construct a three-dimensional Lagrangian gyre boundary. The regions these manifolds cover is the stirring region, where there is a path for water to reach the gyre. On timescales of days to weeks, water from the Atlantic Jet and the northern coast can enter the outer parts of the gyre, but there is a core region in the interior that is separate. Using a gate, I calculate the continuous advective transport across the Lagrangian boundary in three dimensions for the first time. A Lagrangian volume budget is calculated, and challenges in its closure are described. Lagrangian and Eulerian advective transports are found to be of similar magnitudes.

Thesis Supervisor: Larry Pratt
Title: Senior Scientist
Woods Hole Oceanographic Institution

Thesis Supervisor: Irina Rypina
Title: Associate Scientist
Woods Hole Oceanographic Institution

Biography

Genevieve Brett, called Jay by her friends and colleagues, was raised in Connecticut. She attended Hopkins School in New Haven before studying for her B.A. in Mathematics and Physics at Skidmore College in Saratoga Springs, NY. Her first major research was done with Jim Gunton and his group at Lehigh University in the summer of 2011. She was then introduced to physical oceanography by Greg Gerbi, who joined the Skidmore physics faculty in 2011. Encouraged by Gerbi, she was a Winter Fellow at WHOI in 2012, working with Young-Oh Kwon, Magdalena Andres, and then-student Derya Akkaynak. During that fellowship, she became interested in Larry Pratt's work, which led to her joining the MIT-WHOI Joint Program later that year. After graduation, Jay will begin a postdoctoral position with Kelvin Richards of the University of Hawai'i Mānoa.

Acknowledgments

Funding for this work was provided by Woods Hole Oceanographic Institution and the Office of Naval Research. The ONR support was through the MURI on Dynamical Systems Theory and Lagrangian Data Assimilation in 4D and the CALYPSO project.

I would like to thank the scientists, admins, and peers who made the Joint Program a welcoming place for me. Everyone who has asked me about my work and listened to me talk through an issue with it has contributed— thank you. Of course, I would not have gotten to this point without my advisors, who were with me at every turn, or my committee, who shared their insights. Thanks to Greg Gerbi, Magdalena Andres, and Young-Oh Kwon for my introduction to oceanography and my excellent experience as a Winter Fellow at WHOI. I also thank Mike Neubert and the math ecology group for reminding me that math is fun. My family, both biological and chosen, and especially my partner, has supported me throughout my studies. I will be forever thankful to you all, and I hope I am supporting you well in turn.

Contents

List of Figures

List of Tables

Chapter 1

Introduction

Oceanographic models and theories are traditionally Eulerian, examining the ocean from a fixed reference point. The Eulerian viewpoint is also very useful for creating maps of water properties from observations, such as is done for the World Ocean Climate Experiment and Global Ocean Ship-based Hydrographic Investigation Program repeat sections. This view is also convenient for theories of the steady circulation in a basin, such as the traditional Stommel and Munk gyres. However, when considering the evolution of the properties of a parcel of water, a Lagrangian view is more natural. A Lagrangian view is in the frame of the fluid, such that the coordinates are functions of time. Lagrangian measurements of tracers and of the tracks of drifters and floats have improved our knowledge of, for example, the North Atlantic Deep Western Boundary Current (DWBC). The paths followed by water parcels, as measured by floats and drifters, are generally more convoluted than the spatially and time-averaged Eulerian maps of ocean currents would suggest. For example, the path of the DWBC was considered fairly direct, southward along the continental slope, before tracer and float studies demonstrated that there are recirculations eastward into the interior (see Fine 1995 for a review). The possible effects of these recirculations can be demonstrated in laboratory flows (Deese et al. 2002), where stretching and folding of a tracer can cause enhanced mixing, an idea I will return to. Pathways from the boundary current to the interior are also important for the meridional overturning circulation, as these paths demonstrate that newly formed deep waters can spread to the interior of the basin fairly quickly (Bower and Hunt 2000).

The analysis of trajectories from drifters and floats represents a particular case of kinematic analysis of the ocean. Kinematic analysis of geophysically-relevant flows have been improved over the past few decades by the introduction of methods based in dynamical systems theory. I will discuss some of the basic terminology and analyses used for dynamical systems as background. Then I will provide an overview of the types of objects identified in oceanographic applications, before introducing the questions addressed in my research. This background is not a comprehensive review, but rather intended to provide a qualitative understanding of the state of the field so that the impact of the following research is clear.

A dynamical system analysis applies to differential equations or systems thereof. In a deterministic system where the behavior is known over infinite time, the structure of many trajectories, or paths in time, through the phase space can be identified through **invariant surfaces**: surfaces that trajectories are trapped on. The simplest case of an invariant surface is a **fixed point**: a location in the system which, when used as the initial condition, produces a trajectory that does not change with time. In a fluid system, a fixed point is a stagnation point. The qualities of a fixed point depend on the trajectory of nearby initial conditions. Such nearby trajectories may approach the fixed point, move around it at a (nearly) fixed distance, or move farther away. If all points nearby behave in the same manner, the fixed point may be classified as stable, neutrally stable, or unstable, respectively.

In the case of a two-dimensional incompressible fluid flow, a fixed point can be classified as elliptic or hyperbolic (sketches in figure 1-1). Elliptic points are neutrally stable; a physical example is a stagnation point in the center of a steady vortex, where trajectories remain at a similar distance from the center over all time. Flows around a hyperbolic point follow hyperbolic trajectories, approaching and then accelerating away from the point. For hyperbolic points, stable and unstable **manifolds** are curves along which all points asymptotically approach the fixed point in forward or backward time, respectively. Other trajectories approach the region of the fixed point in the direction of the stable manifold and leave the region in the direction of the unstable manifold. With increased numbers of dimensions, the possible geometries of fixed points increase, although the stability can be defined in the same fashion.

Dynamical systems may also have features of interest that are of higher dimensions than points. These include the manifolds associated with hyperbolic fixed points, which organize the nearby trajectories' hyperbolic shape. Another example is closed trajectories, which indicate repeating oscillations of the system and may themselves be stable or unstable. Trajectories may also be

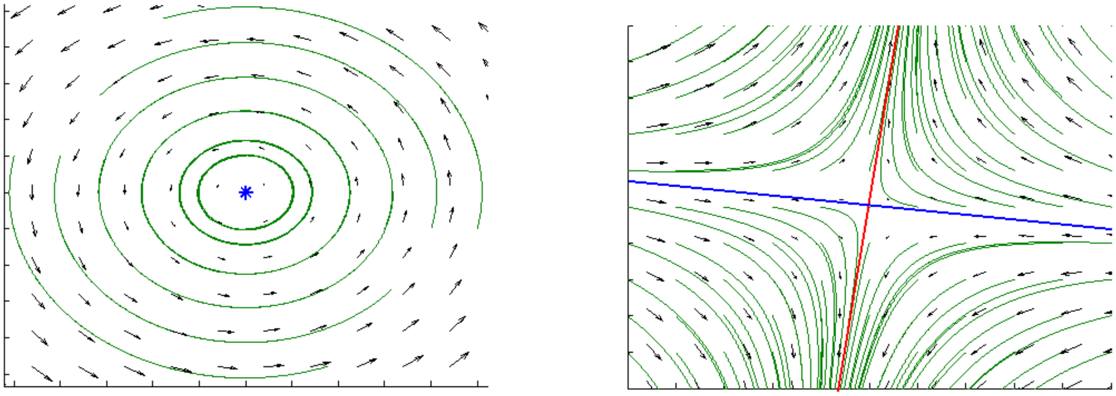

(a) elliptic

(b) hyperbolic

Figure 1-1: Sketch of fixed points possible in two-dimensional incompressible fluid flow. Green curves are sample trajectories; black arrows are sample velocities. Left, elliptic point marked by the blue star. Right, hyperbolic point is located at the intersection of its stable manifold (blue) and unstable manifold (red).

confined to sub-sections of the space, such as along spheres or planes in a 3-dimensional system. It is a general rule that trajectories may not intersect, so if there is a closed curve, for example, in a two-dimensional system, then all trajectories starting inside (outside) that curve must remain inside (outside) for all time. This is true for any material curve in a fluid as well, provided there is not droplet formation. The goal of the dynamical systems-based methods developed for application to geophysical fluids is to identify material contours that are maximal in some sense compared to their surroundings and provide insight into the structure of the flow, generally using information about the flow over a finite time. I will describe two types of contours that are of interest: least-stretching closed contours and most-stretching open contours, each used to identify a different aspect of ocean features.

Least-stretching closed material contours are usually within a set of closed material contours surrounding a vortex or eddy. The minimal stretching of the material indicates that it does not undergo filamentation and can therefore be considered to bind the water inside such that it is not stirred with its surroundings over time. Eddies with such bounding contours are called **coherent**, and there are quite a few methods that may find these contours (see Hadjighasem et al. 2017 for a review). Separating these coherent eddies from others is a case where Lagrangian analysis has improved our understanding of ocean processes.

Eddies appear ubiquitous in altimetry as anomalous sea-surface heights (and anomalous vorticities) that retain this signature over time. Some persistent recirculations are locally very important for the flow; examples include the Great Whirl and the Western Alboran Gyre. Other eddies move in space, often at rates similar to Rossby waves, such as rings that separate from the Gulf Stream and Kuroshio. The extent to which these various eddies are coherent is uncertain. The transport of water by the moving eddies is important for understanding how these observed eddies may contribute to global meridional heat transport, for instance. A large study tracking sea-surface height anomalies by Dong et al. (2014) suggested that these eddies might contribute 20% of the global meridional heat transport. However, a study using transfer operators by Froyland and coauthors (2012) showed that anomaly eddies do not consistently transport water, instead exchanging water with their surroundings. The exchanging eddies are then somewhat wavelike anomalies, a clear signal but not a consistent transport process. A study by Abernathey and Haller (2018) used a Lagrangian method to identify coherent eddies, which do carry water with them. These are generally smaller and shorter-lived than eddies tracked with Eulerian measures, contributing 1% or less to the meridional heat transport of the ocean, which is much smaller than the earlier estimate. The updated idea from this series of studies is that mesoscale eddy motions, including long-lived moving sea-surface height anomalies, are mostly stirring the water, not coherently transporting eddies with disparate properties. However, this has not yet been examined for the more persistent recirculations.

Most stretching (open) material contours identify strong stirring regions in a fluid flow. These can be the manifolds of hyperbolic trajectories, a generalization of hyperbolic fixed points and their manifolds. I use a coastally-trapped recirculation as an example, first with steady flow and then with a time-periodic perturbation (see figure 1-2 for a sketch). In the steady case, there are two stagnation points on the coast. The outer limit of the recirculation is a streamline connecting these points. These stagnation points are hyperbolic, with convergent and divergent flow nearby. For H_1, there is convergent flow along the coast towards the stagnation point and divergence in the offshore direction, while the opposite is true for H_2. With a small perturbation to a time-dependent flow, these stagnation points no longer exist, but are each replaced by a hyperbolic trajectory in the same neighborhood. Then each trajectory has one offshore manifold, but these no longer match each other. The unstable manifold of H_1 and the stable manifold of H_2 cross repeatedly, trapping water in **turnstile lobes** between them. These lobes exchange fluid between the recirculation and the

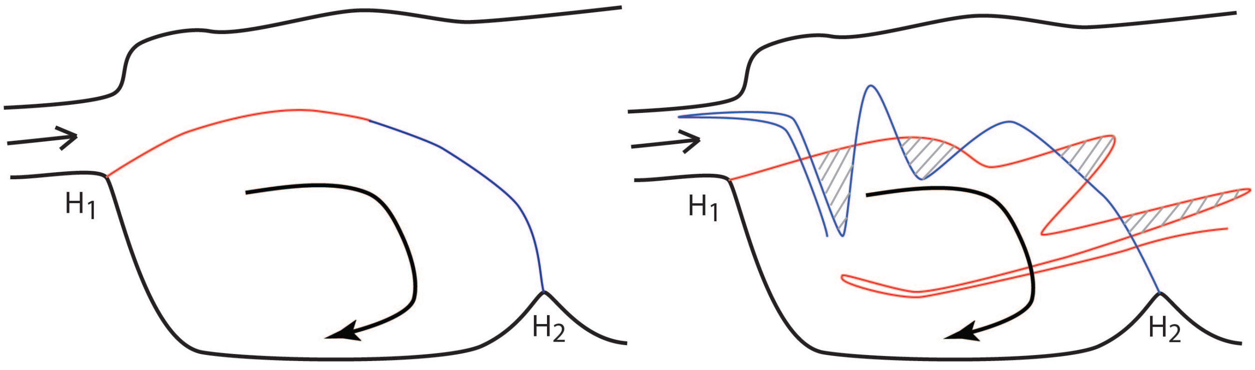

(a) steady (b) time-varying

Figure 1-2: Sketch of a coastally-trapped recirculation. Manifolds are represented by red (unstable) and blue (stable) curves. H1 and H2 are hyperbolic fixed points or trajectories. Left, steady flow, with water trapped in the recirculation for all time. The manifolds of the two hyperbolic stagnation points are a single heteroclinic streamline. Right, a periodic velocity perturbation is added to the flow. Shaded lobes map to each other in time and transport water out of the recirculation. Unshaded lobes transport water into the recirculation.

exterior flow; in the figure, the shaded lobes move water out of the recirculation and the unshaded lobes move water into the recirculation. When the time-dependent perturbation is periodic, the shape of the manifolds will be periodic, with water moving from one lobe position clockwise to the next in each period, shaded lobes mapping to shaded lobes and unshaded to unshaded (see Wiggins' book for mathematical theory). In a simplified system with wind-driven barotropic (depth-independent) flow, Miller et al. (2002) were able to identify these lobes and calculate the related transport. For realistic strengths of the wind forcing, the transport of volume by lobes was larger than the Ekman pumping by the wind. For a realistic simulation of the a Gulf of Mexico eddy, Branicki and Kirwan (2010) were able to show the structure of lobes in three dimensions but did not continue to a transport calculation due to the difficulty of calculation of the lobes' volume.

It is important to realize that the periodic flow described above, with their periodic manifolds, will generally contain aperiodic trajectories. These aperiodic trajectories, including those in the lobes, undergo exponential stretching and folding, separating far from initially-nearby trajectories in time. This behavior of aperiodic trajectories whose later positions are very sensitive to initial conditions is called **chaos** or **chaotic advection**. Chaotic advection was introduced to the fluid dynamics community by Aref (1984) to describe nearly-integrable flow that is sensitive to initial conditions and causes fast stretching and folding of trajectories and water parcels. The stretching and folding are controlled by long-lived structures, meaning that the lifetime of the structures is longer than the time it takes a trajectory to orbit them. This separation of timescales allows regions of chaotic and non-chaotic flow to be identified before the flow structure changes. Least-stretching material contours organize non-chaotic regions, while exponentially stretching manifolds organize chaotic regions.

The turnstile lobes defined by crossing manifolds directly relate to the transport between two different regions of the flow. However, they not only transport the fluid, but also stir it. The lobes become very stretched out near the hyperbolic trajectories, as the manifold of the farther hyperbolic trajectory repeatedly folds over the manifold of the nearby trajectory. This stirring is such that if there is a difference in water properties between the interior and exterior regions, the gradients will be greatly enhanced, in turn enhancing mixing. I will next discuss the relationship between stirring and mixing, which underpins much of the research to follow.

Stirring is a reversible process of shear causing the stretching and contracting of a water parcel. For instance, kneading dough is primarily stirring it, spreading new flour across the existing dough in a very thin layer and folding it into many thin layers. Mixing, by contrast, is an irreversible process where properties become homogenous. Molecular diffusion is a canonical case of mixing, where molecules of two substances, particularly liquids or gasses, become arranged in space in a statistically homogenous distribution through the random motion of molecules due to their temperature (kinetic energy). Turbulent diffusion is an analogous process where turbulent flow exchanges fluid parcels with different properties, such that the properties spread through an area and become more homogenous. Reynolds averaging in a system with scale separation is often used to describe a turbulent diffusivity related to the kinetic energy of small motions.

A Lagrangian view allows for clearer consideration of stirring and mixing than an Eulerian view. Tracking of water parcels through trajectories can allow direct measurement of the stretching and folding they undergo through the separation of trajectories in time. Eulerian measurements, by contrast, only allow evaluation of stretching in a location. As water parcels move, they experience different stretching rates in different locations. The ergodic theory supposes that the total space is sampled by any trajectory, and is sometimes used to avoid considering Lagrangian information. However, in the ocean, physical constraints such as potential vorticity conservation organize the flow, such that ergodicity is less reasonable.

If trajectories and their separations are measured following a water parcel, associated measurements of tracers over time shows the rate at which mixing occurs. Stirring can speed mixing by creating large gradients between adjacent water parcels and increasing the surface area over which exchange can occur. A good image is coffee and cream. If coffee and cream are initially added to a container so that they have only one interface and they are both at rest, mixing can only occur across that interface and will be due to molecular motion alone. Away from the interface, molecular diffusion is mixing each fluid with itself, effecting no change. If the container is stirred, intrusions of each fluid into the other will rapidly increase the surface area of the interface where molecular motion can exchange coffee and cream molecules in space, leading to a mixture indicated by changing color. Coherent eddies in the flow, with their non-filamenting edges, are a particular case with slow mixing. By contrast, chaotic regions in the flow, likely contraining hyperbolic manifolds, will have high stirring rates and fast mixing.

The following chapters will examine two modeled physical systems, an eddy and a gyre. The eddy model is an extension of work by Pratt et al. (2013), which identified the chaotic and regular regions of the flow. I consider whether diffusivity will be important in this system in regards to tracers. There are two complementary issues. First, I consider whether the separation between chaotic and non-chaotic, or regular, regions will survive the addition of diffusion. This survival is important if observational ocean studies are ever to confirm the existence and behavior of Lagrangian structures at submesoscales. In order to observe a chaotic region using dye, for example, the dye would need to be advected along the structure without diffusively spreading out into other flow regions. In essence, the chaotic stretching must dominate over diffusion in the flow's behavior for long enough to take an effective observation. While this may be assumed for a mesoscale ocean feature, at smaller scales diffusion is a more significant component of the tracer evolution. The second question addresses the enhancement of mixing through stirring. Any stirring enhances mixing, but I examine how much chaotic regions increase mixing over regular regions that are stirred. This work is covered in Chapter 2.

The second system, the gyre, is coastally trapped in a geometry like figure 1-2. Either this type of structure, or a double-gyre, has been repeatedly studied in the Lagrangian method literature as a straightforward system with chaotic and regular regions. However, these are usually simplified, with the flow being time-periodic, two-dimensional, or both. I realistically model a three-dimensional aperiodic gyre. I identify the manifolds at the surface and along isopycnals as an approximation of the three-dimensional structure of the manifold surfaces and show an example of a three-dimensional lobe. I also use this setup to quantify the exchange of water into and out of the gyre, which may be the first such analysis for such a realistic system. This exchange forms part of the budgets for volume, heat, and salt of the gyre, and I compare Lagrangian and Eulerian budgets to understand the physical dynamics of the gyre. The model description and Eulerian analysis of the physics in the mean gyre location are covered in Chapter 3. Chapters 4 and 5 present the Lagrangian analysis and discuss the differences from the Eulerian results.

Overall, the following research aims to investigate some aspects of how a Lagrangian perspective applies to oceanographically relevant flows. Including three dimensions, diffusion, and in the second system, aperiodic time dependence, move these works toward the realities of the ocean. The applicability of Lagrangian structures to the classical physical oceanographic concerns of the movement of salt, heat, and vorticity is a question that is just beginning to be addressed. My work aims to fill in some of these gaps with quantitative results from models.

References

Abernathey, Ryan, and George Haller. “Transport by Lagrangian vortices in the eastern pacific." Journal of Physical Oceanography 2018 (2018).

Aref, H. “Stirring by chaotic advection.” Journal of fluid mechanics, 143, (1984): 1-21.

Bower, Amy S., and Heather D. Hunt. “Lagrangian observations of the deep western boundary current in the North Atlantic Ocean. Part II: The Gulf Stream-deep western boundary current crossover." Journal of Physical Oceanography 30.5 (2000): 784-804.

Branicki, M., and A. D. Kirwan Jr. “Stirring: the Eckart paradigm revisited." International Journal of Engineering Science 48.11 (2010): 1027-1042.

Chelton, Dudley B., Michael G. Schlax, and Roger M. Samelson. “Global observations of nonlinear mesoscale eddies." Progress in Oceanography 91.2 (2011): 167-216.

Deese, Heather E., Larry J. Pratt, and Karl R. Helfrich. “A laboratory model of exchange and mixing between western boundary layers and subbasin recirculation gyres." Journal of Physical Oceanography 32.6 (2002): 1870-1889.

Dong, C., J. C. McWilliams, Y. Liu, and D. Chen, 2014: “Global heat and salt transports by eddy movement.” Nature Communications, 5 (2014): 3294.

Fine, Rana A. “Tracers, time scales, and the thermohaline circulation: The lower limb in the North Atlantic Ocean." Reviews of Geophysics 33.S2 (1995): 1353-1365.

Froyland, Gary, et al. “Three-dimensional characterization and tracking of an Agulhas Ring." Ocean Modelling 52 (2012): 69-75.

Hadjighasem, Alireza, et al. "A critical comparison of Lagrangian methods for coherent structure detection." Chaos: An Interdisciplinary Journal of Nonlinear Science 27.5 (2017): 053104.

Haller, G.; Beron-Vera, F.J. Geodesic theory of transport barriers in two-dimensional flows. Physica D (2012).

Miller, Patrick D., et al. “Chaotic transport of mass and potential vorticity for an island recirculation." Journal of Physical Oceanography 32.1 (2002): 80-102.

Pratt, L. J., Rypina, I. I., Ozgokmen, T. M., Wang, P., Childs, H., & Bebieva, Y. “ Chaotic advection in a steady, three-dimensional, Ekman-driven eddy.” Journal of Fluid Mechanics, 738 (2014): 143-183.

Rypina, I.I.; Brown, M.G.; Beron-Vera, F.J.; Kocak, H.; Olascoaga, M.J.; Udovydchenkov, I.A. “Robust transport barriers resulting from strong Kolmogorov-Arnold-Moser stability.” Physical Review Letters 98 (2007): 104102.

Wiggins, Stephen. “Introduction to applied nonlinear dynamical systems and chaos.” Vol. 2. Springer Science & Business Media (2003).

Chapter 2

Competition between Chaotic Advection and Diffusion: Stirring and Mixing in a 3D Eddy Model

Summary

In ocean features, as one moves down to the submesoscale, both vertical motions and diffusion can become non-negligible factors. Vertical motions allow for chaotic advection to be present even in steady flows, as has been shown for an Ekman-driven rotating cylinder analogue of a submesoscale eddy (Pratt et al. 2013). Pratt et al. detailed the undisturbed flow along tori and the effect of a small symmetry-breaking perturbation in creating regions of chaos separated by material barriers. This work adds to that done in Pratt et al. by carefully considering diffusion, which may overcome the barriers to transport identified previously.

The current work considers the importance of small-scale turbulent diffusion as compared to chaotic advection for tracers in this type of rotating cylinder system. Two methods are used to directly quantify this importance: scaling arguments including a Lagrangian Batchelor scale, which I put on firm mathematical footing, and the spread of ensembles of trajectories. Through these complementary methods, I find that chaotic advection will dominate turbulent diffusion in the widest chaotic regions. In this model, these always occur near the center and outer rim of the cylinder and sometimes occur in other regions for Ekman numbers near 0.01. In thin chaotic

regions, diffusion is at least as important as chaotic advection.

I then consider how stirring by chaotic advection enhances mixing in this system. In particular, the analysis of numerical simulations of dye release using a tracer variance function and Nakamura effective diffusivity allow quantification of how much chaotic advection increases the stirring rate and enhances mixing more than non-chaotic stirring. I find that the effective diffusivity can double through the increased stirring by chaotic advection. This enhanced mixing increases with increases in of the perturbation that induces chaos and decreases of the imposed small-scale turbulent diffusion.

2.1 Introduction

Eddies are known to contribute to the transport and mixing of heat, freshwater, and other tracers in the ocean. Models that resolve the mesoscale have been shown to correspond better with satellite measurements and have smaller temperature drift than less-resolved models (Griffies et al. 2015), and describing sub-grid-scale processes is an ongoing challenge (e.g. Hallberg 2013). This work looks at an overturning submesoscale eddy which is smaller than those resolved in many current models and examines how stirring by chaotic advection affects tracer distribution within the eddy in the presence of diffusion.

Chaotic advection, popularized by Aref (1984), accelerates stirring through rapid stretching and folding along chaotic trajectories. These trajectories are controlled by long-lived structures, meaning that the lifetime of the structures is longer than the time it takes a trajectory to orbit them; this property allows regions of chaotic and non-chaotic flow to be identified on useful timescales. Chaos requires at least three degrees of freedom, and is most often studied with a time-dependent 2D system in fluids (i.e. the polar vortex, Rypina et al. 2007). One three-dimensional flow that can exhibit chaotic behavior is the rotating cylinder. The physical system of the rotating cylinder is a cylindrical volume containing a homogeneous and incompressible fluid which is forced by a rigid lid with differential rotation between the lid and walls. This lid motion produces Ekman forcing which induces a swirling, overturning flow, where vertical derivatives are of first-order importance. This type of flow has been studied previously with analytic approximations to the velocity field (Greenspan 1969) or laboratory observations and detailed numerical simulations (Fountain et al. 2000), but was not discussed in an ocean setting until recently. I use a rotating cylinder flow as an analogue for an overturning submesoscale eddy. While many oceanic flows can be well approximated by two-dimensional flows, the third dimension becomes important at the submesoscale.

Pratt et al. (2014) and Rypina et al. (2015) connected the rotating cylinder flow to the ocean as an analogue for a submesoscale eddy. Their work described this rotating cylinder system using a simple kinematic model and a spectral Navier-Stokes simulation. Pratt et al. detailed the undisturbed flow along tori and the effect of a small symmetry-breaking perturbation in creating regions of chaos separated by material barriers. Rypina et al. added periodic time-dependence to the flow, again studying regions of chaos and material barriers; I will not consider periodic flows here. A form of the Kolmogorov-Arnold-Moser, or KAM, theorem specifies that for small perturbations, these chaotic regions and barriers will exist. In section 2, an updated model background flow and steady perturbation are described, followed by a comparison of the model behavior with steady perturbation to spectral simulation results from Pratt et al.

The stretching of fluid elements by chaotic advection increases gradients of any tracer of interest, creating thinning filaments from any initial high-concentration area. Smaller-scale turbulent processes, unresolved in this model, would halt this thinning through diffusive mixing. Although many case studies have been done on possible chaotic regions or processes in the ocean (e.g. Sayol et al. 2013, Olascoaga and Haller 2012, Deese et al. 2002, Miller et al. 2002), there is very limited discussion on the effects of diffusivity for observing such features. In order to observe a chaotic region using dye, for example, the dye would need to be advected along the structure without diffusively spreading out into other flow regions. In essence, the chaotic stretching must dominate over diffusion in the flow's behavior for long enough to take an effective observation. While this may be assumed for a mesoscale ocean feature, at smaller scales diffusion is a more significant component of the tracer evolution. For the opposite extreme in scale, laboratory experiments with a flow of glycerine with similar geometry found that diffusion spread dye along chaotic regions, allowing barriers to be visualized in less time than expected from numerical trajectory integrations (Fountain et al. 2000). I will consider whether the relative strengths of chaotic advection and diffusion will allow similar tracer-based observations for similar features in the ocean. This work adds to that done in Pratt et al. by carefully considering diffusion, which may overcome the barriers to transport identified previously. In section 3, I quantify the competition between chaotic advection and diffusion in several ways. Utilizing scaling arguments, ensembles of trajectories, and numerical dye experiments, I demonstrate in which circumstances chaos is more important for tracer distribution than diffusion. Section 4 discusses relative advantages of the different methods and the implications of this work.

2.2 Kinematic Model

The physical rotating cylinder is a cylindrical volume containing a homogeneous and incompressible fluid which is forced by differential rotation between a rigid lid and the walls. This lid motion produces Ekman forcing which induces a swirling, overturning flow, where vertical derivatives are of first-order importance. For a lid rotating about the center of the cylinder, it is possible to analytically solve for the flow in a piecewise manner (Greenspan 1969). I use a kinematic model rather than a numerical solution or piecewise analytical approximation because it allows me to more thoroughly examine parameter space and more quickly compute trajectories. This kinematic model is simpler and seamless, but is based on the analytic solution, as was the Pratt et al. model. The updated kinematic model adds an Ekman parameter. The model describes an incompressible flow comprised of an overturning streamfunction and an axisymmetric azimuthal velocity. The incompressibility allows the flow to conserve mass for my homogenous fluid. The model system is nondimensionalized by the cylinder height, H, so that the nondimensional cyclinder has height one and radius a, the ratio of radius to height. The boundary conditions are no normal flow on all boundaries and no-slip flow on the sides and bottom. The overturning streamfunction depends on r and z; then any azimuthal flow that is a function of r and z will preserve volume. The streamfunction will have the form

$$\Psi = -E^{1/2} R(r) F(z), \tag{2.1}$$

where E is the Ekman number, $F(z)$ is the vertical portion of the streamfunction, and $R(r)$ is the radial portion of the streamfunction. The Ekman number is defined by

$$E = (\delta_E/H)^2 = \left(\nu/\Omega H^2\right), \tag{2.2}$$

where δ_E is the Ekman layer depth, H is the depth of the eddy and cylinder, and ν is vertical eddy viscosity. The vertical portion of the streamfunction is

$$F(z) = A[\sin(\zeta)\sinh(\zeta) - \cos(\zeta)\cosh(\zeta)] + B[\sin(\zeta)\sinh(\zeta) + \cos(\zeta)\cosh(\zeta)] - D, \tag{2.3}$$

where ζ is a transformed vertical coordinate,

$$\zeta = \frac{z - 1/2}{E^{1/2}},$$

and the constants are defined by

$$\begin{aligned} A &= \tfrac{-1}{2}\tfrac{cS}{s^2C^2+c^2S^2}, \quad B = \frac{1}{2}\frac{sC}{s^2C^2+c^2S^2}, \; D = A(sS - cC) + B(sS + cC) \\ s &= \sin\left(\tfrac{1}{2E^{1/2}}\right), \quad c = \cos\left(\frac{1}{2E^{1/2}}\right), \; S = \sinh\left(\frac{1}{2E^{1/2}}\right), \; C = \cosh\left(\frac{1}{2E^{1/2}}\right). \end{aligned}$$

In the limit of infinite radius, the radial portion of the streamfunction, $R(r)$, can be defined so that the flow is dynamically consistent, preserving momentum in a force balance between Coriolis, pressure gradients, and friction at low E. One such dynamically consistent solution for R is

$$R = \frac{r^2}{2}.$$

For a finite radius, with a assumed to be near 1, this kinematic model cannot fully solve the appropriate momentum equations. In this case, I define R as

$$R(r) = r^2(a - r)^2/2, \tag{2.4}$$

giving velocities

$$\begin{aligned} U &= \tfrac{-\partial\Psi}{\partial z} &= r(a - r)^2[A\sin(\zeta)\cosh(\zeta) + B\cos(\zeta)\sinh(\zeta)], \quad (2.5) \\ W &= \tfrac{\partial\Psi}{\partial r} &= -(a - r)(a - 2r)E^{1/2}F(z) \quad (2.6) \end{aligned}$$

where U is radial and W is vertical.

The axisymmetric azimuthal velocity V is defined

$$V(r, z) = r(a - r)^2[\frac{1}{2} + B\sin(\zeta)\cosh(\zeta) - A\cos(\zeta)\sinh(\zeta)]. \tag{2.7}$$

This velocity leads to typical nondimensional trajectory rotation times of $18 - 200$ for all Ekman numbers examined; the central orbit, beginning at $(r, z) = (0.5, 0.5)$ has a period of 20. Model velocities are typically between 0.01 and 0.1 in magnitude, which are reasonable ocean velocities in meters per second. This choice of the velocity scale being $1m/s$ gives rotation times of about 3.5 hours and overturning times of 7 hours to 3 days. For all parameter values, there is upwelling in the center ($r = 0$) and weaker downwelling near the sides of the cylinder (strongest at $r = 0.75$). There is horizontal convergence near the bottom and divergence near the top; for E near one, these are true for the full bottom and top halves of the system.

As the Ekman number varies, the overturning streamfunction changes qualitatively (figure 2-1). For E greater than 1/60, which is the first bifurcation descending from one, the overturning structure is rounded and has a single cell— there is only one fixed point in the overturning flow away from the boundaries: a periodic circular trajectory in the full flow. For small E, there is vertical rigidity. As E decreases, the time for a trajectory to complete one overturn increases, from about 30 for $E = 0.25$ to about 180 for $E = 0.0005$.

These changes in the streamfunction correspond with an increase in the number of circular periodic trajectories at $r = 0.5$. These trajectories are fixed points in a vertical cross-section, meaning that the vertical and radial velocities are zero; I call these *rz-fixed points*. All rz-fixed points occur at $r = 0.5$; there is always one at $z = 0.5$. New rz-fixed points appear through pitchfork bifurcations, with the first bifurcation at $E = 1/62 \approx 0.016$. Thus for $E \in \{0.25, 0.125, 0.02\}$, there is one rz-fixed point, while for the smallest Ekman number I discuss, $E = 0.0005$, there are 13. Further information about these bifurcations is in Appendix A.

2.2.1 Steady Symmetry-Breaking Perturbation

The perturbation which breaks the axial symmetry in this model approximates a lid rotating off-center. It is a horizontal flow that decays in strength with depth. The streamfunction is:

$$\widetilde{\Psi} = \epsilon \frac{-\sinh(z/E^{1/2})}{2\sinh(1/E^{1/2})}(a^2 - r^2)(\gamma^2 a^2 - s^2), \; s = \sqrt{(x - x_0)^2 + y^2}, \tag{2.8}$$

where s is the distance from the rotational axis of the lid at $y = 0$, $x = x_0$, γ adjusts the radial structure of the perturbation strength, and ϵ sets the overall strength of the perturbation. This streamfunction is for velocities in the x and y directions, unlike the background overturning streamfunction which was for vertical and radial; the velocities from the two are added together. The

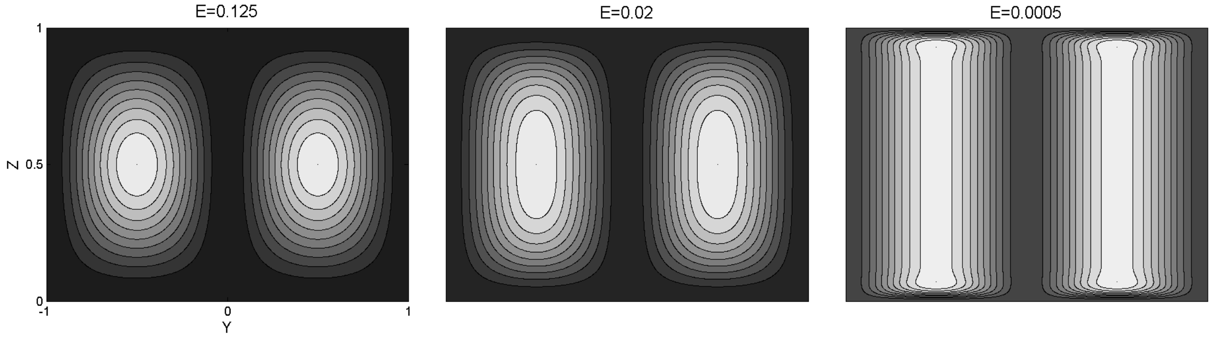

(a) overturning

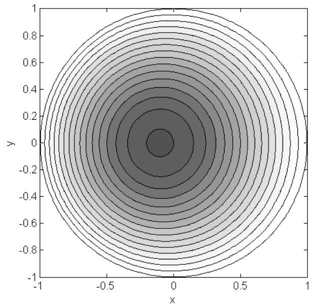

(b) perturbation

Figure 2-1: Background overturning streamfunction for $a = 1$ and horizontal perturbation streamfunction for $\gamma = 2$, $x_0 = -0.5$. Left to right: overturning $E = 0.125$, $E = 0.02$, $E = 0.0005$, horizontal perturbation. Note the vertical structure in the overturning streamfunction becoming similar to Taylor columns as E gets smaller. Note that the center of rotation in the perturbation streamfunction is not at the origin.

perturbation velocities in x and y are

$$\tilde{u} = \partial\widetilde{\Psi}/\partial y = 4y\epsilon\frac{\sinh(z/\sqrt{E})}{\sinh(1/\sqrt{E})}\left[(a^2 - r^2) + (\gamma^2 a^2 - s^2)\right],$$

$$\tilde{v} = -\partial\widetilde{\Psi}/\partial y = -4y\epsilon\frac{\sinh(z/\sqrt{E})}{\sinh(1/\sqrt{E})}\left[(x - x_0)(a^2 - r^2) + x(\gamma^2 a^2 - s^2)\right].$$

One can then write the azimuthal velocity perturbation as

$$\tilde{V} = -2\epsilon\frac{\sinh(z/\sqrt{E})}{\sinh(1/\sqrt{E})}\left[(a^2 - r^2) + (\gamma^2 a^2 - s^2) - \frac{x_0}{r}\cos(\theta)(a^2 - r^2)\right]$$

and the radial as

$$\tilde{U} = 2\epsilon x_0\frac{\sinh(z/\sqrt{E})}{\sinh(1/\sqrt{E})}\sin(\theta)(a^2 - r^2).$$

The horizontal streamfunction of the perturbation changes sign within the domain for small γ, making a section of the perturbation have the opposite sign of rotation, which is not physically possible for a solid lid. The streamfunction's overall strength is proportional to γ for larger values, decaying exponentially with depth. For the rest of the work, I will use $a = 1$ and $\gamma = 2$ (figure 2-1). It is important to note that the total (background plus steady perturbation) azimuthal velocity can be zero at some locations in the domain for certain choices of ϵ, but with $\epsilon < 0.05$ these locations are all very close to the boundaries of the cylinder.

2.2.2 Comparison to Dynamic Model

In this section I compare the kinematic model to the Navier-Stokes simulation of a rotating cylinder flow by Pratt et al. (2013). I will use the kinematic model for the analyses in sections 3.1 and 3.2, and the dynamic simulation for the analysis in section 3.3. I am interested in comparing the qualitative features of the two model flows under steady symmetry-breaking perturbation. It is important to note that the parameters of the two systems are slightly different. The parameters that arise in the Navier-Stokes simulation are the Ekman number, E, the aspect ratio, α, the displacement of the lid's center, x_0, and the Rossby number, Ro. The kinematic model parameters are the Ekman number, E, the aspect ratio, a, the displacement of the perturbation, x_0, and the strength of the perturbation, ϵ. For matching the kinematic model to the dynamic simulation, aspect ratio of one is the same, $\alpha = a = 1$, and I examine four Ekman numbers used in the previous work, $E \in \{0.25, 0.125, 0.02, 0.0005\}$. The displacement and strength of the kinematic perturbation are adjusted to match the behavior for a given Rossby number and displacement of the lid in the dynamic simulation. I do this rather than attempting a mathematical equivalence because the kinematic perturbation has a different form than a physical lid rotating off-center. This kinematic model assumes a small Rossby number, so I compare my results to those from Pratt et al.'s $Ro = 0.2$.

My primary method of looking at structure in the flow is through Poincaré sections, where a vertical slice through the cylinder such as the $y - z$ plane is selected and the crossing locations of certain trajectories is marked by dots. Quasiperiodic trajectories' crossing locations densely cover a curve in the plane, while periodic trajectories have a finite number of crossings. In the unperturbed case, all trajectories are periodic (rz-fixed points in the previous discussion) or quasiperiodic, lying on a toroidal surface. When the perturbation is added, some trajectories change their qualitative behavior, and a third type can be seen: these are chaotic trajectories, which wander through a volume in space aperiodically, never exactly repeating their path. The breakup of periodic trajectories into quasi-periodic ones surrounded by aperiodic regions is the process by which chaos is introduced into the system. Certain quasiperiodic trajectories enclose *islands* of *regular flow* which contain only quasiperiodic and periodic trajectories, in contrast to the chaotic flow nearby. A more detailed discussion of these regions is in Pratt et al. (2013) for this system and in many other works for more general geometries (e.g. Fountain et al. 2000).

Figure 2-2 shows Poincaré maps from the dynamical simulation in the top row with maps from the kinematic model below. There is a good match of qualitative features, meaning the number of islands, their positions, and the widths of chaotic regions. In the central and outermost regions of the cylinder, there is a chaotic region shown across all cases which I call the chaotic sea. In the three smaller E cases there are many more points near the surface than near the bottom; this is due to the higher horizontal velocities near the surface, and is seen in both the dynamic and kinematic model. In $E = 0.25$, both Poincaré sections show a series of nested closed curves which are quasiperiodic trajectories on nested tori. Between these are some thin resonant layers with high numbers of islands, in white, which are regular regions. For $E = 0.125$, the main feature is a series of larger islands between a set of nested tori and the main chaotic region. For $E = 0.02$, there is one large island with a number of resonant layers surrounding it, including small islands. For

$E = 0.0005$, the kinematic model has a more vertical structure than the dynamic, but the surface islands are in the same position and the island chains near the center of the cylinder are present in both.

Altogether, it is clear that the kinematic model's structures match the dynamic simulation in the main patterns: the number of islands is large for small and large E, while the island widths are small for small and large E. The chaotic regions surrounding the islands follow the same pattern in width as the islands. These chaotic region widths will be important in the next section.

A second method to examine the flow is Finite-Time Lyapunov Exponents (FTLEs). FTLEs are the time constants in the exponential rate at which two trajectories separate from each other in a flow:

$$\Delta x_i = e^{\lambda_i \Delta t},$$

where λ_i is the FTLE, Δx_i is the change in the spatial separation, and $i \in [1, 2, 3]$ is the index of direction. In order to measure the maximum stretching rates, the FTLE are calculated from the eigenvalues of the Cauchy-Green deformation tensor, rather than calculating the changes in separation in the x, y, z directions. In a 3D system there are three FTLEs; these may be ordered

$$\lambda_1 \geq \lambda_2 \geq \lambda_3,$$

where for incompressible flow $\lambda_1 > 0,\ \lambda_3 < 0$, and $\lambda_1 + \lambda_2 + \lambda_3 = 0$. I identify the structures here with λ_1 for the kinematic model. FTLEs are not available from the dynamic model. The FTLE calculation is based on initial and final positions of trajectories and the finite amount of elapsed time. I used an initial separation of 0.01 and an integration time of 400. Low values indicate regular regions where, for infinite time, the exponent approaches zero. High values indicate the exponential stretching and folding characteristic of chaos. The colored portions of figure 2-2 show the FTLEs calculated for the kinematic model. Regions in blue-yellow typically are the regular regions and correspond to white islands in the Poincaré section. Red regions generally correspond to chaotic regions. The three higher values of E show a clear correspondence for the main islands. Interestingly, for $E = 0.0005$, trajectory pairs in the near-surface island undergo slower separation than pairs in the bottom island. This difference indicates a better match with the dynamic system, which has only the near-surface island, than seen in the Poincaré map alone. This ability of different

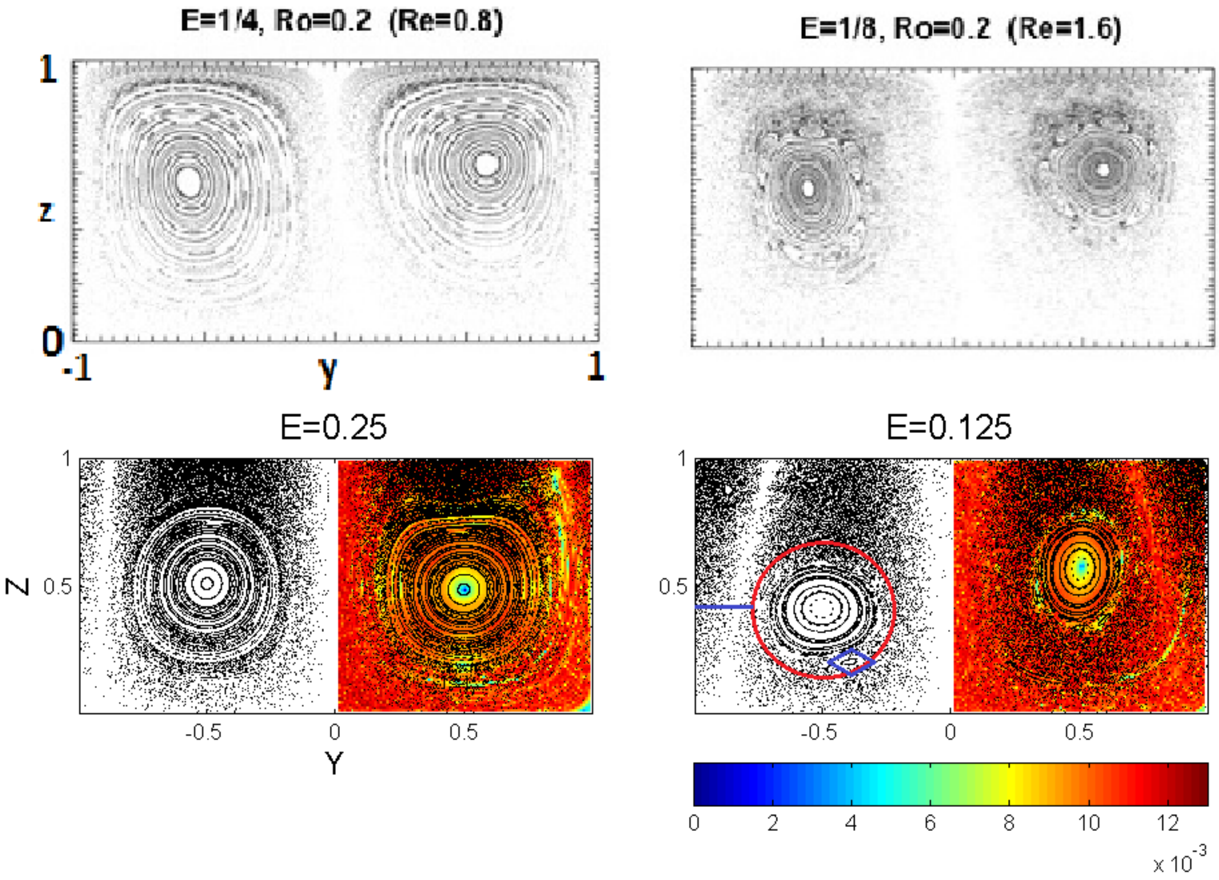

(a)

Figure 2-2: Structures in the kinematic model and dynamical simulation for Ekman numbers of 0.25 and 0.125, continued on next page.

measurements to complement each other is why I examine this system in multiple ways in section 3, and will be discussed further in section 4.

2.3 Observing Chaotic Advection: Can it overcome diffusion?

I examine the relative importance of chaotic advection and eddy diffusion for tracer distribution using three types of methods. I begin with scaling arguments: a Lagrangian Batchelor scale defines the thinnest filaments that can form based on the balance between advection, measured by finite-time Lyapunov exponents (FTLEs), and diffusion, estimated using the Okubo (1971) empirical

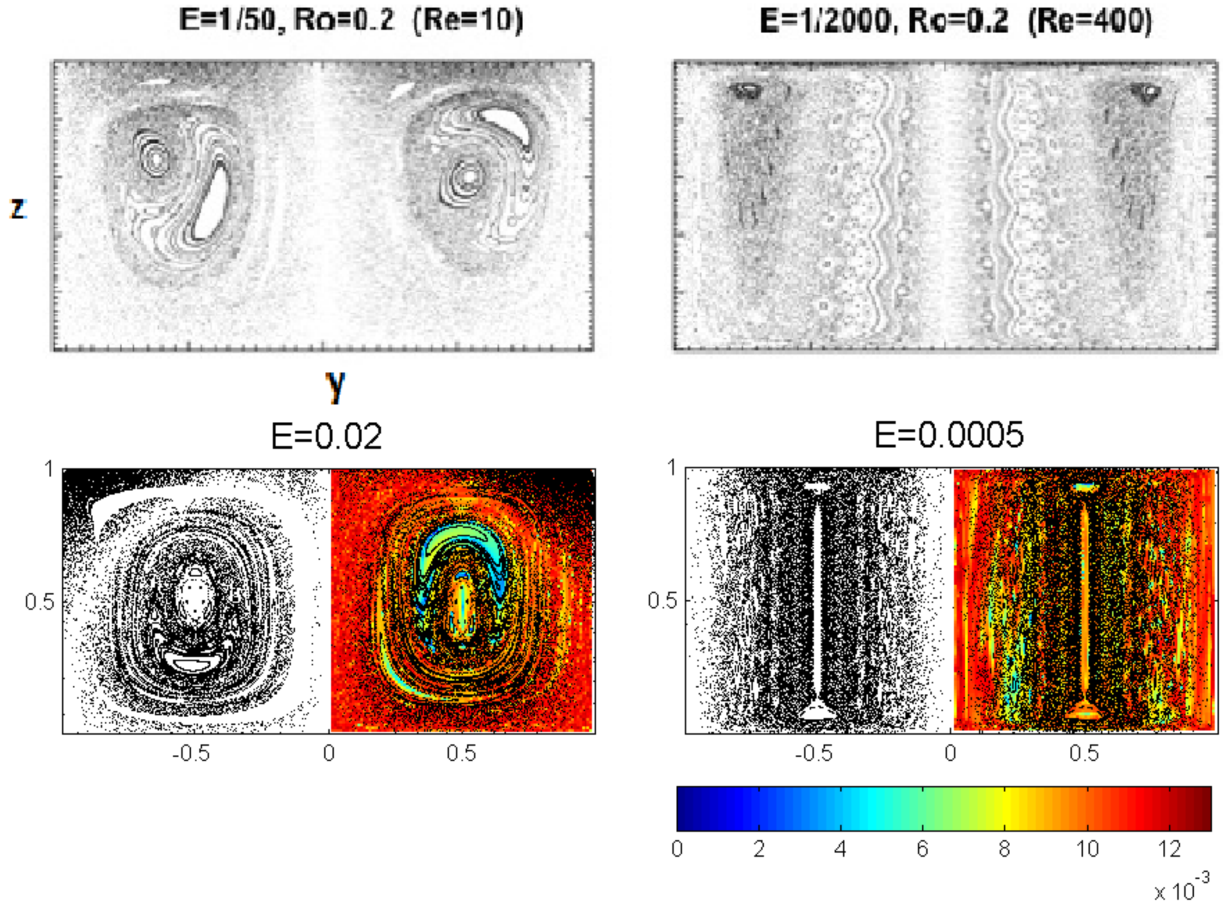

(b)

Figure 2-2: Structures in the kinematic model and dynamical simulation for Ekman numbers of (a) 0.25 and 0.125, (b) 0.02 and 0.0005. Tops: Poincaré maps from Pratt et al. 2013, using the dynamic simulation. Bottoms: in black, Poincaré maps from the current kinematic model with $\epsilon = 0.01$ and x_0 either -0.5 (left) or -0.9 (right); in color, maximum FTLEs calculated for the kinematic model with integration time 400. For $E = 0.125$, red oval approximately separates the resonant and regular layers (inside) from the chaotic sea region (outside), with the blue line segment showing the width of the chaotic sea. The blue diamond shows the width of an island, which is also the width of the resonant layer.

estimates. If the thinnest filaments are wider than the chaotic zone, then I conclude that diffusion is the dominant process. I also compare the timescales of chaotic advection and diffusion: the behavior is dominated by the process with shorter timescales. Second, ensembles of individual trajectories are computed in the kinematic rotating cylinder model with either a steady perturbation that induces chaos, a stochastic perturbation to emulate diffusion, or both. The spread of trajectory ensembles across the background streamlines is used as a measure of the importance of each perturbation, with the dominant perturbation being the one causing a wider spread. Finally, numerical dye releases in a dynamically consistent model are used to quantify the effects of stirring on mixing through the tracer variance function and Nakamura's effective diffusivity. I use the slopes of the tracer variance function and the values of the effective diffusivity to measure the effects of chaotic advection.

To relate the kinematic model to ocean eddies, I set dimensional length and velocity scales. The main parameter of the background model is the Ekman number, which relates the eddy depth to the Ekman depth. Due to the unstratified nature of my flow, I focus on two intermediate Ekman numbers: $E = 0.125$ and $E = 0.02$. Assuming an Ekman depth of about $40m$, within the range of open-ocean observations (see Lenn and Chereskin 2009 and references therein), my shallower eddy is about $110m$ deep. In contrast, $E = 0.02$ would correspond to an eddy depth of about $280m$. Depending on region and season, it is possible for either of these to be within or deeper than the surface mixed layer, which can reach $300m$ in subpolar regions in the winter, but may decrease to a few meters in the summer. In order to relate the model to ocean eddies, it is necessary to dimensionalize velocities. Unfortunately, the background model has only one physical parameter, the Ekman number, which I used for scaling length. Model velocities are typically between 0.01 and 0.1 in nondimensional magnitude, which are reasonable dimensional ocean velocities if imagined to be in meters per second. For that to be the case, the velocity scaling factor is $1m/s$, a choice that gives rotation times of about 3.5 hours and overturning times of 7 hours to 3 days.

2.3.1 Scaling Derivations

Chaotic advection thins tracer patches through exponential contraction in one or two directions, decreasing the relevant lengthscale towards small scales where diffusion is dominant. Diffusion widens tracer patches by moving tracer down its gradient, spreading it out from its maximum. The length scale at which advection and diffusion balance in their respective thinning and widening of a patch of tracer is the Batchelor scale, δ. Below δ, diffusion dominates tracer behavior, while above δ advection dominates. If δ is larger than the structures in the flow induced by chaos, then diffusion will overcome advection and wipe out these structures. The structures of interest, induced by steady perturbation and visible in Fig. 2-2, are the bands of chaos, called resonant layers, that thread between regular islands (see blue diamond in (a), right), and the chaotic sea region (outside the red oval in (a), right), which is near the cylinder perimeter and central axis.

Tracer filaments' thinnest width will approach the Batchelor scale regardless of initial conditions. If one considers an initial patch of tracer that is far from the Batchelor scale, advection and diffusion will not balance. If the patch is larger than the Batchelor scale, chaotic advection exponentially constricts the patch in the direction of fastest contraction so that it approaches the Batchelor scale. If the patch of tracer is smaller than the Batchelor scale, diffusion widens the patch to approach the Batchelor scale. When the width of a filament is at the Batchelor scale, the width will be steady in time but the concentration will continue falling.

Traditional formulations of the Batchelor scale use statistical and Eulerian information about turbulence, particularly strain rate, to find the scale at which advective and diffusive effects balance (Kolmogorov 1941). In a Lagrangian frame moving with the tracer patch, the Lyapunov exponent is the appropriate descriptor of advective stretching. Several rigorous derivations of a Lagrangian Batchelor scale have been presented using wavenumber spectra (e.g. Thiffeault 2008, Fereday and Haynes 2004, DT Son 1999), and a few papers have used this type of scaling to estimate the importance of chaotic advection (Rypina et al. 2010, Ledwell et al. 1993 1998). I present here some intuitive explanations for the formulation of a Lagrangian Batchelor scale that are less rigorous than the former but more in-depth than the latter.

The first formulation of the Lagrangian Batchelor scale is through dimensional analysis. I use the contracting Lyapunov exponent, λ_3, as the inverse timescale together with the diffusivity κ to form the length

$$\delta = \sqrt{\kappa/|\lambda_3|}.$$

I have used the Lyapunov exponent rather than an Eulerian strain rate for two reasons. First, in chaotic flow, the Lyapunov exponent measures time-average strain. Second, I am interested in the width following the tracer filament, so a Lagrangian measure is appropriate.

The second formulation of the Lagrangian Batchelor scale uses the equation for the evolution of the dye gradients, and demonstrates the importance of the gradient of the velocity, a direct connection to the FTLE. The tracer gradient equation can be derived from the tracer evolution equation

$$\frac{\partial C}{\partial t} + (\nabla \cdot \vec{u})C + \vec{u} \cdot \nabla C = \kappa \nabla^2 C,$$

where C is tracer concentration, $\vec{u}$ is a three-dimensional velocity field, and κ is the diffusivity. Given conservation of volume, the second term is zero. The tracer gradient equation is the gradient of the tracer equation, which is

$$\frac{\partial}{\partial t}\frac{\partial C}{\partial z} + \frac{\partial}{\partial z}(\vec{u} \cdot \nabla C) = \kappa \frac{\partial}{\partial z} \nabla^2 C$$

in the z direction and analogous for other directions. Suppose that the tracer gradients in the x and y direction are small, because the advection and diffusion work together to spread the tracer in those directions, becoming fairly uniform compared to the z direction, in which the patch is thin. Then the evolution of the gradients in the z direction can be written as

$$\frac{\partial}{\partial t}\frac{\partial C}{\partial z} + \frac{\partial}{\partial z}\left(w \frac{\partial C}{\partial z} \right) = \kappa \frac{\partial^3 C}{\partial z^3}.$$

Expanding the second term and combining part of it with the first to form the material derivative gives

$$\frac{\partial}{\partial t}\frac{\partial C}{\partial z} + w\frac{\partial^2 C}{\partial z} + \frac{\partial w}{\partial z}\frac{\partial C}{\partial z} = \frac{D}{Dt}\frac{\partial C}{\partial z} + \frac{\partial w}{\partial z}\frac{\partial C}{\partial z} = \kappa \frac{\partial^3 C}{\partial z^3}.$$

When the filament width is near equilibrium, gradients in the thinning direction are changing very little with time while following the filament, so the strain and diffusive terms must be of the same size. To scale $\partial w/\partial z$ I use $|\lambda_3|$, because spatial changes in w determine the rate at which nearby trajectories converge. This can be illustrated with an initial sphere evolving in a linear flow (figure 2-3): while the mean flow moves the trajectories together, the gradients of the flow change their spacing, with linear strain corresponding to exponential changes in ellipsoid axis lengths. This exponential spreading rate can be measured by the FTLE, which averages the strain along trajectory paths during the integration time. I use δ as a scale for distance, giving a balance between advection and diffusion of the form

$$|\lambda_3| \frac{|c|}{\delta} \approx \kappa \frac{|c|}{\delta^3}.$$

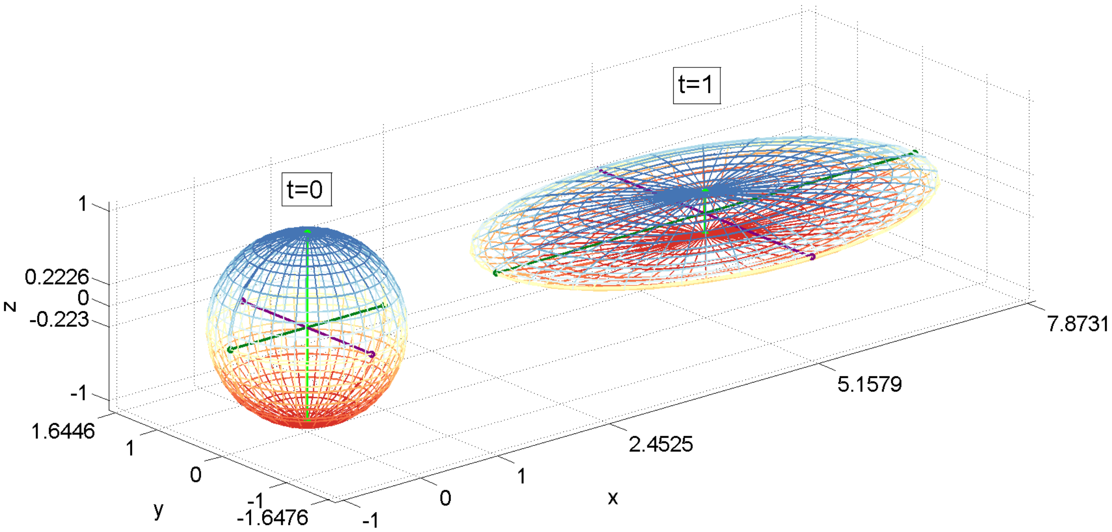

Figure 2-3: An initial sphere in a linear strain field evolving into an ellipsoid during a time of 1. Ellipsoid axes marked by bars, with figure axes ticks showing their initial values of 1 and their individual endpoint values. Color shows z values at $t = 0$, demonstrating the contraction in the z direction. Velocity field $u = 1.5 + x$, $v = 0.5y$, $w = -1.5z$.

Simplifying gives the expected expression for the Lagrangian Batchelor scale:

$$\delta \approx \sqrt{\kappa / |\lambda_3|}, \tag{2.9}$$

with the approximate indication because tracer gradients will decrease slowly as the tracer maximum decreases.

For my final formulation of the Lagrangian Batchelor scale, I show analytically that the width of a Gaussian tracer distribution asymptotically approaches the Batchelor scale in a simple flow field. This derivation is similar to that of Flierl and Woods (2015), which was two-dimensional. First, I assume that in the Lagrangian frame the velocity field is a linear strain with rates λ_i in each direction, such that the sum of the λ is zero, giving an incompressible flow. For example,

$$\begin{aligned}
w &= \lambda_3 z(\vec{x_0}, t), \\
v &= \lambda_2 y(\vec{x_0}, t), \\
u &= \lambda_1 x(\vec{x_0}, t), \\
&\lambda_1 > \lambda_2 > \lambda_3, \\
&\lambda_1 > 0,\ \lambda_3 < 0
\end{aligned}$$

characterizes such a flow with the same properties of λ previously described, with $\vec{x}(\vec{x_0}, t)$ indicating the initial position $\vec{x_0}$ of the water parcel at $t = 0$. The FTLE is an average of the contraction or expansion rate over the path of trajectories, but here the rate is constant. Second, I assume that the tracer concentration C is initially a Gaussian in form in each direction, and look for a solution where it remains that way. This form provides the well-defined width, which is the standard deviation of the Gaussian. Now I write the Lagrangian tracer evolution equation

$$\frac{\partial C}{\partial t} + \lambda_3 z \frac{\partial C}{\partial z} + \lambda_2 y \frac{\partial C}{\partial y} + \lambda_1 x \frac{\partial C}{\partial x} = \kappa \nabla^2 C, \tag{2.10}$$

and the expected form of C

$$C = c_{max}(t) \exp\left(\frac{-x^2 \alpha^2(t)}{2} + \frac{-y^2 \beta^2(t)}{2} + \frac{-z^2 \gamma^2(t)}{2} \right). \tag{2.11}$$

Here, c_{max} is the maximum concentration and α β γ are the reciprocals of the standard deviations in each direction. These four parameters are dependent on time, but not space. The smallest width, or standard deviation, of the distribution is $\sigma = 1/\gamma$ and I look for a stable fixed point of σ. To find the behavior of the parameters I isolate $\partial C/\partial t$ from equations 2.10 and 2.11 and equate them:

$$\frac{\partial C}{\partial t} = \frac{\partial C}{\partial c_{max}} \frac{dc_{max}}{dt} + \frac{\partial C}{\partial \alpha} \frac{d\alpha}{dt} + \frac{\partial C}{\partial \beta} \frac{d\beta}{dt} + \frac{\partial C}{\partial \gamma} \frac{d\gamma}{dt} = -\lambda_3 z \frac{\partial C}{\partial z} - \lambda_2 y \frac{\partial C}{\partial y} - \lambda_1 x \frac{\partial C}{\partial x} + \kappa \nabla^2 C.$$

Plugging in the form for C gives

$$\begin{aligned}\frac{\partial C}{\partial t} &= \frac{C}{c_{max}}\frac{dc_{max}}{dt} - x^2\alpha C\frac{d\alpha}{dt} - y^2\beta C\frac{d\beta}{dt} - z^2\gamma C\frac{d\gamma}{dt} \\ &= \lambda_1 x^2\alpha^2 C + \lambda_2 y^2\beta^2 C + \lambda_3 z^2\gamma^2 C + \kappa C\left[x^2\alpha^4 - \alpha^2 + y^2\beta^4 - \beta^2 + z^2\gamma^4 - \gamma^2\right].\end{aligned}$$

Dividing by C (assuming the dye is not uniformly zero), leaves a single equation but four parameters of interest. This equation is a polynomial in x, y, z, with constant and x_i^2 terms. I can therefore separate these terms by order in x_i, giving

$$\begin{aligned}\frac{1}{c_{max}}\frac{dc_{max}}{dt} &= -\kappa\left(\alpha^2 + \beta^2 + \gamma^2\right), \\ -\alpha x^2\frac{d\alpha}{dt} &= \lambda_1\alpha^2 x^2 + \kappa\alpha^4 x^2, \\ -\beta y^2\frac{d\beta}{dt} &= \lambda_2\beta^2 y^2 + \kappa\beta^4 y^2, \\ -\gamma z^2\frac{d\gamma}{dt} &= \lambda_3\gamma^2 z^2 + \kappa\gamma^4 z^2.\end{aligned}$$

Now I can solve algebraically from the x_i^2 terms, finding

$$\begin{aligned}\frac{d\alpha}{dt} &= -\lambda_1\alpha - \kappa\alpha^3, \\ \frac{d\beta}{dt} &= -\lambda_2\beta - \kappa\beta^3, \\ \frac{d\gamma}{dt} &= -\lambda_3\gamma - \kappa\gamma^3.\end{aligned}$$

The differential equations for α, β, γ only have a fixed point when $\lambda_i < 0$, which is only certain for λ_3. That fixed point occurs when

$$\begin{aligned}\frac{d\gamma}{dt} &= -\lambda_3\gamma - \kappa\gamma^3 = 0, \\ \implies \gamma &= \sqrt{|\lambda_3|/\kappa}, \\ \implies \sigma &= \sqrt{\kappa/|\lambda_3|},\end{aligned}$$

giving that the width of the Gaussian in the fastest contracting direction has a fixed point at the

Batchelor scale, as expected. Mathematically there are also fixed points at $\gamma = 0$ with negative λ_3 and at $\gamma = -\sqrt{|\lambda_3|/\kappa}$ for positive λ_3, but neither corresponds to a real positive tracer distribution. The positive fixed point is attracting if the derivative of $d\gamma/dt$ is negative there, which I check:

$$\begin{aligned} \frac{d}{d\gamma}\frac{d\gamma}{dt} &= \frac{d}{d\sigma}\left(-\lambda_3\gamma - \kappa\gamma^3\right) \\ &= -\lambda_3 - 3\kappa\gamma^2 = \frac{d\gamma}{dt} - 2\kappa\gamma^2. \end{aligned}$$

Since γ and α are positive, this derivative is negative at the fixed point, so this fixed point is attracting. For any initial width, the width in the λ_3 direction will converge to the Lagrangian Batchelor scale. The full solution for γ is

$$\gamma = \sqrt{|\lambda_3|/\kappa}\left((\lambda_3\gamma_0^{-2}/\kappa - 1)e^{2\lambda_3 t} + 1\right)^{-1/2}.$$

Details on this solution and the full solution for C are in Appendix A.

The relative importance of chaotic advection and diffusion may also be thought of in terms of timescales, in that the one which affects tracer gradients faster is more important. The timescale for chaotic advection is the inverse of the Lyapunov exponent, $1/\lambda$. The timescale for diffusion can be found using dimensional analysis. The time it takes for diffusion to spread a tracer across a distance L is

$$\tau = \frac{L^2}{\kappa}, \tag{2.12}$$

where κ is the diffusivity. The processes with the smaller timescale, between τ for diffusion and $1/\lambda$ for advection, is the faster, more dominant process.

2.3.2 Scaling Results

In this section, I calculate the Lagrangian Batchelor scale and the chaotic advection and diffusion timescales for the rotating cylinder. In order to calculate the Lagrangian Batchelor scale, δ, I use an empirical description of oceanic diffusivity as described in Okubo (1971) for diffusivity κ. In the ocean, diffusivity is scale-dependent, increasing with size, as described by Okubo. He used observations of horizontal dye diffusion at various scales ranging between about $20m$ and $2000km$

to find the empirical relationship

$$\kappa = 0.0103 l^{1.15}, \tag{2.13}$$

where l is the horizontal lengthscale of the dye patch in cm and κ is in cm^2/s. Although horizontal and vertical diffusivities in the ocean can vary by orders of magnitude, due to the constant density in my model, I assume an isotropic three-dimensional diffusivity. The scale-dependence of diffusivity means that the strength of the diffusion that balances advection depends on the scale at which the balance occurs. This self-dependence can be solved to find the balancing width, the Batchelor scale δ, by combining Okubo's κ and my δ definitions, with $l = \delta$, as follows:

$$\delta = \kappa^{0.5}\lambda^{-0.5} = (0.0103\delta^{1.15})^{0.5}\lambda^{-0.5},$$
$$\delta = (0.0103/\lambda)^{5/4.25} \approx 0.0046\lambda^{-1.18};$$

with the final expression as in Rypina et al. (2010), remembering that λ here must be dimensional ($1/s$) and δ will be in centimeters. In even slightly stratified ocean flows, the vertical diffusivity is smaller than the horizontal, so the Batchelor scale calculated here is an upper estimate, $\delta_{strat} \leq \delta$. Therefore, when the calculated δ is smaller than the features of interest, one can expect that chaotic advection effects would dominate over diffusion for the spreading of a tracer.

The calculated δ values are shown in figure 2-4 next to the widths of chaotic regions. The range of δ values is due to the range of λ_3 in the region. For the region widths, the resonant layer widths are the width of the embedded islands; the outer chaotic sea width is the range of distances from the edge of outer islands to the cylinder boundary (figure 2-2a has an example). FTLEs are estimated for the most contracting direction over an integration time of about 20 rotations of the central orbit (dimensionally about three days); the range of FTLE magnitudes does not noticeably change from 10 to 20 rotations. The Batchelor scale is generally about $0.01 - 0.08$ in nondimensional width, or $1 - 100m$ dimensionally, which is similar to the resonant layer widths and smaller than the chaotic sea widths. These results imply that chaotic advection is expected to influence tracer distribution throughout the system, but dominate only in the wider chaotic sea region.

To calculate the advective and diffusive timescales, I use the same FTLE and Okubo diffusivities as for the Batchelor scale. I estimate the time it takes for the dye to diffuse across a regular island to quantify the diffusive timescale, τ. I use the numerically estimated island widths, L, from Poincaré

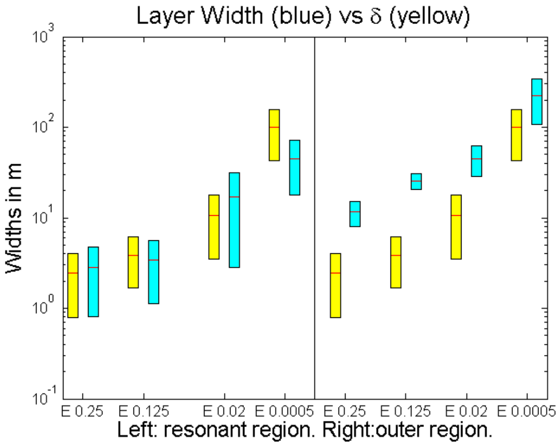

Figure 2-4: Layer widths in blue, Lagrangian Batchelor scale δ in the same region in yellow. Left half, chaotic resonant region between islands; right half, the chaotic sea region. The diffusivities at the Batchelor scale in m^2/s are between 10^{-4} and $6 \cdot 10^{-3}$ for the three larger Ekman numbers and between $1 \cdot 10^{-2}$ and $6 \cdot 10^{-2}$ for $E = 0.0005$.

sections (the same as resonant region widths in figure 2-4), and the diffusivities, κ, from Okubo's scaling to form

$$\tau = \frac{L^2}{\kappa} = \frac{L^2}{0.0103 L^{1.15}} \approx 97 L^{0.85}. \tag{2.14}$$

The diffusive timescale τ can then be compared to the chaotic advective timescale λ^{-1}, which is a few hours. Figure 2-5 shows τ for the model island regions and λ^{-1} for the adjacent resonant layers. These timescales are similar, which is to be expected when the layers are close to the Batchelor scale, as that is the length scale where diffusion and advection balance. For ocean applications, the timescales would inform observations. For the larger Ekman numbers, the timescales are hours, which indicates that observations of these features would require intensive work over about a day once an eddy was located.

2.3.3 Spreading of Trajectory Ensembles

I now examine the dispersion of sets of initially nearby trajectories for the relative effects of turbulent diffusion and chaotic advection. To simulate turbulent eddy diffusion, I add a stochastic velocity perturbation to the flow. I consider chaotic advection dominant compared to diffusion when the ensemble spread is greater for the steady perturbation that induces chaos than the stochastic perturbation that simulates diffusion. I examine ensembles of one hundred to three hundred trajectories

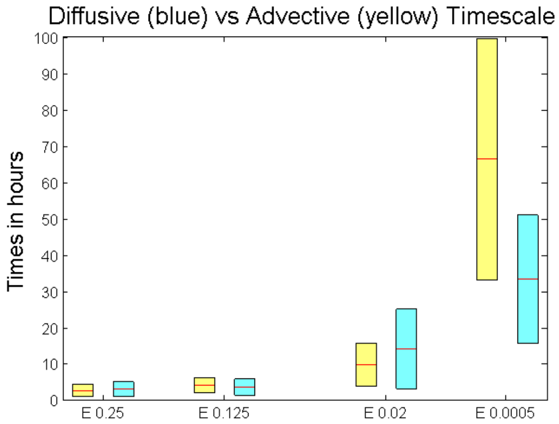

Figure 2-5: Diffusive crossing times for islands compared to chaotic advection timescale for adjacent chaotic resonant layer. Uses Okubo's estimate of diffusivity for the island width.

that begin inside a small sphere for their behavior under various perturbations. Other initial conditions, on a torus or axial circle, give similar results (not shown). The distance between trajectories in terms of ψ values, the streamfunction of the background flow, is then described over time. Examining the spread in ψ is convenient because it leads to zero spread for the background flow. However, it is important to note that this interpretation limits the directions of chaotic stretching that are considered— it is possible for the fastest spreading direction to be along the background streamlines, which would not be visible in the coordinates chosen.

To simulate diffusion, I add a stochastic velocity perturbation to the background model flow. The stochastic perturbation is a random flight model created by adding small pseudorandom values with a Gaussian distribution to the velocity at each timestep within a numerical trajectory integration:

$$\frac{dx_i}{dt} = U_i(\vec{x}) + u_i', \tag{2.15}$$

where i is a direction index, x is distance, U is the steady velocity, and u_i' are the stochastic additions. These velocity additions are uncorrelated and lead to a Gaussian random walk behavior (Zambianchi and Griffa, 1994). With the described stochastic perturbation, the variance of a set of trajectories will grow linearly in time, while the standard deviation grows linearly with the square root of time, as expected for diffusion. The diffusivity, κ, is computed from the 1D relationship for a Gaussian random walk: $\kappa = s^2/2\Delta t$, where s is the standard deviation of step size in the random walk. I primarily use a nondimensional diffusivity of 10^{-6} which corresponds to the Okubo diffusivity for a few meters, at the lower end of the Batchelor scales calculated in the previous section. The Okubo diffusivities at the Batchelor scale is $\kappa \in [10^{-4}, 10^{-2}] m^2/s$, which is nondimensionally $\kappa \in [10^{-6}, 3 \cdot 10^{-5}]$. This level of diffusivity, 10^{-6}, requires a certain step size s, which relates to the distribution of u' by $s = \sigma \Delta t/3$, with σ the standard deviation of u', Δt the numerical timestep (0.01), and the factor of 3 due to the details of a fourth-order Runga-Kutta integration. Together, these give

$$\kappa = \frac{\sigma^2 \Delta t}{18}, \tag{2.16}$$

and so $\sigma = 0.042$. I will also discuss a smaller stochastic perturbation, $\kappa = 10^{-7}$, $\sigma = 0.013$, and a larger one, $\kappa = 10^{-5}$, $\sigma = 0.13$. The stochastic perturbation with $\kappa = 10^{-6}$ has kinetic energy (integrated over the cylinder) that is about the same as the background flow: $\int (\vec{u'})^2 \approx \int (\vec{U}_b^2) \approx 0.63$, where $\vec{u'}$ is the stochastic velocity and $\vec{U}_b$ is the background flow velocity, and both are numerically integrated on the same grid. The perturbation with $\kappa = 10^{-7}$ has kinetic energy about the same as the steady perturbation with $\epsilon = 0.01$, $x_0 = -0.5$, $\int (\vec{u'})^2 \approx 0.075$, where now $\vec{u'}$ can be either perturbation velocity.

I use a straightforward example of the behavior of trajectories in ψ to explain the features of ensembles under chaotic and stochastic perturbations. Trajectories are started on a sphere in the chaotic sea region centered on $(r, z) = (0.1, 0.5)$ in $E = 0.125$ (see figure 2-2 for the Poincaré section). For the steady perturbation, trajectories oscillate through the background streamfunction because the perturbation velocities form an azimuthal wave (figure 2-6, top). Trajectories following the new streamlines are different distances from the initial streamfunction at different θ, nearly repeating due to the toroidal barriers formed by regular regions. The frequency of this oscillation depends on the exact location of the trajectory in the cylinder because the interaction of the steady perturbation and background flow varies in three dimensions. The trajectories, having different but similar frequencies in ψ, appear to have the same frequency and move out of phase over time, but in fact this behavior can be explained by frequency differences. Increases in the spread in ψ are largest near the minima and maxima of the oscillations (figure 2-6, upper). These turning points occur near the central axis of the cylinder, which is where trajectories pass near the central manifolds. These manifolds are two distinct material curves with one end anchored to $r = 0$ on the top or bottom; they are created from the breakup of the heteroclinic trajectory from $(r, z) = (0, 0)$ to $(r, z) = (0, 1)$

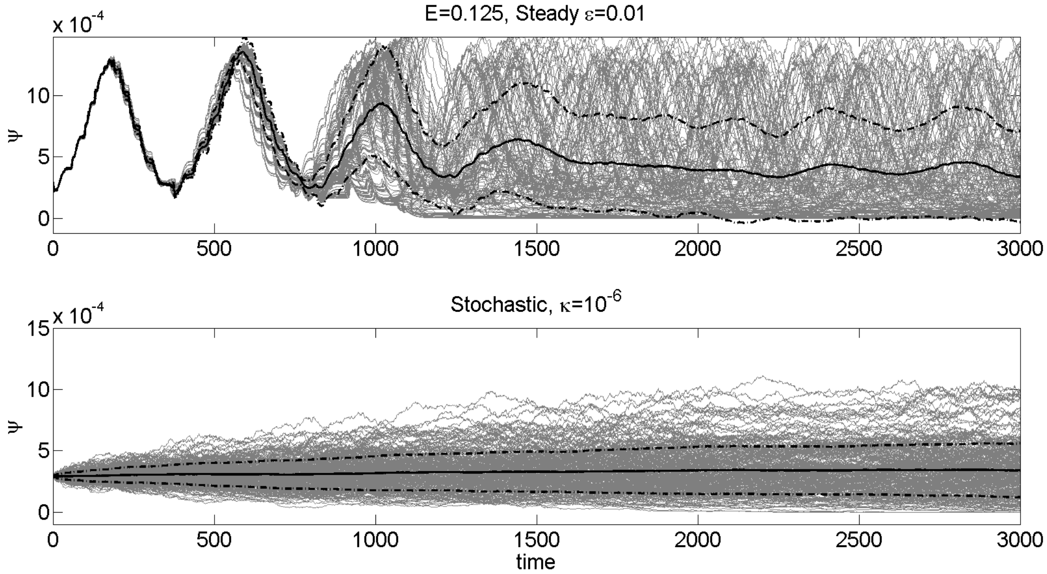

Figure 2-6: Grey lines are individual trajectories in ψ starting from a sphere of radius 0.002 at $(r, z) = (0.1, 0.5)$ with $E = 0.125$. Solid black curves are the mean; black dash-dot lines are ± 1 standard deviations from the mean.

in the background flow by the steady perturbation (see Pratt et al. 2013 for more). It takes a few cycles of overturning to have noticeable spreading, but then the spread grows quickly. The ensemble shown has one of the simpler wave structures I saw, with a large sinusoid dominating the behavior; with different initial conditions or a larger ϵ, the oscillations of individual trajectories in ψ look like a combination of several sinusoids and pulses.

For the stochastic perturbation, trajectories are uncorrelated as they spread across the background streamfunction. There are no repeating oscillations in time (figure 2-6, bottom) because the perturbation acts separately on each trajectory at each timestep, leading to continual spreading of the ensemble. This spreading is similar to diffusion, but it does not depend on the gradients of concentration the way a diffusing tracer would. If both perturbations are included (not shown), individual trajectories maintain most of their oscillatory behavior, but spread out at all times due to the stochastic perturbation, rather than only at the times they pass near the hyperbolic region around the central manifolds.

I next compare the spreading of trajectory ensembles in ψ with a variety of perturbations for the same initial conditions used to create figure 2-6 using the range over time (figure 2-7); results are similar when the variance in ψ is used for comparison (not shown). Chaotic advection dominates when the spread in ψ for an ensemble under steady perturbation is larger than the spread under stochastic perturbation. The spread from the steady perturbation appears exponential for a period of time, as expected, but is limited to the width of the chaotic region in which the ensemble begins. In contrast, the stochastic perturbation will spread with the square root of time until it reaches throughout the cylinder; the $k = 10^{-5}$ cases reach this limit before the end of the experiment. Therefore, the time when the steady perturbation has greater spread will be limited to between when exponential growth starts in the steady perturbation, which requires sufficient interaction with hyperbolic regions, and when the stochastic perturbation spreads the ensemble to the width of the chaotic region, as estimated for resonant layers in the previous section (figure 2-5).

In the chaotic sea region, ensembles with stochastic perturbations all have their ranges in ψ grow like the square root of time, just like they would in physical coordinates, and the spreading is faster for larger k as expected (figure 2-7ac). The ensembles with steady perturbations have a small range until they begin quickly growing between times 100 and 500, reaching the width of the chaotic region between times 500 and 4000. Larger steady perturbations lead to earlier and faster spreading, as well as a wider chaotic region. Comparing the spread of steady and stochastic perturbations for $E = 0.02$ shows that the $\epsilon = 0.01$ steady perturbation only dominates the $\kappa = 10^{-7}$ stochastic perturbation, with a wider spread for $t = 900 - 1100$. For $E = 0.125$, the chaotic sea is wider (see figure 8), and the $\epsilon = 0.01$ steady perturbation has a wider spread than the $\kappa = 10^{-6}$ stochastic perturbation for $t = 1000 - 6500$.

Since the diffusivities calculated near the Lagrangian Batchelor scale tend to be 10^{-6} to 10^{-5}, these results imply that turbulent diffusion would affect tracers more strongly than chaotic advection for $E = 0.02$. These two processes would be of similar strength for $E = 0.125$ in the chaotic sea for these steady perturbation strengths. If I now examine an ensemble with $\epsilon = 0.08$, it has a larger spread than the $\kappa = 10^{-7}$ ensemble from shortly after it begins spreading exponentially throughout the examined period for $E = 0.125$ and until at least $t = 4000$ in $E = 0.02$. This larger steady perturbation also spreads wider than the $\kappa = 10^{-6}$ ensemble for $t = 200 - 400$. For $E = 0.125$, the $\epsilon = 0.08$ ensemble spreads throughout the width of the cylinder, reaching that point at about $t = 300$, before the $\kappa = 10^{-5}$ ensemble, which is the upper limit of diffusivities calculated for the Batchelor scale. These results show that with stronger chaotic stirring from a stronger perturbation, chaotic advection would have a stronger effect on a tracer than diffusion in the chaotic sea.

As in the previous section, I can also consider the timescale of these processes. If I use the dimensionalization from the previous section, the timestep is 800s ($E = 0.125$) or 2000s($E = 0.02$), which means each section of length $t = 1000$ is about 10 days. These ensembles show that for the first day or two, turbulent diffusion dominates the spread, as chaotic advection does not yet show significant growth. Then, when the chaotic advection has caused spreading throughout the chaotic region, it will dominate over turbulent diffusion of similar kinetic energy for between two days and a month, before that diffusion is able to cause spreading across the chaotic region. Of course, these processes will be acting at the same time, not separately; the red curves in figure 2-7 are an example of small perturbations of both types. Spreading of the ensemble begins immediately, as with the stochastic perturbation, but experiences periods of pronounced growth and some oscillations, as seen with the steady perturbations. Therefore, I would expect to see filamentation and folding in physical space for some time in ensembles in the chaotic sea region with both perturbations; before and after this period, the ensemble would appear to be unstructured.

I also examined the behavior of trajectories beginning at $(r, z) = (0.4, 0.5)$, in the central region a small distance from the central fixed orbit. In these cases, the same behavior as in the chaotic sea region occurs for the spreading under stochastic perturbations (figure 2-7b,d). The spreading under steady perturbations is much smaller than in the outer chaotic sea region for $\epsilon = 0.01$, being bounded by islands. For these resonant regions, there is no single period of exponential growth apparent, rather a slower growth at all times. With $\epsilon = 0.08$, the steady perturbation shows exponential spreading to a saturated state as seen in the chaotic sea region; this large perturbation has eliminated the barriers seen in the small perturbation, and there is a wide chaotic region close to the central orbit.

From the spreading of ensembles of trajectories, one can see that the wider chaotic regions are where chaotic advection dominates over turbulent diffusion, as expected from the scaling results. However, those scalings did not include considerations of time, particularly when exponential stretching begins; the delay in the stretching decreases the period of time when chaotic advection is important. The $E = 0.02$ case for the resonant layer is also surprising, given the very large size of the main island and associated resonant region. It appears from the results that there are boundaries within that apparent resonant region, leading to the ensemble spreading into a thinner than expected chaotic region. From these ensembles, I would expect a set of passive 3D drifters or

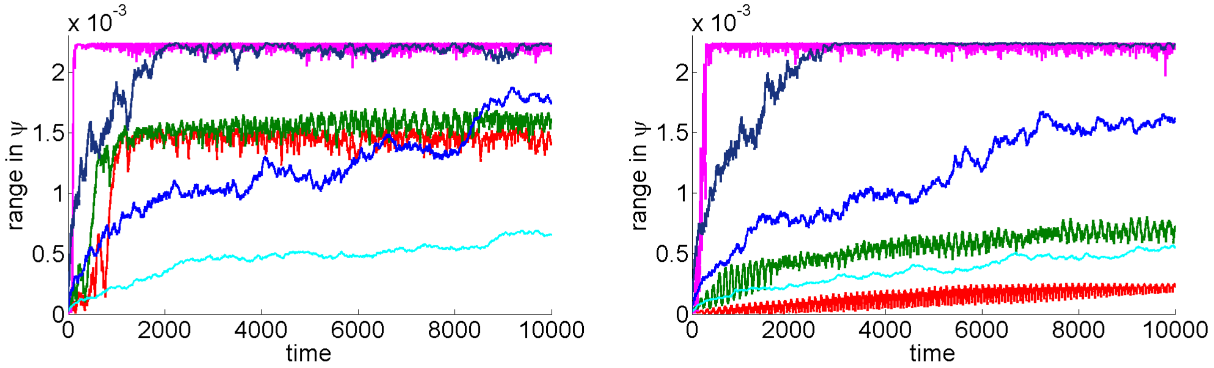

(a) $E = 0.125$ (b) $E = 0.125$

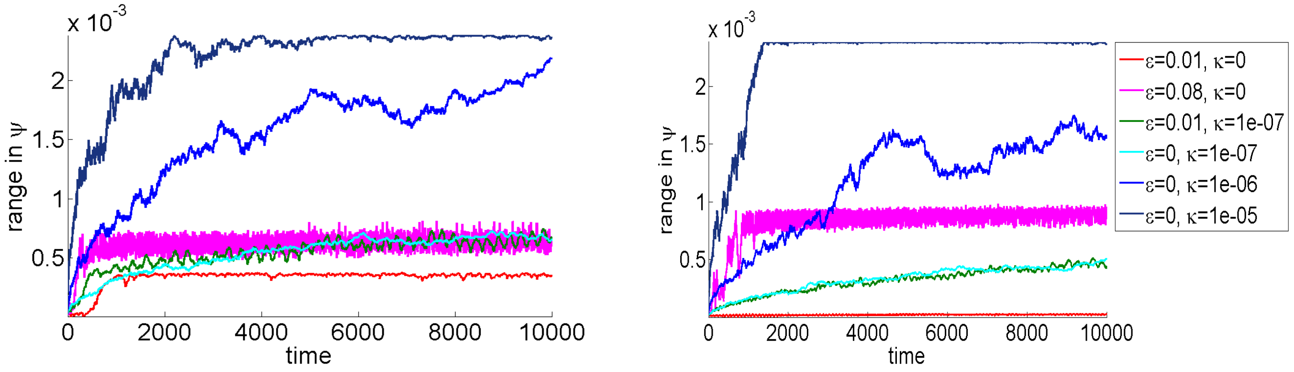

(c) $E = 0.02$ (d) $E = 0.02$

Figure 2-7: Range in ψ for ensembles of trajectories started from a sphere of radius 0.002. Steady perturbation ($\epsilon \in \{0.01, 0.08\}$), stochastic perturbations ($\kappa \in \{10^{-5}, 10^{-6}, 10^{-7}\}$), or both ($\kappa = 10^{-7}$, $\epsilon = 0.01$), are added to the background flow. Left: Initial sphere in the chaotic sea region, away from fixed points, at $(r, z) = (0.1, 0.5)$. Right: Initial sphere centered on $(r, z) = (0.4, 0.5)$, a resonant region.

an injected tracer beginning in a blob to spread out as a blob diffusively, then be stretched into a filament and folded through the eddy, before losing its maxima and appearing well-mixed through the eddy. In the next section, I will examine some dye examples.

2.3.4 Tracer Release Simulations

In this section, I analyze the effects of the symmetry-breaking, chaos-inducing perturbation on tracer distribution directly, using a numerical simulation of a dye release in the dynamically-consistent model which includes diffusion. Dye experiments are often used in both the ocean and the laboratory to understand the stirring and mixing in a fluid (examples include Ledwell et al. 1993 and 1998 and Fountain et al. 2000). The distributions of passive tracers like dye are created by the advective and diffusive patterns without the feedback onto the flow that would occur with temperature or salinity, allowing for insight into those processes. An understanding of how chaotic and non-chaotic stirring each enhance mixing, and how that changes with diffusivity, will give insight into when chaos is important for understanding tracer movement in the ocean.

My main quantification tool is Nakamura's effective diffusivity: a background diffusivity scaled by a representation of the stretching of dye concentration contours by advection. Two-dimensional and quasi-three-dimensional analyses of effective diffusivity have been applied to the atmosphere and ocean (Nakamura 1996,1997, Marshall et al. 2006, Haynes and Shuckburgh 2000). For my fully three-dimensional system with constant density, the effective diffusivity can be written as

$$\kappa_{eff}(C) = k\frac{1}{(\partial C/\partial V)^2}|\widehat{\nabla C}|^2, \tag{2.17}$$

where k is numerically imposed background diffusivity, C is tracer concentration, V is volume, and $\hat{f}$ indicates an average of function f along a concentration surface. The volume V is a one-to-one mapping of tracer concentration and volume such that $V(C)$ is the volume integral of locations in the system with higher tracer concentration. The derivation of κ_{eff} is included in Appendix A and is the first to my knowledge that is fully three-dimensional. Equation 2.17 describes an effective diffusivity that is different from the imposed diffusivity by a function of properties of the concentration contour. The units of the effective diffusivity are applied diffusivity, typically m^2/s, multiplied by m^4, or volume squared divided by length squared, which is the same as surface area squared. Larger effective diffusivity leads to larger diffusive fluxes of tracer. This amplification can be understood as advection stretching and folding of tracer contours increasing its surface area and thus the area where mixing can occur. This function is precisely the surface area squared in the rare situation where $|\nabla c|$ is constant on a c surface (see Appendix A for proof).

Both advection and diffusion redistribute tracer concentration and influence effective diffusivity. As advection stretches and folds the initial tracer, creating filaments, the surface area of a contour and gradients of the tracer increase, leading to larger κ_{eff}. Then, as diffusion smooths the tracer field, wiping away the filaments, gradients decrease and contours become more smooth, with a lower surface area to volume ratio. I compare the effective diffusivity with a steady perturbation to that without; any increase is due to increased stirring, and gives a quantitative measure of how important that chaotic stirring is for the distribution of tracer in each region of the flow.

As a secondary quantification tool, I use the tracer variance function, χ^2 (Pattanayak 2001):

$$\chi^2 = \int_V |\nabla c|^2 dV \Big/ \int_V |c|^2 dV. \tag{2.18}$$

Stirring increases the variance of a tracer, while mixing deacreases it. When χ^2 is increasing, stirring is dominant and the slop is the stirring rate. The tracer variance function was used to relate Ekman number, perturbation strength, and stirring rate for the rotating cylinder in Pratt et al. 2013; the authors found that stirring increased with larger perturbations and was nonmonotonic with E, peaking at $E \approx 0.01$.

The numerical simulations are run using NEK5000 for several diffusivities and strengths of the symmetry breaking perturbation. This model solves the incompressible Navier-Stokes equations using a spectral element method (see https://nek5000.mcs.anl.gov, Pratt et al. 2014, Fischer 1997). The domain has radius and height one, matching the kinematic model as I have been using it. The perturbed cases have their strength set by x_0, how far the lid rotation axis is offset from the cylinder axis; I use $x_0 \in \{0, -0.02, -0.16\}$. The $x_0 = -0.02$ case is what was used to compare Poincaré sections with the kinematic model, so qualitative features match the $\epsilon = 0.01$ cases. The $x_0 = -0.16$ case is significantly larger, similar to the $\epsilon = 0.08$ case in the previous section. The nondimensional imposed tracer diffusivity, k, is 10^{-4} or 10^{-6}. Using Okubo's scaling, the lower diffusivity is appropriate for scales near $1m$, while the larger is appropriate for scales near $50m$. After the simulated velocity field is spun up, the tracer concentration, c, is initialized with a constant vertical gradient, $c = 1 - z$.

The set of simulations performed allow for an examination of the effects of changing E, k, and x_0. They are $E = 0.125$, $k = 10^{-4}$, $x_0 \in \{0, -0.02, -0.16\}$ and $E = 0.02$, $k \in \{10^{-4}, 10^{-6}\}$, $x_0 \in \{0, -0.02\}$, for a total of seven simulations. Each simulation is run for a time of 300 after the tracer is initialized. I begin by discussing the evolution in time of the tracer variance function and Nakamura effective diffusivity integrated across the volume of the cylinder.

The tracer variance function over time initially grows nearly linearly as stirring creates filaments and large gradients. The function then has a single maximum that occurs at the time when diffusive mixing starts to overcome stirring, so that the variance of the tracer begins to decrease. The maximum occurs earlier when either the imposed diffusivity or the strength of the steady perturbation increase. Increasing the diffusivity makes the maximum occur earlier by increasing the strength of the mixing (figures 2-8 (a) to (b)). Increasing the steady perturbation also makes the maximum occur earlier as faster stirring creates larger gradients, in turn increasing diffusive fluxes (figure 2-8 (c), red curve).

The maximum of the tracer variance function increases with decreased diffusivity, as more filamentation can occur before diffusion wipes the filaments out. This change of maximum is most evident in the difference between $k = 10^{-4}$ and $k = 10^{-6}$ for $E = 0.02$, where the decrease in diffusivity increases the maximum of the tracer variance function by an order of magnitude (figures 2-8 (a) to (b)). Changes in the maximum as the size of x_0 is increased from 0 to 0.02 are small and negative, because the slightly earlier time of maximum combined with similar stirring rates leads to a slightly smaller maximum with the perturbation. In the case of $E = 0.125$, $x_0 = -0.16$, the maximum is larger than with either $x_0 = 0$ or $x_0 = -0.02$ due to faster stirring and a different spatial pattern of the dye, which will be discussed later.

Integrated over the total volume, the effective diffusivity, κ_{eff}, shows an overall progression similar to the tracer variance function, which indicates the dominance of the gradient term over both the $\partial c/\partial V$ term in κ_{eff} and the $|c|^2$ term in χ^2 (figures 2-8def). The initial slope and details of the maximum can be understood as relating to perturbation and diffusivity strengths in the same manner as for χ^2. At longer times, the integrated effective diffusivity reaches a fairly constant positive value unlike χ^2, which aproaches zero. This constant value can be estimated by using the surface area representation of κ_{Eff}. At long times, here meaning after many overturns but before diffusion removes all gradients, the shape of tracer surfaces are distorted nested tori (see

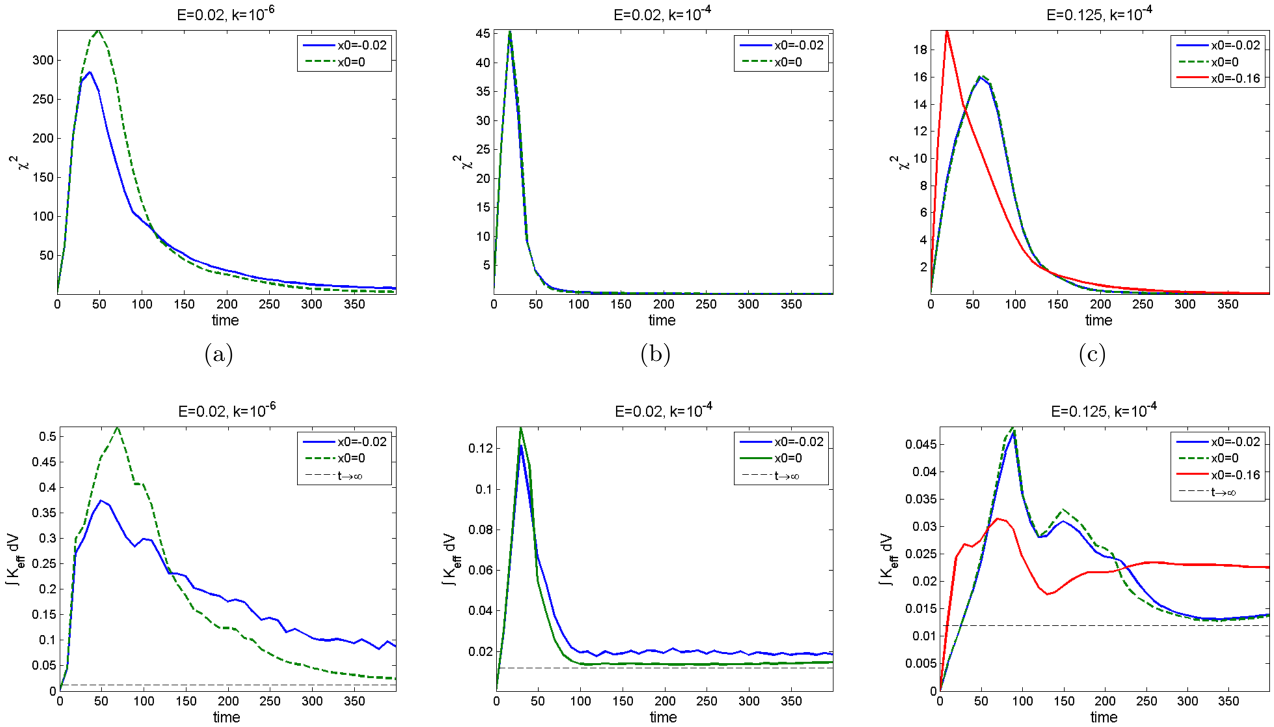

(a) (b) (c)

(d) (e) (f)

Figure 2-8: Top, tracer variance, χ^2; bottom, κ_{eff} integrated over volume. Left: $k = 10^{-6}$, $E = 0.02$, middle: $k = 10^{-4}$, $E = 0.02$, right: $k = 10^{-4}$, $E = 0.125$. Solid blue lines include the steady perturbation which induces chaos, $\epsilon = -0.02$, green dashed lines are unperturbed, solid red lines include the steady perturbation with $\epsilon = -0.16$. Black dashed lines indicate κ_{eff} integrated over volume in the case of nested circular tori.

figure 2-9h). If the c surfaces were nested circular tori, $|\nabla c|$ would be constant along the surfaces, and then $\kappa_{eff} = kA^2$, where A is the surface area of a given toroidal tracer contour. The volume integral of the squared surface area of circular tori nested around $(r, z) = (0.5, 0.5)$ multiplied by the background diffusivity is $k\pi^6/8$, which I expect to be the minimum for $\int \kappa_{eff} dV$ in this system while gradients are nonzero (see Appendix A for details). This value is shown as black dashed lines in figures 2-8def and is just below the lowest $\int \kappa_{eff} dV$ value seen. The higher values for κ_{eff} with steady perturbations at long times corresponds to persistent asymmetries in the tracer field which result in larger constant concentration surface areas. The extreme case is $E = 0.125,\ x_0 = -0.16$, which has the most asymmetric dye contours; here, the long time value of $\int \kappa_{eff} dV$ is about twice as large as for circular tori.

I now describe the behavior of the dye in the simulations. Initially, the tracer's gradients are vertical, leading to large changes in the field during the initial overturn by the flow. After a few overturns, the dye maximum is near the central orbit and concentrations decrease toward the central axis and walls of the cylinder. The time it takes for dye to move from vertical to mostly toroidal gradients is $2 - 4$ overturns of the dye by the vertical flow, and the overturning time depends on the Ekman number. For $E = 0.125$, an overturn takes about 60 timesteps, while the $E = 0.02$ case takes only about 15 timesteps. Therefore I include cross-sections of the cylinder at $y = 0$ for $t = 39$ which corresponds to one to two overturns and for $t = 299$ which corresponds to about 10 overturns to reference for the evolution of the dye (figures 2-9 and 2-10).

In the early cross-sections, figures 2-9 and 2-10 row 1, the dye contours are spirals. At early times with small perturbations, $x_0 = -0.02$, regardless of Ekman number or diffusivity, the breaking of azimuthal symmetry can be seen, with the strongest asymmetries in the contours occuring in two places. First, there are radial assymetries in the contours near the cylinder center ($x = 0$, especially toward $z = 1$), due to the breakup in the central manifold (see description in section 3.3 and discussion in Pratt et al., 2013). Second, there are differences in dye values between the left and right halves near the central orbit ($(r, z) = (0.5, 0.5)$), indicating that dye contour locations are dependent on θ. With the large perturbation, $E = 0.125,\ x_0 = -0.16$, the early dye snapshot shows a larger break from symmetry, with the central axis tilted by about 45° from vertical (figure 2-10). Increasing the diffusivity from $k = 10^{-6}$ to 10^{-4} gives a smaller range of dye concentrations with fewer streaks. In all cases, there are streaks or filaments visible at the early times which smooth out and widen in the later cross-section.

In the late cross-sections, $t = 299$, the unperturbed dye contours are nested ellipses, while asymmetries from the early times persist in the perturbed cases (figures 2-9 and 2-10 row 3). The $E = 0.02,\ x_0 = -0.02$ dye fields contain bean-shaped patches of concentration out of alignment with the outer elipses near the central orbit similar to those at $t = 39$. It is not obvious from inspecting these (or similar) sections whether these patches are the islands visible in Poincaré sections of this flow (review figure 2-2). The $E = 0.125,\ x_0 = -0.02,\ t = 299$ snapshot shows contours near the central axis that still contain the deviations from $t = 39$, and the $E = 0.125,\ x_0 = -0.16$ snapshot shows the tilted central axis. The persistence of these features over time is due to the continual action of steady advection.

The Nakamura effective diffusivity is a function of dye concentration, but the values are quite difficult to interpret without corresponding spatial information. I therefore show κ_{eff} mapped onto cylinder cross-sections at the same times $(39, 299)$ as the dye sections (figures 2-9-2-10). As I discuss the results of examining these maps, it is important to keep in mind that κ_{eff} depends on properties of the entire surface of a given dye concentration. At early times, the κ_{eff} fields are fairly noisy, as the dye has streaks, meaning small changes in dye concentration can correspond to larger changes in surface area. The broad patterns show enhanced κ_{eff} where tracer gradients appear high, along the edges of concentration contours. The $E = 0.02, k = 10^{-4}$ case stands out, having a clear correspondence of high κ_{eff} to the edges between concentration values for both the background and perturbed flow; this also matches the peak of κ_{eff} at $c = 0.5$ (not shown).

At $t = 299$, the highest effective diffusivities are along the largest toroidal dye concentration curves, with wider regions of enhancement in the perturbed cases reaching toward the central orbit, where the noticeable asymmetries persist as described in the dye field discussion (figures 2-9 and 2-10). One exception is the $E = 0.02,\ k = 10^{-6}$ case where the edges of small tracer patches, two on the right and one elongated just left of center, also have high κ_{eff} (figure 2-9j). This large κ_{eff} is partially due to the gradient in dye values between the patch and the surrounding region, but note that the dye concentration of the patches matches that of much of the chaotic sea region. Because the value of κ_{eff} depends on averages of gradients over all regions of a given dye concentration, information from both the chaotic sea and these patches are included. These patches are the smallest features that are clear in my examples at $t = 299$. Similarly sized high-κ_{eff} ridges exist in the early snapshot of $E = 0.02, k = 10^{-4}$ around patches formed in the early overturns (figure 2-9f), but are eliminated at the later times due to the larger imposed diffusivity. This scale limitation aligns with the earlier discussion of the Batchelor scale for this flow.

For a different perspective, I examine the mean κ_{eff} in subdomains of the system corresponding to a regular island and a region of the chaotic resonant layer of the same size. The cross-sections of the cylinder along the x and y axes are broken into different regions using the matching Poincaré sections of the perturbed flow (figure 2-11). Unfortunately, finding appropriate subdomains was only possible for $E = 0.02$, with its large island and extended resonant region. The $E = 0.125$ cases have islands and resonant chaotic regions that are too small to separate for $x_0 = -0.02$ and there are no clear islands with resonant regions for $x_0 = -0.16$ (not shown). The mean κ_{eff} in the chosen subdomains gives a clear result in the $E = 0.02,\ k = 10^{-4}$ case (figure 2-11c), where at long times, when the overall gradients have smoothed out, the resonant regions have about twice the effective diffusivity as the islands. The islands' κ_{eff} at that time approximately matches the value from the same region in the unperturbed simulation, indicating that chaos has not affected this area. In the $E = 0.02,\ k = 10^{-6}$ case (figure 2-11d) the mean κ_{eff} is typically higher in the resonant region, but the differences are less clear, because κ_{eff} is larger in the island than in the same unperturbed region (the no-chaos match in the figure). This behavior may be because the lower background diffusivity has not smoothed out some asymmetric patches of tracer which do not exactly correspond to the island but can overlap it and the resonant region, such as the ones highlighted in figure 2-9l.

Overall, these dye experiments show that chaotic advection enhances Nakamura effective diffusivity at some times and in some regions of the flow in all cases examined. This enhanced diffusivity is evident at the system level, such as the difference in long-time volume-integrated κ_{eff}, but is primarily due to enhancement within the chaotic regions of the flow. In this system, the amount of enhancement is controlled by both the size of the perturbation and the imposed diffusivity. A larger perturbation leads to more stirring and greater enhancement. A smaller diffusivity leads to less mixing and greater enhancement.

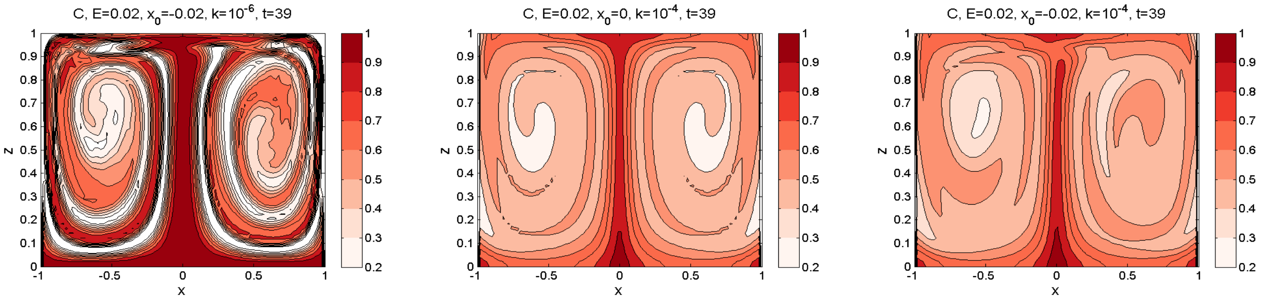

(a) $x_0 = -0.02$ (b) $x_0 = 0$ (c) $x_0 = -0.02$

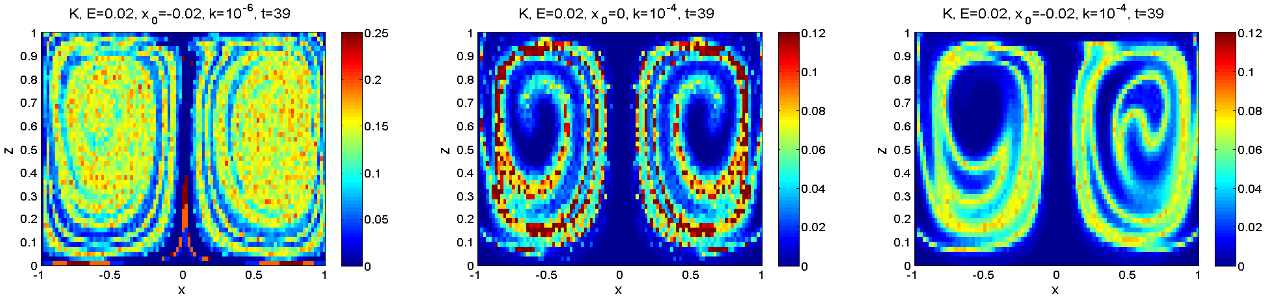

(d) $x_0 = -0.02$ (e) $x_0 = 0$ (f) $x_0 = -0.02$

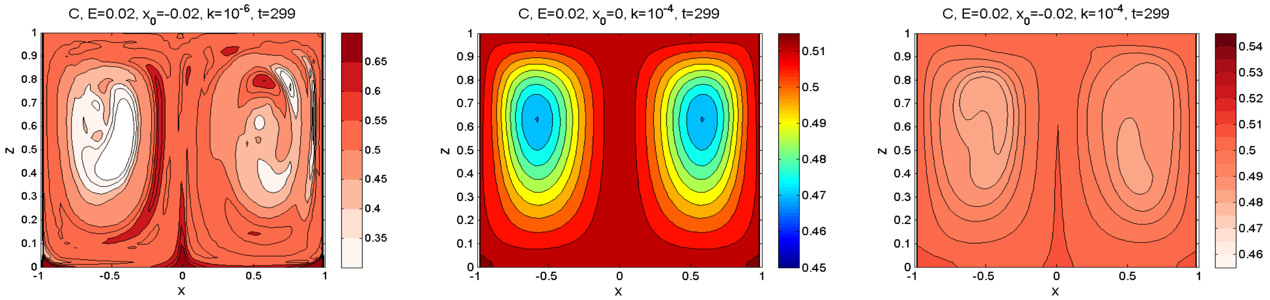

(g) $x_0 = -0.02$ (h) $x_0 = 0$ (i) $x_0 = -0.02$

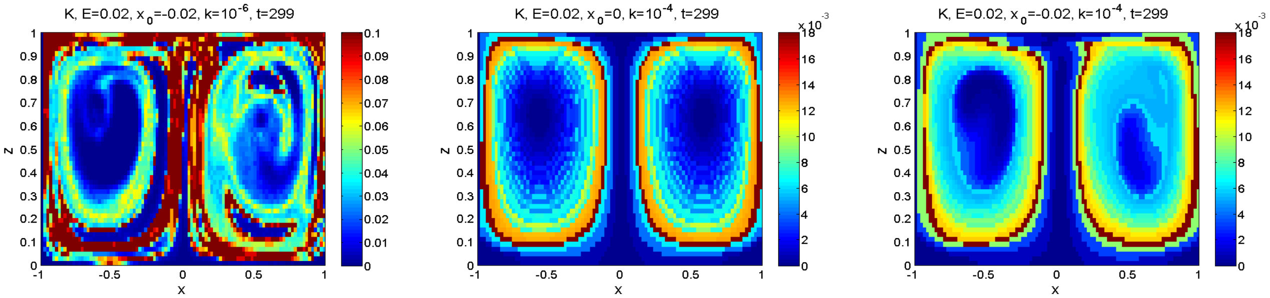

(j) $x_0 = -0.02$ (k) $x_0 = 0$ (l) $x_0 = -0.02$

Figure 2-9: $E = 0.02$ for three cases: left, $x_0 = -0.02$, $k = 10^{-6}$, middle, $x_0 = 0$, $k = 10^{-4}$, bottom, $x_0 = -0.02$, $k = 10^{-4}$. The $x_0 = 0$, $k = 10^{-6}$ case is not shown, but is qualitatively similar to the $x_0 = 0$ $k = 10^{-4}$ case. Top: Dye, $t = 39$. Row 2: κ_{eff}, $t = 39$. Row 3: Dye, $t = 299$. Bottom: κ_{eff}, $t = 299$.

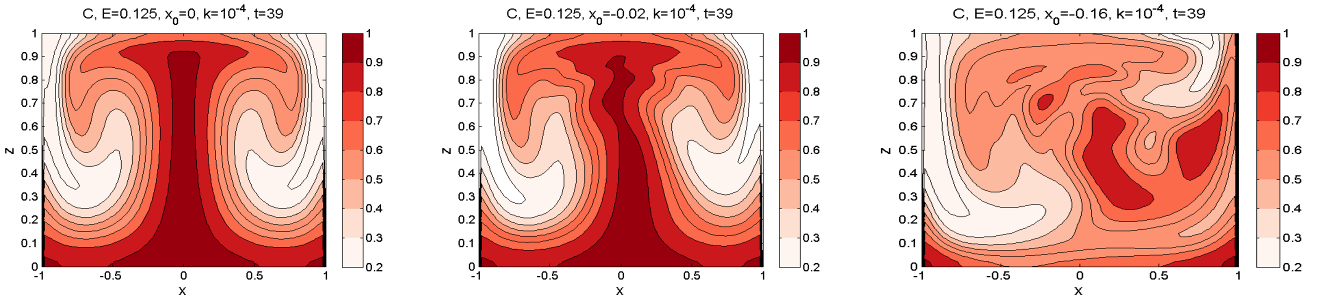

(a) $x_0 = 0$ (b) $x_0 = -0.02$ (c) $x_0 = -0.16$

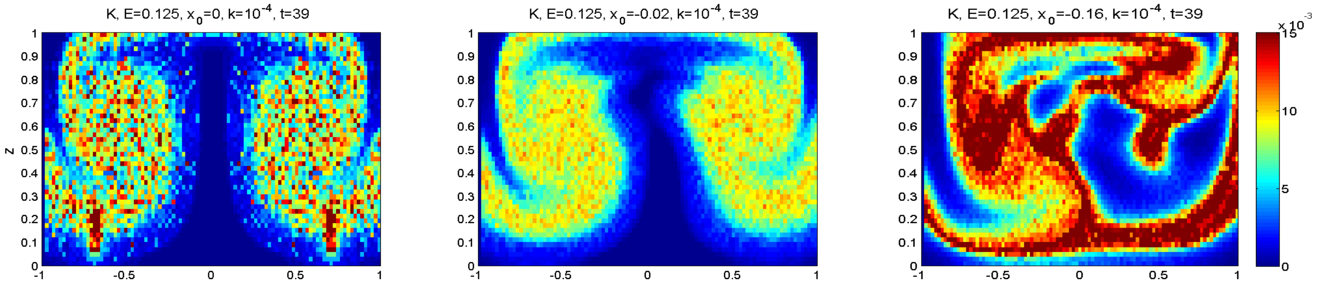

(d) $x_0 = 0$ (e) $x_0 = -0.02$ (f) $x_0 = -0.16$

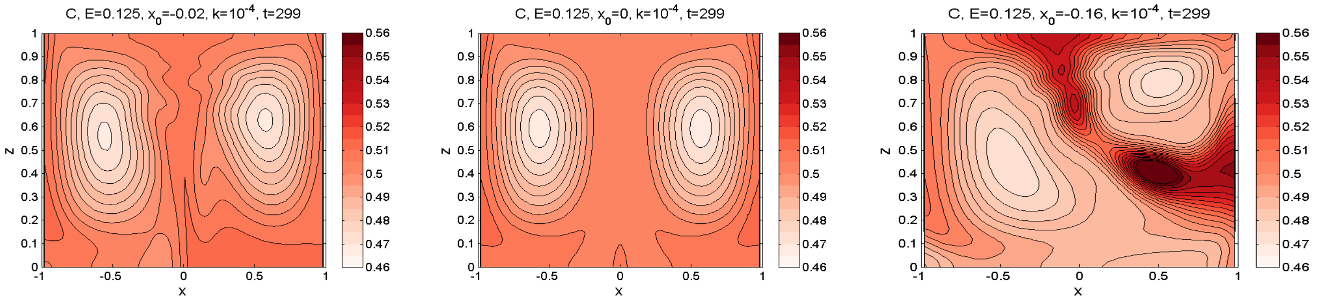

(g) $x_0 = 0$ (h) $x_0 = -0.02$ (i) $x_0 = -0.16$

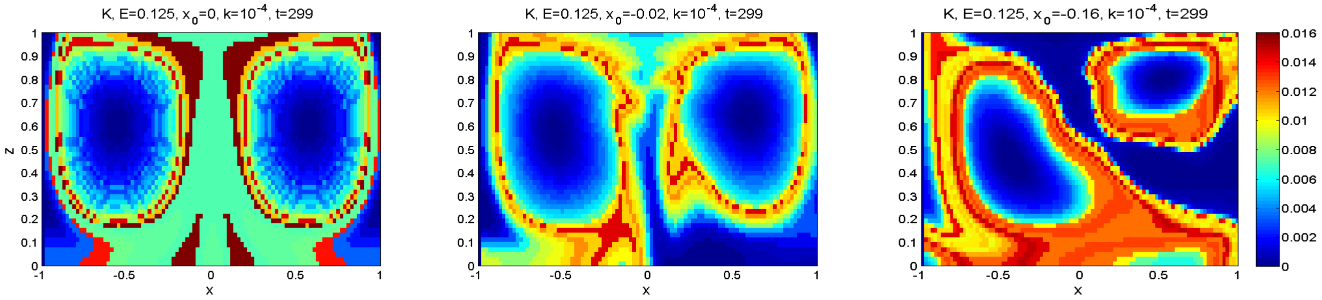

(j) $x_0 = 0$ (k) $x_0 = -0.02$ (l) $x_0 = -0.16$

Figure 2-10: $E = 0.125$ for three steady perturbation levels: left, $x_0 = 0$; middle, $x_0 = -0.02$; right, $x_0 = -0.16$. Top: Dye, $t = 39$. Row 2: κ_{eff}, $t = 39$. Row 3: Dye, $t = 299$. Bottom: κ_{eff}, $t = 299$.

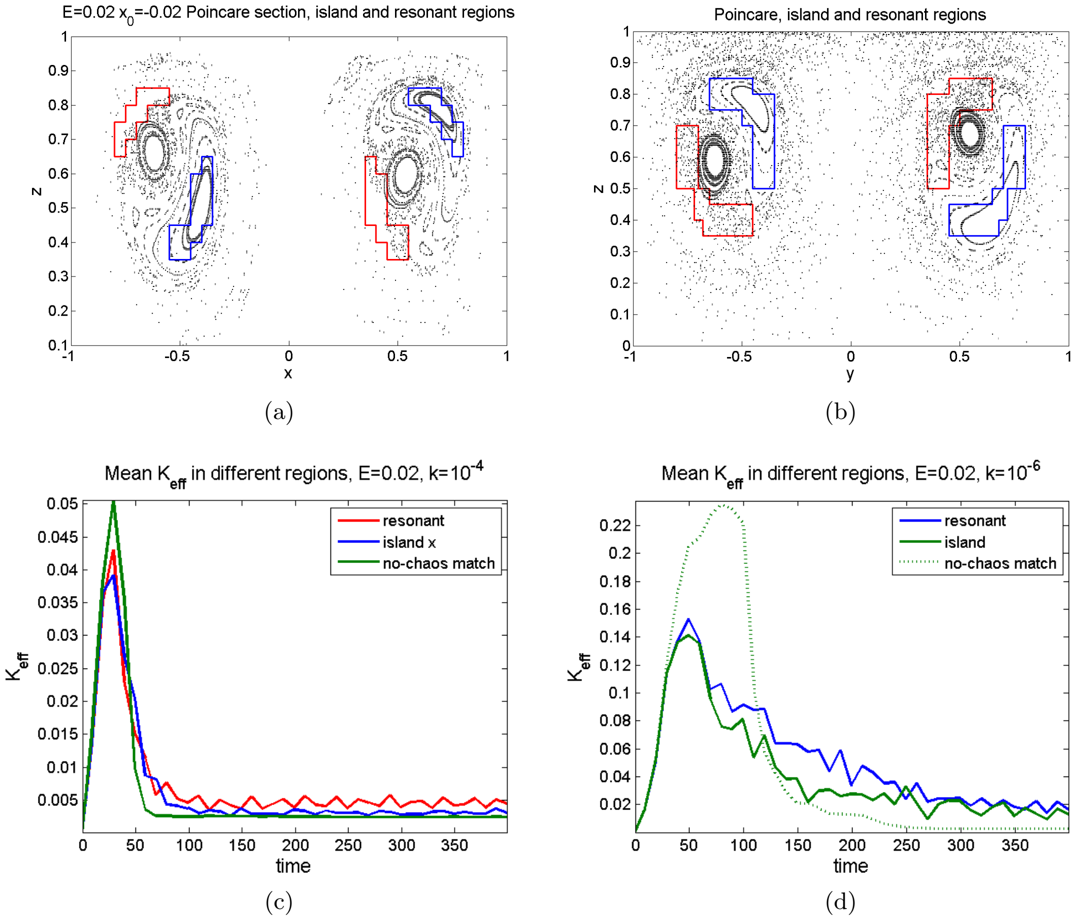

(a) (b)

(c) (d)

Figure 2-11: $E = 0.02$ Poincaré sections in the (a)$x - z$ and (b)$y - z$ planes in black. Polygons show the island (blue) and resonant (red) regions used for analysis (c) and (d), mean κ_{eff} over time in these regions under both applied background diffusivities. The no-chaos match case is the same area as the island in the unperturbed flow.

2.4 Discussion

I have compared the effects of chaotic advection and turbulent diffusion on tracers within a rotating cylinder model of an overturning submesoscale eddy. In general, I find that the structures within the flow with the deterministic symmetry-breaking perturbation are a predictor of where chaotic advection will be important when diffusion is included: the wider the chaotic regions, the more that stirring can affect a tracer in the chaotic region. I now summarize the results of my analyses and discuss the differences.

I first used scaling analyses to determine the relative importance of chaotic advection and diffusion in my kinematic model. The Lagrangian Batchelor scale estimates the width of a tracer filament when advective thinning and diffusive widening balance; when this width is smaller than that of the chaotic regions, chaotic advection dominates. The Batchelor scale was smaller than the width of the chaotic sea region, but similar in size to the resonant regions between regular islands, indicating that chaotic advection dominates only in the widest chaotic regions. I also compared timescales for the diffusion in a regular island and for chaotic stretching in neighboring resonant chaotic regions, finding them to be the same magnitude, as is implied by these features being near the Batchelor scale. This timescale comparison also provided the information that the timescales for the chaotic advection and for diffusion across the islands are several hours to one day, using my dimensionalizations.

Second, I examined the spreading over time of initial small clusters of trajectories. Specifically, I examined the spread across the background streamfunction, to eliminate the associated shear. I examined trajectory ensembles with stochastic perturbations to simulate diffusion of various strengths and with the deterministic symmetry-breaking perturbations that induce chaos at two strengths. For $E = 0.125$, small chaos-inducing deterministic perturbations cause more spreading than stochastic perturbations in the chaotic sea, and similar amounts of spreading in the resonant layers, consistent with the scalings. However, my results for $E = 0.02$ had the diffusivity causing more spreading than the chaos for all regions, which is contrary to the scaling, where the chaotic sea was larger than the Batchelor scale. The change is due to the time dependence of the spreading. Although the width of the chaotic region is larger than the spread by diffusion over the timescale of the chaotic advection ($1/\lambda$), the time it takes for the trajectories to spread across the chaotic region is longer than the spreading timescale. This difference of scales is evident in the difference between the time over which the spread increases rapidly, $(1/\lambda)$, and the longer time from the beginning of the trajectory integrations to the end of that rapid spreading (figure 2-7a,c, red curves). Larger symmetry-breaking perturbations reach the rapid stretching period more quickly (figure 2-7, magenta curves), but still do not immediately begin stretching rapidly. Thus, the long-time Lyapunov exponent does not capture the early-time behavior, and diffusion's immediate spreading can cause it to reach the chaotic region width before the chaotic spreading.

Finally, numerical dye releases in a spectral simulation of the Navier-Stokes equations allowed me to examine system-wide effects of advection and diffusion using the tracer variance function and Nakamura effective diffusivity. The tracer variance function showed a decreased maximum in tracer gradients with the chaos-inducing perturbation, indicating that mixing was enhanced by stirring. Integrated over the domain, κ_{eff} was increased by including the symmetry-breaking perturbation in all cases. However, for larger $k = 10^{-4}$, this enhancement is about a 10% change. With the smaller diffusivity and the same small symmetry-breaking perturbation or the larger diffusivity and a larger symmetry-breaking perturbation, the integrated κ_{eff} was doubled at times near the end of the simulations. These times are intermediate, in the sense that chaotic spreading has had enough time to cause stretching and folding, but diffusion has not yet eliminated the majority of gradients in the tracer. When κ_{eff} was evaluated with spatial information, it was clear that chaotic regions are where the enhancement was strong. Chaotic resonant regions could have κ_{eff} twice that of comparable regular regions in a $x_0 = -0.02$ example. Although local comparisons showed that chaotic advection and diffusion are of similar strength in resonant regions, this doubling of κ_{eff} is large enough to affect the tracer— the range of tracer values in the vicinity of the resonant region is smaller that in the unperturbed case, indicating enhanced mixing from the stirring. I conclude that the spatial structures of chaotic and regular regions can play an important role in how a tracer is distributed.

I now discuss the way the different analysis methods complement each other, and the advantages or challenges in using each. Both the Lagrangian Batchelor scale and the timescale analyses require the same information, λ and κ. The use of a Lyapunov exponent as the advective timescale is suitable for a system like the rotating cylinder where chaos is a strong feature of the advection, but would not be as applicable to, for example, the basin-scale ocean. Despite the simplicity of scaling arguments, the Lyapunov exponent is somewhat computationally expensive, requiring the integration of a dense initial grid of trajectories for a long time quite accurately (see Hadjighasem et al. 2017 for details and other options). The use of the FTLE for λ and Okubo's formula for κ are classic choices, but other options exist such as finite-size Lyapunov exponents (FSLE) and microscale diffusivity estimates. Finally, it is important to remember that scalings do not include information on the progression over time, as some of my other methods do. They also do not directly consider simultaneity of effects.

Trajectory ensembles are computationally cheap compared to Lyapunov exponent calculations and allow for examination of the progression of a perturbation's effect over time. However, stochasticity is not an accurate representation of diffusion, in the sense of diffusion causing irreversible property exchange— there is no direct connection to tracer gradients, and there is no scale dependence in my formulation. Also, although my trajectory ensembles were calculated with a symmetry-breaking or a stochastic perturbation, in the real system both occur at once. Trajectory ensembles with both included are difficult to interpret because the individual contributions are obscured.

Both scaling arguments and trajectory ensembles are comparisons of advection and diffusion for a local area of the flow. For measures of the effect of chaotic regions on the stirring and mixing throughout the system, I used numerical simulations of dye, which is the most computationally expensive method in this work. The Nakamura effective diffusivity and tracer variance function use the variations in tracer concentration to describe the conditions induced by the flow, with the effective diffusivity taking averages of tracer gradients along tracer isosurfaces. Both functions can give global information on the progression of stirring and mixing when integrated over the domain. The effective diffusivity is also useful in connecting enhanced mixing to spatial locations through the tracer concentration surfaces on which it is calculated. However, because the effective diffusivity for a tracer concentration depends on the average of the gradients over all the surfaces with that concentration in the domain, if disparate flow regions have the same tracer concentration, all those regions affect $\kappa_{eff}(C)$. Therefore, the selection of the tracer contours must be done carefully.

2.5 Conclusion

Chaotic advection causes strong stirring of tracers through the exponential stretching and folding of fluid parcels. This stirring can enhance mixing in the presence of diffusion, whether molecular or from small-scale turbulence. Since Aref brought chaotic advection to the attention of fluid dynamicists in the 1980s, a fairly large body of work has developed which examines chaotic and regular regions in the ocean (e.g. Rypina et al. 2010, Marshall et al. 2006). Although these case studies have brought up interesting examples of stirring enhancing or suppressing, for example, biological production (i.e. Hernandez-Garcia et al. 2004, Hernandez-Carrasco et al. 2014), consideration of the relative strengths of chaotic advection and turbulent diffusion have been less prominent. This lack is in part because of the fact that studies typically integrate trajectories from Eulerian velocity fields, either from altimetry or models, where diffusion (real or parameterized) has acted in the creation of the velocities, but is not included directly in the calculation of trajectories.

In this chapter, I examined these relative strengths for the redistribution of a passive tracer in a rotating cylinder flow as an analogue for an overturning submesoscale eddy. All three types of analysis showed that chaotic advection does affect a tracer's distribution. In thin chaotic regions, such as the resonant regions between regular islands, chaotic advection and turbulent diffusion have effects on tracers of the same magnitude. In large chaotic regions, chaotic advection can dominate. However, this only occurs at times when the rapid stretching and folding of chaotic advection is occuring. In the trajectory ensembles, I found a delay before the stretching became rapid, requiring sufficient interaction with hyperbolic regions to begin. This delay caused stochastic perturbations to cause more stretching than the symmetry-breaking perturbation in one case where scaling estimates predicted the opposite. In the dye simulations, the symmetry-breaking perturbation led to enhancement of the stirring rate from the beginning, due to the spatial integration including the hyperbolic regions that have rapid stretching begin quickly. The effective diffusivity can be doubled in chaotic regions even in my larger diffusivity, small symmetry-breaking perturbation case where the spatially-integrated increase is about 10%. Decreasing the diffusivity (to $k = 10^{-6}$ or increasing the symmetry-breaking perturbation (to $x_0 = -0.16$) cause the integrated κ_{eff} to acheive this doubling.

Future work of this type could use one or more of the methods implemented here to determine whether an apparent chaotic region is likely to be important for understanding a given ocean feature, such as an eddy or front. If so, observation and modeling efforts would need to capture the flow in its full dimensionality and time dependence. Work on simple flows like this could also be of benefit to the Lagrangian coherent structures field, where there has been discussion of resolution and noise in the velocity field but much less on the applicability of the structures found when turbulent diffusion is present.

2.6 References

Aref, H. “Stirring by chaotic advection.” Journal of fluid mechanics, 143(1984): 1-21.

Deese, H. E., Pratt, L. J., & Helfrich, K. R. (2002). “A laboratory model of exchange and mixing between western boundary layers and subbasin recirculation gyres.” Journal of physical oceanography, 32(6), 1870-1889.

Fereday, D. R., and P. H. Haynes. “Scalar decay in two-dimensional chaotic advection and Batchelor-regime turbulence.” Physics of Fluids 16.12 (2004): 4359-4370.

Fischer, Paul F., James W. Lottes, and Stefan G. Kerkemeier. “nek5000 Web page.” Web page: http://nek5000. mcs. anl. gov (2008).

Fischer, Paul F. “An overlapping Schwarz method for spectral element solution of the incompressible NavierâĂŞStokes equations.” Journal of Computational Physics 133.1 (1997): 84-101.

Fountain, G. O., Khakhar, D. V., MeziĂĞ, I., & Ottino, J. M. “Chaotic mixing in a bounded three-dimensional flow.” Journal of Fluid Mechanics, 417 (2000): 265-301.

GREENSPAN, H. P. 1969 The Thoery of Rotating Fluids. Cambridge University Press.

Griffies, S. M., Winton, M., Anderson, W. G., Benson, R., Delworth, T. L., Dufour, C. O., ... & Wittenberg, A. T. (2015). “Impacts on ocean heat from transient mesoscale eddies in a hierarchy of climate models.” Journal of Climate, 28(3), 952-977.

Hallberg, R. “Using a resolution function to regulate parameterizations of oceanic mesoscale eddy effects.” Ocean Modelling, 72 (2013): 92-103.

Hadjighasem, Alireza, et al. “A critical comparison of Lagrangian methods for coherent structure detection.” Chaos: An Interdisciplinary Journal of Nonlinear Science 27.5 (2017): 053104.

Haynes, Peter, and Emily Shuckburgh. “Effective diffusivity as a diagnostic of atmospheric transport: 1. Stratosphere.” Journal of Geophysical Research: Atmospheres 105.D18 (2000): 22777-22794.

Hernandez-Carrasco, Ismael, et al. “The reduction of plankton biomass induced by mesoscale stirring: A modeling study in the Benguela upwelling.” Deep Sea Research Part I: Oceanographic Research Papers 83 (2014): 65-80.

Hernandez-Garcia, Emilio, Cristobal Lopez, and Zoltan Neufeld. “Small-scale structure of nonlinearly interacting species advected by chaotic flows.” Chaos: An Interdisciplinary Journal of Nonlinear Science 12.2 (2002): 470-480.

Kolmogorov, Andrey Nikolaevich. “Dissipation of energy in locally isotropic turbulence.” Dokl. Akad. Nauk SSSR. Vol. 32. No. 1. 1941.

Ledwell, J. R., Watson, A. J., & Law, C. S. (1993). “Evidence for slow mixing across the pycnocline from an open-ocean tracer-release experiment.” Nature, 364(6439), 701-703.

Ledwell, J. R., McGillicuddy, D. J., & Anderson, L. A. (2008). “Nutrient flux into an intense deep chlorophyll layer in a mode-water eddy.” Deep Sea Research Part II: Topical Studies in Oceanography, 55(10), 1139-1160.

Lenn, Y. D., & Chereskin, T. K. (2009). “Observations of Ekman currents in the Southern Ocean.” Journal of Physical Oceanography, 39(3), 768-779.

Marshall, John, et al. “Estimates and implications of surface eddy diffusivity in the Southern Ocean derived from tracer transport.” Journal of Physical Oceanography 36.9 (2006): 1806-1821.

Nakamura, N., “Two dimensional mixing, edge formation, and permeability diagnosed in area coordinates,” J. Atmos. Sci., 53, 1524âĂŞ1537, 1996.

Nakamura, N., J. Ma, “Modified LagrangianâĂŘmean diagnostics of the stratospheric polar vortices, 2, Nitrous oxide and seasonal barrier migration in the CLAES and SKYHI GCM.” Journal of Geophysical Research, 102 (1997): 25712âĂŞ25735.

Okubo, A. (1971, August). “Oceanic diffusion diagrams.” In Deep sea research and oceanographic abstracts (Vol. 18, No. 8, pp. 789-802). Elsevier.

Olascoaga, M. J., & Haller, G. (2012). “Forecasting sudden changes in environmental pollution patterns.” Proceedings of the National Academy of Sciences, 109(13), 4738-4743.

Pattanayak, Arjendu K. “Characterizing the metastable balance between chaos and diffusion.” Physica D: Nonlinear Phenomena 148.1-2 (2001): 1-19.

Pratt, L. J., Rypina, I. I., Ozgokmen, T. M., Wang, P., Childs, H., & Bebieva, Y. “Chaotic advection in a steady, three-dimensional, Ekman-driven eddy.” Journal of Fluid Mechanics, 738 (2014): 143-183.

Rypina, I. I., Brown, M. G., Beron-Vera, F. J., Kocak, H., Olascoaga, M. J., & Udovydchenkov, I. A. (2007). “On the Lagrangian dynamics of atmospheric zonal jets and the permeability of the stratospheric polar vortex.” Journal of the Atmospheric Sciences, 64(10), 3595-3610.

Rypina, Irina I., et al. “Chaotic advection in an archipelago.” Journal of Physical Oceanography 40.9 (2010): 1988-2006.

Rypina, I. I., Pratt, L. J., Wang, P., Ozgokmen, T. M., & Mezic, I. (2015). “Resonance phenomena in a time-dependent, three-dimensional model of an idealized eddy.” Chaos: An Interdisciplinary Journal of Nonlinear Science, 25(8), 087401.

Son, D. T. “Turbulent decay of a passive scalar in the Batchelor limit: Exact results from a quantum-mechanical approach.” Physical Review E 59.4 (1999): R3811.

Thiffeault, J-L. “Scalar decay in chaotic mixing.” Transport and Mixing in Geophysical Flows. Springer, Berlin, Heidelberg, 2008. 3-36.

Zambianchi, Enrico, and Annalisa Griffa. “Effects of finite scales of turbulence on dispersion estimates.” Journal of marine research 52.1 (1994): 129-148.

Chapter 3

The Western Alboran Gyre: an Eulerian Analysis of its Properties and their Budgets

Summary

The Alboran Sea, the westernmost basin of the Mediterranean Sea, contains many of the circulation features of larger basins. Two of the largest and most persistent features of the circulation are the Atlantic Jet (AJ), a meandering, surface-intensified jet that carries Atlantic Water eastward from the Strait of Gibraltar, and the Western Alboran Gyre (WAG), an anticyclonic recirculation extending through most of the water column, bounded near the surface by the AJ to the north and the Moroccan coast to the south. These features are fairly well observed, both from in-situ and satellite efforts. The AJ is connected to the surface inflow at the Strait of Gbraltar, where a reverse estuarine exchange also carries Deep Mediterranean Water out into the Atlantic. The inflowing waters are very slighty cooler and fresher than the Modified Atlantic Water across much of the Alboran. The WAG has very similar properties to the AJ near its edges, with a gradient of increasing temperature towards the center. Below the surface, the WAG contains a salinity minimum in its center.

Although the Western Alboran Gyre is fairly well observed, its most studied aspect is the dynamics of its occasional collapse and re-formation, which are still not well understood. In contrast, very little work has addressed its typical features when it is present, and there are several outstand-

ing questions. For instance, geostrophic streamlines from satellite altimetry observations separate the AJ and the WAG, but the salinity minimum water should have originated from the Strait of Gibraltar. This observation begs the questions of what sets the salinity minimum and whether there is exchange between the AJ and the WAG that could be part of the process. Simpler questions are also unanswered, such as what sets the temperature maximum at the center, and what drives the WAG rotation— wind, lateral forcing from the AJ, or something else. Here I use a numerical model of the Alboran Sea to gain insight into these questions.

I have used the MIT general circulation model to simulate the Alboran for part of 2007 and 2008. I used high spatial resolution, accurate bathymetry, and reanalysis forcing at both the surface and the open boundaries to the Atlantic and Mediterranean to gain a circulation that has realistic features and behavior for several months. My aim is to understand the processes contributing to the properties of the WAG. These processes can be described by the physical equations for tracers and momentum that are represented in the model. I form budgets for the WAG comprised of each term from the physical equations and then examine their magnitudes and timeseries in order to tease apart information on which processes most influence the properties in the questions above.

A volume budget adresses the exchange of water between the AJ and the WAG through quantifying transport across the sides of the WAG. The net transport through the sides is balanced primarily by transport through the bottom, which is closely linked to the bottom isopycnal moving across its mean depth. This isopycnal motion is then driving a squashing-stretching motion of the water column, which means the net transport across the sides is probably stirring water between the AJ and WAG near the edges, not driving water into or out of the core of the WAG.

A salt budget for the region containing the salinity minimum addresses the question of what processes set the minimum. The terms in the budget include advection of salt through the top, bottom, and sides, horizontal and vertical diffusion, and changes in salt content. The total advection closely matches the daily changes in salt content, indicating that advection controls the short-term changes in salinity. However, over the study period, the salinity minimum becomes more saline, primarily due to salt advected into it. The budget cannot directly explain the creation of the minimum, but because none of the advective terms are on average freshening the region, it shows that there is not a direct exchange from the AJ supporting the minimum. The remaining option, given that the basin is evaporative and without major rivers, is that the minimum is created during the formation of the WAG, with a buildup of water from the Strait of Gibraltar inflow.

In order to address the warmth of the WAG compared to its surroundings, I form a heat budget for the full gyre. Advective transport of heat through the sides and bottom are the largest terms. The total advective transport drives changes in heat storage, with a secondary contribution from surface forcing. In the time mean of the analyzed period, the gyre is cooling, as warming by the surface and advection through the sides is overcome by advection and diffusion through the bottom. Because it is warmer than its surroundings, the WAG may be warm due to warmer surface Atlantic waters involved in its formation, rather than warming over time. This warmth from formation is consistent with the salinity minimum forming the same way.

A budget for the relative vorticity of the WAG elucidates which processes drive or suppress the anticyclonic rotation. The large terms in the depth-integrated timeseries are changes in the vorticity, windstress, advection, vertical diffusion, lateral diffusion, and drag. Because of its changes in time, the windstress curl is not always supporting the anticyclonic rotation of the WAG and so is not the main driver. The vertical diffusion primarily transports the windstress downward, into the gyre. In the mean, the changes in the vorticity are small, and so there is a balance between advection, diffusion, and drag. Advection and drag add positive vorticity, slowing the gyre. Therefore, lateral diffusion of vorticity, or a pushing by the AJ, drives the gyre.

Overall, budgets for volume, salt, heat, and vorticity have contributed to understanding what sets the properties of the Western Alboran Gyre by allowing an examination of each term in the physical equations for the system. Using a model run with forcing that is realistic, rather than idealized, makes analysis more difficult but means that it is more relatable to observations. In the end, we have learned that the AJ and WAG have an exchange that likely stirs their edges together; that the salinity minimum and overall warmth of the WAG are decaying, likely from their formation with the WAG, while short-term changes are driven by advection; and that lateral diffusion of vorticity is the main driver of the WAG, while both advection and drag suppress the rotation.

3.1 Introduction and Background

The Alboran Sea in the Mediterranean Sea, just east of the Strait of Gibraltar, contains many of the circulation features of larger basins. Two of the largest and most persistent features of the circulation are the Atlantic Jet (AJ), a meandering, surface-intensified jet that carries Atlantic Water eastward from the Strait of Gibraltar, and the Western Alboran Gyre (WAG), an anticyclonic recirculation extending through most of the water column, bounded near the surface by the AJ to the north and the Moroccan coast to the south. These features are fairly well observed, both from in-situ and satellite efforts (e.g. Heburn and Violette 1990, Viudez et al. 1996, Renault et al. 2012). The AJ is connected to the surface inflow at the Strait of Gbraltar, where a reverse estuarine exchange also carries Deep Mediterranean Water out into the Atlantic. The inflowing waters are fresher than the Modified Atlantic Water across much of the Alboran. The AJ leaves the interior of the Alboran Sea and attaches to the African coast near the eastern edge of the Alboran, often at the Almeria-Oran front, a boundary between Modified Atlantic Water and Mediterranean Sea Water. The WAG has very similar properties to the AJ near its edges, with a gradient of increasing temperature towards the center. Below the surface, usually near 50m, the WAG contains a salinity minimum in its center. Deeper, Intermediate and Deep Mediterranean Sea Waters enter the Alboran Sea from the east, outflowing through the Strait of Gibraltar and occasionally forming Atlantic Meddies (GRID-Arendal 2013).

Although the Western Alboran Gyre is fairly well observed, its most studied aspect is the dynamics of its occasional collapse and re-formation (e.g. Sanchez-Garrido et al. 2013, Preller 1986, Whitehead & Miller 1979). In contrast, very little work, generally only observational, has addressed its typical features when it is present, and there are several outstanding questions. For instance, geostrophic streamlines from satellite altimetry observations separate the AJ and the WAG, but the salinity minimum water should be connected to the Strait of Gibraltar (see discussion in Viudez et al. 1996). This observation begs the questions of what sets the salinity minimum and whether there is exchange between the AJ and the WAG that could be part of the process. Related questions are also unanswered, such as what causes the gyre to stay warmer than its surroundings, and what drives the WAG rotation. Candidates for drivers of the rotation include wind, lateral forcing from the AJ, and added anticyclonic vorticity from the rising deep waters flowing towards the Strait of Gibraltar. Here I use a numerical model of the Alboran Sea to gain insight into these questions.

In this work, I will address the questions of the controls on the features of the WAG through the formation of budgets for the volume, temperature, salinity, and vorticity using a mesoscale-resolving numerical model of the Alboran Sea. Specifically, I have used the MIT general circulation model to simulate the Alboran for part of 2007 and 2008. I used high spatial resolution, accurate bathymetry, and reanalysis forcing at both the surface and the open boundaries to the Atlantic and Mediterranean to gain a circulation that has realistic features and behavior for several months; details are in Section 2. My aim is to understand the processes contributing to the properties of the WAG. These processes can be described by the physical equations for tracers and momentum that are represented in the model. In Section 3, I form budgets for the WAG comprised of each term from the physical equations and then examine their magnitudes and timeseries in order to tease apart information on which most influence the properties in the questions above. A volume budget adresses the exchange of water between the AJ and the WAG through the term describing transport across the sides of the WAG. A salt budget for the region containing the salinity minimum addresses the question of what processes set the minimum. A heat budget for the WAG addresses what mechanisms keep it warmer than the adjacent AJ. Finally, a budget for the relative vorticity of the WAG elucidates which processes drive the rotation.

3.2 Model Description

3.2.1 Model Setup

The physical model I use is the Massachusetts Institute of Technology general circulation model (MITgcm) in hydrostatic mode (Marshall et al. 1997). The specific configuration is similar to that of Sánchez-Garrido et al. (2013), with resolution increased roughly by a factor of three in the Alboran. This model solves the Boussinesq form of the Navier-Stokes equations for an incompressible fluid with a finite-volume spatial discretization on a curvilinear grid with typical horizontal resolution of 1 to 3 km (see figure 3-1). The vertical grid has 5m resolution at the surface, decreasing with depth, and 46 vertical levels. The model domain includes the Strait of Gibraltar and has open boundaries in the Atlantic and Mediterranean. Surface forcing is provided by 6-hourly, 1/4-degree, 10m wind fields from the IFREMER CERSAT Global Blended Mean Wind Fields. Surface heat and salt fluxes are from the ERA-Interim reanalysis daily fields. Open east and west boundary forcing of velocity, salinity and temperature are from the 1/12-degree, daily Atlantic-Iberian Biscay Irish-Ocean Physics Reanalysis (AIBIOPR).

Initial conditions were based on September 2011 output from Sánchez-Garrido et al. (2013), with some temporal and latitudinal averaging so that the circulation is relatively stable. The model was run for 55 days with ocean boundary conditions from the fall 2007 average of the AIBIOPR and without atmospheric forcing. Average atmospheric forcing from fall 2007 was then added gradually, followed by a transition to the October and then November monthly averages for all forcing; this was spaced over 75 simulated days. After a total of 130 days spinup, the fully-forced simulation began running from November 1 2007. The initial run ends at the end of 2008, which is the end of the chosen wind field data.

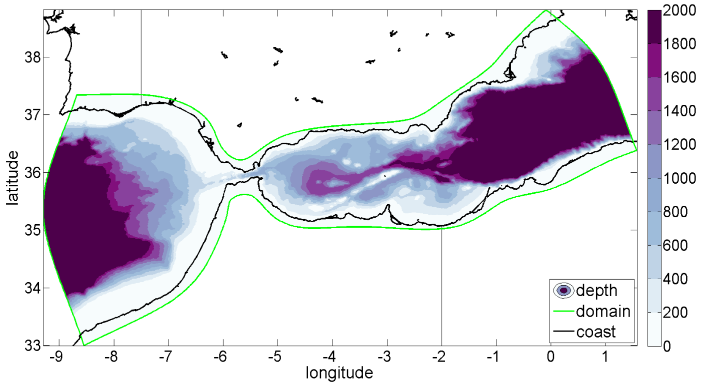

(a) bathymetry

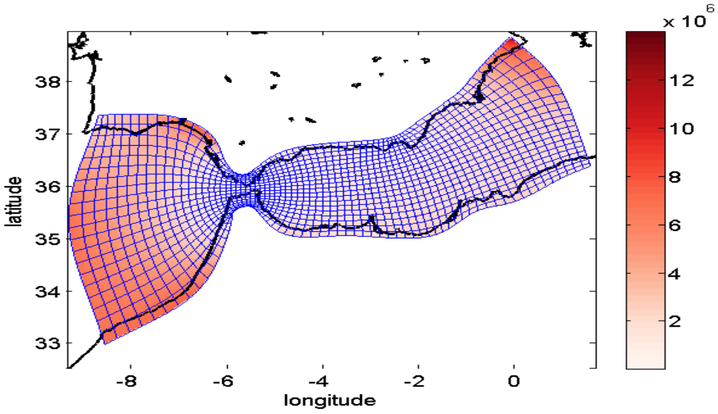

(b) grid areas, m^2

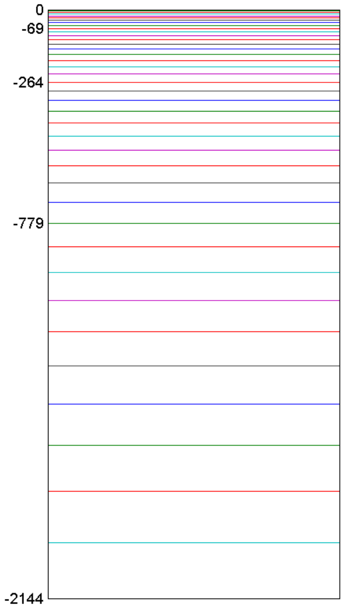

(c) layer depths, m

Figure 3-1: (a) Domain of the simulation. Color is bathymetric depth, black curves are coast. Black lines on land indicate approximate borders between Portugal and Spain (northern) and Morocco and Algeria (southern). (b) Model grid, with every 10th gridline in blue over the area of each cell in reds (m^2), and the coast indicated in black. (c) Depth grid spacing in meters, top 40 interfaces, interfaces 1, 10, 20, 30, and 40 labeled.

3.2.2 Model Validation

Although no model can exactly simulate the ocean, I compare my output with observations to demonstrate that five months of the model run are realistic. The MITgcm output sea surface height (SSH) is compared with satellite-measured gridded daily fields from AVISO as the primary check. When patterns of SSH match, the near-surface geostrophic flows are similar, which is generally the case in the WAG area. Secondarily, an examination is performed on the magnitude of exchange at the Strait of Gibraltar, comparing the model outflow to outflow measured by ADCP during the same time period.

The monthly mean SSH patterns in the model match those from AVISO well during the first 5 months and final month of the model run (figures 3-2-3-3). The WAG is evident as a positive anomaly in about the same position in all of these months in both the model and the observations. Farther east, the AJ attached to the African coast is often also clear as a positive anomaly. The change in SSH between the WAG and the northern coast is larger in the model, which may indicate a faster AJ, but could also relate to errors in SSH observations due to the nearby coast. In the first 5 months, no Eastern Alboran Gyre is evident in either the model's monthly SSH maps or the observed SSH, but one does appear in May through November in the observed SSH. Cyclonic features in the interior, east of the WAG, are present in both model and observations. However, the generally cyclonic circulation of the Alboran Sea in the model from April to September is not representative of any observed patterns. A spatial correlation of daily SSH shows that at about day 149 of the simulation, the correlation between output and observations drops, eventually becoming negative for several months (figure 3-4), durigh which the monthly SSH patterns indicate this cyclonic flow over most of the basin. I therefore use the first 148 days of output for the analysis.

The mean and variance of SSH match reasonably well for this initial 148-day period (figure 3-5). The mean patterns are similar to the monthly maps, with the WAG clear and centered at about $4°W$. East of the WAG, there are two cyclonic features, near $2°W$ and $0°E$, with the western of the two being stronger in the observations and the eastern one being stronger and larger in the model. The variance patterns have a matching high in the east, near the Almeria-Oran front, and a local high where the AJ typically turns southward, at the eastern edge of the usual WAG position. However, the high variance values in the model output just east of the WAG is not confirmed by observations, and the high variance in observations over the WAG is not well represented in the model.

The magnitude of exchange at the Strait is commonly observed to be about 1 Sverdrup (1 Sv=$10^6 m^3/s$) in either direction, eastward into the Alboran in a surface layer and westward toward the Atlantic at depth. Sammartino et al. (2015) examine Mediterranean to Atlantic flux estimates over 10 years of velocity date from a mooring on the western side of the Strait. Typically the outflow is below 190m (interface depth) and between 0.75 and 0.9 Sv, highest in the spring and lowest in late summer. My simulated time period is covered, and it appears that the seasonal cycle was somewhat unusual that year, with lowest outflow in May (not shown, see reference). The simulated outflow is of the correct magnitude, ranging from 0.6 to 1.4 Sv (mean 1.1 Sv), see figure 3-6a, but is generally larger than the measured outflow. This slightly large outflow is consistent with the mean SSH having a larger difference between the WAG and the northern coast, which indicates a faster inflow than observed. The overall exchange is forced in part by the exchanges at the open boundaries (set from AIBIOPR, typically 5-10Sv), so the increases compared to observations may not only be due to internal dynamics. The interface between inflow and outflow in the model is somewhat higher than observed, most commonly 163m, but given the vertical resolution at those model depths (about 20m) this is only a difference of one to two grid cells (figure 3-6b). These differences in the exchange flow may also be due to the lack of tides in the model run, which greatly changes the variability of the flow in the strait, although the Sammartino et al. (2015) data for comparison is filtered to subinertial periods. I will not be analyzing the flow in the Strait directly, focusing on the WAG, which has longer timescales, but these differences should be kept in mind.

3.2.3 Model Output Description

Before moving on to the analysis of the WAG, I describe here the main features of the WAG in the model results using the mean fields during my 148-day analysis period. As shown in figure 3-5a, the model flow contains the WAG in the same position as observed, with approximately the correct extent. However, the model mean WAG is more circular than the observed WAG, and more separated from the northern coast in terms of mean SSH anomaly differences. For subsurface patterns, I first show two north-south sections of the mean zonal velocity field with mean potential density contours overlaid, one in the Strait and one through the WAG (figure 3-8). The inflow and outflow are separated at about the $\sigma_\theta = 27.5$ to $\sigma_\theta = 28$ isopycnals, with the inflowing Atlantic Jet

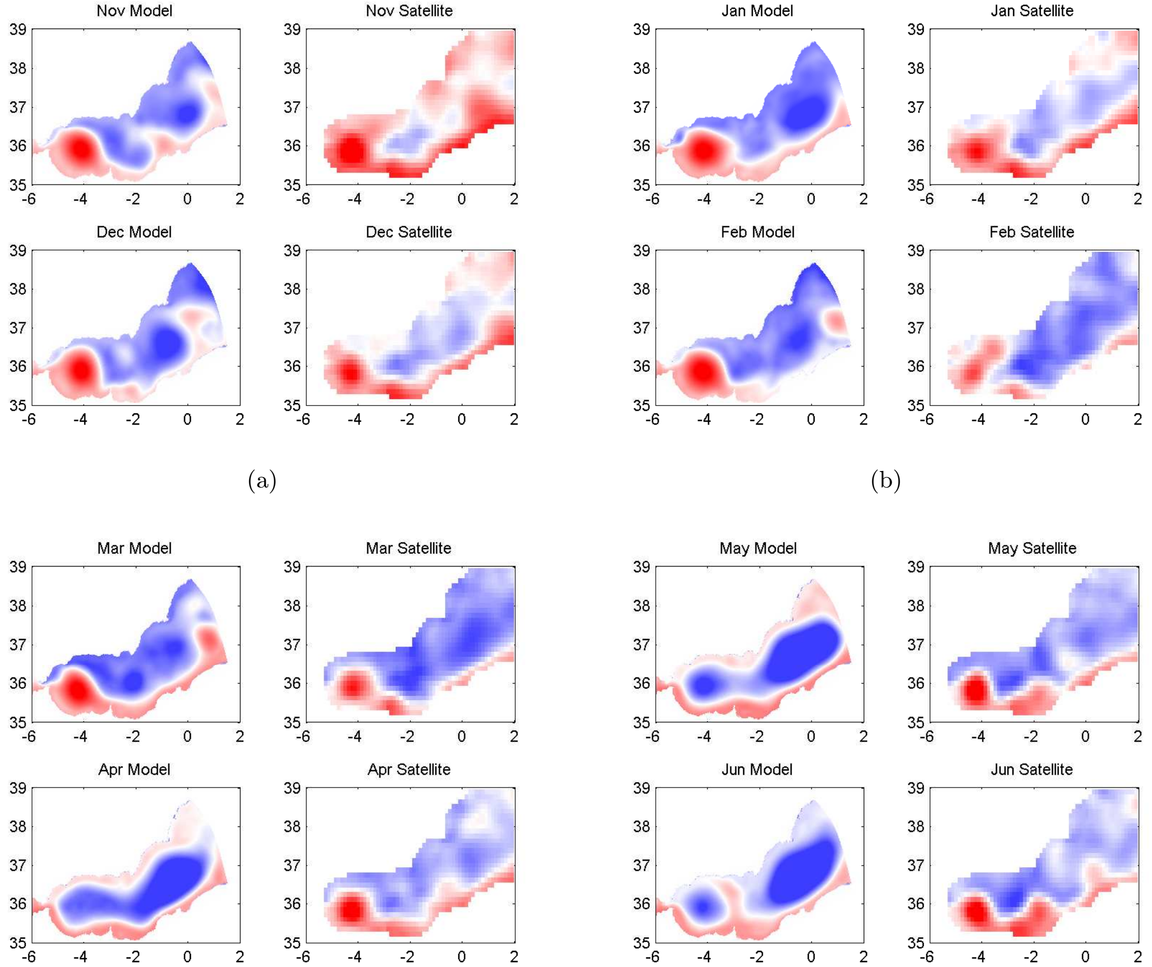

(a)

(b)

(c)

(d)

Figure 3-2: Monthly mean SSH (saturated colors at $0.2m$ red and $-0.2m$ blue), comparison between MITgcm output and AVISO data. November 2007 through June 2008.

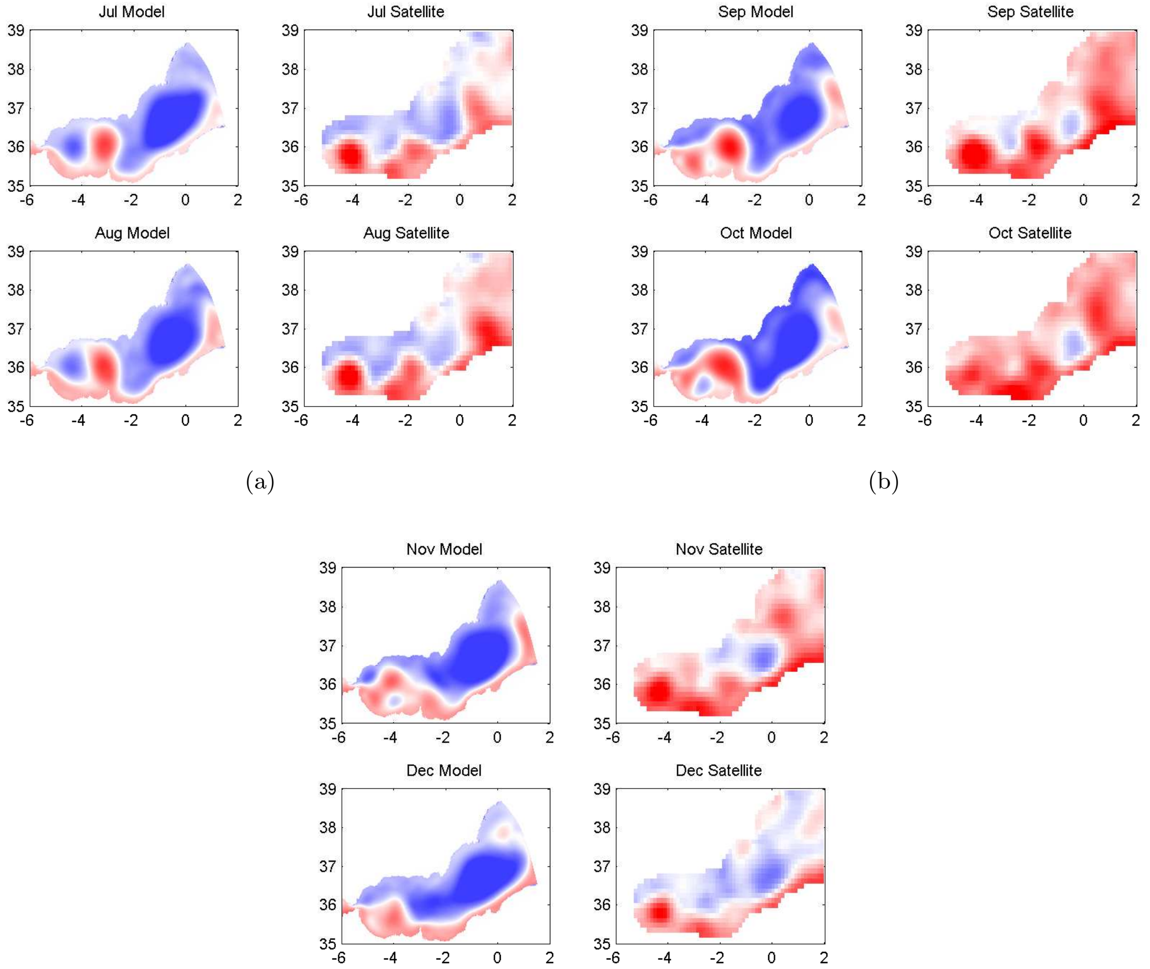

(a)

(b)

(c)

Figure 3-3: Monthly mean SSH (saturated colors at $0.2m$ red and $-0.2m$ blue), comparison between MITgcm output and AVISO data. July through December 2008.

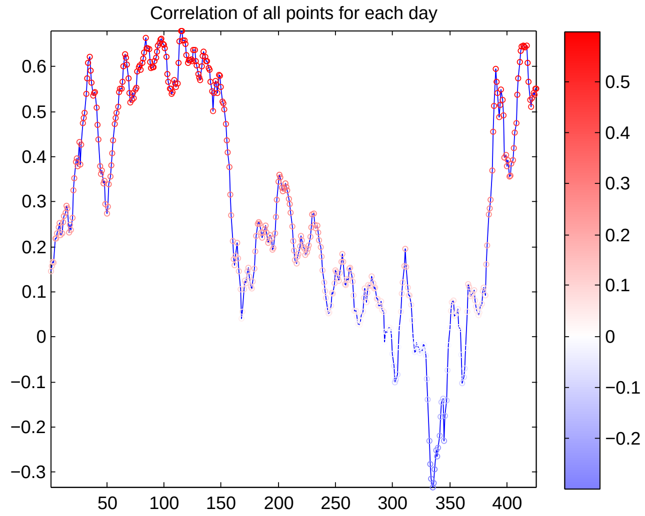

Figure 3-4: Daily SSH correlation ($y - axis$ position and color) between output and observations for all points each day of the simulation, where day 1 is November 1, 2007.

strongest in the top 100m north of $36.3°N$. The WAG's center shifts northward near 200m depth and $\sigma_\theta = 28$, corresponding with outflow through the Strait coming from near the African shore (as described in Bryden and Stommel, 1982). My analysis will focus on the near-surface WAG, above $\sigma_\theta = 27.5$; inspection of the details of the lower WAG and the associated outflow through the Strait is outside the scope of this work.

Looking directly at the potential density, now with isohalines overlaid, on the same sections, shows that the pycnocline is near $150m$ in the southern Strait and the WAG (figure 3-9). Above this, $\sigma_\theta < 26.5$, is fairly unstratified, as are the deep waters with $\sigma_\theta > 28$. The isohalines indicate salinity minima below the surface on the southern side of the strait and near the center of the WAG, but are similar to isopycnals elsewhere. These minima are roughly consistent with observations in their position and depth (Viudez et al. 1996). Sections of salinity (figure 3-9) also show these minima, more clearly in the Strait than in the WAG. Isotherms overlaid on the salinity sections are generally parallel to the isohalines and isopycnals, especially near the pycnocline. However, the salinity minimum in the southern Strait does not have a noticeable match in temperature. The thermoclines are mostly bowl-shaped in the near-surface WAG, similar to the isopycnals. Below the pycnocline, there are temperature minima in both sections within regions with nearly constant salinity and density. The minimum in the Strait is very slight both in this mean view and in daily

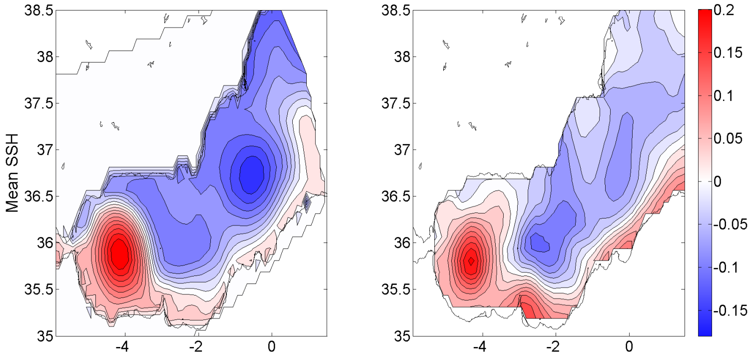

(a) SSH mean

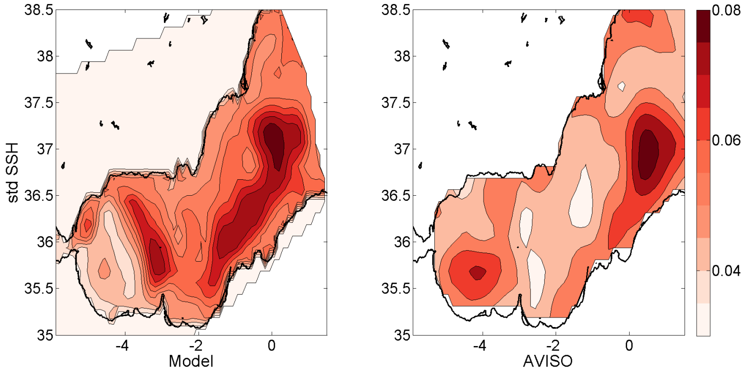

(b) SSH standard deviation

Figure 3-5: (Top) Mean SSH (m) over the 148-day well-correlated period, comparison between MITgcm output (left) and AVISO data (right). (Bottom) Standard deviation of daily SSH (m^2) over the same period.

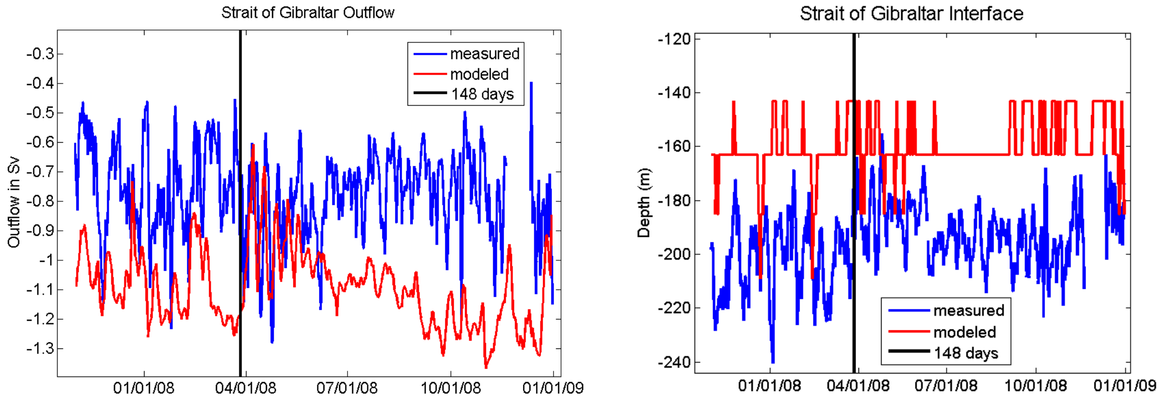

(a) outflow

(b) interface

Figure 3-6: (a) Outflow (Sv) from all depths along a meridional section going through Sammartino et al.'s mooring location compared to Sammartino et al.'s subinertial outflow measurement. (b) Interface depth (meters below surface). Measured is Sammartino et al.'s zero-crossing from mooring data. Model interface is defined by the bottom of the deepest cell where the mean across-section flow is toward the Alboran. In both, the black vertical line indicates the end of the 148-day period analyzed further.

sections (not shown), but in the WAG the minimum is about 12.5° compared to surrounding water about 13°, but changes latitude, leading to the slight minimum in the mean. Again, I will focus on the WAG that is connected to the inflow, which is above these features.

In order to delineate the WAG region horizontally, I use a mean salinity contour of 36.475 at the surface. This salinity value was chosen because it encompasses the WAG region from the corner at the southeastern edge of the Strait of Gibraltar (Ceuta) to Cabo Tres Forcas, the cape at about 3W, without continuing in the AJ farther east (figure 3-7). Definitions using mean potential density ($\sigma_\theta = 26.3$) or SSH ($\eta = 0.04m$) are very similar. The vertical extent of the WAG is defined as the mean $\sigma_\theta = 27.5$ isopycnal depth. Modified Atlantic Water is present throughout the WAG above $\sigma_\theta = 27.5$, or about $160m$ depth (salinity below 37.5). Below that, the salinities and temperatures are consistent with a layer of Leventine Intermediate Water (salinity of $38 - 39$ and temperatures of $13 - 15 \circ C$) above Western Deep Mediterranean Water (salinity above 38, temperature below $13 \circ C$), which lies below about 200m (a more detailed discussion of water masses is in Gascard and Richez 1985).

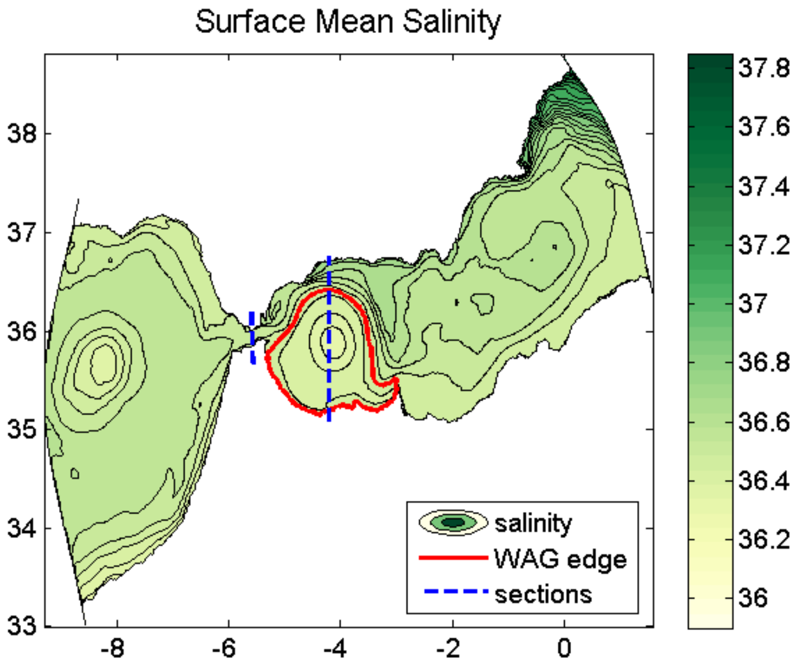

Figure 3-7: Mean surface salinity of the 148-day analysis period in greens with the chosen WAG boundary in red. Blue dashed lines indicate the location of sections shown in the next figures.

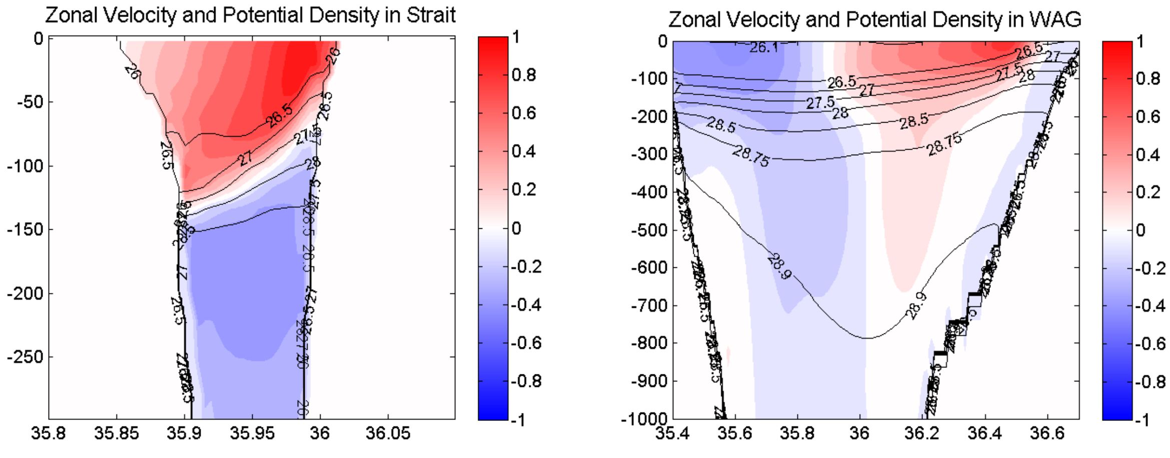

(a) strait

(b) WAG

Figure 3-8: Two north-south sections, facing west, of the 148-day mean zonal velocity field with mean potential density contours overlaid. Left, in the Strait of Gibraltar. Right, in the Western Alboran Gyre.

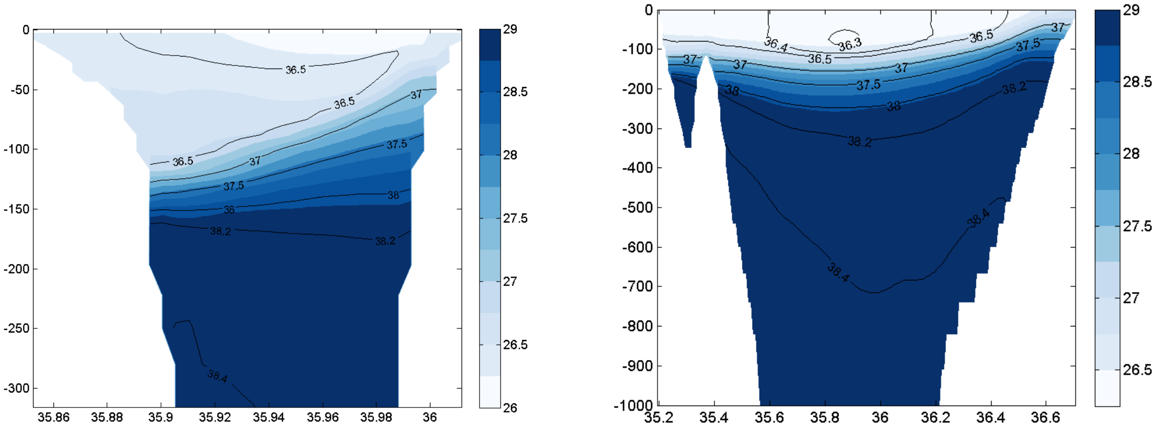

(a) strait

(b) WAG

Figure 3-9: Two north-south sections, facing west, of the 148-day mean potential density field, blues, with mean salinity contours overlaid. Left, in the Strait of Gibraltar. Right, through the Western Alboran Gyre.

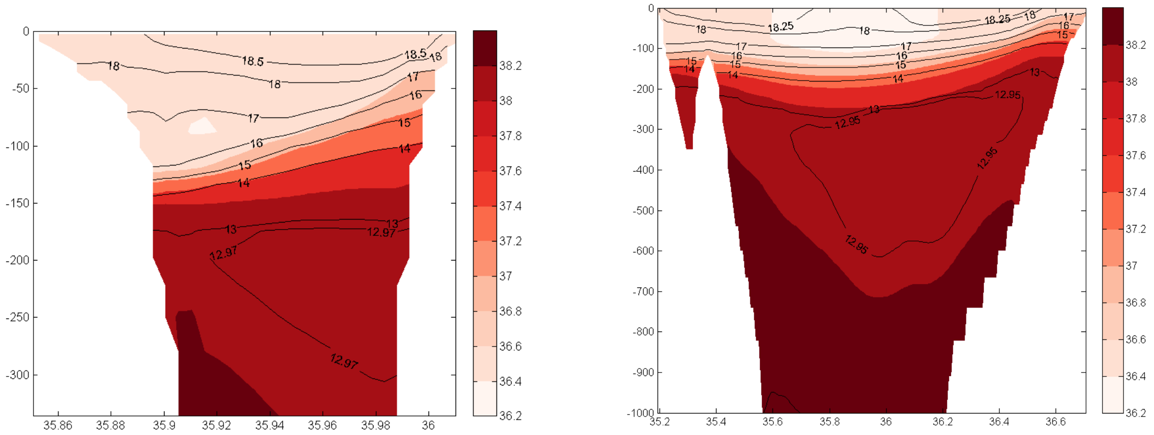

(a) strait

(b) WAG

Figure 3-10: Two north-south sections, facing west, of the 148-day mean salinity field, reds, with mean potential temperature contours overlaid. Left, in the Strait of Gibraltar. Right, through the Western Alboran Gyre.

3.3 Results

In this section, I analyze the Eulerian transport of water and its properties in and out of the WAG or a subset of it. The aim of forming budgets for the water and its properties is to examine terms from the governing physical equations in order to elucidate the drivers of typical WAG features. A volume budget addresses the rate of exchange of water between the AJ and the WAG. A heat budget for the WAG addresses what keeps it warmer than the adjacent AJ. A salt budget for the region containing the salinity minimum addresses the question of what processes set that minimum. Finally, a budget for the relative vorticity of the WAG elucidates which processes drive the rotation.

For the budgets of the full WAG, I limit the control volume in the horizontal direction to locations with surface time-mean salinities below 36.475 and in the vertical to locations with time-mean $\sigma_\theta < 27.5$ (figure 3-7 shows the surface limits). I compute the volume fluxes through the boundaries and the changes in SSH storage to form the volume budget (figure 3-11). The volume budget has four terms: advection through the sides, advection through the bottom (across the mean $\sigma_\theta = 27.5$ isopycnal), precipitation and evaporation through the surface, and volume storage from changes in sea-surface height. The budget may be written as

$$\begin{aligned} \frac{dV_{SSH}}{dt} &= \int_{sides} \vec{u} \cdot dA + \int_{\sigma} \vec{u} \cdot dA + \int_{surface} F_{PR}\, dA \qquad (3.1) \\ &= \sum_{side} (U_W A_W - U_E A_E + V_S A_S - V_N A_N) \\ &\quad + \sum_{\sigma} (U_W A_W - U_E A_E + V_S A_S - V_N A_N + W A_Z) + \sum_{surface} F_{PR} A_Z, \end{aligned}$$

where the term on the left is the storage and the first on the right is convergence of advection through the sides with (U, V, W) indicating zonal, meridional, and vertical velocity at the centers of the cell faces, A the area of the model cell face, and N, S, E, W the face of the cell that is at an edge of the WAG. The second term on the right is the convergence of advection through the bottom, which is the mean $\sigma_\theta = 27.5$ surface, and includes the vertical velocities. Horizontal velocities are included because the bottom is not flat. The final term is the precipitation and evaporation over the surface of the WAG, F_{PR}, where A_Z is the area of the top of the cell, which is the same as the bottom for this grid. This budget calculation uses the model daily mean velocities, sea-surface height, and surface evaporation-precipitation; details for this calculation and all other budgets is in

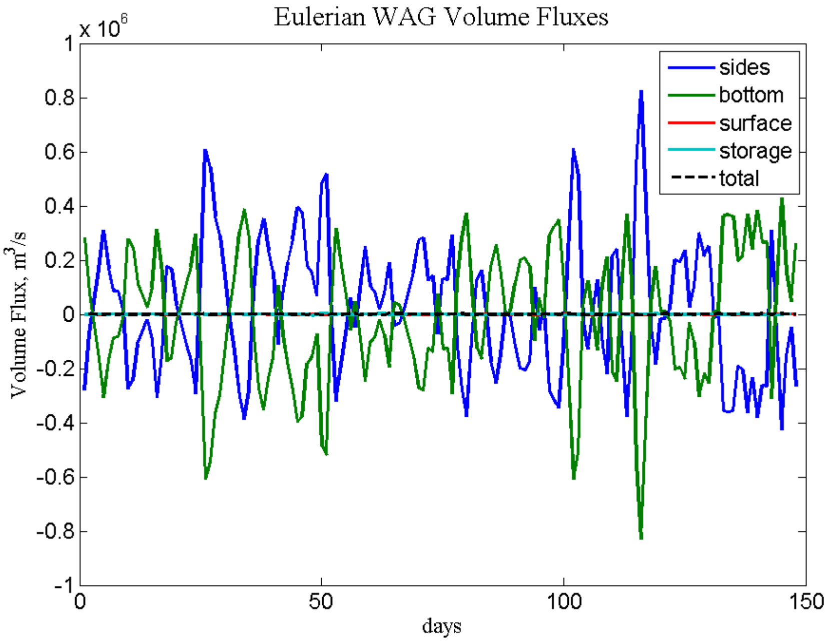

Figure 3-11: Total Euler WAG volume budget, m^3/s. These are the net volume transports through the sides (dark blue), bottom (dark green), and top (red), and the volume transport form of the change in storage due to changing SSH (light blue).

Appendix B.

The primary balance in the volume budget of the WAG is between advection through the sides and advection through the bottom, with changes in storage from sea-surface height and the evaporation-precipitation surface flux two orders of magnitude smaller (figure 3-11); mean values are in Table 3.1. The advective transports on the order of $10^5 m^3/s$ are up to about half the magnitude of the Atlantic Jet (about $1Sv$) and about a fifth of the recirculation of the WAG ($2-3Sv$ above $\sigma_\theta = 27.5$). The signs of the advective terms change frequently, but not regularly. Please note that an inspection of the spectra of these transports shows no peaks, meaning that these are aperiodic motions; this is to be expected with realistic forcing over less than one seasonal cycle when tides are not included.

The volume budget shows the net transports, but the total gross advective transports through the boundaries, the sum of the magnitude through each cell on each edge, is about ten times larger (figure 3-12). The gross transport magnitudes of the surface and storage terms are close to the magnitudes of the net surface and storage terms. The difference in magnitude of the gross transports through the sides and bottom is due to the areas of each surface and the typical magnitude of the velocities.

Table 3.1: Time-mean volume transports across the Euler WAG boundaries, m^3/s, positive into the gyre, rounded to three significant digits.

Volume Transport	Mean Value
Advection through sides	$25,100$
Advection through bottom	$-24,900$
Precipitation-Evaporation	-6.97
Change in storage via SSH	-41.8

While the bottom surface has a much larger area of about $10^{10}m^2$, velocities are about $10^{-4}m/s$, giving smaller gross transport than that through the sides with total area of about $5 * 10^7 m^2$ but velocities about $0.4m/s$. The difference in magnitude between the net and gross advective terms may be due to a combination of a path of water through the Eulerian gyre, such as the edge of the Atlantic Jet; recirculations near the edges, from transient eddies; and an overall residual directional flow, which could occur if the Lagrangian gyre moved across the Eulerian boundaries in one direction.

The mean transports show a spatial pattern that supports the idea that the edge of the AJ is contributing to the gross transports, in that the transports through the sides of the gyre are nearly along the edges and so are due to the mismatch between the edge and a Lagrangian path along the edge of the gyre (figure 3-13). The spatial pattern of the vertical transports includes upwelling in the northwest, although this is too far from the coast to be due to wind-driven upwelling, and in the center of the WAG. There is also downwelling in the eastern part of the WAG. Large values exist near the seamounts in the gyre; these means are large, but the spatial pattern around a seamount changes with the averaging time-interval.

The net volume transports from advection are likely largely due to the reshaping of the water that makes up the gyre in a stretching-squashing manner. A comparison between the vertical volume flux and the mean motion of the $\sigma_\theta = 27.5$ isopycnal, figure 3-14, demonstrates this possibility. If the bottom isopycnal moves up, or water flows in through the fixed bottom, the water above must move up or spread outward to conserve volume. Large matching changes in sea-surface height do not occur, but the outflow of water across the fixed boundary does. This set of processes is like squashing the water into a flatter shape. When water flows in horizontally across the edges, it also flows out across the fixed bottom and the bottom isopycnal moves down. This processes is like stretching the water into a narrower, longer region.

The WAG volume budget is formed in order to better understand the exchange of water between the AJ and WAG. The primary term that does the exchanging is the transport across the sides of the WAG. The gross transport across the sides is nearly $10^7 m^3/s$, while the net transport is about $1 - 5 \cdot 10^5 m^3/s$. The difference in magnitude between the net and gross advective terms may be due to a combination of a path of water through the Eulerian gyre, such as the edge of the AJ; recirculations near the edges, from transient eddies; and an overall residual directional flow, which would occur if the Lagrangian gyre moved across the Eulerian boundaries in one direction. Of these three options, the edge of the AJ overlapping the fixed boundaries seems likely from the pattern of the mean transports (figure 3-13), although I cannot completely discount horizontal movements of the full gyre, which would not be obvious from a mean.

The net transport through the sides is balanced primarily by transport through the bottom, which is closely linked to the bottom isopycnal moving across its mean depth. This isopycnal motion is then driving a squashing-stretching motion of the water. Because the sign of the net transport changes about once a week, in that time only about 10% of the volume of the WAG, which is about $2 \cdot 10^{12} m^3$, can be exchanged. This implies the net transport across the sides is stirring water between the AJ and WAG near the edges, not driving water into or out of the core of the WAG, which would require a larger exchange.

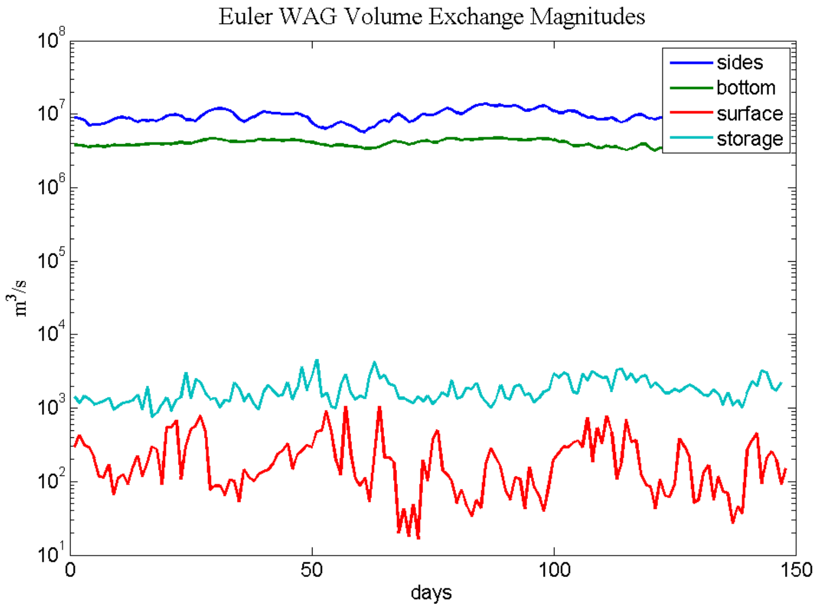

Figure 3-12: Magnitudes of the Euler WAG volume budget, m^3/s. These are the gross volume transports, the sum of the absolute value of the volume transport through each cell edge at the boundaries of the Eulerian WAG.

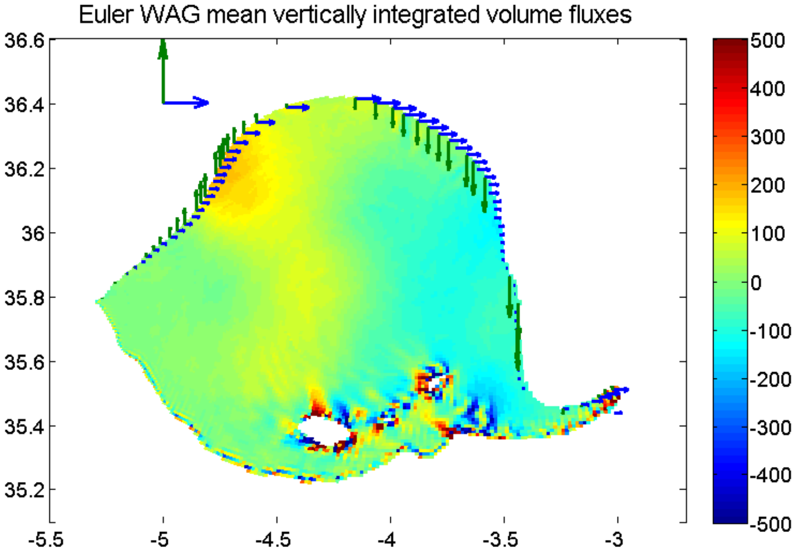

Figure 3-13: Mean vertically-integrated advective volume transports for the Euler WAG. Colors show transport through the bottom, arrows show transport through the sides. Top left arrows show scale, $5 \cdot 10^5 m^3/s$. White patches indicate seamounts.

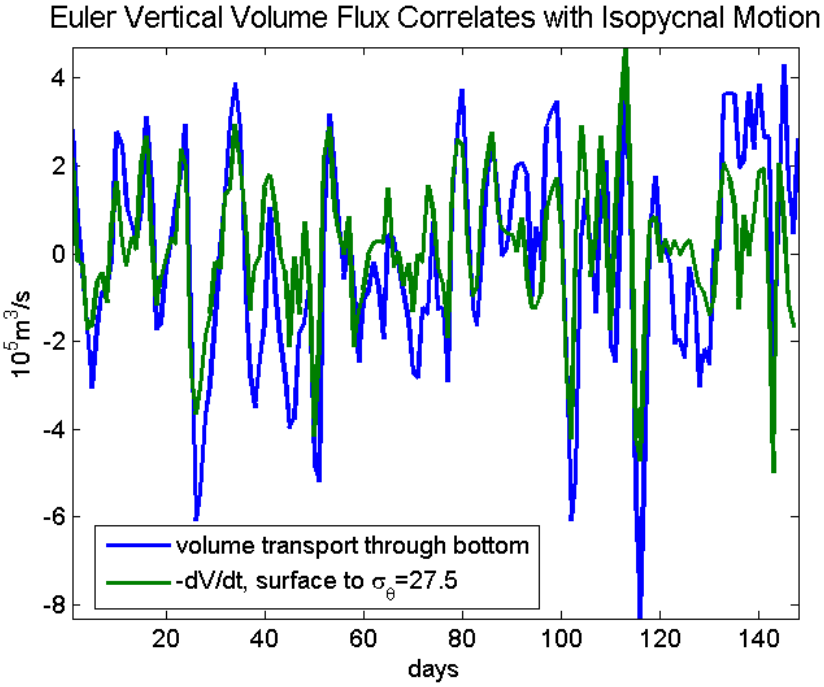

Figure 3-14: Euler WAG net vertical volume transport is primarily the $\sigma_\theta = 27.5$ isopycnal moving across the fixed bottom boundary, which is its mean depth. The vertical volume transport and the derivative of the volume above the isopycnal in the WAG are shown. These correlate with $r = 0.7447$ and $p < 0.0001$

3.3.1 Salt and Heat

I next compute the budgets for salt and heat using the model diagnostics of the transports of salinity and potential temperature (again, see Appendix B for details of computations). These include the change in storage, advective transports across the sides and bottom, diffusive transports across the sides and bottom, and surface forcing. The concentration budget terms for the full WAG can be represented by

$$\begin{aligned} \frac{d}{dt}\int c\,dV = &\int_{side} \vec{u}c\,dA + \int_{\sigma} \vec{u}c\,dA \\ &\int_{side} \kappa\nabla_h c\,dA + \int_{\sigma} \kappa\frac{\partial c}{\partial z}\,dA + \int_{surface} F\,dA, \end{aligned} \tag{3.2}$$

where each term is in the order listed above; c is either salinity or potential temperature, $\vec{u}$ is the velocity vector, κ is the numerical diffusivity including that from turbulence closure, and F is the surface forcing. The surface forcing of the concentration includes the effects of changing volume from evaporation and precipitation. Integrals are taken over the appropriate surface to separate transports through the sides, bottom ($sigma = 27.5$ mean surface), and air-sea interface (surface). These concentration terms are translated into salt and heat transports using density and specific heat.

The salt and heat budgets are intended to provide insight into how the core of the WAG remains fresher than the surroundings and how the WAG is warmer than the AJ. The question about temperature can be examined using the same full-WAG control volume as previously described for the volume budget, so I start there. The heat budget from the model diagnostics, figure 3-15, indicates that advection is the largest term. This advective heat transport follows the same spatial patterns as the volume transport (figure 3-15), demonstrating that the variations in temperature are not large enough to qualitatively change the advective patterns.

In order to understand how the advective transport is affecting the heat in the gyre, I remove the volume transport of the mean gyre temperature ($16.99°C$) using equation 3.1, scaled with the mean temperature and the appropriate density and specific heat. The resulting heat transports are positive when water with higher than average temperature is moving into the gyre or water with lower than average temperature is moving out of the gyre. In the mean-referenced heat budget, figure 3-16, changes in heat storage are now often the largest term, with advective transports a close second, followed by the surface forcing. The sum of the advection terms drive the changes in heat storage, which is clear from the anticorrelation between the advection and $-dH/dt$, figure 3-17. When the two are combined, the next-largest term, the surface forcing, is their primary balance. Diffusion terms are very small and negative, because the WAG is warmer than its surroundings.

Time means show that advection through the sides is generally positive but smaller than the average surface heating, even though the timeseries often shows the opposite (figure 3-16). This switch is due to occasional large negative daily advection through the sides. Advection and diffusion through the bottom cool the gyre in the mean. Overall, the gyre is cooling during the analyzed period. Because it is warmer than its surroundings, my understanding is that the WAG is warm due to the warmer surface Atlantic waters involved in its formation. An example of a large recirculation forming is shown in figures 3-18 and 3-19, where it appears that the AJ is bringing warm water along the southern coast, which is then entrained into a large gyre. After formation, in the analyzed situation, heat is lost to the deep waters faster than the air or the advection through the sides can warm it.

With regards to the maintenance of a subsurface salinity minimum in the WAG, the total WAG salt budget is not the most appropriate measurement. Instead, I examine a budget for just the region where the mean salinity is below 36.3, which is the mean location of the salinity minimum. The only change in the form of the budget is that there is advection through the top of the volume rather than surface forcing. Overall, the largest terms are advection and the changes in salt content, figure 3-20. The advection through the top is sometimes of the magnitude of the advection through the bottom and of opposite sign, as would happen if nearby isopycnals are moving in the vertical without changing width. The total advection nearly matches the changes in salt content, similarly to the relationship in the heat budget. Vertical diffusion is the next largest term, but it is rarely as large as advection.

The salinity minimum in the WAG is most likely connected to the minimum in the southern subsurface Strait of Gibraltar. However, this connection seems to be missing when the WAG is present, as evidenced by the lack of clear addition of lower-salt water through advection. In the mean, the total advection and the vertical diffusion are positive, driving an increase in salinity over time (figure 3-21). In this case, as with the discussion of the heat budget, my interpretation is that the salinity distribution is set by the formation of the WAG and is then eroded over time.

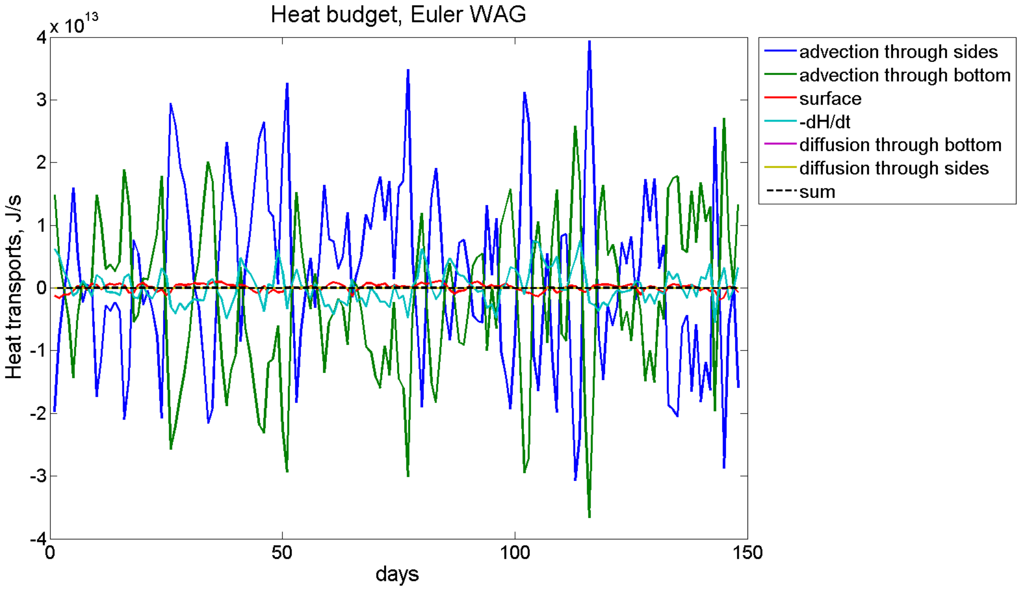

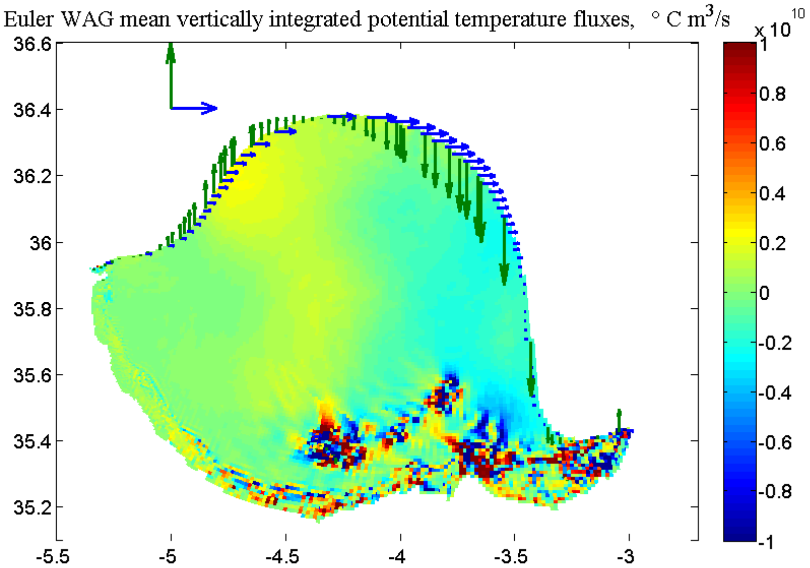

Figure 3-15: Top, total Euler WAG heat budget, J/s. Bottom, mean vertically-integrated advective potential temperature transports for the Euler WAG. Colors show flux through the bottom, arrows show flux through the sides. Top left arrows show scale, $5 \cdot 10^{10} {}^{\circ}Cm^3/s$. Seamounts do not appear as empty space as they did for the mean volume transports because the transport across the bottom-most wet cell is used rather than the σ_θ surface.

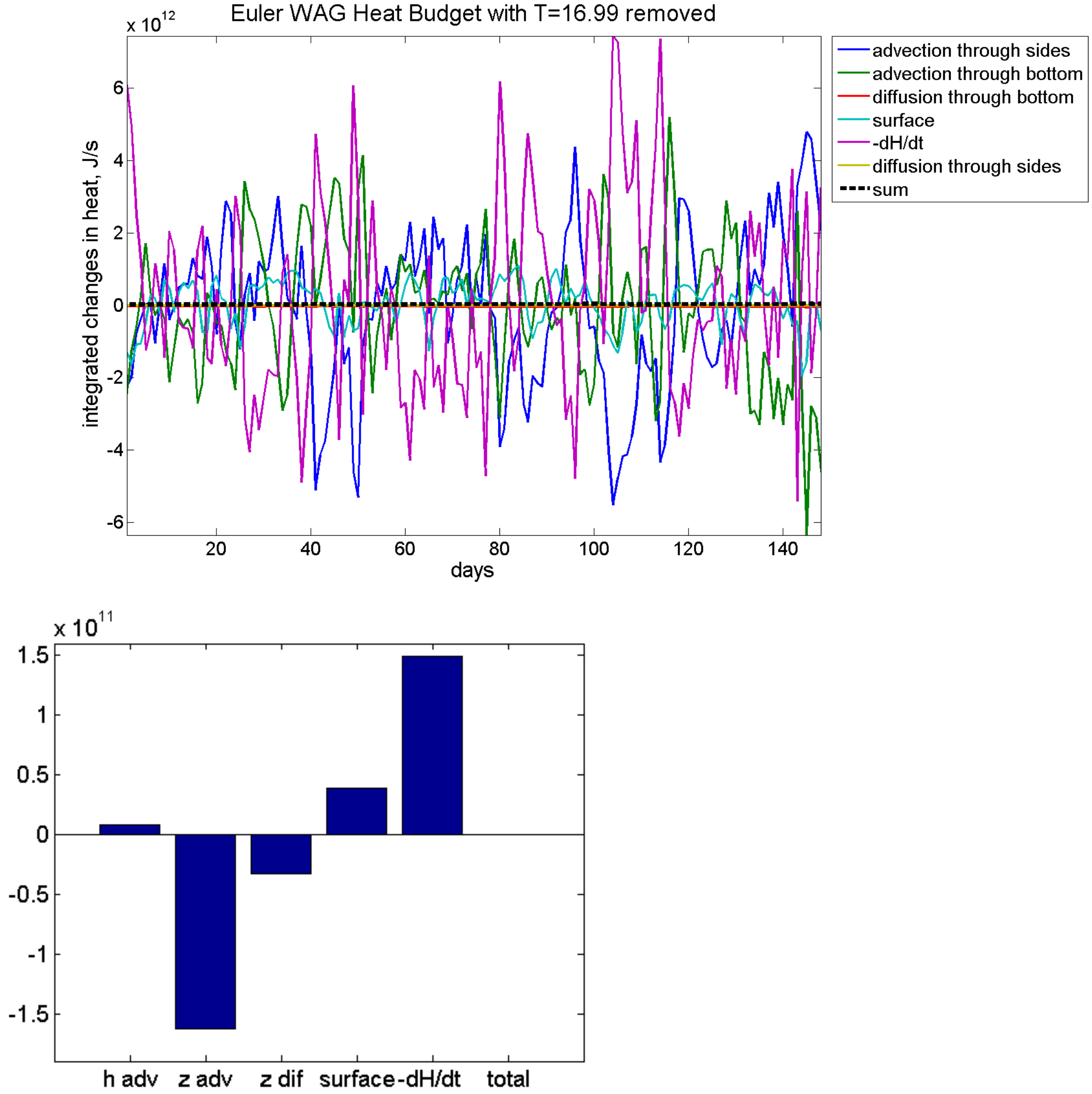

Figure 3-16: Top, Euler WAG heat budget, J/s, with the transports of heat by the volume transports of the mean gyre temperature, $16.99°C$, removed. Bottom, time-mean transports of heat, J/s, with the transports of heat by the volume transports of the mean gyre temperature removed. Terms are, left to right, advection through the sides, advection through the bottom, vertical diffusion, surface forcing, $-dH/dt$, and the sum of the terms.

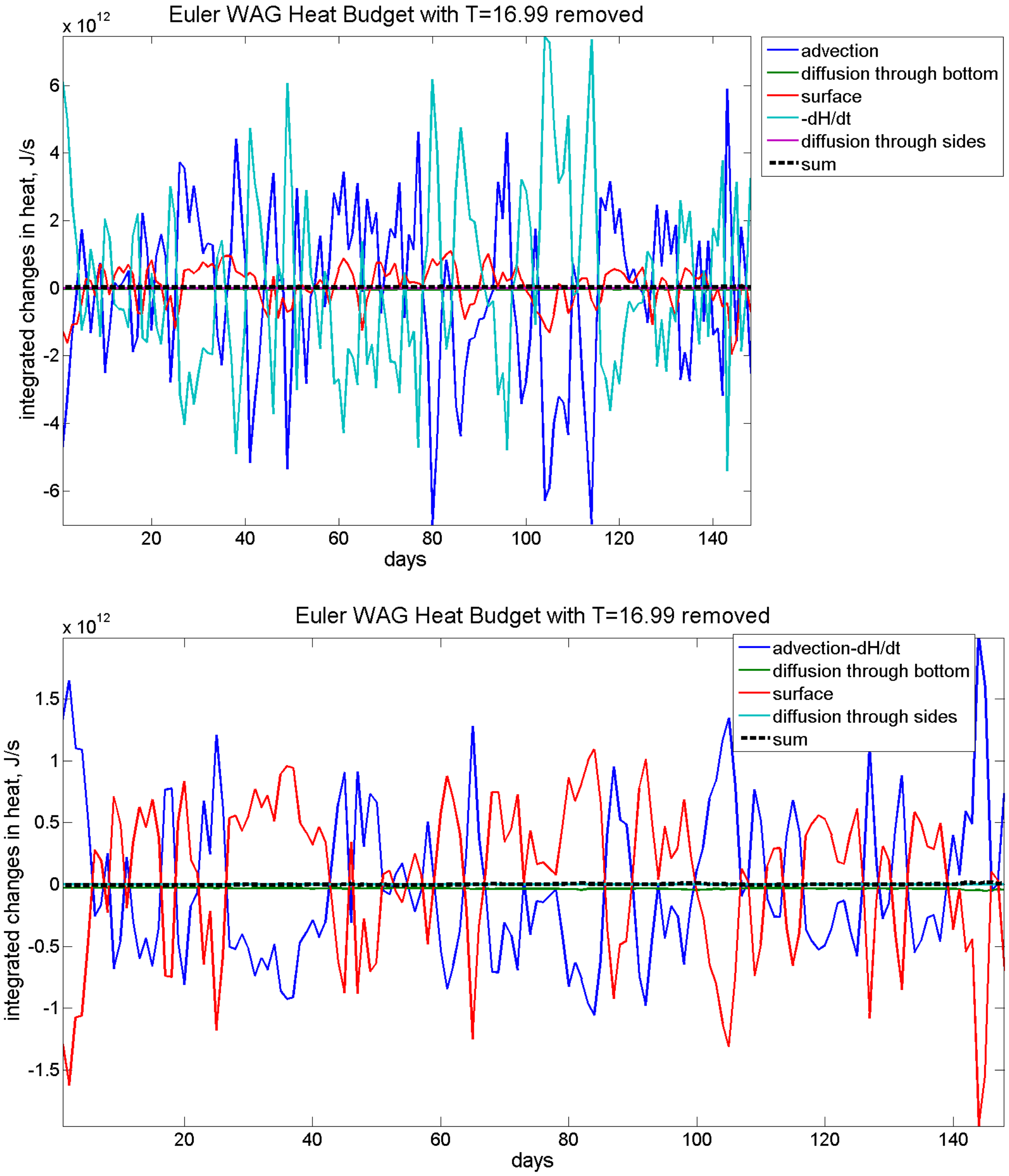

Figure 3-17: Top, Euler WAG heat budget, J/s, advection combined, with the transports of heat by the volume transports of the mean gyre temperature, $16.99°C$, removed. Bottom, same budget, with advection and $-dH/dt$ combined to show smaller terms.

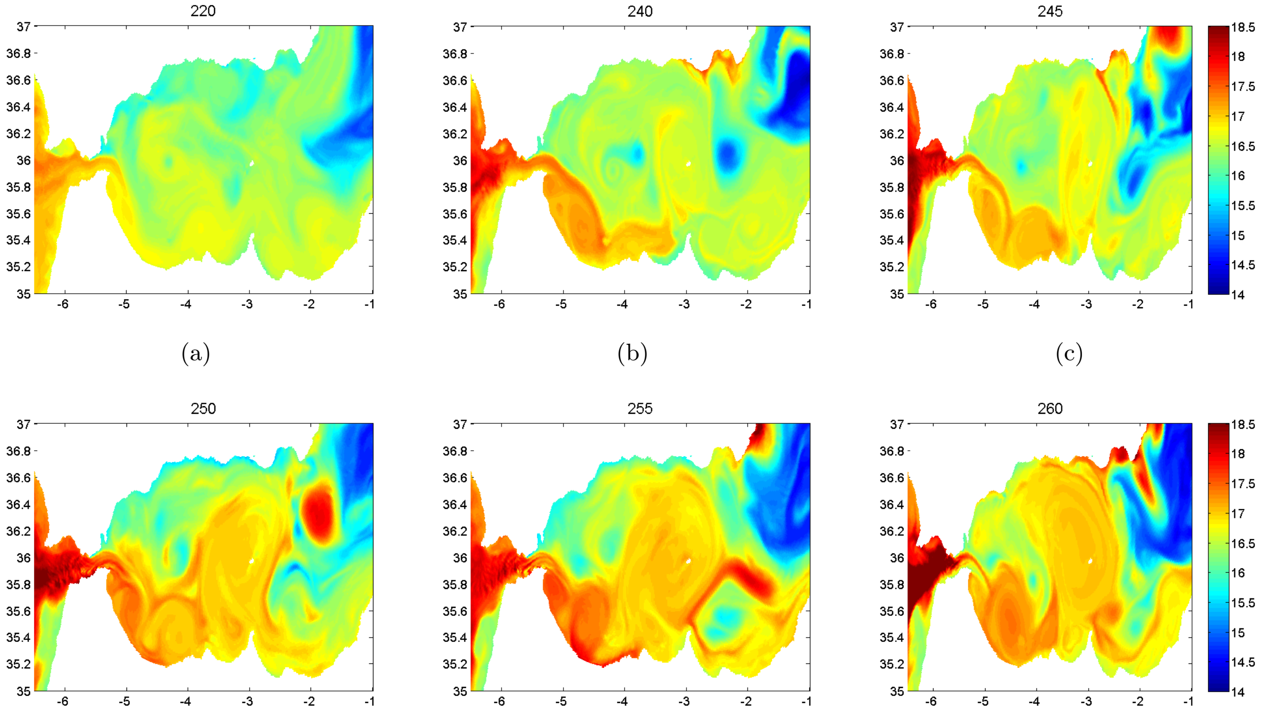

(a) (b) (c)

(d) (e) (f)

Figure 3-18: Potential temperature at 25m on simulation days 220, 240, 245, 250, 255, and 260. Day 220 is typical of the case where the AJ is attached to the African coast. The remaining days show how the AJ carries Atlantic water that forms a recirculation of nearly WAG size.

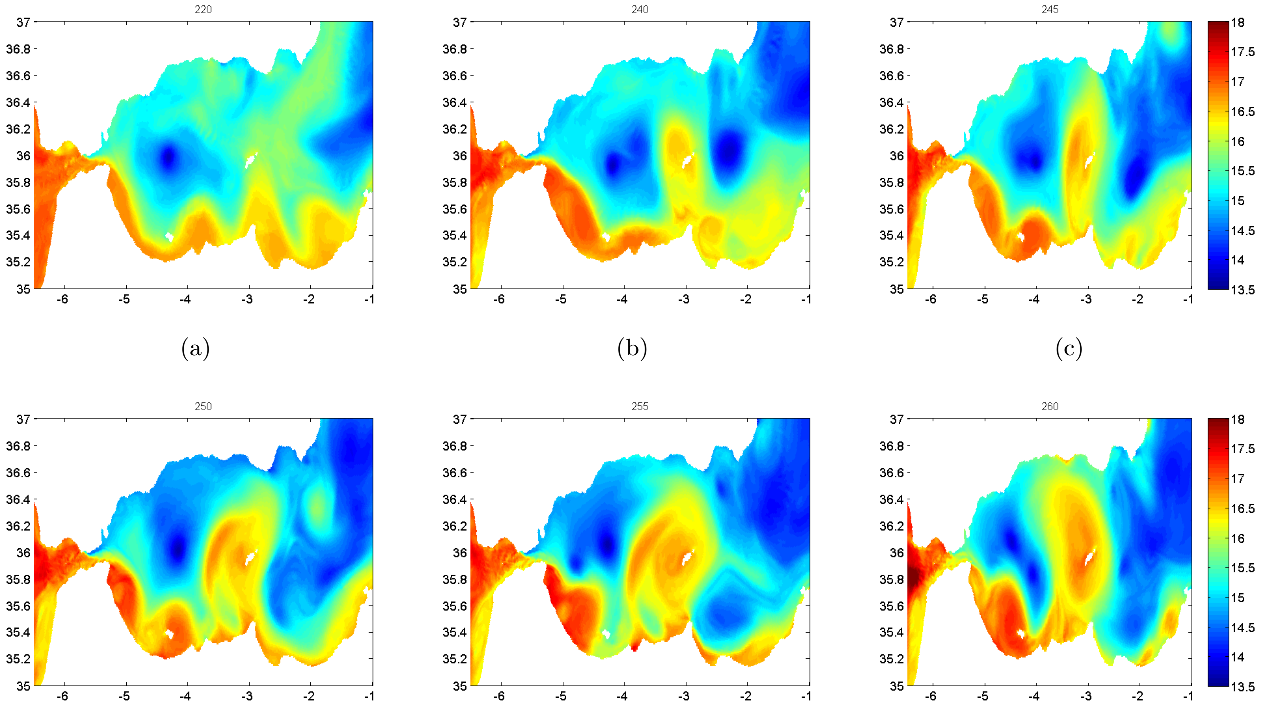

(a) (b) (c)

(d) (e) (f)

Figure 3-19: Potential temperature at 75m on simulation days 220, 240, 245, 250, 255, and 260. Day 220 is typical of the case where the AJ is attached to the African coast. The remaining days show how the AJ carries Atlantic water that forms a recirculation of nearly WAG size.

The time-variation discussed in Viudez et al. (1996) is more dramatic in my interpretation than the authors likely expected, being related to the collapse and reformation of the gyre rather than its smaller, more common variations. An example of the salinity patterns in a recirculation as it is forming is shown in figure 3-22 at the subsurface level where the minimum is often observed. Although this recirculation is transient and not in the same location as the typical WAG, this example demonstrates the possibility of my theory.

These Eulerian budgets of volume, salt, and heat in the WAG demonstrate that advection is the dominant process. It is possible that the advective terms in all three budgets indicate the reshaping of the Lagrangian gyre, in the squashing-stretching behavior described for volume. However, the changes in heat and salt due to the total advection match the changes in heat and salt content, so it could also be indicating the exchange between the WAG or its salinity minimum region and the surrounding waters. Given the consistent reversals, it is difficult to determine from the timeseries whether this exchange mostly changes the water properties or if it is a measure of fronts moving across the Eulerian boundaries. However, the time means indicate overall increases in salt and decreases in heat over the analysis period of five months. These changes are of the same sign as the transports through the bottom by mean advection and diffusion. Therefore, interactions with the deeper waters appear to be important drivers of the water properties of the gyre.

Both the salinity minimum and the overall heat of the WAG appear to be erroding over time. Not long after the end of the analysis period, the modeled WAG collapses. Past the analyzed period in the original simulation, a gyre-sized recirculation forms in the Alboran, near the Alboran Island. This reforming gyre is warmer and fresher than its surroundings, with a clear connection to the Strait of Gibraltar visible when examining a series of subsurface images from this gyre formation (figures 3-18,3-19,3-22). As stated previously, I suspect that the formation of the WAG sets the anomalous salinity and temperatures of the WAG as compared to its surroundings, and that the slow erosion of these properties may contribute to its collapse. However, further research would be needed to verify this hypothesis.

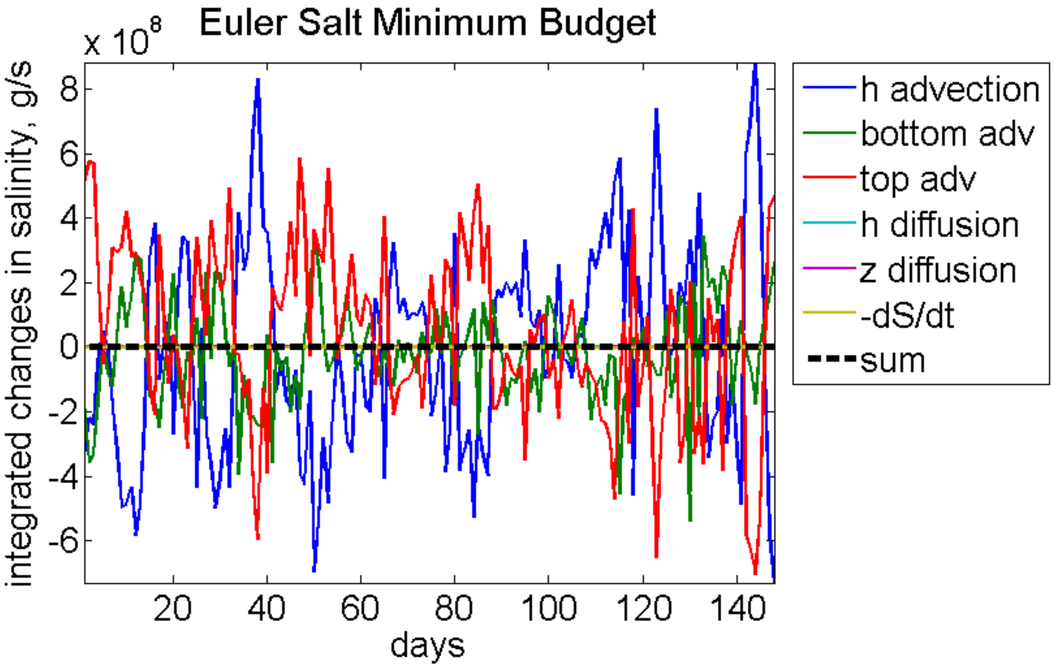

(a)

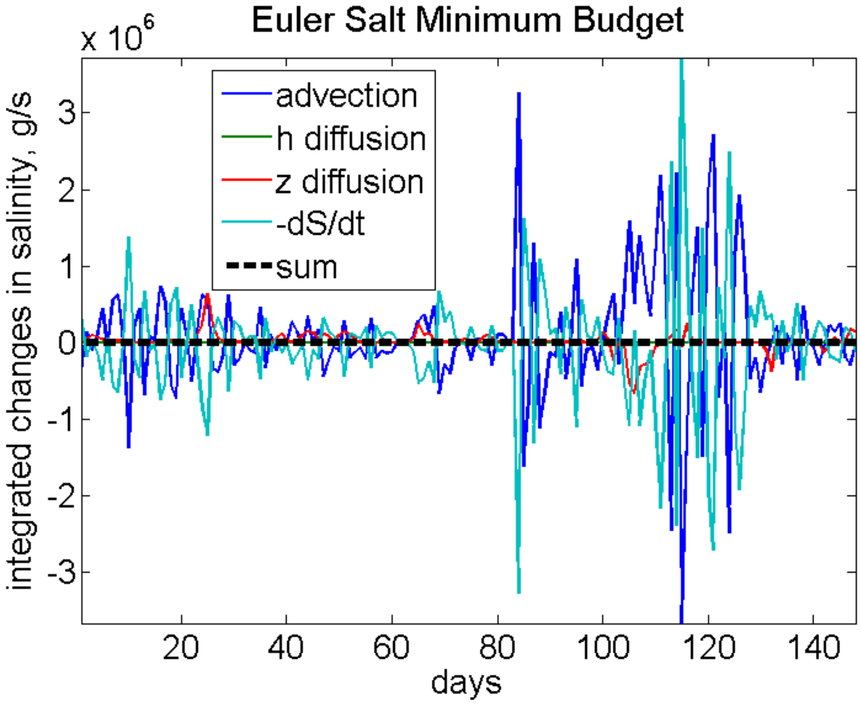

(b)

Figure 3-20: Euler salinity minimum region volume-integrated salt budget, g/s. Top, all terms; bottom, advection terms combined. In the legends, 'h' indicates horizontal, 'z' indicates vertical, and 'adv' is for advection.

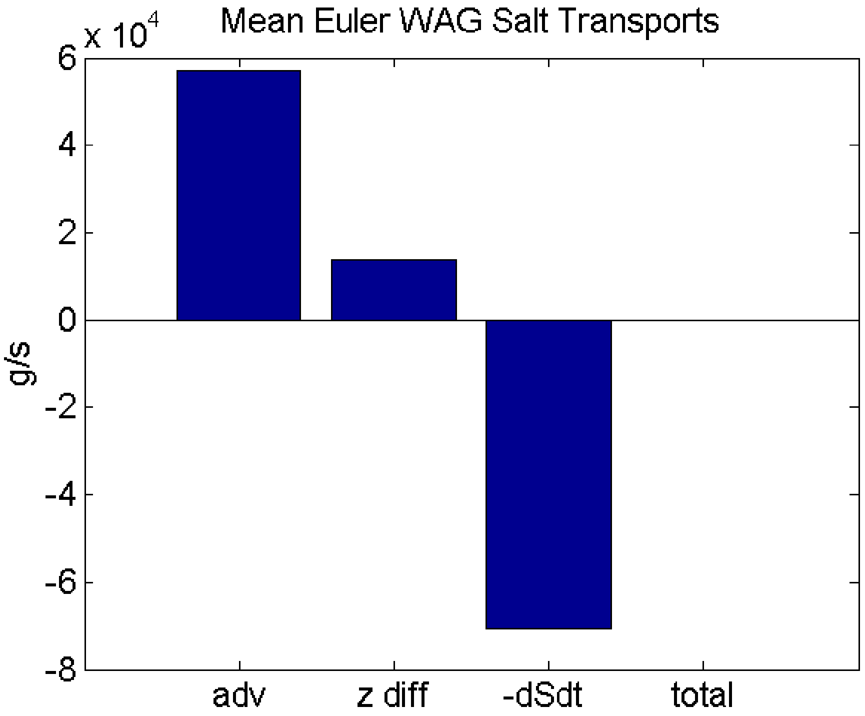

Figure 3-21: Euler salinity minimum region volume-integrated salt budget, g/s, time means. Left to right, terms are the total of the advection terms, the vertical diffusion, the negative changes in salt content, and the sum of these terms.

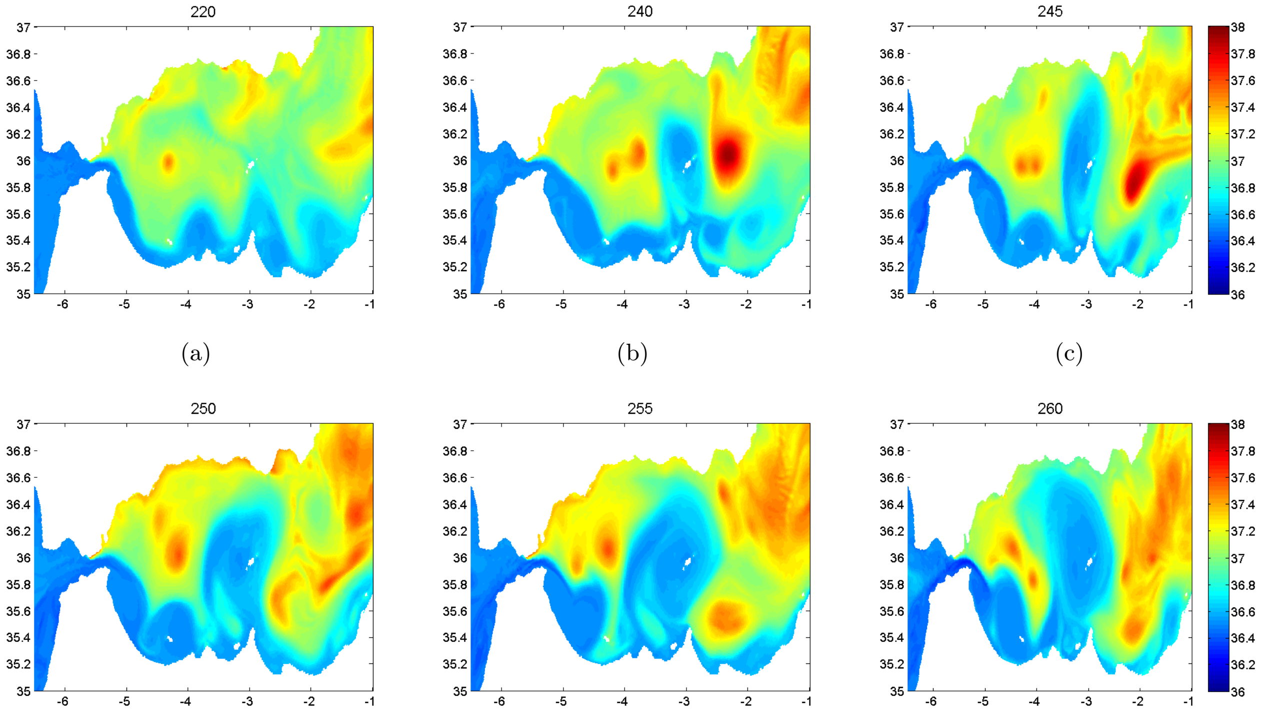

(a) (b) (c)

(d) (e) (f)

Figure 3-22: Salinity at 50m on simulation days 220, 240, 245, 250, 255, and 260. Day 220 is typical of the case where the AJ is attached to the African coast. The remaining days show how the AJ carries Atlantic water that forms a recirculation of nearly WAG size.

3.3.2 Dynamics of the WAG: Vorticity

The WAG has anticyclonic circulation which is clear from the mean surface relative vorticity as well as the mean surface velocities (figure 3-23). In order to understand what drives the collapse of the gyre, Sanchez-Garrido et al (2013) have suggested that advection into the gyre of cyclonic features causes it to become unstable. However, no vorticity budgets were shown, so I now examine the vorticity budget for this case with a consistent WAG to understand whether such advection could be a dominant term. The physical vertical vorticity equation is

$$\frac{\partial \zeta}{\partial t} + \vec{u_h} \cdot \nabla \zeta + f \nabla \cdot \vec{u}_h + \beta v = \frac{1}{\rho^2}(\nabla P \times \nabla \rho) + \nu \nabla^2 \zeta + \nabla \times \vec{F}, \tag{3.3}$$

where ζ is relative vorticity and β is the meridional derivative of the coriolis parameter, f. This is derived from the curl of the momentum budgets. In order, the terms are the change of relative vorticity in time, the advection of relative vorticity, the coriolis effects, the baroclinic pressure term, the viscous diffusion of relative vorticity, and forcing, from both wind and topographic drag. All necessary diagnostics to calculate the terms in the Navier-Stokes momentum equations are available as outputs from the MITgcm except the barotropic portion of the pressure gradient term, which can be calculated from SSH (details in Appendix B). To calculate the vorticity budget, I integrated the parallel part of each momentum term around the edge of the WAG, which is equivalent to the area integral of the curl by Stokes' theorem. For example, to calculate the change in time of the area-integrated vorticity from the changes in time of velocity, the formula is

$$\frac{d}{dt} \iint \zeta \, dA = \iint \nabla \times \frac{d\vec{u_h}}{dt} \, dA = \oint \frac{d\vec{u_h}}{dt} \cdot d\vec{s} = \frac{d\Gamma}{dt}; \tag{3.4}$$

where ζ is the relative vorticity, $d\vec{u}_h/dt$ is a vector of zonal and meridional velocity changes in time, dA is the WAG area, $d\vec{s}$ is the WAG edge, and Γ is the circulation. The full vorticity equation in this form is

$$\frac{d\Gamma}{dt} + \oint \zeta_a \vec{u} \cdot \hat{n} ds = \oint \frac{-1}{\rho} \nabla P \cdot d\vec{s} + \oint \nu \nabla \zeta \cdot \hat{n} ds + \oint \vec{F} \cdot d\vec{s}, \tag{3.5}$$

where the terms are in the same order: change in time, advection and coriolis, pressure gradient force, diffusion, and surface forcing. Here, ζ_a is the absolute vorticity, $\zeta_a = \zeta + f$. The integral calculations for each term are done for each layer of cells, then integrated using the height of each

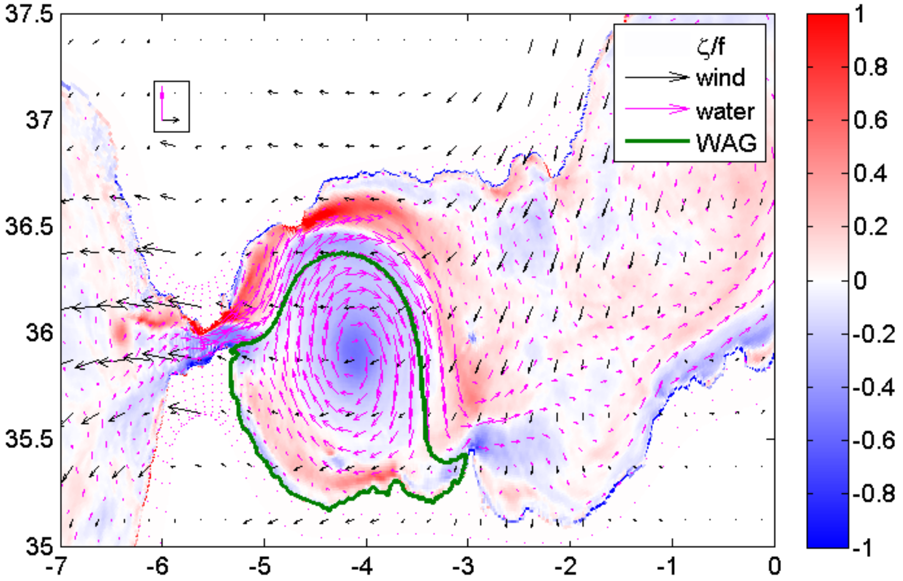

Figure 3-23: Mean surface relative vorticity normalized by planetary vorticity, f, in color. Magenta vectors show the mean surface water velocity, with a scale of $0.5m/s$ shown in the box near $(-6, 37)$. Black vectors show the mean wind stress, with a scale of $0.05Pa$ shown in the box near $(-6, 37)$.

cell to form the total. This method avoids introducing errors from taking the derivatives for the curl, so that the total of other terms matches the change in vorticity (see Appendix B for discrete calculation details).

In the depth-integrated vorticity budget, changes in vorticity, advection, and horizontal diffusion are the largest terms, with changes in vorticity and advection changing signs frequently (figure 3-24). The drag is slightly smaller and always positive. Windstress and vertical diffusion, shown together because windstress is the vertical diffusion of vorticity from the air, is similar in size to drag but does change signs. The Coriolis term is several orders of magnitude smaller than the five terms described. The pressure gradient and timestep terms are typically 5 orders of magnitude smaller than the five terms described and are not shown; both of these would be zero except for numerical approximation. Carefully examining the depth-integrated timeseries shows that depth-integrated advection is correlated with the changes in vorticity, but the other terms are not.

The frequent changes in sign of several vorticity budget terms makes time means of most of them sensitive to the period over which they are taken (figure 3-25). Drag is always positive, or cyclonic, which means it is slowing down the gyre. Advection is overall positive when integrated

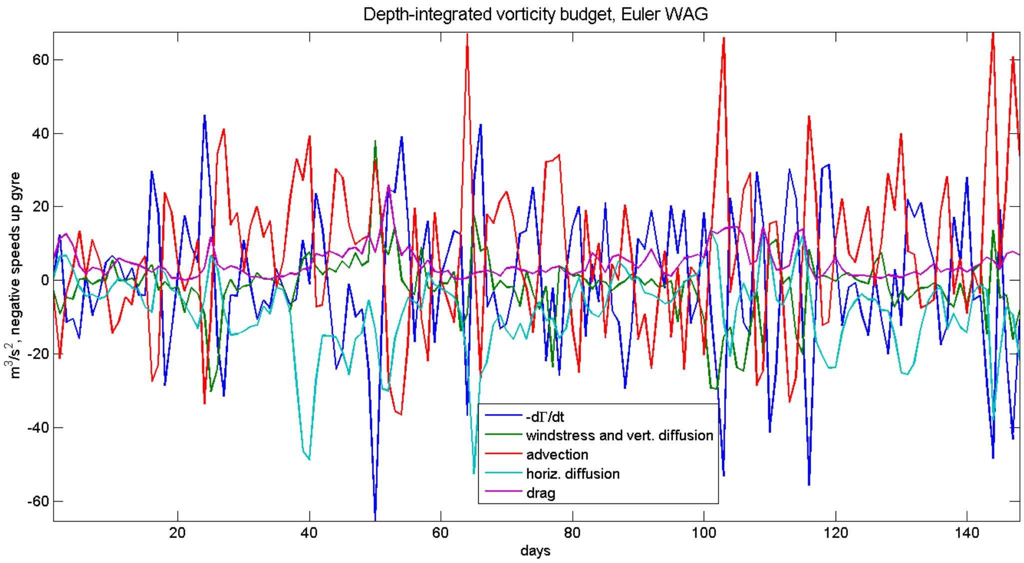

Figure 3-24: Vorticity budget for the Eulerian WAG, volume-integrated terms, m^3/s^2. Pressure and model time-stepping terms not shown, on the order of $10^{-5}m^3/s^2$. Coriolis term not shown, less than $1m^3/s^2$ in magnitude.

in depth and averaged in time, meaning that advection is also slowing down the gyre. Windstress and viscous diffusion are generally negative (anticyclonic). In particular, horizontal diffusion is the most anticyclonic in the total or monthly means, which indicates that it is the main driver of the WAG. Over the 148 day period, the mean change in integrated relative vorticity is fairly small but negative, indicating that the WAG speeds up slightly.

The depth structure of the budget terms adds spatial information about what is happening. However, most terms change signs in depth as well as time, including when looking at the means over different periods (figure 3-26). The exception is still drag, which is always positive, slowing down the gyre due to the model no-slip boundary conditions (figure 3-27a). In general, advection is negative near the surface and positive below, vertical diffusion becomes small below about $80m$, and horizontal diffusion has a subsurface maximum. At the surface, advection, diffusion, drag, and windstress together change the relative vorticity. Just below the surface, the advection and drag slow the gyre while the horizontal and vertical diffusion speed it up, probably in part by transferring wind stress downward. Past about $80m$, the vertical diffusion is small, and advection and drag are balanced by horizontal diffusion.

The small but negative values of vertical diffusion at depth may be important for the dynamics.

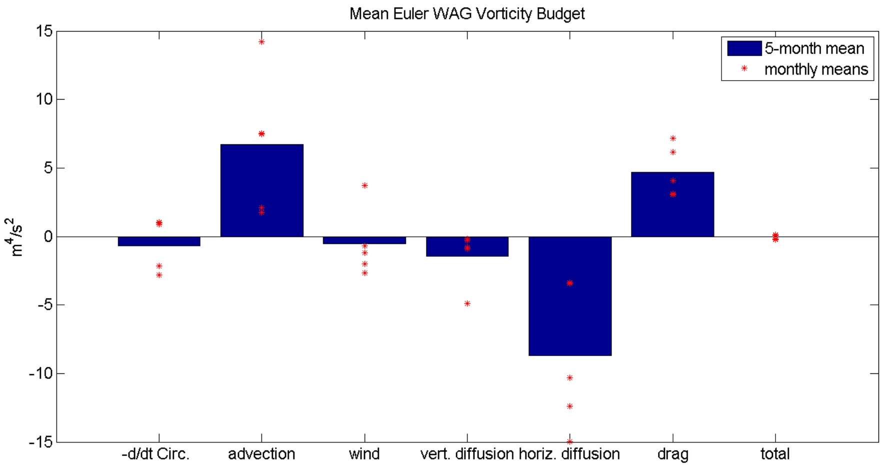

Figure 3-25: Time means of the volume-integrated vorticity budget terms, m^3/s^2, 148-day period in blue bars, red stars for each month's means.

In the mean, the vertical diffusion drives the WAG more than the wind stress. This driving effect may be due to the deep outflow current along the African coast driving the southern part of the WAG that lies above it. This forcing of the gyre was discussed by Bryden and Stommel (1982). The location of the deep outflow in the model during the analysis period supports this possibility (figure 3-28).

Returning to the structure of the vorticity budget terms, the mean magnitudes have a quite consistent pattern with depth. The mean magnitudes of each depth-integrated term are $2-20m^3/s^2$ (not shown), and the layered mean magnitudes are $0.05-0.35m^2/s^2$ and decrease with depth (figure 3-27). The vertical diffusion decays with depth fastest and most consistently, rather than having subsurface maxima (figure 3-27). This decay makes sense in terms of an Ekman effect, and is more clear in the mean magnitudes than in means due to the changes in windstress direction. Fitting an exponential to the magnitudes of vertical diffusion gives a decay scale of $37m$, which is consistent with observed ocean Ekman layer depths, and indicates that the gyre has an Ekman number of about 0.04.

Altogether, the vorticity in the WAG is driven by diffusion and wind but slowed by advection and drag. The day-to-day sign variations of the terms in the vorticity budget makes it hard to interpret their timeseries, but the depth structure of the time mean and the depth-integrated time means are more clear. The wind drives the surface, with the vertical diffusion also speeding up the gyre in

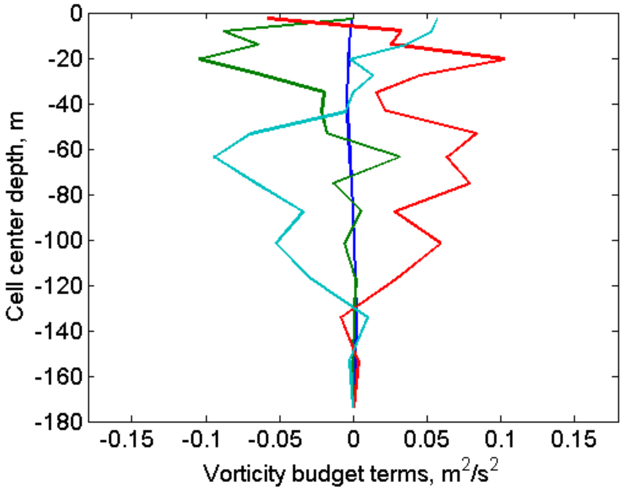

(a) 148 day mean

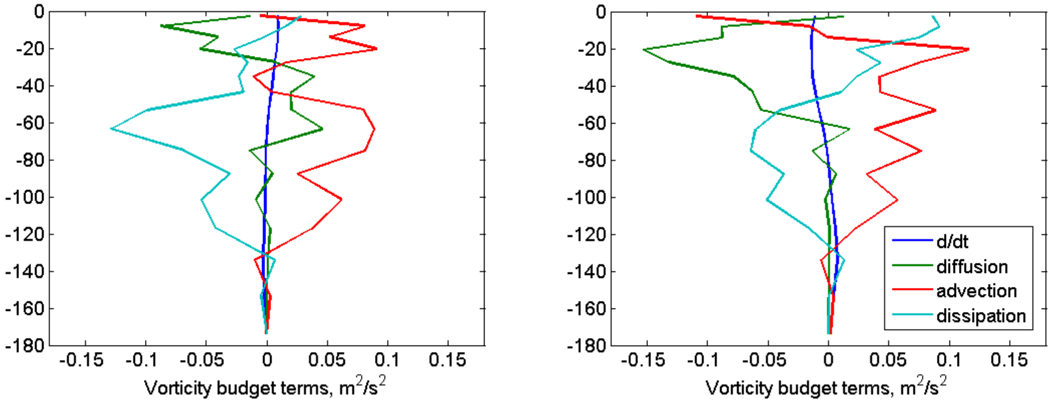

(b) mean days 1-74

(c) mean days 75-148

Figure 3-26: Euler WAG area-integrated vorticity budget in horizontal layers, mean of all terms vs. layer center depth, m^2/s^2. Top, full 148-day mean; left, first 74-day mean; right, last 74-day mean. Dissipation is the combination of drag and horizontal diffusion.

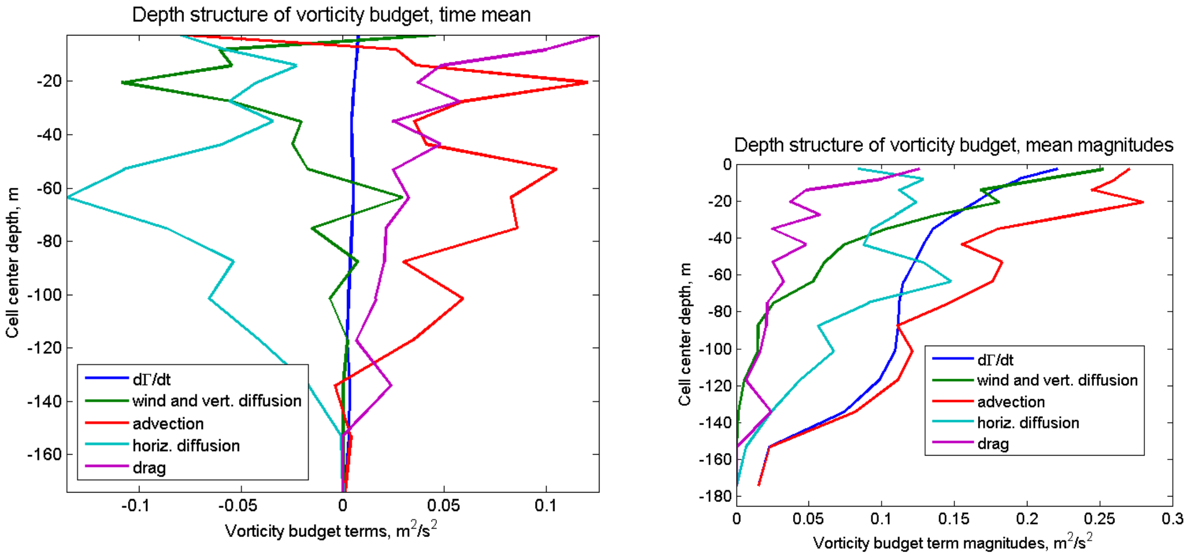

(a) 148 day mean

(b) mean magnitudes

Figure 3-27: Euler WAG area-integrated vorticity budget in horizontal layers, mean of all terms vs. layer center depth, m^2/s^2. Left, full 148-day mean; right, 148-day mean magnitudes. The decay in the diffusion term has a scale of about 37m.

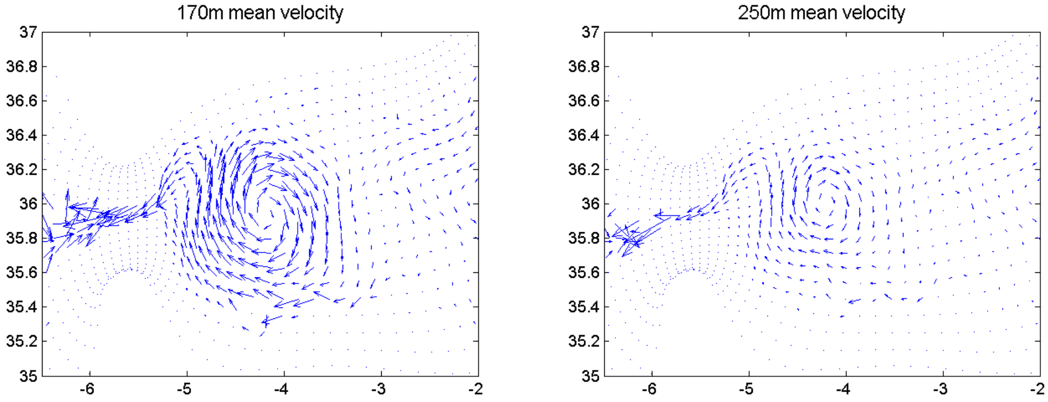

(a)

(b)

Figure 3-28: Mean velocity at 170m (a) and 250m (b) over the 5 months analyzed. Note the westward current along the southern coast that connects to the outflow through the Strait of Gibraltar.

the top half of the water column; below that, horizontal diffusion speeds the gyre. Drag from the topography on the sides and bottom slows the gyre, and integrated advection does as well, although the near-surface advection can be of opposite sign. The fact that the advective term here does slow the gyre by adding positive vorticity supports the possibile mechanism of WAG collapse being advection, as put forth by Sanchez-Garrido et al. (2013). In the timeseries, advection frequently changes sign, but if it were positive (cyclonic) for a longer period, it is reasonable to expect it could destabilize the WAG.

3.4 Discussion and Conclusions

This work used a numerical model of the Alboran Sea to examine, from an Eulerian perspective, transports of properties in and out of the Western Alboran Gyre. The model output was shown to produce a realistic flow with a consistent WAG for about 5 months, which is the period analyzed. The main volume analyzed was limited by a mean surface salinity of 36.475 and the mean depth of the $\sigma_\theta = 27.5$ isopycnal. Overall, budgets for volume, salt, heat, and vorticity have contributed to understanding what sets the properties of the Western Alboran Gyre by allowing an examination of each term in the physical equations for the system. Using a model run with forcing that is realistic, from reanalyses, rather than idealized, makes analysis of the budgets more difficult but means that results should be more relatable to observations.

The volume budget for the WAG had compensating horizontal and vertical advective transports, with the vertical volume transport through the bottom being driven by the motion of the $\sigma_\theta = 27.5$ isopycnal. Surface evaporation and precipitation and the changes in volume storage due to SSH variations were orders of magnitude smaller than these advective fluxes. The horizontal and vertical advective volume transports are likely largely due to the reshaping of the water that makes up the gyre in a stretching-squashing manner, as discussed with the comparison between the vertical volume transport and the mean motion of the $\sigma_\theta = 27.5$ isopycnal (figure 3-14). The magnitude of these transports are equivalent to about 1% of the volume of the gyre moving across the boundary in one day. Due to the frequent changes in sign, the transport across the sides of the WAG is probably stirring water between the edges and the AJ, but not reaching the WAG core. These net transports across the sides and bottom do not capture the possible motion of the WAG horizontally across the boundaries, which is part of the difference in magnitude between the gross and net transports.

The heat budget was examined to understand why the WAG remains warmer than the surrounding waters of the Alboran. The dominance of the advective transports through the sides and bottom of the WAG in volume carries over into the heat budget computed for the same volume. These largest transports are due primarily to the volume transport and do not indicate large changes in the salt and heat storage of the gyre. The vertical and horizontal advection again mostly compensate, but their sum correlates well with the changes in time, i.e. storage, of the heat inside the WAG. When the movement of the mean temperature by the volume transports are removed, the avective transports are reduced by about 80%, showing more clearly their relationship to changes in storage. The surface forcing is a secondary contributor to the changes in storage. Diffusive transports were quite small and nearly constant in time, in contrast to the advective fluxes and surface forcing, indicating the consistency of the magnitude and direction of gradients of salinity and heat. Overall, the gyre is cooling in the time mean, primarily due to advection and diffusion of heat through the bottom to deeper water. It is likely that the WAG is warm due to the advection of warm water from the Atlantic into the area during the WAG's formation and not an ongoing heating process.

The WAG contains a salinity minimum at $40-100m$ depth in both observations and the model output. Previous discussion on the maintenance of this minimum by Viudez and coauthors (1996) indicated that the options for transport from the Strait of Gibraltar are a mean ageostrophic flow or time variation in the flow. A salt budget for the volume containing the mean salinity minimum confirmed that advective transports of salinity are much larger than other terms in the budget. Overall, the salinity increased in time, due primarily to advection. Therefore, as with the analysis of heat, I expect the formation of the WAG plays a primary role in the formation of the salinity minimum, which is then degraded over time by advective stirring. I expect a Lagrangian analysis of the source of water advected into this region during the formation and when the WAG is present would be the next step in understanding the minimum, but such an analysis was outside the scope here.

The vorticity budget for the WAG was examined to understand what drives the gyre. Overall, the vorticity budget shows that advection, winds, diffusion, and drag all contribute to the dynamics of the WAG. While drag and advection add positive vorticity, slowing the gyre, windstress and diffusion add negative vorticity and drive the continued rotation. The largest driver on average is the lateral diffusion of vorticity, which is due to the AJ pushing the WAG clockwise. A balance between diffusion of vorticity from the faster AJ and drag from the coast is consistent with theory about smaller-scale recirculations (e.g. Hill 2013), but these theories do not include wind or advective exchange. Comparing the vorticity budget results to observations will also be complicated by the fact that the diffusion and drag are parameterized to account for unresolved motions.

Past theories about what is controlling the WAG include advection of relative vorticity (Sanchez-Garrido et al. 2013), windstress (Perkins 1990), and the inflow strength (Preller 1986). The vorticity budget suggests that advection of relative vorticity has a larger impact than windstress on the maintenance of the gyre. In their timeseries, both windstress and advection terms were sometimes the same magnitude, partially confirming the suggestions of both past papers. However, in the time mean, advection slowed the gyre much more than the wind drive it. The third theory, regarding the influence of the inflow through the Strait, is less directly related to the budgets formed here. Inflow may relate to the large-scale pressure gradients, which are important for the large-scale geostrophic balance of the WAG. However, the inflow time series, which is very similar to the outflow in figure 3-6a, did not correlate with the pressure gradient term from the model diagnostics for any lag. Overall, the advection of positive vorticity into the WAG may contribute to its collapse, while lateral forcing from the AJ is very important for its continued anticyclonic rotation.

A significant complication in interpretation of the Eulerian WAG budgets is that the area chosen does not correspond to a “dynamical" gyre, in that the boundaries of the “dynamical" gyre evolve in time, crossing my fixed boundaries. These crossings probably contribute to the very large horizontal advective fluxes in all budgets shown here. A Lagrangian approach that tracked the edges of the gyre should give more clear results, but has its own challenges in identifying the evolving boundaries.

3.5 References

Bormans, M., & Garrett, C. (1989). A simple criterion for gyre formation by the surface outflow from a strait, with application to the Alboran Sea. Journal of Geophysical Research: Oceans, 94(C9), 12637-12644.

Bryden, Harry L., and Henry M. Stommel. “Origin of the Mediterranean outflow.” J. Mar. Res 40 (1982): 55-71.

Gascard, J. C., & Richez, C. (1985). Water masses and circulation in the Western Alboran Sea and in the Straits of Gibraltar. Progress in Oceanography, 15(3), 157-216.

GRID-Arendal 2013, http://www.grida.no/graphicslib/detail/mediterranean-sea-water-masses-vertical-distribution_d84b#.

Heburn, George W., and Paul E. La Violette. "Variations in the structure of the anticyclonic gyres found in the Alboran Sea." Journal of Geophysical Research: Oceans 95.C2 (1990): 1599-1613.

Hill, D. F. “Simple Model for the Recirculation Velocity of Open-Channel Embayments." Journal of Hydraulic Engineering 140.4 (2013): 06014004.

Marshall, J., A. Adcroft, C. Hill, L. Perelman, and C. Heisey (1997) A finite-volume, incompressible

Navier Stokes model for studies of the ocean on parallel computers. J. Geophysical Res., 102(C3), pp 5753-5766

Perkins, H., Kinder, T., & Violette, P. L. (1990). The Atlantic inflow in the western Alboran Sea. Journal of Physical Oceanography, 20(2), 242-263.

Preller, R. H. (1986). A numerical model study of the Alboran Sea gyre. Progress in Oceanography, 16(3), 113-146.

Renault, L., et al. “Surface circulation in the AlborÃąn Sea (western Mediterranean) inferred from remotely sensed data." Journal of Geophysical Research: Oceans (1978âĂŞ2012) 117.C8 (2012).

Sammartino, Simone, et al. “Ten years of marine current measurements in Espartel Sill, Strait of Gibraltar." Journal of Geophysical Research: Oceans 120.9 (2015): 6309-6328.

Sanchez-Garrido, J. C., G. Sannino, L. Liberti, J. GarcÃŋa Lafuente, and L. Pratt (2011), “Numerical modeling of three-dimensional stratified tidal flow over Camarinal Sill, Strait of Gibraltar," J. Geophys. Res., 116, C12026.

Sanchez-Garrido, Jose C., et al. “What does cause the collapse of the Western Alboran Gyre? Results of an operational ocean model." Progress in Oceanography 116 (2013): 142-153.

Viudez, Alvaro, Joaquin Tintore, and Robert L. Haney. “Circulation in the Alboran Sea as determined by quasi-synoptic hydrographic observations. Part I: Three-dimensional structure of the two anticyclonic gyres." Journal of Physical Oceanography 26.5 (1996): 684-705.

Whitehead, J. A., & Miller, A. R. (1979). Laboratory simulation of the gyre in the Alboran Sea. Journal of Geophysical Research: Oceans, 84(C7), 3733-3742.

Chapter 4

Chaotic Advection in the Alboran Sea, I: Lagrangian Geometrical Analysis of the Western Alboran Gyre

Summary

Fluids are studied from either Eulerian or Lagrangian reference frames, depending on the types of information available and the questions being asked. The Eulerian frame has a fixed reference point and coordinates, which is useful for creating maps of water properties from observations, such as for Global Ocean Ship-based Hydrographic Investigation Program repeat sections, and for theories of the steady circulation in a basin, such as the traditional Stommel gyres. In contrast, the Lagrangian frame is that of the fluid, where coordinates are functions of time following a fluid parcel. The Lagrangian view is most useful when considering the evolution of the properties of a parcel of water and its path.

From the results of the Eulerian analysis of the Western Alboran Gyre (WAG), there appears to be a large transport of water across the northern boundary. I interpreted this transport as an exchange between the Atlantic Jet (AJ) and the WAG, which have slightly different physical properties including temperature and salinity. However, it is possible that this transport could be due to the WAG moving across the fixed Eulerian boundaries. I will now use a Lagrangian definition of the WAG edge to elucidate the movement of the edge of the WAG and the paths of exchanged

water.

A Lagrangian edge for the WAG would ideally be a material contour that separates water that recirculates in the gyre from water that passes by the gyre, with some capacity to identify water that will be exchanged. In order to construct such an edge, I use special material contours called manifolds that are connected to hyperbolic trajectories on the coast where the eastward current associated with the Atlantic Jet separates and then reconnects. The sketch of the WAG in the introduction, figure 1-1b, shows these manifolds in a time-dependent case. The two hyperbolic trajectories each have an associated material manifold that extends offshore. The western separation point has an offshore unstable manifold, separating water inside the WAG, to the south of the curve, from water that flowed through the Strait of Gibraltar, to the north of the curve. The eastern reconnection point has an offshore stable manifold, separating water that continues eastward, to the north of the curve, from water that turns westward and recirculates inside the WAG, to the south of the curve.

The stable manifold of the eastern hyperbolic trajectory and the unstable manifold of the western hyperbolic trajectory do not coincide, but instead cross each other. With multiple crossings of these material contours, it is possible for water to be trapped between them in *lobes*. These lobes contain water that is being exchanged between the WAG and the rest of the Alboran. For instance, when a lobe is bounded to the north by the unstable manifold and to the south by the stable manifold, it contains water that started inside the WAG but exits it, going farther east. In the opposite case, the lobe contains water that started outside the WAG and now enters it.

I find the manifolds numerically using direct trajectory integration by following an initially small blob of fluid that originate near the hyperbolic trajectories. These manifolds are computed at the surface and along several isopycnals. In order to use these manifolds to understand the exchange between the WAG and the AJ, I do two analyses. First, I create maps of the frequency with which a manifold passes through each point. These maps demonstrate the region where the manifolds and lobes exist. Therefore, this is the region where water is exchanged between the WAG and the AJ on the timescale of the manifold integration.

The stirring region includes the Eulerian WAG edge and, interestingly, can reach the northern coast, where there is upwelling. This extent indicates that upwelled nutrient can reach the WAG on fairly short timescales, which may be important for phytoplankton productivity. The extent of the stirring region becomes narrower with depth. The narrowing of the stirring region can be explained by the slower velocities at depth, leading to longer exchange timescales.

A complementary result to the stirring region is the location and extent of the core of the WAG: a region in the center of the WAG where manifolds do not enter. This core region is not in contact with the AJ or any other part of the ocean outside the WAG on the timescale of the manifold integration. The core is larger with depth as the stirring region is narrower. When 14-day integrations are used instead of 8-day, the core region shrinks to one point at the surface. Therefore, at the surface, the WAG can exchange water throughout its extent on timescales of weeks. This result is consistent with the timescale observed for the collapse of the WAG.

For the second analysis, I indentify individual lobes in three dimensions and examine their evolution. As an example, one of the larger lobes is shown in three layers on three different days as it enters the WAG. The lobe shrinks in horizontal extent as it moves south, corresponding to the deepening of the isopycnals toward the interior of the WAG. The lobe approximately conserves volume.

The size of the lobes and their water properties provide another insight into the exchange between the WAG and the AJ. The timescale of transport is related to the time for water parcels to traverse from one hyperbolic point to the other, about one week at the surface. From observing the surface lobes' movement, I chose a two day timescale, enough time for most lobes to move farther than they are long. With the two-day timescale, three-dimensional lobes extending from the surface to the $\sigma_\theta = 26.5$ isopycnal transport water at the rate of about 10^5 m^3/s, with associated transports of 10^8 kg/s, 10^6 kg/s of salt, and 10^12 J/s of heat. The cumulative transport shows that the WAG is increasing in volume, mass, and heat but decreasing in salt due to near-surface horizontal lobe advection. To know whether these trends will hold for the evolution of the WAG properties would require examining the full content of the WAG over time and estimating the other transports associated with diffusion, surface forcing, and other physical processes.

4.1 Introduction and Background

The Alboran Sea, just east of the Strait of Gibraltar, is where Atlantic water enters the Mediterranean in the form of the Atlantic Jet (AJ). After passing through the strait, this jet interacts with coastal recirculations, most notably the Western Alboran Gyre — a persistent anticyclonic mesoscale eddy along the African coast. Typical forms of the circulation can also include the Central Cyclonic Gyre and the Eastern Alboran Gyre (Renault et al. 2012). The AJ attaches to the African coast near the eastern edge of the Alboran Sea, often at the Almeria-Oran front, a boundary between Modified Atlantic Water and Mediterranean Water. Below the surface, Intermediate and Deep Mediterranean Sea Waters enter from the east, outflowing through the Strait of Gibraltar and contributing to Atlantic Meddies.

The Western Alboran Gyre (WAG) is warmer and fresher than the surrounding water, containing an observed below-surface salinity minimum (Viudez et al. 1996, 40-150m deep). As discussed in Chapter 3, although the WAG has been observed and modeled for some time, the processes that control its features are not well understood. I used Eulerian budgets for volume, salt, heat, and vorticity to elucidate these processes. In the results of my analysis of the WAG, there appears to be a large transport of water across the northern boundary, which I interpreted as an exchange between the Atlantic Jet and the WAG. However, this transport could be due to the WAG moving across the fixed Eulerian boundaries. In this chapter, I use a Lagrangian definition of the WAG edge to elucidate the paths of exchanged water.

Several recent studies have calculated statistics on the variability of the surface flow (eg Renault et al. 2012 and Peliz et al. 2013), but have not discussed the implications for transport. In a different approach, Sayol et al. (2013) used Finite-Size Lyapunov Exponents (FSLEs), a Lagrangian measure of chaos, to examine the sea surface transport. The authors found that the exterior of the WAG has high rates of stretching of fluid parcels as measured by the exponential separation rate of virtual particles. These high stretching rates indicate chaos, which suggests exchange across the WAG edge with enhanced mixing rates of the different waters. I will examine the geometry of this exchange, to elucidate the region with high stretching rates using information about the range of exchanged water on timescales of weeks.

In order to examine the exchange of fluid across the time varying boundaries of the Lagrangian WAG, I apply Lagrangian analysis techniques from dynamical systems to a model flow field from the Massachusetts Institute of Technology general circulation model (MITgcm, Marshall et al. 1997). The model flow is three-dimensional with a horizontal resolution of about $1km$ in the WAG and variable in time, forced by 6- and 12-hourly reanalysis data. These analysis techniques have been developed over the past few decades (see Haller 2015, Wiggins 2003) to locate coherent structures that constrain the transport of the fluid in physical flows. In a study of transport into a coastally-trapped recirculation in an idealized model (Miller et al. 2002), Lagrangian dynamical systems methods, specifically lobe analysis, provided a clear accounting of the exchanged water. In particular, the authors were able to clearly define the moving gyre boundary and avoid spurious fluxes caused by the gyre moving across its time-mean boundaries. I will apply similar methodology to examine the three-dimensional exchange between the AJ and WAG over about five months, the same period as described in Chapter 3. This is the first, to my knowledge, three-dimensional application of these methods to an aperiodic flow. I define the edge of the WAG in a time-varying manner, determine the stirring region where exchange can occur through chaotic advection, and quantify the lobe transports that occur into and out of the gyre.

4.2 Methods

4.2.1 Model

The physical model I use is the Massachusetts Institute of Technology general circulation model (MITgcm) in hydrostatic mode (Marshall et al. 1997). The specific configuration is similar to that of Sánchez-Garrido et al. (2013), with resolution increased roughly by a factor of three in the western Alboran. This model solves the Boussinesq form of the Navier-Stokes equations for an incompressible fluid with a finite-volume spatial discretization on a curvilinear grid with typical horizontal resolution of 1 to 3 km. The vertical grid has 5m resolution at the surface, decreasing with depth, and 46 vertical levels. The model domain includes the Strait of Gibraltar and has open boundaries in the Atlantic and Mediterranean. Surface forcing is provided by 6-hourly, 1/4-degree, 10m wind fields from the IFREMER CERSAT Global Blended Mean Wind Fields. Surface heat and salt fluxes are from the ERA-Interim reanalysis daily fields. Open east and west boundary forcings of velocity, salinity and temperature are from the 1/12-degree, daily Atlantic-Iberian Biscay Irish-Ocean Physics Reanalysis.

Details of the initial conditions and spinup are in Chapter 3. After 130 days of spinup, the full run began for November 1, 2007. Due to the behavior of the output as compared to Aviso daily fields and the Sammartino et al. (2015) measurements of flow through the Strait of Gibralter, the first 148 days will be analyzed. This is a period of about 5 months, November 2007 through March

2008. For a more detailed discussion of the output and validation, see the previous chapter.

4.2.2 Velocity Field Analysis

I use a Lagrangian perspective and dynamical systems methods to analyze the daily-average velocity fields from the MITgcm at the surface and along potential density surfaces. For potential density surfaces, the depth of the surface is found through linear interpolation for each day, and the horizontal velocity field is interpolated to that depth. This method assumes trajectories remain isopycnal, as no vertical velocity is explicitly considered. Generally, this assumption is reasonable for low Rossby number flows; for the full WAG, $Ro = u/fL \approx 0.25(m/s)/(8 \cdot 10^{-5}s^{-1} \cdot 10^5 m) \approx 0.03$, which is small. I use the surfaces $\sigma_\theta \in 26.3, 26.5, 26.75, 27, 27.5$ for my analysis of the exchange between the WAG and the Atlantic Jet.

In order to construct a Lagrangian edge for the WAG, I use special material contours called **manifolds** that are connected to hyperbolic trajectories on the coast. These trajectories are where the eastward current associated with the Atlantic Jet separates from and then reconnects to the African coast. Figure 4-2 sketches out the relevent geometry. The hyperbolic points ($H_1,\ H_2$) are along at corners of the coast (black). The unstable manifold from H_1 is the offshore material contour comprised of points that approach H_1 asymptotically in backwards time. This manifold separates water that begins inside the WAG, to the south of the curve, from water that just flowed through the Strait of Gibraltar, to the north of the curve. The stable manifold from H_2 is the offshore material contour comprised of points that approach H_2 asymptotically in forward time. This manifold separates water that continues eastward, to the north of the curve, from water that turns westward and recirculates inside the WAG, to the south of the curve. In a steady two-dimensional flow, the two manifolds would coincide and there would be no exchange between the gyre and the rest of the domain (see figure 4-2a). In a time-varying flow, the two manifolds can cross. Since water cannot cross material contours, the water between the manifolds is trapped, moving along the edge of the gyre with the manifolds until the relevent crossing passes H_2 (see figure 4-2b). These trapped parcels of water are called **lobes**, and are the only advective exchange across the edge of the gyre.

In order to numerically calculate the manifolds, I integrate trajectories from initial circles of about 100 points with radius $10km$ centered on the topographic corners marked as hyperbolic points in the geometry sketch. The hyperbolic trajectories in my model flow can move, but they are usually close to these corners. The initial circles are intended to allow for the movement of the hyperbolic trajectories, but changes in their position do not change the position of the manifold away from the coast (figure 4-1 shows an example for the stable manifold). The unstable, or forward, manifold is found by integrating forward from the coast at the southeast edge of the Strait of Gibraltar, $(-5.35°, 35.86°)$. For the trajectory integration, I use an explicit Runge-Kutta 4.5 order scheme with linear interpolation in space and time from daily-averaged horizontal velocities. The integration time is 8 or 14 days, with daily reseeding along the curve of the manifold each day to have a resolution of $2km$ or better, allowing the shape of the manifold to be well-resolved. The stable, or backward, manifold is integrated backwards in time from the African coast at the typical eastern extent of the WAG, $(-3.05°, 35.4°)$, with the same method and reseeding of trajectories over time. Trajectories move toward the hyperbolic point along the stable (unstable) manifold in forward (backward) time initially and extend away from the hyperbolic point along the unstable (stable) manifold in forward (backward) time, so an initial circle of points becomes a line along the unstable (stable) manifold at the end of integration. Similar methods have been used in Miller et al. 2002, Rypina et al. 2010, and Mancho et al. 2003, but with a line of initial points, which is most appropriate when the hyperbolic point and manifold direction are known.

An 8-day integration period for the manifolds was chosen so that at the surface, the unstable manifold from the western hyperbolic point and the stable manifold from the eastern hyperbolic point typically meet or cross. As an example of the geometry in the model gyre, I show the manifolds for the mean flow over the 148 day study period in figure 4-3. At the surface and isopycnals $\sigma_\theta = 26.3$ to $\sigma_\theta = 27$, the stable manifold is outside of the unstable manifold, showing that the flow is into the gyre. This convergence is consistent with anticyclonic gyres' typical downwelling behavior. At $\sigma_\theta = 27.5$, the manifolds are nearly matching each other, with the stable manifold just inside the unstable. This arrangement indicates a very small flux out of the gyre near this layer, and so I will consider it the bottom of the gyre for my analysis. Below the $\sigma_\theta = 27.5$ isopycnal, particles released near H_1, the western point, go west, part of the outflow through the Strait of Gibraltar.

Next, I use the manifolds and lobes associated with the WAG to elucidate the Lagrangian geometry of the Alboran Sea. I will begin by describing the regions covered by manifolds and untouched by them. I will then describe the behavior of lobes and use them to estimate the rate of

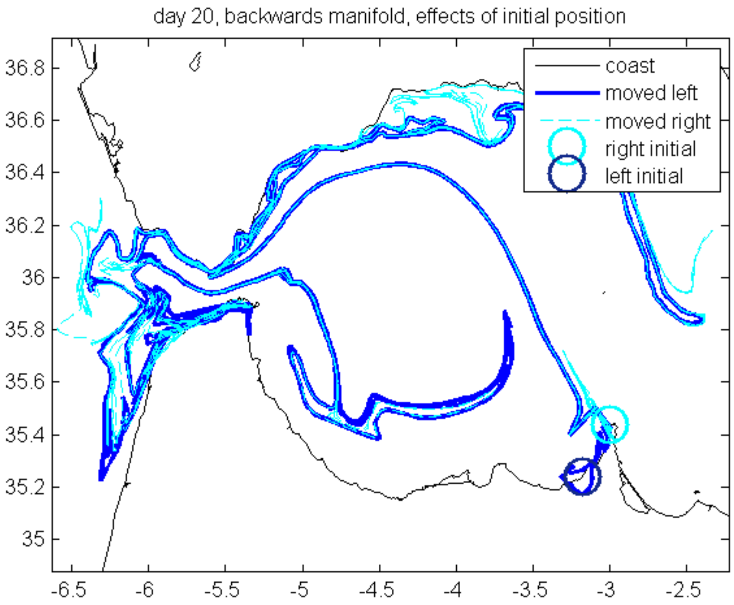

Figure 4-1: Surface stable manifold integrated over 14 days from two different initial positions. Note that in the interior of the Alboran Sea, these two calculations match.

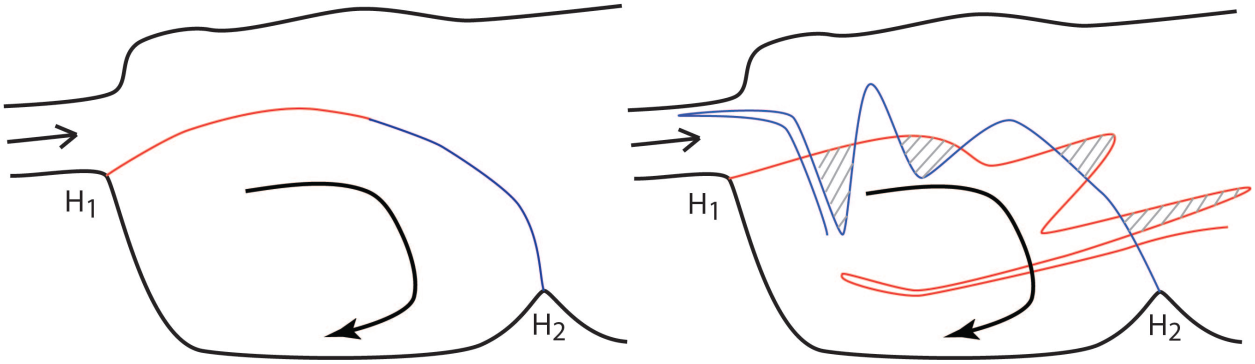

(a) steady (b) time-varying

Figure 4-2: Definition Figure : Unstable (red) and stable (blue) manifolds . Hyperbolic points H1, H2. Left, steady. Water is trapped in the gyre for all time. Right, periodic. Shaded lobes map to each other in time and transport water out of WAG. Unshaded lobes transport water into WAG.

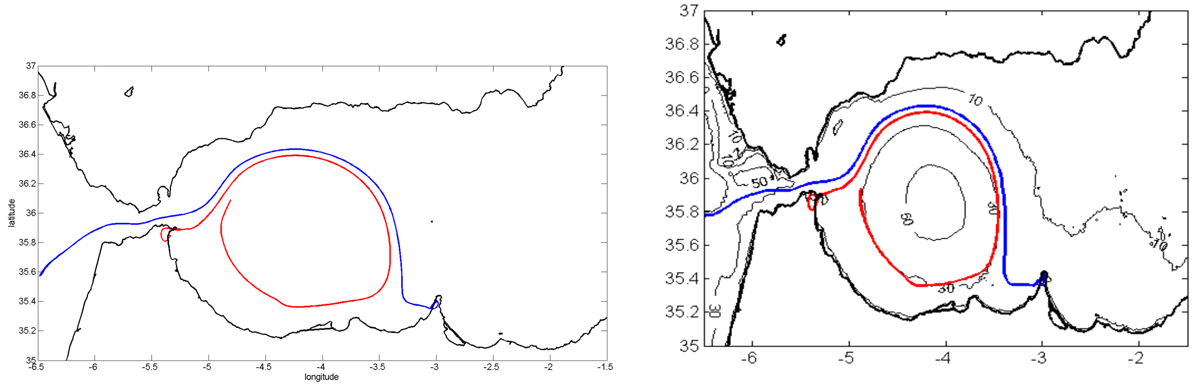

(a) surface

(b) $\sigma_\theta = 26.3$

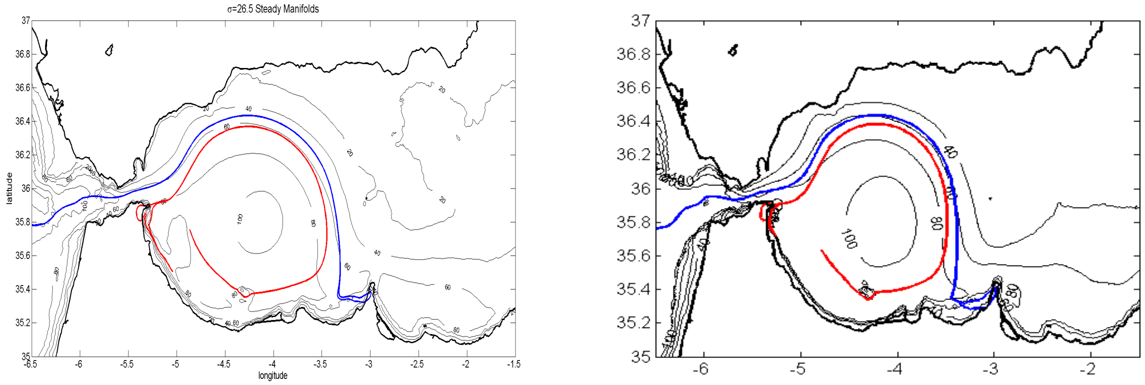
σ=26.5 Steady Manifolds

(c) $\sigma_\theta = 26.5$

(d) $\sigma_\theta = 26.75$

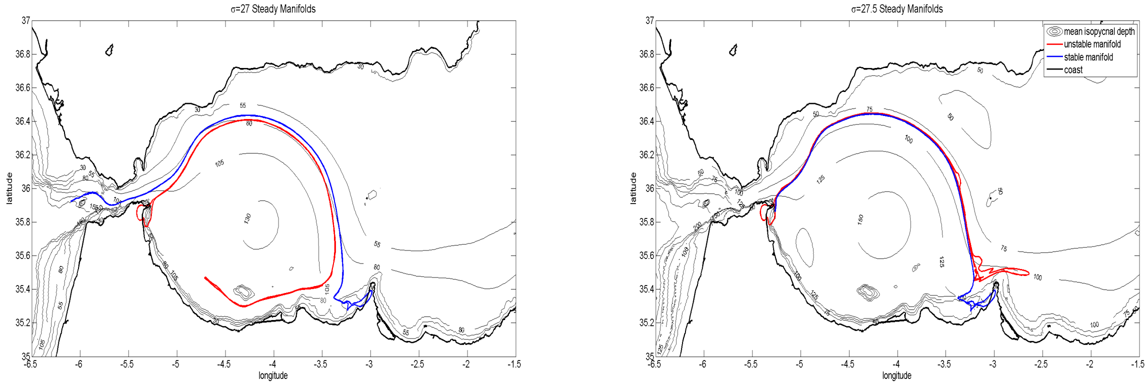
σ=27 Steady Manifolds

σ=27.5 Steady Manifolds

(e) $\sigma_\theta = 27$

(f) $\sigma_\theta = 27.5$

Figure 4-3: Manifolds on the surface and 5 isopycnals using the 148-day mean flow. Integration time 14 days, resolution 2km. Red, unstable manifold; blue, stable manifold; thin black contours, isopycnal mean depth; thick black, coast.

exchange of material into and out of the WAG.

4.3 Results

4.3.1 WAG core and stirring regions

Manifolds trace water that asymptotically approaches the hyperbolic points that define the limits of the WAG and delineate the entering and exiting lobes of water between their intersections. Although in the next section I will examine individual lobes, here I describe the typical location of the manifolds and, by extension, the lobes. The region where manifolds are typically located is the region where lobes are typically located; the regions beyond the extent of the manifolds do not exchange water across the edge of the WAG on the manifold integration timescale.

For the five-month period of analysis, manifolds are integrated for 8 or 14 days; 8 days typically allows a closed curve at the surface from the combination of forward and backward manifolds to define the WAG, while 14 days typically is long enough for this closing at deeper isopycnals. I examine manifolds from the surface and potential density surfaces $\sigma \in 26.3, 26.5, 26.75, 27, 27.5$ which all have mean inflow through Gibraltar. Maps of the probability of a manifold crossing small location bins were created, and show that the manifolds are typically in the area that is expected to form the 'edge' of the WAG (figure 4-4. I call the region covered by manifolds the **stirring region**, because it is the region where water can be exchanged across the WAG edge on relatively short times, 1 day to 2 weeks. The stirring region is similar to the high-valued regions in the Sayol et al. (2013) mean FSLE map at the surface. At increasing depth (density), these stirring region maps have thinner high-probability regions and a lower integrated probability over the domain. This decrease can be explained by manifolds being shorter with depth as the typical velocities decrease. Equivalently, the smaller exchange area with depth indicates longer timescales for exchange.

At the surface, I also show the probability maps of the location of the forward and backward manifold separately (figure 4-5) to describe the regions of the Alboran that can reach the hyperbolic regions within the 8 day integration time. Interestingly, the northern shore is included in the stirring region; in particular, the northwestern Alboran front (NWAF) region which often has upwelling is included for connections along the backward manifold, implying that some of this water is likely to be advected into the outer edges of the WAG and thus might be brought to the interior via a lobe. For phytoplankton, this is important because the upwelling region would add nutrients to the water and the WAG would retain it for a fairly long time, such that there might be growth of plankton along the edges of or inside the WAG that is connected to the added nutrient from the NWAF. Further explanation of why this may be important and how it could be investigated are in Appendix C.

The core of the WAG, a region where water is retained over long times, moves with the gyre over time, but a statistical Eulerian location for the core is the area with a low likelihood of manifolds inside of the high-probability region. I use the contour of zero manifold probability to define the core (figure 4-6a). As defined, this core region is not in contact with the AJ or any other part of the ocean outside the WAG on the timescale of the manifold integration. Although this is not a rigorous technique to find a Lagrangian coherent structure, such as the least-stretching contour (Haller and Beron-Vera, 2012), I found that passive particles seeded inside these contours stayed within the WAG over time. Particles started within the region where no manifolds are observed tend to stay together as a cluster inside of the daily manifolds over a 12 day integration time (not shown). The core region expands with depth, implying a dome-shaped region in three dimensions. This expansion relates again to the decrease of velocities with depth, which creates longer timescales for exchange.

The exact contours of the core are particular to both the period analyzed, as more days of manifolds gives a greater certainty in the probability maps, and the integration time of the manifolds, as longer integration lengthens the manifold and covers more of the Alboran Sea. For comparison, the contours of zero manifold probability for 14-day manifolds is shown (figure 4-6b), which has a reduced area at each depth but follows the same pattern of expanding with depth. With the 14-day timescale, the core region shrinks to one point at the surface. Therefore, at the surface, the WAG can exchange water throughout its extent on timescales of weeks. This result is consistent with the timescale of about two weeks observed for the collapse of the WAG.

4.3.2 Advective Transport by Lobes

Lobes of water are trapped between the stable and unstable manifolds. They move around the edge of the WAG as they move from the inside to the outside or vice-versa. When a lobe is bounded to the north by the unstable manifold and to the south by the stable manifold, it contains water from

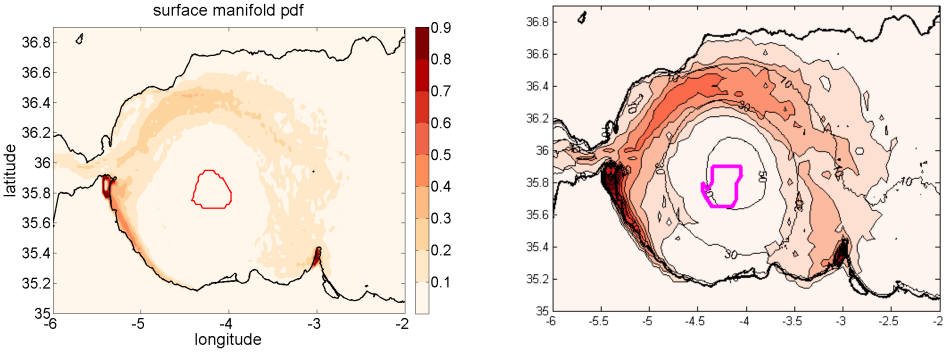

(a) surface

(b) $\sigma_\theta = 26.3$

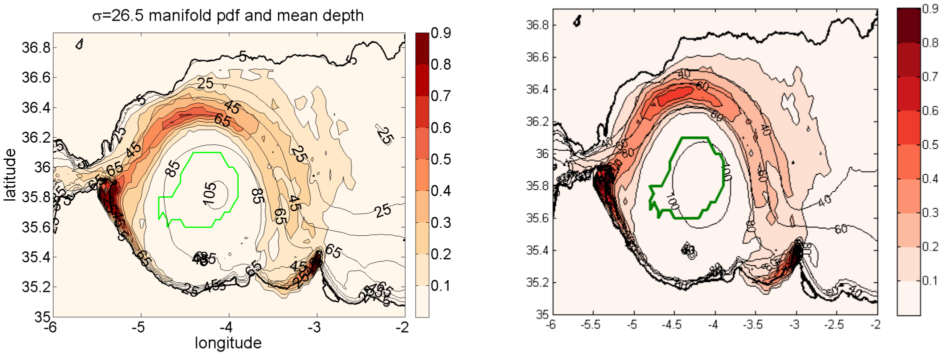

(c) $\sigma_\theta = 26.5$

(d) $\sigma_\theta = 26.5$

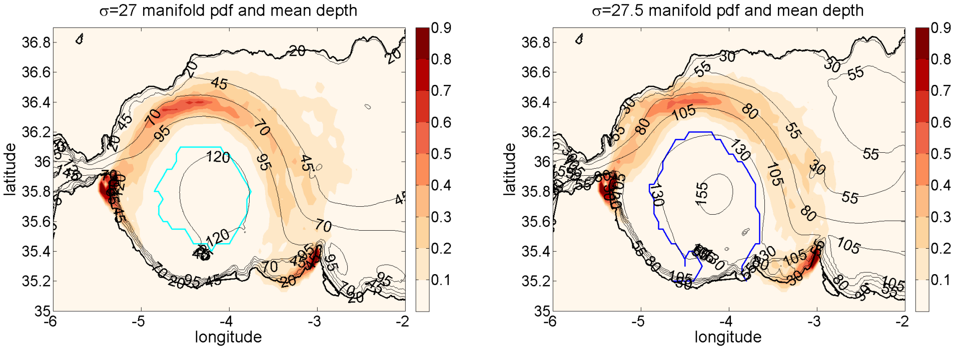

(e) $\sigma_\theta = 27$

(f) $\sigma_\theta = 27.5$

Figure 4-4: Probability of a manifold crossing each location on a given day, color. Daily horizontal velocities 8-day integration, 2km resolution. For (b)-(e), black contours are mean isopycnal depth and velocities are horizontal at the daily depth of the isopycnal. Contrasting color is the zero probability curve of the probability field.

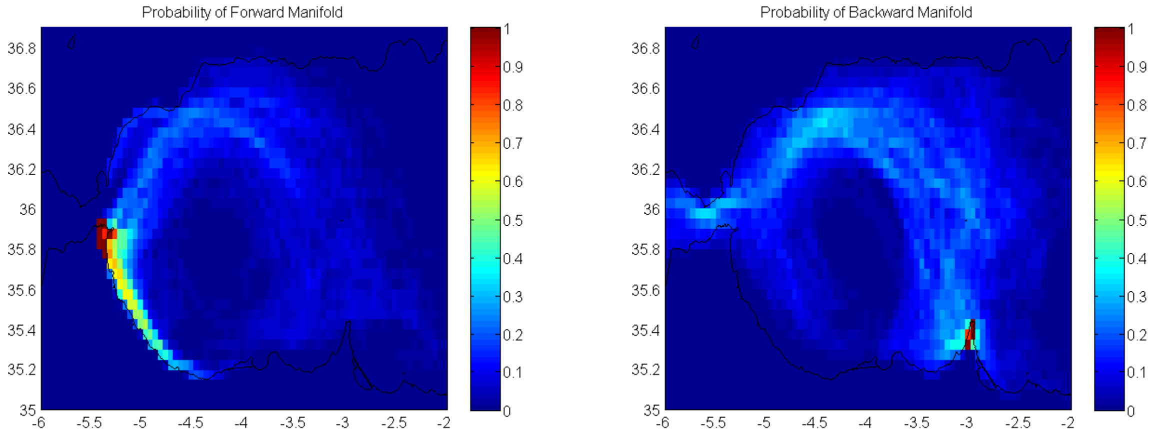

(a) forward

(b) backward

Figure 4-5: Probability of a manifold crossing each location on a given day. Surface velocity, 8-day integration, 2km resolution. (a)Unstable manifold. (b)Stable manifold.

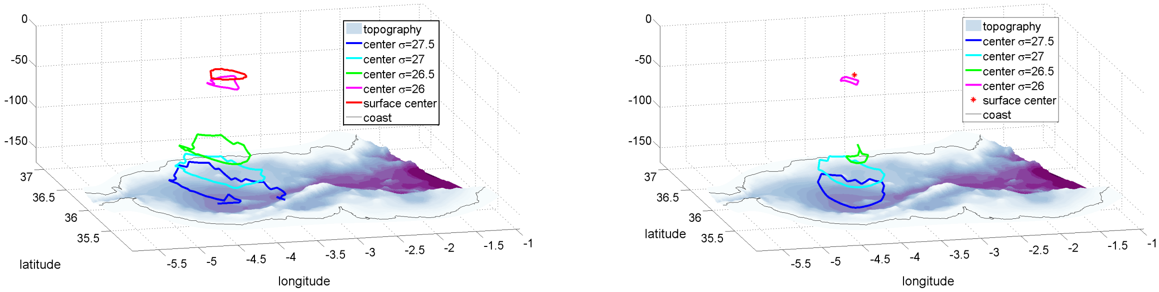

(a) 8 day

(b) 14 day

Figure 4-6: The center region of the WAG. Zero contour of the manifold probability field from the surface and 4 isopycnals ($\sigma_\theta = 26.75$ skipped for readability). Left, 8 day manifolds. Right, 14 day manifolds.

inside the WAG that will now leave it, going farther east into the Mediterranean. In the opposite case, the lobe contains water that started outside the WAG and now will enter it. The location of these lobes and their sizes describe the water that is exchanged between the WAG and the rest of the Alboran. Manifolds along isopycnals, discussed in the previous section, can show the shape of lobes with depth and allow estimates of their volume.

The depth to which I examine the lobes is limited by the inflow density, typically giving my deepest analyzed isopycnal ($\sigma_\theta = 27.5$) a depth of 80-150m. The lobes identified at the surface are usually visible in the $\sigma_\theta = 26.3$ isopycnal, but less often in deeper sections. These changes in depth are large when using finite manifolds of the same integration time, because often lobes are not closed on the lower isopycnals, but decrease if the integration time is adjusted to resolve the same average length of the manifold at each level. The manifolds I use for finding lobe volumes are all resolved on the same day along each isopycnal, and for about the same distance, in the hope that this will better represent the three-dimensional structure of the manifold and the lobe.

Unfortunately, identifying lobes is a non-trivial task; see figure 4-7 for an example of manifolds on two days. I identify lobes throughout the 148-day period at the surface and $\sigma_\theta = 26.3$, but only fully identify lobes during the first month on deeper isopycnals. 33 lobes are found at the surface, 29 of which are also found on $\sigma_\theta = 26.3$ which also had 12 other identified lobes. In the examination of deeper isopycnals, in the first month 5 lobes were identified which corresponded to those seen at both the surface and $\sigma_\theta = 26.3$. As an example of the 3D structure of lobes, one of the larger lobes is shown (figure 4-8) in three layers on three different days as it enters the WAG. The lobe shrinks in horizontal extent as it moves south, corresponding to the deepening of the isopycnals toward the interior of the WAG. Therefore, the lobe approximately conserves volume. It is still difficult to calculate a quantitative volume at this vertical resolution, particularly with uncertainty regarding the full vertical extent, as the lobe is clear at $\sigma_\theta = 26.5$ but not below, and manifolds are not attached to the same coastal locations for $\sigma_\theta = 28$ or below, where the water flows westward in the Strait of Gibraltar.

For an estimate of the lobe transport, I use the surface and $\sigma_\theta = 26.3$ lobe edges and the depth of the $\sigma_\theta = 26.5$ isopycnal as the vertical extent of the lobes. Near-surface volume, mass, salt, and heat transports are estimated using the average content of each lobe and a timescale of two days. The transports are on the order of 10^5 m^3/s for volume, 10^8 kg/s for mass, 10^6 kg/s for salt, and

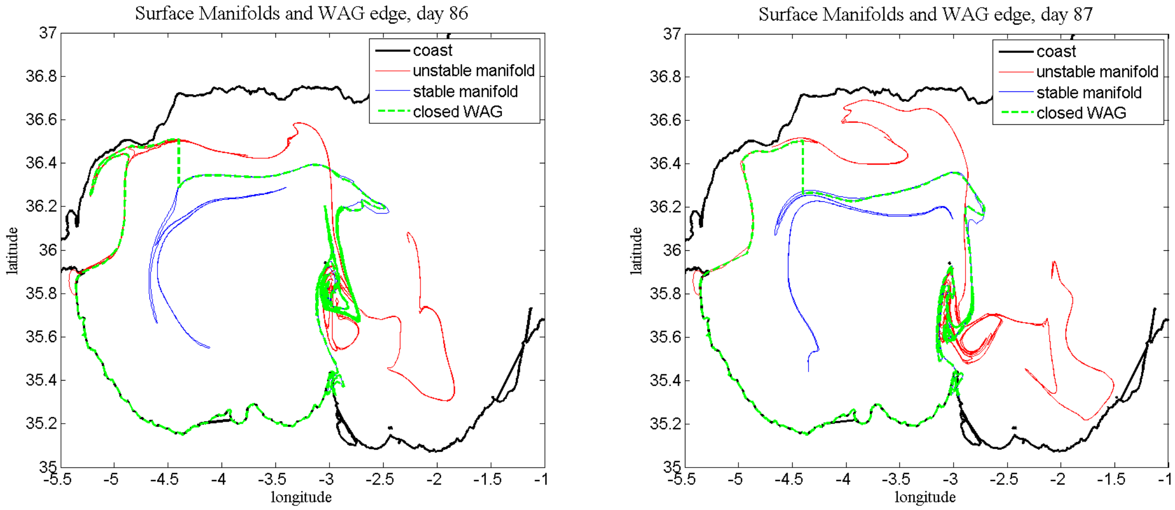

(a) (b)

Figure 4-7: Lagrangian WAG edge (green dashed curve) using gate to connect the unstable (red) and stable (blue) manifolds. A lobe is visible near $(-3, 36)$. Note the complicated folding of the manifolds.

10^12 J/s for heat. The cumulative transport due to near-surface horizontal lobe advection shows that the WAG is increasing in volume, decreasing in salt, and increasing in heat. However, without the full depth of lobes or the diffusive fluxes, it is not clear whether these trends hold. The next chapter will use other methods to re-examine the contribution of horizontal advection by lobes to the changes in water properties of the layer of the WAG connected to the inflow.

4.4 Discussion and Conclusions

So far, I have examined the geometry of the Alboran Sea around the WAG from a Lagrangian perspective. The manifolds that form the edge of the WAG extend through much of the Western Alboran Sea on timescales of 1-2 weeks, showing that water from the Strait of Gibraltar, the northern (Spanish) coast, and the Alboran Island can all interact with the gyre in that time. The core region of the WAG that is disconnected from these outside areas is fairly small by comparison, nearly disappearing at the surface for the two-week integration case. These paths for water between regions in the Alboran Sea indicate that it is well connected. This connectivity can be important for management in terms of both pollution, e.g. runoff and oil spills, and fisheries management for

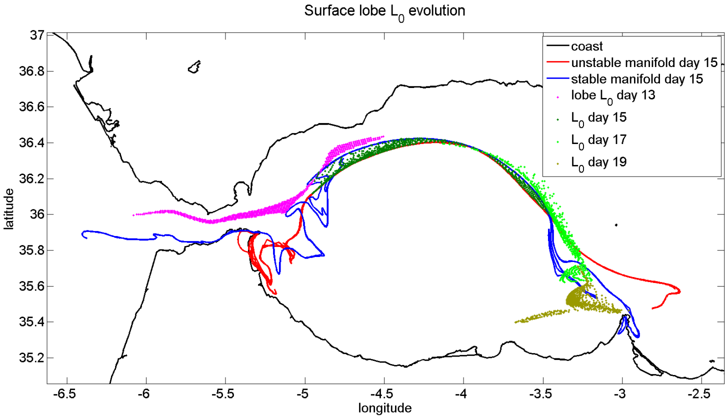

(a)

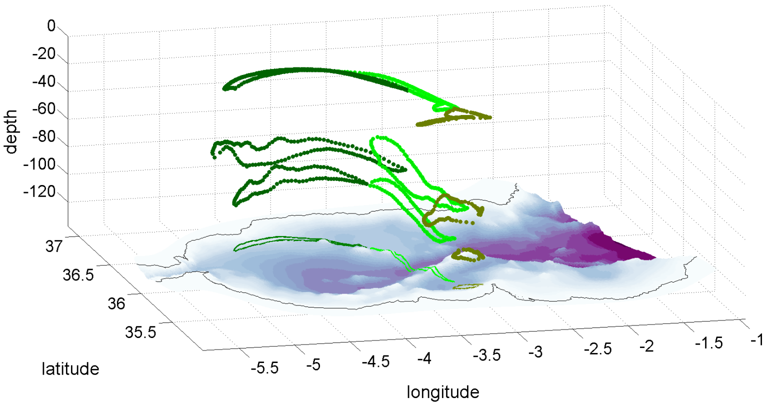

(b)

Figure 4-8: Evolution of one lobe in 2D and 3D. (a) Points inside the lobe are shown on simulation days 13, 15, 17, and 19 at the surface, with the manifolds from day 15 also shown. (b) Points show the edges of the lobe on days 15, 17, and 19 at the surface and on isopycnals $\sigma_\theta = 26.5$, $\sigma_\theta = 27$ which are sections of the stable and unstable manifolds on those surfaces. Bottom topography is shown with purple deeper regions; green curves on the topography are the projection of the $\sigma_\theta = 27$ lobe edges on the three days.

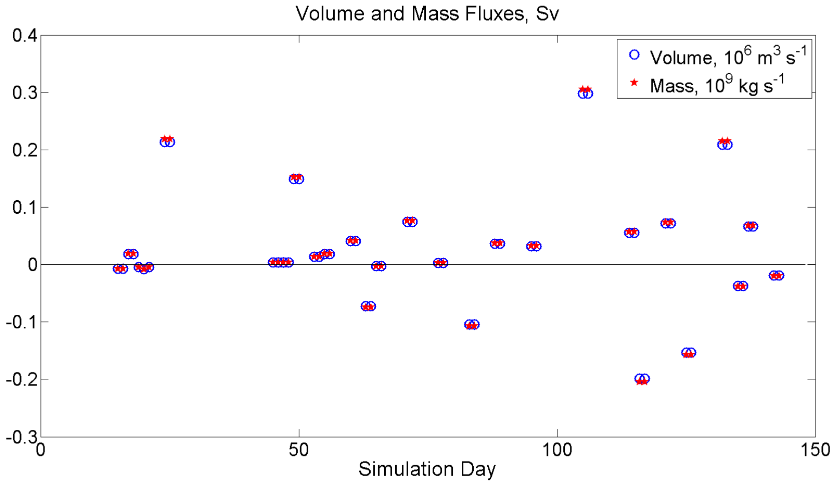

(a) Water

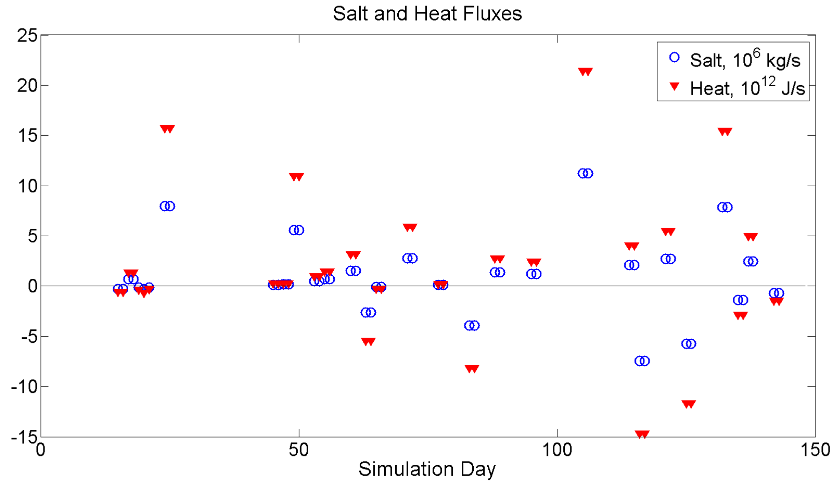

(b) Salt, Heat

Figure 4-9: Lobe fluxes, positive into WAG. Lobe depth is the deeper of the $\sigma_\theta = 26.5$ isopycnal or the top grid cell (5m). Lobes were used to estimate fluxes into the WAG, assuming a 2 day timescale.

the nearby populations of Spain and Morocco.

Details of the exchange of water across the Lagrangian edge of the WAG were discussed in terms of lobes. Lobes are water trapped between intersections of the stable and unstable manifolds and exchanged across the boundary of the gyre. From the near-surface manifolds, I found about 40 lobes during the 148-day period analyzed. These lobes travel completely around the offshore edge of the WAG and into the interior (or out from it) on timescales of about one week. Estimates of their near-surface transport using a two-day timescale, during which they tend to travel more than their own length, gives transport rates on the order of 10^5 m^3/s for volume, 10^8 kg/s for mass, 10^6 kg/s for salt, and 10^12 J/s for heat. Given a WAG volume of about $2 \cdot 10^{12}$ m^3, daily transports at this rate would take about four months to fully replace the water. There is likely to be more exchange below the $\sigma_\theta = 26.5$ isopycnal, not identified here due to the challenges involved in identifying lobes in complicated manifolds. Although the WAG is connected to the inflow for about 50m below this isopycnal, velocities are lower with depth, so it is not clear how much larger the full exchange would be. The next chapter will examine that question using a different method to quantify the Lagrangian exchange.

In the previous chapter, I quantified the Eulerian exchange of water across fixed boundaries for the WAG. The volume transport through the sides, the term most similar to the lobe exchange, was also on the order of 10^5 m^3/s. This consistency is intruiging, but is an apples-to-oranges comparison and should not be over interpreted. In particular, the Lagrangian exchange is localized to individual lobes, while the Eulerian exchange is across the full side of the gyre and may include the AJ passing through or the reshaping of the Lagrangian gyre across the fixed boundaries.

Overall, a Lagrangian examination of the geometry of the Western Alboran Sea as connected to the Western Alboran Gyre shows the area to be well-connected. The core of the WAG is small compared to the stirring region where water can be exchanged with the WAG edges over days to weeks. This stirring region reaches the Strait of Gibralter, the upwelling region in the north-west, and slightly past the Alboran Island to the east. The exchange rate of the top $5 - 50m$ through lobes could replace the water throughout the WAG over a season. Understanding how this stirring exchange connects to the features of the WAG, including its size, temperature, and salinity, will be the focus of the next chapter.

4.5 References

Haller, George. “Lagrangian coherent structures.” Annual Review of Fluid Mechanics 47 (2015): 137-162.

Haller, George, and Francisco J. Beron-Vera. “Geodesic theory of transport barriers in two-dimensional flows.” Physica D: Nonlinear Phenomena 241.20 (2012): 1680-1702.

Mancho, A. M., D. Small, S. Wiggins, and K. Ide. “Computation of stable and unstable manifolds of hyperbolic trajectories in two-dimensional, aperiodically time-dependent vector fields.” Physica D, 182 (2003): 188âĂ§222.

Marshall, J., A. Adcroft, C. Hill, L. Perelman, and C. Heisey. “A finite-volume, incompressible Navier Stokes model for studies of the ocean on parallel computers.” Journal of Geophysical Research, 102(C3) (1997): 5753-5766

Miller, Patrick D., et al. “Chaotic transport of mass and potential vorticity for an island recirculation.” Journal of Physical Oceanography 32.1 (2002): 80-102.

Peliz, Alvaro, Dmitri Boutov, and Ana Teles-Machado. “The Alboran Sea mesoscale in a long term high resolution simulation: Statistical analysis.” Ocean Modelling 72 (2013): 32-52.

Renault, L., et al. “Surface circulation in the Alboran Sea (western Mediterranean) inferred from remotely sensed data.” Journal of Geophysical Research: Oceans (1978-2012) 117.C8 (2012).

Rypina, Irina I., et al. “Chaotic Advection in an Archipelago.” Journal of Physical Oceanography 40.9 (2010): 1988-2006.

Sammartino, Simone, et al. “Ten years of marine current measurements in Espartel Sill, Strait of Gibraltar.” Journal of Geophysical Research: Oceans 120.9 (2015): 6309-6328.

Sayol, J.M., et al. “Sea surface transport in the Western Mediterranean Sea: A Lagrangian perspective.” Journal of Geophysical Research: Oceans 118.12 (2013): 6371-6384.

Viudez, Alvaro, Joaquin Tintore, and Robert L. Haney. “Circulation in the Alboran Sea as determined by quasi-synoptic hydrographic observations. Part I: Three-dimensional structure of the two anticyclonic gyres.” Journal of Physical Oceanography 26.5 (1996): 684-705.

Wiggins, Stephen. Introduction to applied nonlinear dynamical systems and chaos. Vol. 2. Springer Science & Business Media, 2003.

Chapter 5

Chaotic Advection in the Alboran Sea, II: Lagrangian Analysis of Property Budgets of the Western Alboran Gyre

Summary

From chapter 3, it is clear that although the Western Alboran Gyre (WAG) is in an approximately constant location, its slight variations in position cause large transports of water across the boundaries, in both the horizontal and vertical directions. For instance, most of the volume transport across the fixed lower boundary is associated with the motion of the bottom isopycnal a few meters per day across its mean depth. Chapter 4a elucidated the geometry of the WAG, showing the horizontal range of manifolds, where water can be exchanged between the WAG and the rest of the Alboran. However, the description of the lobes that carry the exchanging water left questions about both the rate of the exchange, due to picking a fixed timescale, and how this exchange compares to the total change in properties of the WAG, due to other processes not being considered. In this section, I continue from the Lagrangian perspective, quantifying the exchange transport using a gate method and then formulating Lagrangian budgets for the properites of the WAG.

I now define the Lagrangian WAG boundary to include a section of the unstable manifold from the western hyperbolic tranjectory that ends at a fixed longitude, a section of the stable manifold from that longitude to the eastern hyperbolic trajectory, the coast between the two hyperbolic trajectories, and the latitudinal segment connecting the two manifold sections, which I call the *gate*. This gate is the only section of the closed WAG boundary that by definition allows advection across it.

The advective transport perpendicular to the gate is computed numerically by integration for volume, salt, heat, and relative vorticity for the gates at the surface and along several isopycnals. Typical magnitudes of the gate transports are $1Sv$ for volume, $10^7 kg/s$ for salt, $10^{13} W$ for heat, and $10m^3/s^2$ for relative vorticity. These transports through the gate are consistent with the surface lobe analysis. Also, the transport magnitudes are of the correct size such that, if they had a constant sign, the WAG could be emptied in about 10 days to 3 weeks, consistent with the timescale on which the surface core disapears and over which observed WAG collapses occur. However, the sign of the gate transports do change, leading to a mean exchange over five months that is an order of magnitude smaller than the daily exchange; the exact values are sensitive to the time averaging interval. Overall, the gate transports increase the WAG volume and its salt and heat content while slowing down its rotation. This is consistent with the lobe analysis for the volume and heat, but not salt.

In order to understand the impact of the advective exchange through the gate on the WAG, it is necessary to compute the other terms in a Lagrangian budget for the WAG. For example, a Lagrangian volume budget includes the change in the Lagrangian WAG volume over time, the gate transport, the surface evaporation and precipitation, and cross-isopycnal diffusive transport at the bottom isopycnal. Similar Lagrangian budgets can be computed for salt, heat, and vorticity. From the volume budget I see that the gate transport and the changes in WAG volume over time are the two largest terms and are correlated, indicating that the advective exchange at the gate is the dominant control over the WAG volume. Advection being the dominant term is consistent with the Eulerian budgets in chapter 3. However, the Lagrangian volume budget does not close, and so these results may be erroneous. Several sources of error may prevent the closing of this budget. The known errors include insufficiently long manifolds to reach the gate longitude, which can be fixed by longer integration; the rapid movement of manifolds causing the gate to change on timescales shorter than one day, which may be fixed by higher time resolution; and errors in computing the daily volume of the WAG due to very complicated manifolds, which are not easily remedied.

5.1 Introduction

From chapter 3, it is clear that although the Western Alboran Gyre (WAG) is in an approximately constant location its slight variations in position cause large transports of water across the boundaries, in both the horizontal and vertical directions. For instance, most of the volume transport across the fixed lower boundary is associated with the motion of the bottom isopycnal a few meters per day across its mean depth. Chapter 4, the first part of the Lagrangian analysis, elucidated the geometry of the WAG, showing the horizontal range of manifolds, where water can be exchanged between the WAG and the rest of the Alboran. However, the description of the lobes that carry the exchanging water left questions about both the rate of the exchange, due to picking a fixed timescale, and whether this exchange describes the total change in properties of the WAG, as other processes were not considered. In this section, I continue from the Lagrangian perspective, quantifying the exchange transport using a gate method and then formulating a Lagrangian budget for the volume of the WAG.

Lagrangian budgets for volume, salt, heat, and vorticity would allow the examination of each physical process affecting the WAG properties as a term in the budget. This examination, as done for the Eulerian WAG in chapter 3, could elucidate which processes are the dominant controls on the size, temperature, salinity, and vorticity of the WAG. The advantage of a Lagrangian WAG budget is that the water is tracked over time as it moves, eliminating any error due to the WAG moving across fixed boundaries. The challenge in a Lagrangian budget is in correctly identifying the moving edges. Such budgets have rarely been presented; for one case, with an idealized coastal recirculation, see Miller et al. (2002). To my knowledge, this is the first attempt to close a Lagrangian budget for an aperiodic, three-dimensional ocean feature.

5.2 Methods

As described in the previous chapter, manifolds from the hyperbolic separation points on the coast can delineate the WAG from the rest of the gyre. The unstable manifold connected to the western

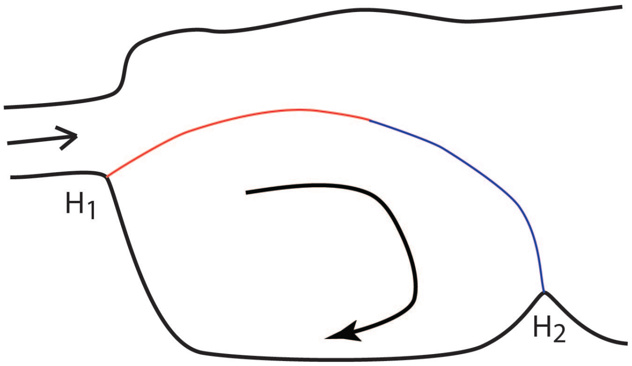

(a) steady (b) time-varying

Figure 5-1: Definition Figure : Unstable (red) and stable (blue) manifolds . Hyperbolic points H1, H2. Left, steady. Water is trapped in the gyre for all time. Right, periodic. Shaded lobes map to each other in time and transport water out of WAG. Unshaded lobes transport water into WAG. Orange gate connecting the manifolds allows a well-defined gyre boundary.

hyperbolic trajectory, where the Atlantic Jet (AJ) separates fromt the coast, separates water that begins inside the WAG, to the south of the curve, from water that just flowed through the Strait of Gibraltar, to the north of the curve. The stable manifold connected to the eastern hyperbolic trajectory, where the AJ reconnects to the African coast, separates water that continues eastward, to the north of the curve, from water that turns westward and recirculates inside the WAG, to the south of the curve. I now define a unique, piecewise-continuous Lagrangian WAG boundary.

In order to consistently have a unique boundary, segments of the stable and unstable manifolds are joined by a *gate* (figure 5-1). This gate is then the single part of the boundary where advected water crosses the boundary (see Haller and Poje 1998 for a mathematical treatment of this behavior). A 14-day integration period for the manifolds is chosen so that on the below-surface isopycnals, the unstable manifold from the western hyperbolic point and the stable manifold from the eastern hyperbolic point typically pass some of the same longitudes. I then use a longitudinal north-south oriented line segment as the gate, which connects the manifolds. A segment of coast between the separation points closes the WAG boundary.

The Lagrangian nature of the boundary formed from these manifolds should mean that the boundary advected from one day to the next lies on top of the new boundary, except for that region involving the gate. To demonstrate this property, I show a series of three days' boundaries with the boundary from the previous day advected forward (figure 5-2). These days have an extremely

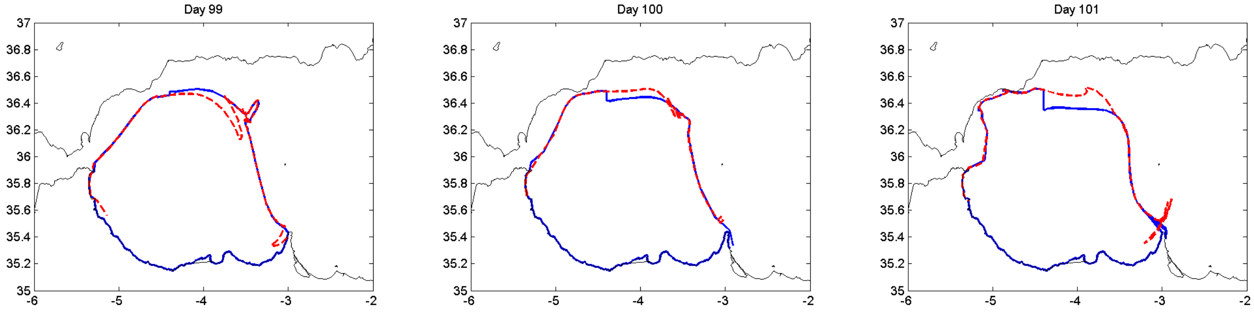

(a) day 99 (b) day 100 (c) day 101

Figure 5-2: WAG Lagrangian boundary on the surface in blue. Red dashed curves are the previous day's offshore boundary advected forward one day. Axes are longitude and latitude.

good match, except for near the gate and very close to the coast. Near the gate, the mismatch is due to the segment of the forward manifold that is advected past the gate being separate from the backwards manifold. The region inside this mismatch is part of a lobe passing through the gate (lobes were discussed in the previous chapter). The coastal differences near the eastern hyperbolic trajectory are related to the unstable manifold of that hyperbolic trajectory folding and extending along-coast there, because forward integration of any slight errors will follow the unstable rather than stable manifold. The coastal differences near the western hyperbolic trajectory are related to that trajectory's movement in time, such that the resolution of the boundary may not allow an exact alignment near the coast after being advected offshore.

In the results section, I will quantify the advective exchange through the gate for the full depth of the WAG connected to the inflow from the Straight of Gibraltar, down to $\sigma_\theta = 27.5$. The gate transport is computed by two-dimensional numerical integration on the vertical stack of gates at the surface and on each isopycnal (figure 5-3). The integrand is the perpendicular velocity for volume, the appropriate advective model diagnostic for salt and heat, or velocity multiplied by the vertical component of relative vorticity for vorticity. This exchange through the gate is simpler to compute than identifying individual lobes, as it only requires the intersections of manifolds with a fixed longitude, rather than finding intersections between manifolds. However, it is the same process of exchange (see Haller and Poje 1998 for a more detailed discussion of this fact). I will then consider this advective exchange through the gate in the context of a full Lagrangian volume budget.

Computation of the full Lagrangian volume budget requires several terms beyond the transport

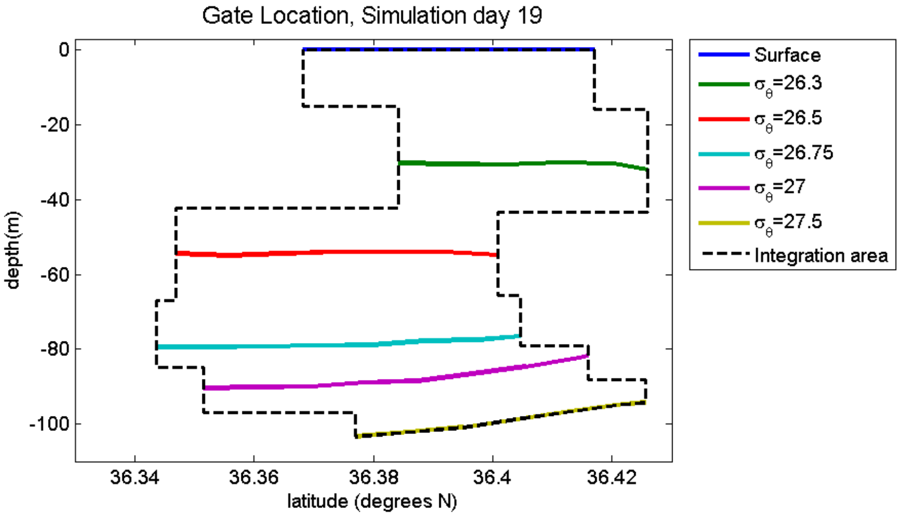

Figure 5-3: WAG Lagrangian gate for simulation day 19. The gate locations at the surface and on 5 isopycnals are shown (solid lines), plus the edge of the full two-dimensional area the transport is integrated over (dashed).

through the gate. These include air-sea exchange, or evaporation and precipitation; the cross-isopycnal volume transport due to the diffusive movement of the isopycnals; the cross-manifold transport, which is due to errors in manifold computation; and the change in total WAG volume over time. The precipitation and evaporation are integrated from model diagnostics (listed in appendix B) over the surface of the Lagrangian WAG.

The diffusive volume transport is the change in volume above an isopycnal due to the motion of that isopycnal from diffusion of heat and salt; a more detailed description of where this applies is in the budget section of the results. The change in density over one day is computed by updating the temperature and salinity from a snapshot at the beginning of the day using the model diagnostics of their daily-average diffusive changes (listed in appendix B), then computing an updated density using the TEOS-10 seawater equation of state (McDougall and Barker, 2011). The depth of the isopycnal in the updated density field is found using linear interpolation, and its change from the beginning of the day, multiplied by the cell area, is the cross-isopycnal transport at that point.

The cross-manifold transport should be zero if manifold segments for each day are exact Lagrangian matches to manifold segments on the following day. The error is computed from the perpendicular distance between the Lagrangian boundary on one day and the Lagrangian boundary from the previous day advected forward over that day. The advection is done in the same manner as the original manifold integration. Transports are computed by multiplying the perpendicular distanceby the distance along the manifold between points and the depth between layers.

Finally, the change in total WAG volume is computed from the volume of cells inside the Lagrangian WAG boundary each day. The daily-average density of each cell determines which boundary curve applies. For example, the manifold segments, gate, and coast segment that comprise the boundary for $\sigma_\theta = 26.5$ apply to cells with densities between $\sigma_\theta = 26.4$ and $\sigma_\theta = 26.625$, as those are halfway to the next analyzed isopycnals. All cells with their corners fully inside the boundary have their full volume included. Cells that intersect the boundary have the polygonal area inside the horizontal extent of the cell and inside the boundary calculated; these areas are then multiplied by the height of the cell for the volume. Occasionally, multiple intersections with one cell prevent reasonable computation, in which case either the fraction of corners inside the boundary are used as the fraction of the cell inside the boundary, or the boundary of the WAG at that level is simplified by hand. Errors associated with this problem will be discussed in the results section on the volume budget.

5.3 Results

5.3.1 Gate Transport

From both the time-mean manifolds (figure 4-3) and the surface lobe volume fluxes (figure 4-9) in the previous chapter, there is a positive volume flux into the WAG. To quantify the time-varying fluxes continuously, I have redefined the boundary of the gyre using segments of the coast and the 14-day manifolds joined by a gate, a nonmaterial surface where all advective transports occur. This gate method allows computation of the same advective exchange as using the lobes, but with a clear definition of the rate at which they occur, due to not needing to pick a timescale.

Advection of volume, salt, heat, and vorticity through the gate are calculated for each vertical layer as defined on isopycnals by the manifolds computed on that isopycnal, with the vertical extent being limited to halfway to the adjacent isopycnals. The transports through the gate from each layer and the total are in figure 5-4, with salt fluxes of $10^7 kg/s$ and heat transports of $10^{13} W$. These follow the same overall patterns as the volume transport through the gate, which is often on the order of $1 Sv$. In fact, using the mean salinity and temperature from the Eulerian WAG in the previous chapter, the volume transport through the gate with these reference water properties almost exactly matches the total gate transport of salt and heat (figure 5-5). The relative vorticity transport is on the order of $10m^3/s^2$. The planetary vorticity multiplied by the volume transport through the gate is generally larger in magnitude than the relative vorticity transport through the gate and more clearly shows the differences in the patterm over time, which indicates that the relative vorticity is more variable than the temperature or salinity at the gate.

These transports through the gate are consistent with the magnitudes from the near-surface lobe analysis, which covered $10 - 60\%$ of the WAG depth. Also, the gate transport magnitudes are of the correct size such that, if they had a constant sign, the WAG could be emptied in about 10 days to 3 weeks, consistent with the timescale on which the surface core disapears and over which observed WAG collapses occur. However, the sign of the gate transports do change, leading to a mean transport an order of magnitude smaller than the daily exchange; the exact values are sensitive to the time averaged over. Overall, the gate transports' means describe a WAG that is getting larger, increasing in salt and heat, and slowing down its rotation. These signs are consistent with the signs of the means from lobe analysis for the volume and heat, but not salt.

5.3.2 Budgets using the gate method

In order to describe a budget for the Lagrangian WAG, I first define the volume of interest. The area is limited using the piecewise-continuous boundary decribed above at the surface and on every isopycnal analyzed, comprised of the coast, the stable and unstable manifolds, and the gate. In the vertical, the top of the volume is at the sea surface and the bottom is the $\sigma_\theta = 27.5$ isopycnal. I will look at the evolution of volume, salt, heat, and vorticity for this approximately Lagrangian volume. Unfortunately, closing these types of budgets is exceedingly difficult. I will describe all the terms of the volume budget and the most important challenges preventing the closing of this budget. After that, I will present a comparison of the transports through the gate and the changes in storage of salt, heat, and vorticity, which I expect to be the largest terms in those budgets.

The volume of the Lagrangian WAG can change through precipitation and evaporation through the surface, advection through the gate, and diffusive movement of the $\sigma_\theta = 27.5$ isopycnal. The diffusive movement of the bottom boundary is the change in depth of the $\sigma_\theta = 27.5$ isopycnal due to the diffusion of salt and heat across this surface, changing the local density and therefore the

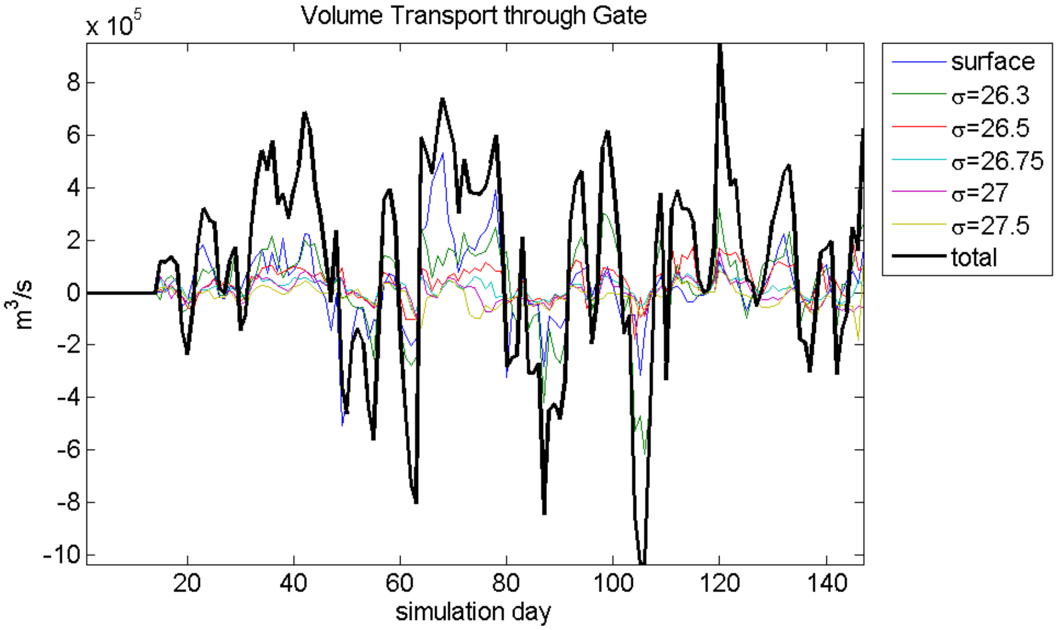

(a) volume

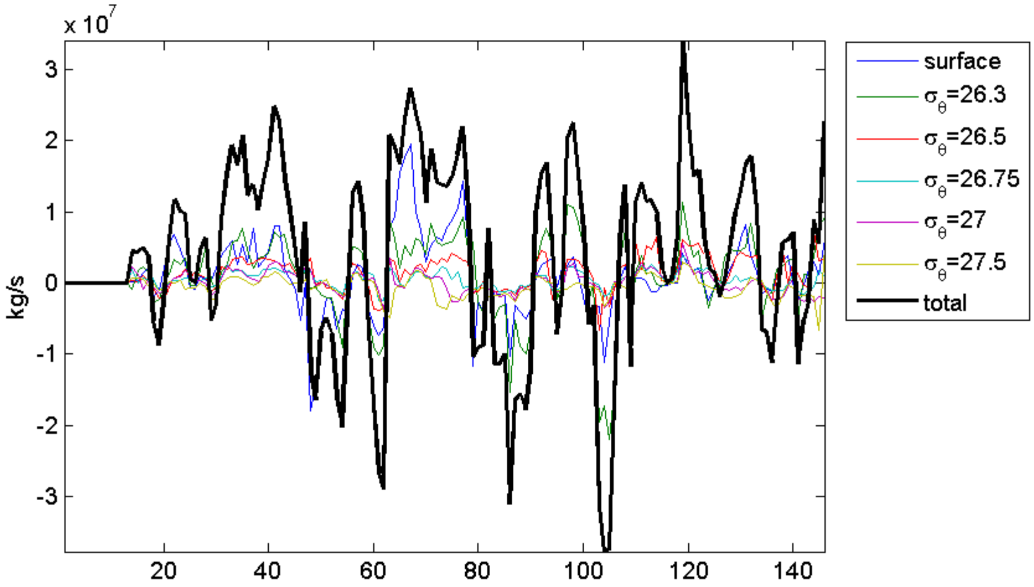

(b) salt

Figure 5-4: Advective transports through the gate at each layer and total for volume (a, top), salt (b, bottom); more on next page.

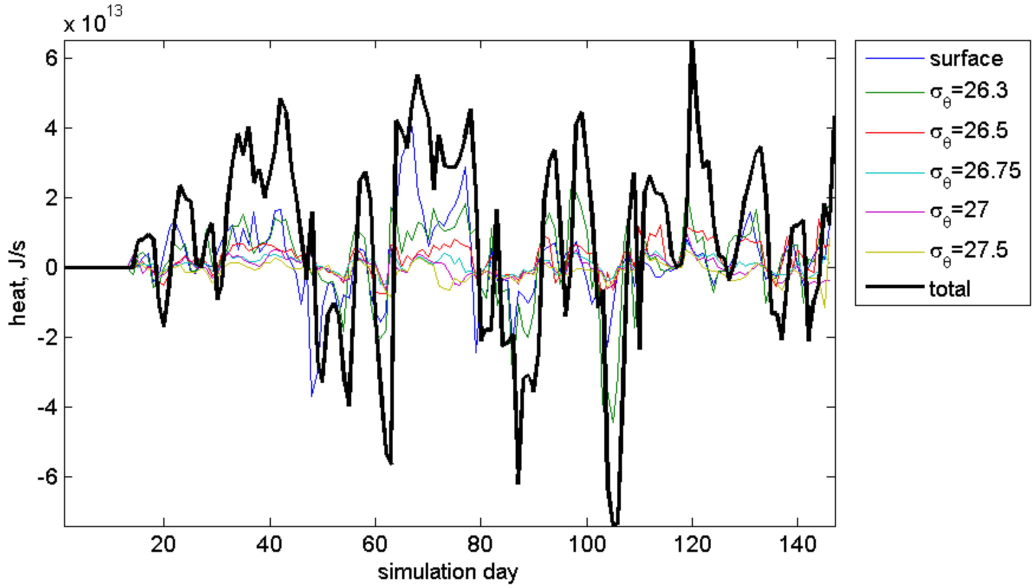

(c) heat

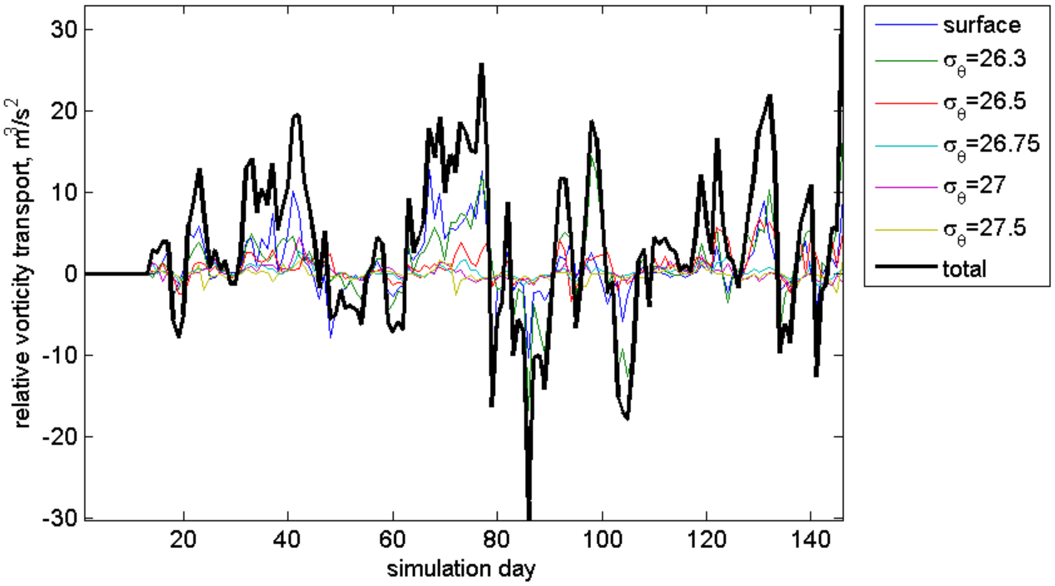

(d) vorticity

Figure 5-4: Advective transports through the gate at each layer and total for volume (previous page), salt (previous page), heat (c, top), and vorticity (d, bottom).

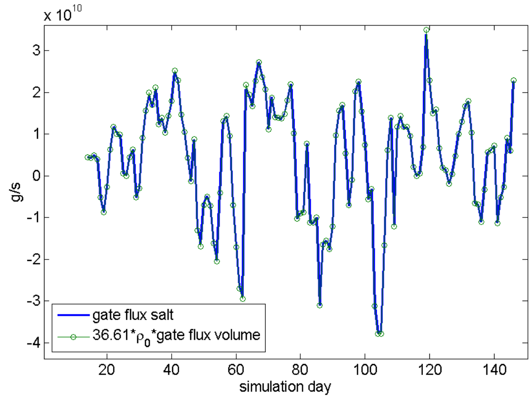

(a) salt and volume

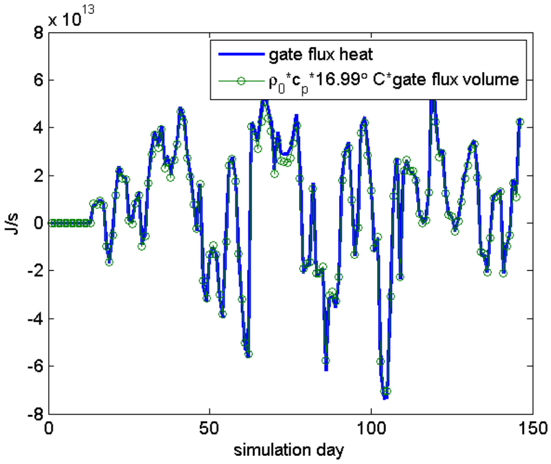

(b) heat and volume

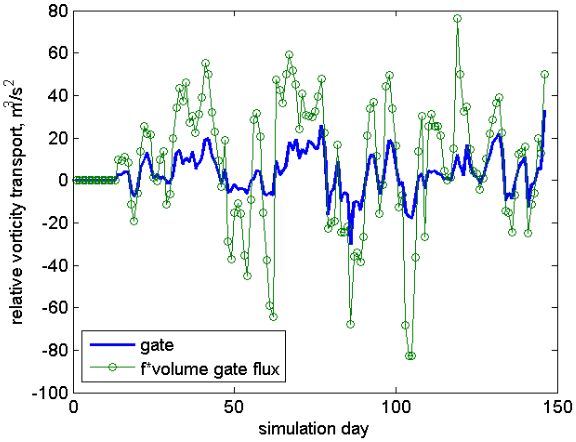

(c) vorticity and volume

Figure 5-5: Advective transport through the gate compared with that done by the volume transport at a representative salinity, temperature, or vorticity.

volume above the isopycnal. The sum of these three transports would be equal to the change in volume over time if the boundary were exactly mapped onto itself by advection, except for the gate. However, the discrete depths where manifolds are calculated brings in an additional term of the diffusive movement of each isopycnal in the areas where the boundary is "open" in the vertical because it is inside the Lagrangian boundary at one isopycnal and not the next, or vice-versa. An example of two manifolds on different isopycnals is shown in figure 5-6; generally, the blue boundary, which is higher, is larger than the green. Then upward diffusive movement of the isopycnal between them decreases the volume inside the gyre, indicating cross-isopycnal volume transport out of the gyre.

The volume budget can then be written

$$\frac{dV}{dt} = \iint_{gate} U \cdot dA + \iint_{surface} P - E\, dA + \iint_{\sigma=27.5} \frac{dh}{dt} dA + \iint_{steps} \frac{dh}{dt} dA, \tag{5.1}$$

where U is the velocity perpendicular to the gate (eastwards), $P - E$ is precipitation minus evaporation, and h is the depth of the isopycnal. The dh/dt is transport due to diffusion of salt and heat over one day, calculated as described in the methods section. The *steps* term occurs at the isopycnals halfway between those used to define the gyre boundaries, with the area pertaining to water where only one side of the isopycnal is inside the gyre. A budget for a volume vertically bounded between any two isopycnals would not have a step term. Furthermore, the precipitation minus evaporation term and $\sigma_\theta = 27.5$ diffusive term will be replaced by diffusive terms for the upper and lower isopycnals.

I first show a budget for the bottom layer of the Lagrangian WAG. This volume is limited by the $\sigma_\theta = 27$ manifolds and gate in the horizontal, and extends in the vertical between the $\sigma_\theta = 27$ and $\sigma_\theta = 27.5$ isopycnals (figure 5-7). This layer is defined by the manifolds at the top of it, rather than in the middle as I described above, to have the simplest example case with the same type of budget. The volume transport at the gate is generally between $10^4 m^3/s$ and $10^5 m^3/s$, taking both signs as the manifolds change their order: if the unstable manifold is north of the stable one, the transport is negative, out of the gyre, while if the stable manifold is north of the unstable one, the transport is positive, into the gyre.

The diffusive movement of the top and bottom isopycnals are generally an order of magnitude or two smaller, $10^3 - 10^4 m^3/s$. The larger diffusive transports are similar to the isopycnal moving $1cm$

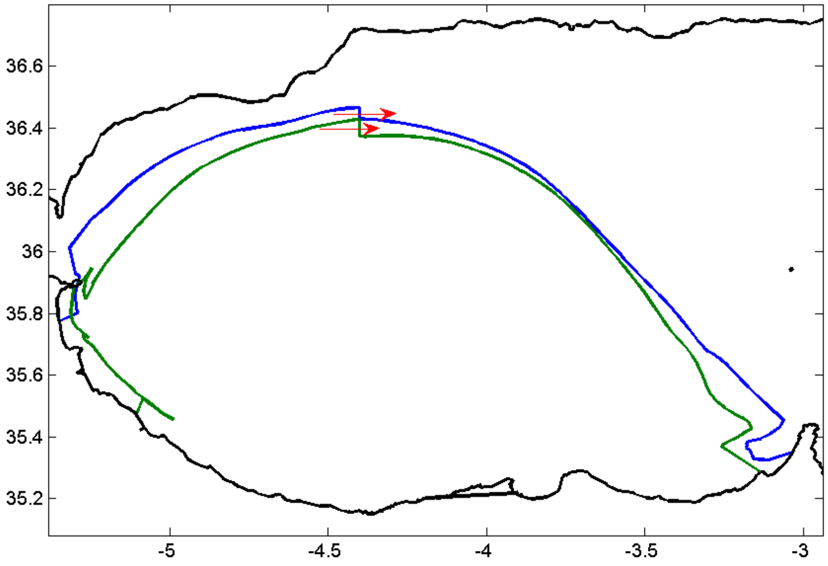

Figure 5-6: WAG edge at $\sigma_\theta = 26.5$ (blue) and $\sigma_\theta = 27.5$ (green) on day 38 of the simulation for illustration. Advection through the gate is represented by red arrows. Volume transport implied by the diffusive movement of $\sigma_\theta = 27.5$ will occur over its whole area. That from diffusive movement of the $\sigma_\theta = 27.25$ isopycnal, where the boundary takes a "step", will occur wherever only one boundary covers the area.

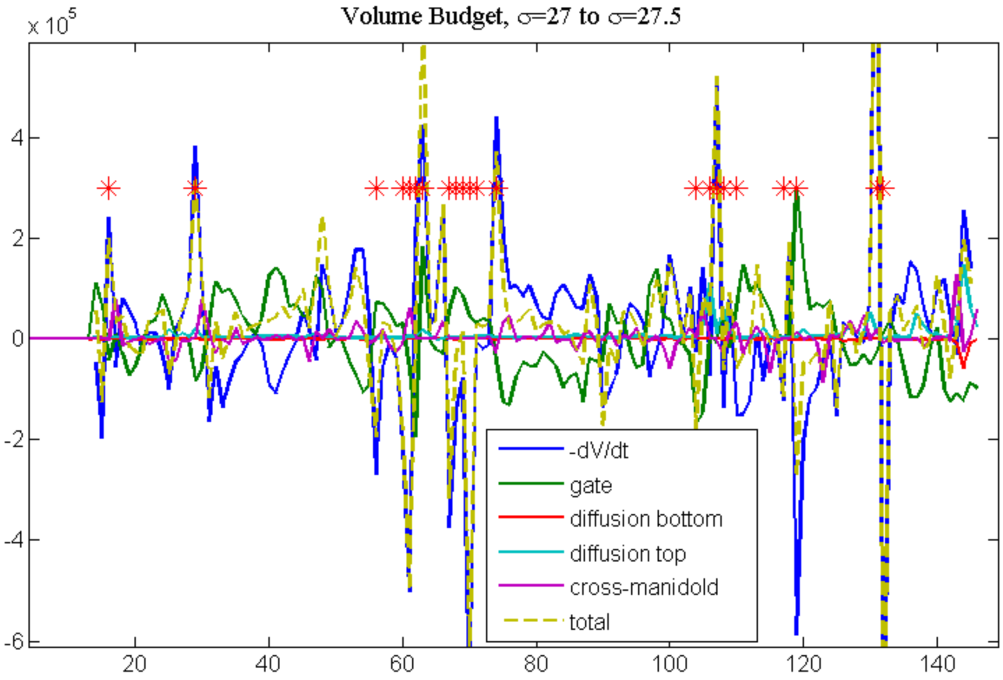

Figure 5-7: WAG volume budget for the region defined by the $\sigma_\theta = 27$ manifolds and ending at $\sigma_\theta = 27.5$. Red stars indicate days with known problems of ill-defined boundaries, fast time dependence, or large errors in dV/dt from manifold surgery. Transports in m^3/s.

in the vertical over the whole gyre due to one day's diffusion. These three volume transports should sum to the change in volume of this layer of the WAG. The daily volume is calculated similarly to the method described in the methods section, by finding the areas of the model's grid cells inside the horizontal boundary on $\sigma_\theta = 27$ as described and then multiplying by the distance between the two isopycnals in the vertical for each. The daily volume is on the order of $10^{11}m^3$, and its discrete derivative is generally on the order of $10^5 m^3/s$. However, there are occasions where the change in volume spikes. Even when there are no spikes, the change in volume does not quite match the sum of the other transports. An examination of the timeseries shows that the transport through the gate, which is the dominant term, is correlated with the time-derivative of the volume (figure 5-7, green and negative blue curves), but that the total of the three transports minus dV/dt is not close to zero.

I know about several sources of error within this volume budget and will describe them before showing the budget for the full vertical extent of the WAG. First, occasionally the manifolds from trajectories integrated for 14 days will not reach the position of the gate (example in figure 5-8a). The gate position was chosen to minimize these occurances, but there are still a few. In these cases, a bounded WAG is defined using the nearest isopycnal boundary that is closed. This problem can be remedied with longer integration times.

Second, calculating the area inside the boundary can be nearly impossible when manifolds are very complicated, folding back on themselves or curling around repeatedly in an eddy, such that model grid cells are intersected repeatedly (example in figure 5-8b). I therefore simplified the boundaries by hand, connecting subsets of points from the original boundary to remove the folding and curling sections without changing the nature of the included area. This "manifold surgery" generally does not change the area much from estimates using only cells with one or no crossings by the boundary. When the area is different by similar amounts to daily changes, I consider the day with the large changes to have a poorly defined volume and dV/dt, so the budget will not generally close. Another problem is that the manifold surgery can cause the boundaries to not exactly advect onto eachother from day to day, creating a cross-manifold volume transport. This transport, which is usually small, is calculated from the mismatch in the position of boundary points advected from the previous day and the day's boundary, as described in the methods section. Neither of these issues with the manifolds' complications and the associated surgery can be improved by better resolution or longer integration; those are more likely to exacerbate the issues.

Third, sometimes the velocity field and the manifolds are evolving more quickly than can be resolved by daily positions. This is clear when, for instance, the gate positions from one day to the next are far from eachother. The gate longitude is fixed, so this type of change means that the manifolds have moved latitudinally more than the width of the gate in one day (example in figure 5-8c). Then the advective transport through the gate, using the daily gate position and the daily-averaged velocities there, is not a good approximation of the transport through the moving gate. To improve the gate transport, manifolds must be calculated more frequently, which requires more resolution in time from the model. This is possible, but costly in terms of storage and use of the increased output. An example of the gate transport and changes in volume at this improved resolution is shown for two days (figure 5-9). The volume transport through the hourly gate is quite variable, and its daily means, while similar to the transport through the daily gate, are not the same value as those daily computed values. The hourly volume transport and changes in volume

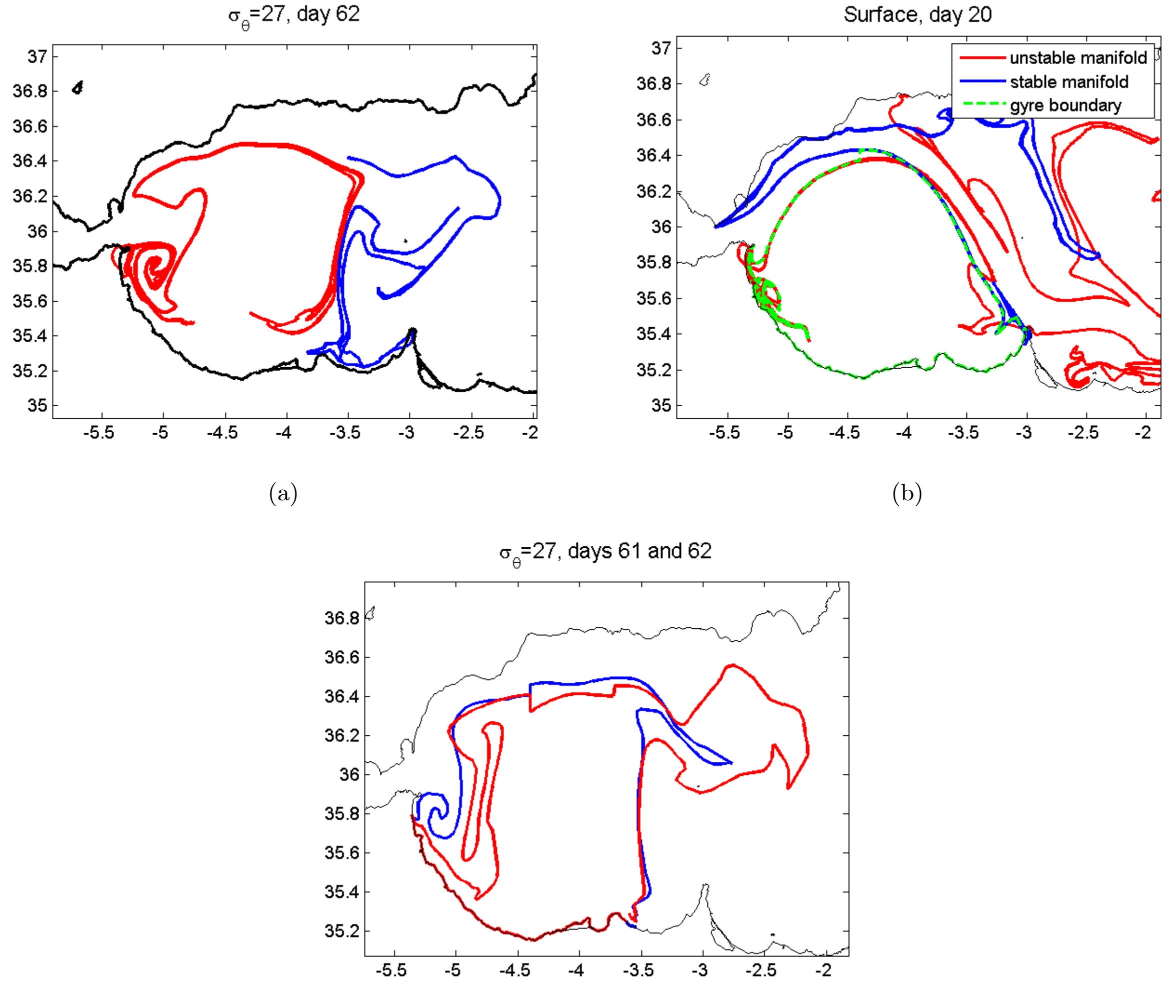

(a)

(b)

(c)

Figure 5-8: Lagrangian budget error examples. Left top, σ_θ manifolds for simulation day 62 with 14 day integration do not reach the gate location of $4.4°W$. Right, surface manifolsa and boundary on simulation day 20. Note the complicated and self-intersecting edge in the southwest. Bottom, σ_θ manifolds for simulation days 61 and 62, over which the gate moves farther than its width.

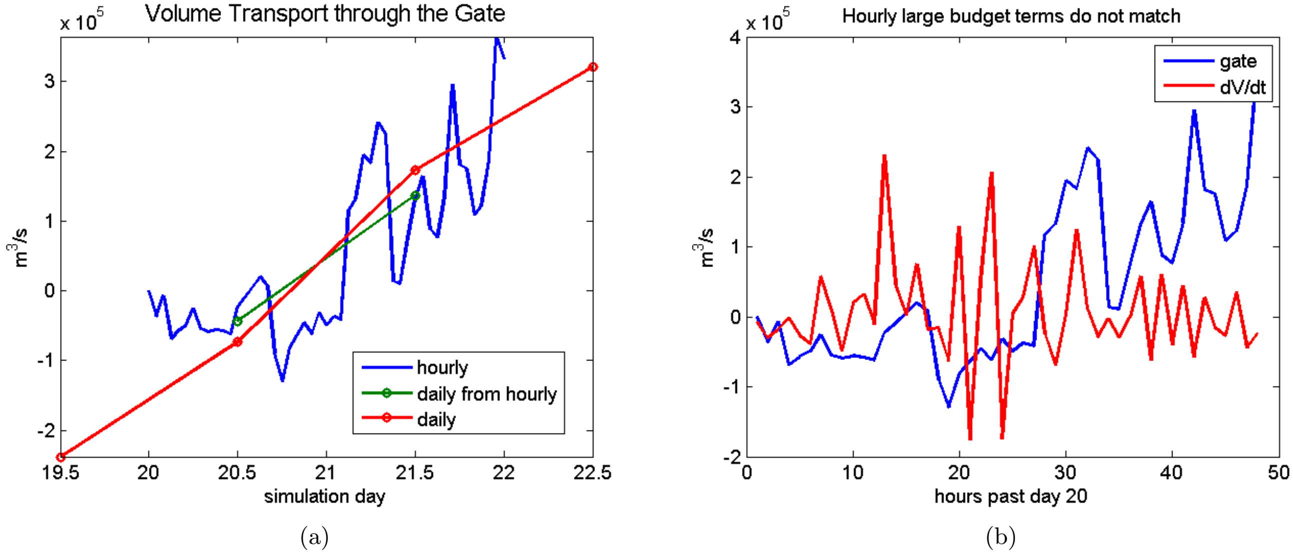

(a) (b)

Figure 5-9: Example of terms in an hourly Lagrangian volume budget over simulation days 20 and 21. Left, volume transport comparison between daily and hourly. Right, comparison of the hourly gate transport and changes in Lagrangian volume.

on these two days are an even worse match than for most of the daily estimates I will describe. This mismatch is without any problems with manifolds not reaching the gate location or needing to be simplified by hand, and indicates that either the surface and diffusive terms are fairly large, or there is a term missing in the budget. Unraveling this budget was outside the scope of work that time allowed.

Returning to the lower WAG budget, the cross-manifold transport is shown in purple and is included in the total. Days when the horizontal boundary is from a different isopycnal, the gate moves farther than its length, or the manifold surgery changed the volume significantly are marked by red stars. These errors explain the more egregious mismatches between the changes in volume and the calculated transports, although errors still can reach about 50% of the change in volume. One further error, which I have not been able to calculate, is the effect of vertical shear. If vertical shear is large, the manifolds may not be an accurate representation of water slightly above or below them. Then the cross-manifold transports may be much larger than calculated above. Improving this error would require either using more isopycnals or else changing methods to one that is fully three-dimensional.

With all of the known errors described, I present the volume budget calculated for the full

Lagrangian WAG (figure 5-10). The total transports of each type are shown, the sum of those terms from each layer. As an example of how the layers contribute to the whole, figure 5-4 shows the component gate transports. Generally, the transport timeseries have similar patterns, but the transports near the surface are larger because the velocities are larger there. In the full budget, as with the lower layer budget, the transport through the gate and the changes in volume are the dominant terms. They are both typically on the order of $1Sv$, which is similar to the transport of the inflow through the Strait of Gibraltar and about 1/2 to 1/3 the recirculating volume in the Eulerian WAG (definition in Chapter 3). This transport through the gate is consistent with the surface lobe analysis, as the total depth covered here is about ten times the depth of the surface layers analyzed there. It is also worth noting that when the WAG has been observed to move eastwards or collapse, these large circulation changes occur over about 2 weeks (e.g. Heburn and Violette, 1990). The gate transports of 1-3 Sv, if consistent, could drain the WAG ($\approx 10^{12}m^3$) in 1-3 weeks. Thus, these volume fluxes are in line with what has been observed.

The diffusive movement of $\sigma_\theta = 27.5$ is still typically 10^3-$10^4 m^3/s$, and the precipitation-evaporation is even smaller, with a mean of $-8m^3/s$. The diffusion at the steps is larger, 10^4-$10^5 m^3/s$, mostly due to the movement of the $\sigma_\theta \in 26.2, 26.4$ isopycnals, which can move several meters a day due to the small density gradients near the surface. The cross-manifold transport is about the same size, $10^4 - 10^5 m^3/s$, which is usually small compared to the gate and dV/dt terms. Days with known problems of manifolds that did not reach the gate, fast time dependence, or large changes in area from the manifold surgery are marked. Unfortunately, because these errors occur at different times at the different depths, this indicates problems on most days. Overall, the known transports do correlate with the calculated changes in volume ($\rho \approx 0.6$), but differences are in no way negligible. Looking at just the periods of time with the fewest days with known errors (figure 5-11), the unaccounted-for volume changes are still more than 20% of the total dV/dt on many days. However, it is more clear in these sections that the transport through the gate is the major contributer to the changes in volume. Also, the cross-manifold transport and the diffusive movement of isopycnals are sometimes as large as the error, so on those days the budget is approximately closed.

Given the uncertainties in the volume budget and the fact that the calculated transports do not match the calculated changes in volume, it is not possible to close the budgets for water properties carried by these transports. However, I still present a comparison between the advective transport

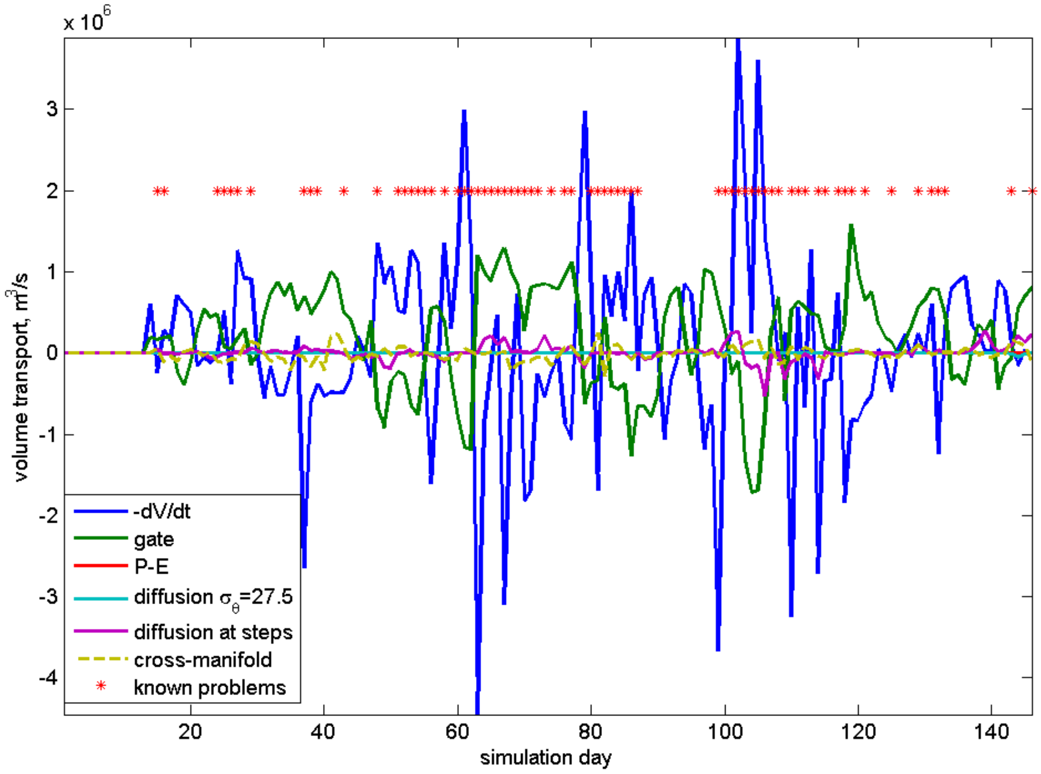

Figure 5-10: WAG volume budget for the full analyzed section, surface to $\sigma_\theta = 27.5$. Red stars indicate days with known problems of ill-defined boundaries, fast time dependence, or large errors in dV/dt from manifold surgery. Transports in m^3/s for the 148 days analyzed.

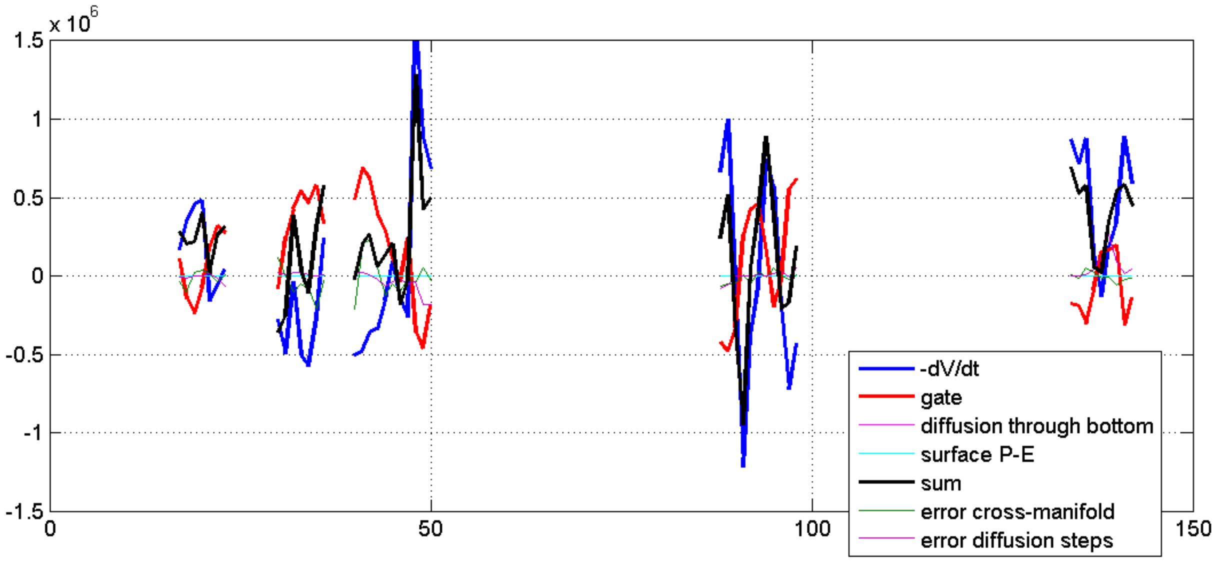

Figure 5-11: WAG volume budget for the time periods without known large errors, surface to $\sigma_\theta = 27.5$. Transports in m^3/s. Here, total is the gate transport plus surface flux plus diffusive movement of the bottom isopycnal minus the time derivative of the volume. The diffusive movement of isopycnals at the steps and the cross-manifold transport are also plotted.

through the gate and the changes in the storage for salt, heat, and vorticity. These are likely to be the largest terms, at least for salt and heat, as they are in the Lagrangian volume budget and the Eulerian budgets from the previous chapter, and their order of magnitude should be accurate, as demonstrated by the similar values for gate transport in hourly and daily computations.

The changes in storage of salt and heat are calculated by adding together the values in each cell multiplied by the portion of the cell's volume and then differentiating in time. The same challenges in finding the included volume persist. The changes in storage are shown with their associated gate transports in figure 5-12, and are, similarly to the volume transports and changes in storage, correlated but of different values.

The volume-integrated relative vorticity and its time derivative are calculated in the same manner as for salt and heat. Several of the large spikes carry over from the problems in calculating the WAG volume. However, as with the gate transport, this does not match the volume storage changes as well as the heat and salt storage changes. It is possible that the other terms of windstress, diffusion, and drag are important for the Lagrangian vorticity budget in the same way they were in the Eulerian budget. In the next section, I will discuss the relationship between the Eulerian and Lagrangian transports and budgets.

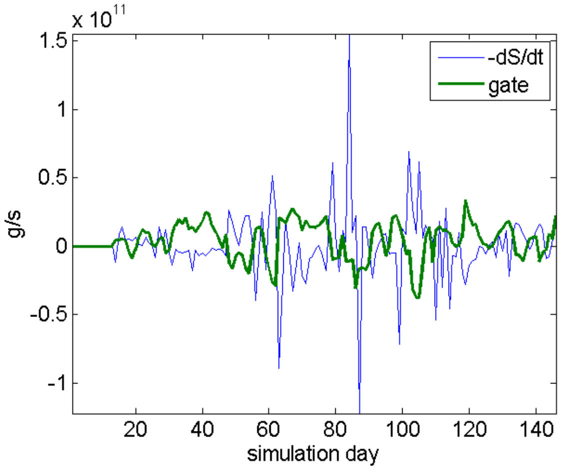

(a) salt

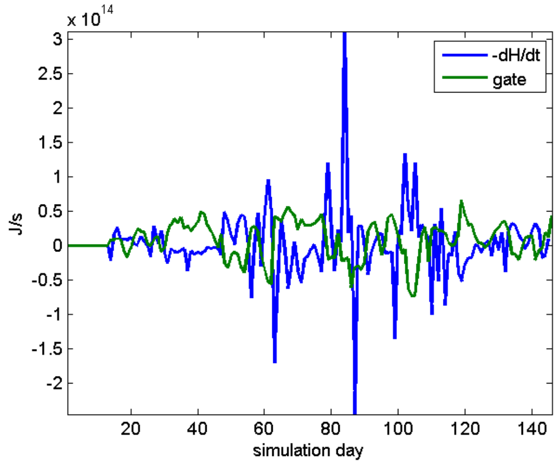

(b) heat

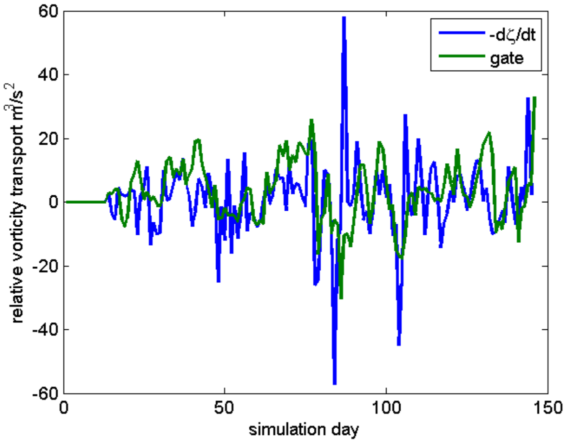

(c) vorticity

Figure 5-12: Lagrangian budget terms: transport through the gate and changes in storage for salt, heat, and vorticity.

5.4 Discussion

Throughout my work on the WAG, I have been examining its exchange with its surroundings. The Eulerian budgets had the complication that the dynamical edges may not match the fixed edges, leaving uncertainty about what part of the computed transport through the sides was really exchange between the WAG and AH. In the previous chapter, I estimated transport across a Lagrangian WAG boundary using lobes. However, identifying individual lobes was complicated and I had to make assumptions about their vertical structure and the time over which they moved from the interior to the exterio of the WAG or vice-versa. In this chapter, I haveredefined the Lagrangian WAG boundary and used a gate to find the transport into and out of the gyre in a more continuous way.

The volume, salt, heat, and vorticity transports through the gate are equivalent to the transport by lobes and are the Lagrangian analogue of the net advective transports through the sides of the Eulerian WAG. Comparing the two (figure 5-13) shows that they are the same magnitude for volume, salt, and heat. These three transports are driven by the volume transport in both Eulerian and Lagrangian frames, with variations in temperature and salinity making very small changes to the transport. For vorticity, the Lagrangian transport across the gate is 5-10 times larger than the net Eulerian advection across the boundary. The vorticity transport also does not follow the same patterns in time as volume transport, indicating that there are relatively large variations in vorticity near the gate. The mismatch in vorticity advection here, as with the mismatch between gate transport and integrated changes in vorticity, implies that other terms in the vorticity budget will be important. As this was true for the Eulerian budget, with five terms of similar magnitudes, further analysis of the Lagrangian vorticity budget requires aditional calculations. Unfortunately, using Stokes' theorem to calculate the area integral of the curl from the line integral along the boundary will be much less useful in this case, due to the very complicated boundaries on many days. I have not presented such calculations due to the large errors involved in either integration method, around the boundary or the area integral of the curls.

The qualitative features of these transports are that they take both signs in all layers, that typically the fluxes are of the same sign with depth, and that the signal is aperiodic (no peaks were found in spectra computed using 28-day segments). As mentioned previously, the lobe and gate transports agree in the magnitude of the transport. Generally, there is also agreement with the magnitude from the Eulerian analysis. These consistencies in this aperiodic, depth-dependent flow are encouraging

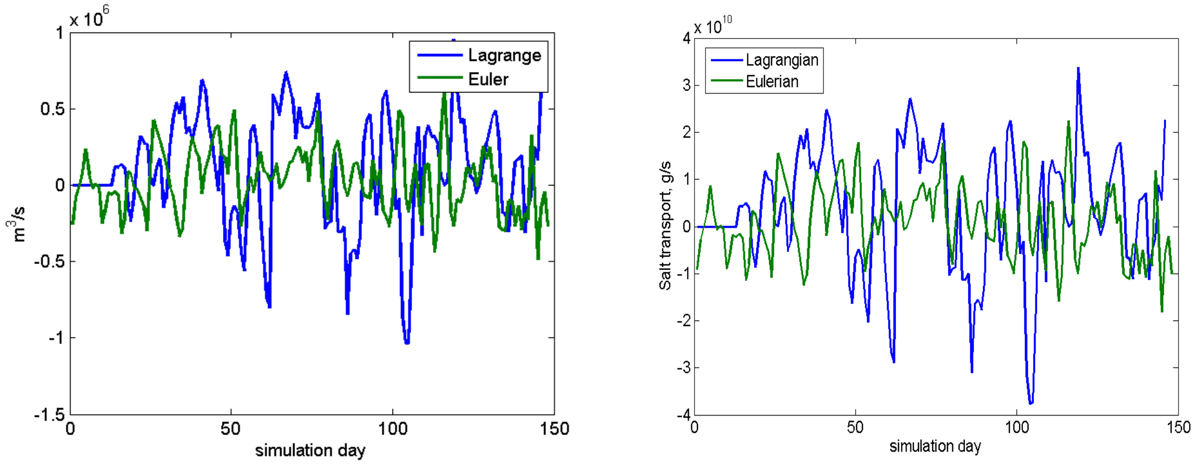

(a) volume (b) salt

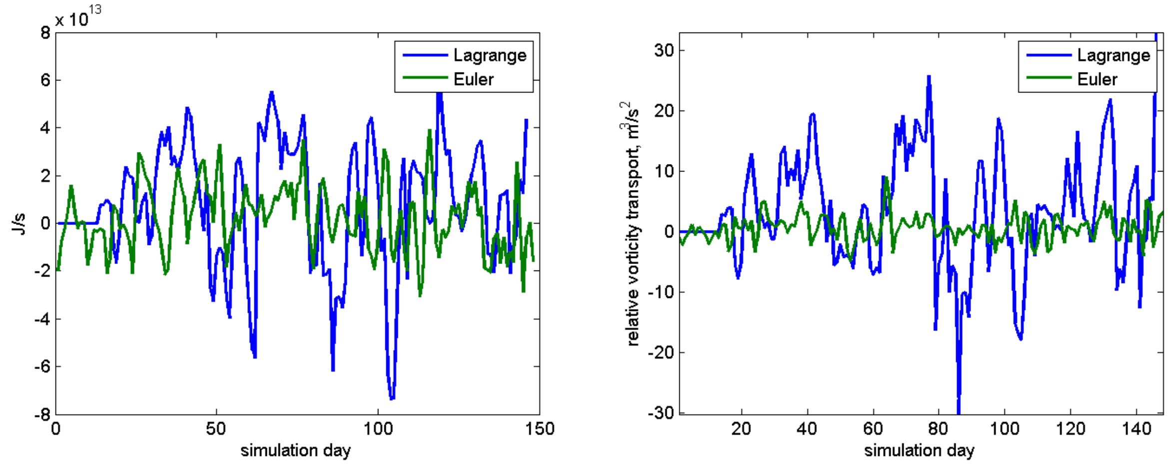

(c) heat (d) vorticity

Figure 5-13: Comparison of transport through the sides of the WAG from the Lagrangian and Eulerian analyses. Transport of volume, salt, heat, and vorticity are shown.

for the general use of these Lagrangian methods in other oceanic flows. However, the challenges in closing the budgets require additional methodological work before three-dimensional Lagrangian budgets will allow for a clear interpretation. Some of the problems described for the budgets are tractable to solve, such as needing longer manifold integration times for a closed boundary, or repeating the analysis with varied numbers of layers to determine the errors from shear. Problems with accurately calculating the volume, and thereby correct storage terms, are not easily remedied, and may require new methods to be developed.

Altogether, the Lagrangian analysis has shed some light on what controls the features of the Western Alboran Gyre. Advection is the largest driver of changes in water properties and mostly explains the short-term changes in storage, so time-dependent advection is most likely controlling the salinity minimum and temperature maximum in the gyre. However, the Eulerian analysis suggested that these extrema were created with the WAG and decaying over time. Given the lack of closed budgets, I cannot confirm or contradict this suggestion with the Lagrangian information from this chapter. However, from chapter 4 it is clear that it takes more than two weeks for water from the edges of the WAG to reach the core region where the extrema are located. If water is mixed through diffusion along the way, it is reasonable to expect the extrema to be fairly unaffected by the exchange across the WAG edge.

While Eulerian and Lagrangian analyses have large differences, the magnitudes of transports are similar, implying that some of the conclusions from the Eulerian budgets will probably hold for fully-formed Lagrangian budgets. Questions about the collpase of the WAG might benefit from an analysis like this for a simulated collapse (such as done by Sanchez-Garrido et al. 2013), but it will probably be necessary to more carefully track the hyperbolic trajectories for integrating manifolds, as such a collapse changes the geometry of the system. As discussed earlier, it may also be necessary to have higher time resolution to close a Lagrangian budget than an Eulerian one, and in the case of a collapsing WAG this need for high time resolution is likely to increase.

5.5 References

Haller, George, and A. C. Poje. “Finite time transport in aperiodic flows.” Physica D: Nonlinear Phenomena 119.3-4 (1998): 352-380.

Heburn, George W., and Paul E. La Violette. “Variations in the structure of the anticyclonic gyres found in the Alboran Sea." Journal of Geophysical Research: Oceans 95.C2 (1990): 1599-1613.

McDougall, T.J. and P.M. Barker, 2011: Getting started with TEOS-10 and the Gibbs Seawater (GSW) Oceanographic Toolbox, 28pp., SCOR/IAPSO WG127, ISBN 978-0-646-55621-5.

Miller, Patrick D., et al. "Chaotic transport of mass and potential vorticity for an island recirculation." Journal of Physical Oceanography 32.1 (2002): 80-102.

Sanchez-Garrido, Jose C., et al. "What does cause the collapse of the Western Alboran Gyre? Results of an operational ocean model." Progress in oceanography 116 (2013): 142-153.

Chapter 6

General Discussion and Conclusions

In this work, I have examined two model flows based on oceanographic features: a submesoscale overturning eddy and the Western Alboran Gyre. My goal was to understand the role of advection for tracers in each case, particularly from a Lagrangian viewpoint. Here I will summarize the findings in the previous three chapters and discuss both how these improve past understandings and what questions remain for future work.

In Chapter 2, I presented a kinematic submesoscale overturning eddy model based on the rotating cylinder. Following work in Pratt et al. (2013) on the chaotic and regular regions in the system, bounded by Lagrangian barriers to transport, I considered the question of how the described chaotic advection and oceanic turbulent diffusion might affect tracer distribution. I used the kinematic model for trajectory integration to find out whether chaotic advection or turbulent diffusion would dominate the flow in the chaotic sea and resonant regions. Using the Batchelor scale and trajectory ensembles, I found that chaotic advection is dominant when the chaotic region is larger than the Batchelor scale, which is several meters to tens of meters using the scalings presented. This result supports the use of Lagrangian coherent structures identified as barriers to transport as such, even in the presence of diffusion, if the chaotic regions or adjacent regular regions identified are much larger than the Batchelor scale. In the past, mesoscale features (usually several kilometers or more across) have been the main focus; these are not in danger of being overrun by turbulent diffusion. However, there is a lower limit on the scales where that is the case, and this should be checked for the systems under consideration.

A second aspect of the work in Chapter 2 examined the evolution of a tracer in a dynamic simulation of the rotating cylinder flow. In the cases with chaotic advection due to symmetry breaking by an off-center rotating lid, the increased stretching and folding of water parcels in chaotic regions increased the full-cylinder stirring rate measured by the tracer variance function and increased the volume-integrated Nakamura effective diffusivity. Larger off-center perturbations and lower imposed numerical diffusivity amplified these changes. Overall, chaotic advection could double the mixing of a tracer through stirring, but did not change it by a large amount such as an order of magnitude. Therefore, when there is a combination of chaotic and regular regions stirring a fluid, mixing will occur faster in the chaotic regions, but not dramatically faster.

Chapter 2 and Appendix A also presented some mathematical derivations that are new. First, there is the evolution of a Gaussian tracer distribution in linear three-dimensional flow, updated from a similar derivation by Flierl and Woods (2015). Second, a derivation of the Nakamura effective diffusivity in a constant-density fluid in three dimensions, updated from a two-dimensional presentation by Nakamura (1996). Hopefully both of these will be of use to researchers working on stirring and mixing. One aspect of theory that could be improved, building on these terms, is a clear mathematical connection between Lyapunov exponents, Nakamura effective diffusivity, and the tracer variance function.

Other, more oceanographic directions for future work include examining more open flows with submesoscale features and considering the effects of stirring and mixing in the rotating cylinder on phytoplankton. The biggest limitation of the rotating cylinder as an analogue of an eddy, in my view, is that it is closed. In the ocean, most features are not exactly closed, exchanging some water with their surroundings. Even eddies identified as coherent are often the core of a larger rotating feature that is exchanging water. It would be very interesting work to look at the effects of realistic eddies on the stirring and mixing of tracers. On a large scale, I have done this for the Western Alboran Gyre, which I will discuss shortly, but for the submesoscale, the lack of observations of overturning eddies leaves room for the development and analysis of another model.

The effects of an overturning flow on phytoplankton production and diversity is another interesting direction for future work. Vertical mixing of phytoplankton is strongly connected to productivity through the mean level of light, and competition depends somewhat on how intermixed different species are. Looking at the effects of an overturning circulation on initial conditions with different light-adapted phytoplankton at different depths may provide insight into how transient eddies affect competition in the ocean. Alternatively, looking at the dominant type of phytoplankton that wins out from a large pool of initial traits in a permanent overturning feature would allow for consideration of whether such traits are found in the ocean, such as regions with frequent convection and this strong overturning.

In Chapters 3-5 I presented Eulerian and Lagrangian analyses of the Western Alboran Gyre, WAG, from five months of a realistic simulation using the MITgcm. The WAG is an anticyclonic gyre just east of the Strait of Gibraltar in the westernmost basin of the Mediterranean Sea. Outstanding oceanographic questions about the WAG include the maintenance of the horizontal gradients of temperature and salinity and the vorticity balance that maintains the structure. There is also a variety of work addressing the occasional collapse of the gyre, but I did not examine this behavior.

From the Eulerian analysis of the budgets for the properties of the WAG I was able to conclude that advection is a significant driver. In budgets of volume and heat for the WAG, the total advection (net through all sides) generally was the same magnitude as and correlated with the changes in the storage of the property of interest. A salt budget for the region containing the salinity minimum addressed the evolution of the minimum, finding that advection drove its decay. For both salt and heat, the local extrema appear to be decaying from values set during the formation of the WAG. In the vorticity budget, there was a complicated balance including advection, wind stress and the downward viscous diffusion of that force, and drag and horizontal viscous diffusion. All of these and the changes in time of the integrated relative vorticity were sometimes of similar magnitudes. Lateral viscous diffusion was the largest driver in the mean, with wind and vertical diffusion adding smaller amounts of anticyclonic vorticity. Drag and advection opposed the rotation of the WAG. Advection as a large contributor is consistent with the suggestion that advection of cyclonic vorticity into the gyre may prompt its collapse (Sanchez-Garrido et al. 2013), even though the time period analyzed here does not include a collapse.

The balance of advection through the sides and bottom in the Eulerian volume budget of the WAG was an outstanding feature, where each was much larger than the total advection which drove the changes in volume. The advection through the bottom of the WAG was associated with the motion of the $\sigma_\theta = 27.5$ isopycnal. The anticorrelation between this bottom transport and the net transport through the sides indicates a stretching-squashing motion of the water in the area. This overall rearrangement of water on timescales of a few days indicates that a Lagrangian view may give better insight into the physical processes occurring, without the obscurement of these large motions.

A set of Lagrangian budgets parallel to the Eulerian ones would still have advection through the sides, but now localized to the gate. Advection through the bottom is replaced by changes in storage when the bottom isopycnal moves due to advection. Smaller terms due to diffusion and surface forcing are also present. Due primarily to challenges in computing the Lagrangian WAG volume, it was not possible to close such budgets. It is necessary to use manifolds which are longer and more frequently resolved in time to get a more exact estimate of the transports involved. Unfortunately, often the manifolds are complicated, and errors are introduced from the process of simplifying them enough to be able to calculate the area inside. These challenges did not totally prevent the calculation of the storage and advective terms of the budgets for volume, salt, heat, and vorticity. However, because the volume budget is not closed, it is not possible to strongly state a balance of terms for anything else. Nonetheless, there are similarities between the Eulerian and Lagrangian advection through the sides of the gyre. These are often of the same magnitude, and in both cases the transport can take both signs in an aperiodic fashion.

This is the first time transport estimates from lobes and a gate have been calculated in three dimension for an aperiodic three-dimensional flow. Further development of Lagrangian methods for budgets would allow for clarity in the types of budgets presented here. So far, the results were somewhat similar to Eulerian budgets, so it is not entirely clear that further improvements in the same methods will allow budgets that add significantly to the results in terms of what the major balances are. Nonetheless, a Lagrangian budget would be exactly relatable to the properties of a more fixed set of water parcels than an Eulerian budget can be, and there is an advantage in interpretation there.

In that vein, the Lagrangian information about the paths of transport into and out of the gyre that connect to other regions of the Alboran Sea and to the Strait of Gibraltar are useful on their own, and were presented in chapter 4. Lagrangian manifolds outlined a three-dimensional lobe's evolution and the shape of three-dimensional stirring region and core of gyre. Interestingly, the stirring region can reach the northern coast, where there is upwelling; this indicates that upwelled nutrient can reach the WAG on fairly short timescales, which may be important for phytoplankton productivity. The extent of the stirring region becomes narrower with depth. The narrowing of the stirring region can be explained by the lower velocities at depth, leading to longer exchange timescales. The Lagrangian connections between different regions matter for understanding the Alboran Sea, showing that the WAG is less separate from the Atlantic Jet and northern coast than an Eulerian geostrophic picture, such as from satellite observations, would suggest. Given the fast changes in time and in the vertical seen here that caused problems closing budgets, past work done with altimetry for Lagrangian structures may be missing part of the dynamics. It would be useful to do a repeat study of the WAG using altimetric geostrophic velocity fields to examine how large the differences are.

In chapter 4, I also identified individual lobes, masses of water bounded by manifolds that are exchanged between the WAG and its surroundings, in three dimensions and examined their evolution. As an example of the 3D structure of lobes, one of the larger lobes is shown in three layers on three different days as it enters the WAG. The lobes were used to estimate the transport across the WAG boundary near the surface, over the top $5-50m$, with results of $10^5 m^3/s$ of volume transported, with associated transports of $10^8 kg/s$, $10^6 kg/s$ of salt, and $10^1 2J/s$ of heat. These transports are smaller than those from the gate transport due to the greater depth of the gates included.

Finally, another avenue for future work is to examine the impact of the WAG stirring region on biology. Some past studies have shown a large impact on productivity through the ageostrophic flow in the Atlantic Jet (e.g. Oguz et al. 2014), and a connection between the variability in sea-surface height patterns and chlorophyll concentrations (Navarro et al. 2011). The advection of nutrient-enriched water from the Strait of Gibraltar, where there is high vertical mixing by tides, and the northwestern coastal region, where there is upwelling, has not been examined. Stirring of these waters into the WAG may impact both productivity and diversity; an in-depth discussion of possible methods for studying these impacts is in Appendix C. Finally, the connectivity of the WAG to the coast of Spain can impact the management of fish populations. An ongoing study is examining larval dispersal of sardine and hake in light of these possible connections (Sanchez-Garrido, pers. comm.).

Altogether, the research described here has reexamined model oceanographic flows using Lagrangian methods but including aspects that are often neglected, such as diffusivity, three dimensions, and aperiodic flows. I can conclude that turbulent diffusivity in the ocean will not destroy

Lagrangian coherent structures that are large compared to the Batchelor scale; that advective transport through a gate is similar in magnitude to the net Eulerian transport through the sides of the same structure; and that Lagrangian budgets require sufficient resolution in space and time but may still not close exactly when manifolds are very complicated. There are many opportunities for further work regarding biological impacts, Lagrangian budget methods, and a detailed understanding of measures of stirring and mixing.

References

Flierl, Glenn R., and Nicholas W. Woods. “Copepod aggregations: influences of physics and collective behavior." Journal of Statistical Physics 158.3 (2015): 665-698.

Nakamura, N., Two dimensional mixing, edge formation, and permeability diagnosed in area coordinates, J. Atmos. Sci., 53, 1524âĂŞ1537, 1996.

Navarro, Gabriel, et al. "Understanding the patterns of biological response to physical forcing in the Alboran Sea (western Mediterranean)." Geophysical Research Letters 38.23 (2011).

Oguz, Temel, et al. “Fueling Plankton Production by a Meandering Frontal Jet: A Case Study for the Alboran Sea (Western Mediterranean)." PloS one 9.11 (2014): e111482.

Pratt, L. J., Rypina, I. I., Ozgokmen, T. M., Wang, P., Childs, H., & Bebieva, Y. (2013). Chaotic advection in a steady, three-dimensional, Ekman-driven eddy. Journal of Fluid Mechanics, 738, 143-183.

Sanchez-Garrido, J. C., G. Sannino, L. Liberti, J. GarcÃŋa Lafuente, and L. Pratt (2011), “Numerical modeling of three-dimensional stratified tidal flow over Camarinal Sill, Strait of Gibraltar," J. Geophys. Res., 116, C12026.

Appendix A

Rotating Cylinder Appendix

This appendix includes detailed information associated with Chapter 2. These details are likely only necessary if you wish to work with this model of the rotating cylinder yourself, and thus much of it has been omitted from the main text.

A.1 Bifurcation Analysis

Here I go into more detail about the bifurcations of the background velocity field in the kimenatic model of the rotating cylinder. I first repeat the definitions of the velocity field and our definitions of fixed points. Then I present the bifurcation diagram and an example of the flow with many fixed points.

The overturning streamfunction for the kinematic model of the rotating cylinder is

$$\Psi = -E^{1/2} R(r) F(z), \tag{A.1}$$

where E is the Ekman number,

$$F(z) = A[\sin(\zeta)\sinh(\zeta) - \cos(\zeta)\cosh(\zeta)] + B[\sin(\zeta)\sinh(\zeta) + \cos(\zeta)\cosh(\zeta)] - D, \tag{A.2}$$

ζ is a transformed vertical coordinate,

$$\zeta = \frac{z - 1/2}{E^{1/2}},$$

and the constants A, B, D are defined as in section 2 of the main text. For a cylinder height of 1 and finite radius, a, assumed to be near 1, we define R as

$$R(r) = r^2(a-r)^2/2, \tag{A.3}$$

giving velocities

$$\begin{aligned} U &= \tfrac{-\partial\Psi}{\partial z} &&= R(r)[A\sin(\zeta)\cosh(\zeta) + B\cos(\zeta)\sinh(\zeta)], && \text{(A.4)} \\ W &= \tfrac{\partial\Psi}{\partial r} &&= -(a-r)(a-2r)E^{1/2}F(z) && \text{(A.5)} \end{aligned}$$

where U is radial and W is the vertical. The axisymmetric azimuthal velocity V is defined

$$V(r,z) = r(a-r)^2[\frac{1}{2} + B\sin(\zeta)\cosh(\zeta) - A\cos(\zeta)\sinh(\zeta)]. \tag{A.6}$$

For all parameter values, there is upwelling in the center and weaker downwelling near the sides of the cylinder. There is horizontal convergence near the bottom and divergence near the top.

The azimuthal velocity V has a value of zero only at $z = 0$ and $r \in 0, a$. At $z = 0$ and $r = a$, the vertical and radial velocities are also zero, meaning that along the bottom and outer walls, every point is fixed. There are no other points in the flow where the total velocity is zero. However, because the azimuthal velocity is axisymmetric, points with zero vertical and radial velocity are circular periodic orbits. These trajectories are fixed points in a vertical cross-section, so we will call these *rz-fixed points*. At the surface, $z = 1$, the vertical and radial velocities are zero, so every point is an rz-fixed point.

All rz-fixed points in the interior occur at $r = 0.5a$, because this is the only place where $W = 0$ in the interior. Finding the rz-fixed points is thus the process of finding $U = 0$ at $r = 0.5a$, which we have done numerically by finding the values of z where U changes sign. It is equivalent to numerically find the local extrema of Ψ at $r = 0.5a$. There is always an rz-fixed point at $z = 0.5$.

New rz-fixed points appear through pitchfork bifurcations, where new pairs split from $z = 0.5$ and move apart in z as E decreases from one (figure A-1). It is possible to classify the rz-fixed points as elliptic or hyperbolic according to their behavior in the $r - z$ plane: the overturning streamfunction is a local maximum at elliptic points and a saddle at hyperbolic points, where it is a minimum along $r = 0.5a$ but a maximum for its value of z. At $E = 1$, the $(r, z) = (0.5, 0.5)$ point

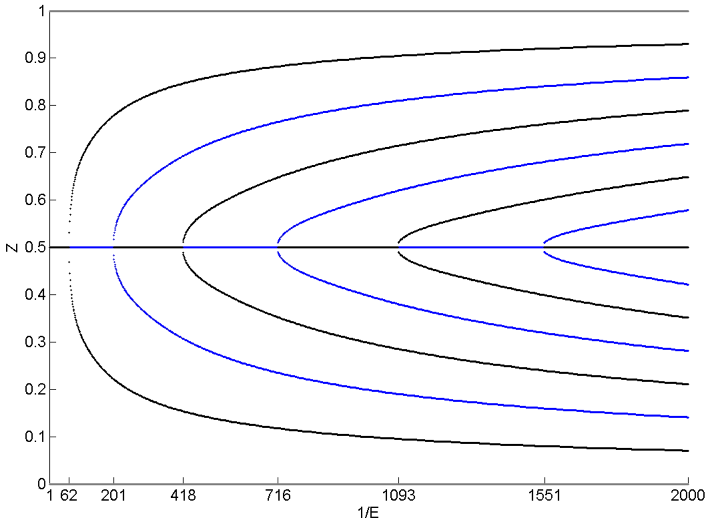

Figure A-1: Height of rz-fixed points in the vertical plane at $r = 0.5a$. Black indicates elliptic points, blue hyperbolic, gray the neutrally stable points at the top and bottom. New fixed point pairs separate symmetrically from $z = 0.5$ as E decreases. At each bifurcation, the central fixed point changes stability.

is elliptic. As E decreases to about $1/62$, the first bifurcation creates two elliptic points which move away from the central, now-hyperbolic, point. The next bifurcation creates two hyperbolic points, and the central fixed point becomes elliptic again. This process continues; the growth in number of fixed points as E decreases is due to repeated pitchfork bifurcations of the $z = 0.5$ fixed point. Thus, as these bifurcations occur, their effects remain within a region bounded by trajectories between the first pair of hyperbolic points, meaning that their effects are quite local. The spreading of the first pair of hyperbolic points, and not the total increase in rz-fixed points, causes the increasing vertical homogeneity of the flow with decreasing E which appears qualitatively similar to Taylor columns. An example with 9 rz-fixed points is shown in figure A-2 for $E = 0.00125$; the central point is now elliptic. Trajectories in the vertical plane are level curves of the streamfunction; these show the elliptic and hyperbolic nature of the rz-fixed points, where a point near an elliptic point remains nearby but a point near a hyperbolic point may travel a long distance before returning or may move toward another hyperbolic point.

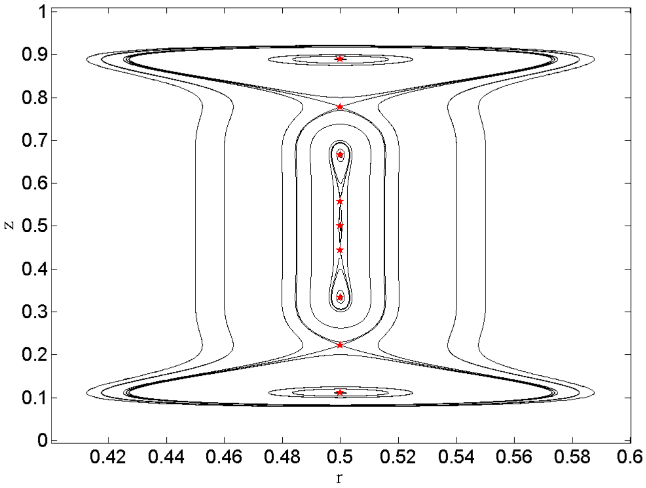

Figure A-2: Trajectories in the vertical plane for $E = 0.00125$, $a = 1$. There are 9 rz-fixed points along $r = 0.5$, marked with red stars. Note the closed curves between the outermost hyperbolic points which surround the interior 5 rz-fixed points; these limit the effects of those points to the local area.

A.2 Gaussian Tracer in Linear Strain

In this section, I finish the derivation of the evolution of a three-dimensional tracer in a steady linear strain flow. This was omitted from the main text because there I was primarily interested in showing that the thinnest width will asymptotically approach the Lagrangian Batchelor scale. I first repeat the definitions of the velocity field, the tracer evolution equation, and the form of the solution. Then I present the remainder of the derivation for the full time-dependent solution from the differential equations for each parameter.

We are solving for the evolution of tracer concentration, C, with a solution in the form

$$C = c_{max}(t) \exp\left(\frac{-x^2\alpha^2(t)}{2} + \frac{-y^2\beta^2(t)}{2} + \frac{-z^2\gamma^2(t)}{2}\right), \tag{A.7}$$

where c_{max} is the maximum concentration and α β γ are the reciprocal of the standard deviations in each direction. These four parameters are dependent on time but not space. The smallest width of the distribution is $\sigma = 1/\alpha$ and in the main text we found a stable fixed point of $\sigma = \sqrt{\kappa/|\lambda_3|}$, where λ_3 is the contraction rate of the velocity field. The velocities are defined in the Lagrangian frame by

$$u = \lambda_3 x(\vec{x_0}, t), \tag{A.8}$$

$$v = \lambda_2 y(\vec{x_0}, t), \tag{A.9}$$

$$w = \lambda_1 z(\vec{x_0}, t), \tag{A.10}$$

$$\lambda_1 > \lambda_2 > \lambda_3, \tag{A.11}$$

$$\lambda_1 > 0,\ \lambda_3 < 0, \tag{A.12}$$

with $\vec{x}(\vec{x_0}, t)$ indicating the initial position $\vec{x_0}$ of the water parcel at $t = 0$. The Lagrangian tracer evolution equation is

$$\frac{\partial C}{\partial t} + \lambda_3 x \frac{\partial C}{\partial x} + \lambda_2 y \frac{\partial C}{\partial y} + \lambda_1 z \frac{\partial C}{\partial z} = \kappa \nabla^2 C, \tag{A.13}$$

where κ is the diffusivity.

In the main text, the form of C and the tracer evolution equation allowed us to find differential equations for each of our four parameters, which are

$$\frac{1}{c_{max}} \frac{dc_{max}}{dt} = -\kappa \left(\alpha^2 + \beta^2 + \gamma^2 \right), \tag{A.14}$$

$$\frac{d\alpha}{dt} = -\lambda_3 \alpha - \kappa \alpha^3, \tag{A.15}$$

$$\frac{d\beta}{dt} = -\lambda_2 \beta - \kappa \beta^3, \tag{A.16}$$

$$\frac{d\gamma}{dt} = -\lambda_1 \gamma - \kappa \gamma^3. \tag{A.17}$$

A full solution for C can be written by solving the differential equations for all four parameters. The width parameters' equations are nonlinear, but rewritten in terms like α^{-2} give:

$$\frac{d\alpha^{-2}}{dt} = 2\lambda_3 \alpha^{-2} + 2\kappa,$$

$$\frac{d\beta^{-2}}{dt} = 2\lambda_2 \beta^{-2} + 2\kappa,$$

$$\frac{d\gamma^{-2}}{dt} = 2\lambda_1 \gamma^{-2} + 2\kappa,$$

which are Bernoulli equations, solvable with integrating factors, giving

$$\begin{aligned}
\alpha &= \sqrt{|\lambda_3|/\kappa}\left((\lambda_3 {\alpha_0}^{-2}/\kappa - 1)e^{2\lambda_3 t} + 1\right)^{-1/2}, \\
\beta &= \left(({\beta_0}^{-2} + \kappa/\lambda_2)e^{2\lambda_2 t} - \kappa/\lambda_2\right)^{-1/2}, \\
\gamma &= \sqrt{\lambda_1/\kappa}\left((\lambda_1 {\gamma_0}^{-2}/\kappa + 1)e^{2\lambda_1 t} - 1\right)^{-1/2},
\end{aligned}$$

where subscript 0 indicates the value at $t = 0$. The differences in these equations is due to the different signs of each λ, with the ambiguity of the sign of λ_2 preventing its factoring.

The c_{max} equation depends on the width parameters and is not simple to solve directly. However, some inspection shows that $c_{max}/(\alpha\beta\gamma)$ is conserved, so we can write

$$c_{max}(t) = c_0\alpha(t)\beta(t)\gamma(t).$$

For anyone in doubt, we plug in this solution to check it:

$$\begin{aligned}
\frac{dc_{max}}{dt} &= \frac{d}{dt}(c_0\alpha\beta\gamma) = c_0\left(\beta\gamma\frac{d\alpha}{dt} + \alpha\gamma\frac{d\beta}{dt} + \alpha\beta\frac{d\gamma}{dt}\right), \\
&= c_0\left(-\alpha\beta\gamma(\lambda_3 + \kappa\alpha^2) - \alpha\beta\gamma(\lambda_2 + \kappa\beta^2) - \alpha\beta\gamma(\lambda_1 + \kappa\gamma^2)\right), \\
&= -c_0\alpha\beta\gamma\left(\lambda_1 + \lambda_2 + \lambda_3 + \kappa[\alpha^2 + \beta^2 + \gamma^2]\right), \\
\implies \frac{1}{c_{max}}\frac{dc_{max}}{dt} &= -\kappa\left(\alpha^2 + \beta^2 + \gamma^2\right).
\end{aligned}$$

C then has been fully solved:

$$\begin{aligned}
C(x,y,z,t) =& c_0\sqrt{|\lambda_1\lambda_2\lambda_3|/\kappa^3}\left([(\lambda_3{\alpha_0}^{-2}/\kappa + 1)e^{2\lambda_3 t} - 1][(\lambda_2{\beta_0}^{-2}/\kappa + 1)e^{2\lambda_2 t} - 1][(\lambda_1{\gamma_0}^{-2}/\kappa + 1)e^{2\lambda_1 t} - 1]\right)^{-1/2} \\
&\cdot \exp\left[\frac{-x^2\lambda_3}{2\kappa[(\lambda_3{\alpha_0}^{-2}/\kappa + 1)e^{2\lambda_3 t} - 1]} + \frac{-y^2\lambda_2}{2\kappa[(\lambda_2{\beta_0}^{-2}/\kappa + 1)e^{2\lambda_2 t} - 1]} + \frac{-z^2\lambda_1}{2\kappa[(\lambda_1{\gamma_0}^{-2}/\kappa + 1)e^{2\lambda_1 t} - 1]}\right].
\end{aligned}$$

For a three dimensional Gaussian tracer in a linear strain field, in the Lagrangian frame the width will increase in the stretching direction(s) forever, but reach a fixed value in the contracting direction(s).

A.3 Nakamura Effective Diffusivity

A.3.1 Derivation

I follow the derivation of Nakamura's (1996) effective diffusivity, updating it to be in three dimensions rather than two. Mathematically, there are no large changes; I simply replace areas with volumes and curves with surfaces, as appropriate. It should be noted that the q in Nakamura's work is a density-weighted tracer concentration. The rotating cylinder as formulated has a constant density, and so this weighting is not included.

I begin with a tracer advection-diffusion equation assuming no sources:

$$\frac{\partial c}{\partial t} + \vec{u} \cdot \nabla c = k \nabla^2 c, \tag{A.18}$$

where c is the tracer concentration, $\vec{u}$ is the fluid velocity, and k is the diffusivity without stirring. The goal is to form an equation that appears to include only diffusion:

$$\frac{\partial}{\partial t} c = \frac{\partial}{\partial V} \kappa \frac{\partial c}{\partial V},$$

where κ is an effective diffusivity. To do so, I will change to volume coordinates.

I first define a relationship between volume, V, and c as

$$V(c) \equiv \iiint_{c^* \geq c} (1) dV; \tag{A.19}$$

note that c^* denotes values of c inside integrals. This definition of $V(c)$ gives the total volume in the system where dye concentration is larger than c, so it is zero at the maximum dye concentration and is the total volume of your system at the minimum of dye concentration. Regardless of the arrangement of dye, $V(c)$ is a one-to-one relationship between volumes and concentrations. The volume can be rewritten using ν, an integral operator on a scalar defined as

$$\nu \equiv \iiint (\ ) dV; \tag{A.20}$$

then the volume is

$$V(c,t) \equiv \nu(1).$$

These integrals can be rewritten in two coordinates along the c surface and one across so that the unit volume changes form:

$$dV = dxdydz = ds_1 ds_2 \frac{dc}{|\nabla c|},$$

where the gradient of c is the determinant of the Jacobian for changing coordinates in an integral. Then ν can be written as

$$\nu(\,) = \int_{c^* \geq c} dc^* \oiint_{c^*} ds \frac{(\,)}{|\nabla c^*|}, \tag{A.21}$$

where ds now stands for a small area on the surface. This form describes integrating a series of shells in c for whatever scalar function is chosen. Reversing the inequality changes the side of the chosen c surface integrated over, and islands can be included without changing the function. However, it is assumed that the domain boundaries are c surfaces; for the rotating cylinder problem, there is no flux across the boundaries, and this condition is met.

If there are no non-conservative processes affecting c, here meaning no diffusion, then $V(c)$ will be a constant relationship in time. With the addition of diffusion, the change in V with time at a constant c will be nonzero. The evolution of $c(V)$ due to diffusion should take the usual form,

$$\frac{\partial c(V)}{\partial t} = k\nabla^2 c(V), \tag{A.22}$$

One can take the time derivative of ν as defined in Eqn. 3 to find the time derivative of V:

$$\begin{aligned} \frac{\partial}{\partial t}V &= \frac{\partial}{\partial t}\nu(1) = \frac{\partial}{\partial t}\int_{c \geq c^*} dc^* \oiint_{c^*} ds \frac{1}{|\nabla c^*|} && \text{(A.23)} \\ &= \frac{\partial}{\partial c}\int_{c^* \geq c} dc^* \frac{\partial c^*}{\partial t} \oiint_{c^*} ds \frac{1}{|\nabla c^*|} \\ \frac{\partial V}{\partial t} &= \frac{\partial}{\partial c}\nu\left(\frac{\partial c}{\partial t}\right) && \text{(A.24)} \\ &= -1 \oiint_{c} ds \frac{\partial c/\partial t}{|\nabla c|}. && \text{(A.25)} \end{aligned}$$

The negative one comes from taking the derivative of a semi-definite integral, using the fundamental theorem of calculus:

$$\frac{\partial}{\partial x}\int_{x^*}^{a} f(x)dx = -\frac{\partial}{\partial x}\int_{a}^{x} f(x^*)dx^* = -f(x).$$

Because the relationship between c and V is one-to-one, one can use the evolution of V above to determine the evolution of c:

$$\frac{\partial}{\partial t}c = \frac{\partial c}{\partial V}\frac{\partial V}{\partial t} \tag{A.26}$$

$$= \frac{\partial c}{\partial V}\ \frac{\partial}{\partial c}\ \nu\left(\frac{\partial c}{\partial t}\right)$$

$$= \frac{\partial}{\partial V}\ \nu\left(\frac{\partial c}{\partial t}\right) = \frac{\hat{\partial} c}{\partial t}. \tag{A.27}$$

The V derivative of ν is equivalent to the average of the scalar function along the chosen c surface; here, that means the evolution of $c(V)$ on a surface is the average of the changes along it, which is intuitively correct. In volume coordinates $\partial c/\partial t$ is the righthand term in Eqn 4. Putting that term into the c evolution and rearranging, we will soon find the effective diffusion equation. First, put in the correct term, using the volume-integration form of ν:

$$\frac{\partial}{\partial t}c = \frac{\partial}{\partial V}\ \nu\left(\frac{\partial c}{\partial t}\right)$$

$$= \frac{\partial}{\partial V}\ \nu\left(k\nabla^2 c\right)$$

$$= \frac{\partial}{\partial V}\ \iiint_{c^*\geq c}\left(k\nabla^2 c^*\right)\, dV. \tag{A.28}$$

Then use the appropriate divergence theorem, $\iiint \nabla\cdot f\ dv = \oiint f\cdot\vec{n}\ ds$, and rewrite the normal vector in terms of the gradient of c:

$$\frac{\partial}{\partial t}c = \frac{\partial}{\partial V}\ \iiint_{c^*\geq c}\left(k\nabla^2 c^*\right)\, dV$$

$$= \frac{\partial}{\partial V}\ \oiint_{c=c^*}\left(k\nabla c^*\right)\cdot\vec{n}\ ds$$

$$= \frac{\partial}{\partial V}\ \oiint_{c=c^*}\left(k\nabla c^*\right)\cdot\frac{\nabla c^*}{|\nabla c^*|}\ ds$$

$$= \frac{\partial}{\partial V}\ k\oiint_{c=c^*}\frac{|\nabla c^*|^2}{|\nabla c^*|}\ ds \tag{A.29}$$

$$= \frac{\partial}{\partial V}\ k\frac{\partial}{\partial c}\nu\left(|\nabla c|^2\right), \tag{A.30}$$

where the final equality depends on the derivative $\partial\nu/\partial c$, Eqn 6. Now, to have the derivatives in

V, use

$$\frac{\partial}{\partial c} = \frac{\partial V}{\partial c}\frac{\partial}{\partial V} = \frac{1}{\partial c/\partial V}\frac{\partial}{\partial V},$$

which gives

$$\begin{aligned}
\frac{\partial}{\partial t}c &= \frac{\partial}{\partial V}\;k\frac{\partial}{\partial c}\nu\left(|\nabla c|^2\right), \\
&= \frac{\partial}{\partial V}\;k\frac{\partial \nu\left(|\nabla c|^2\right)}{\partial V}\frac{1}{\partial c/\partial V} && \text{(A.31)} \\
&= \frac{\partial}{\partial V}\;k\frac{\partial \nu\left(|\nabla c|^2\right)}{\partial V}\frac{1}{(\partial c/\partial V)^2}\frac{\partial c}{\partial V} && \text{(A.32)} \\
&= \frac{\partial}{\partial V}\kappa\frac{\partial c}{\partial V}, && \text{(A.33)}
\end{aligned}$$

where

$$\begin{aligned}
\kappa &= k\frac{\partial \nu\left(|\nabla c|^2\right)}{\partial V}\frac{1}{(\partial c/\partial V)^2} \\
&= k\frac{1}{(\partial c/\partial V)^2}\frac{\partial}{\partial V}\iiint |\nabla c|^2\,dV \\
&= k\frac{1}{(\partial c/\partial V)^2}|\hat{\nabla c}|^2. && \text{(A.34)}
\end{aligned}$$

Eqn 17 shows that the effective diffusivity is a function of the average gradient, $|\hat{\nabla c}|^2$, along the relevant c contour and the slope of $c(V)$. This expression can be interpreted as an effective surface area. To demonstrate the connection to surface area, we reconsider the average gradient and volume slope terms as integrals of the same form:

$$\begin{aligned}
\frac{1}{(\partial c/\partial V)^2}|\hat{\nabla c}|^2 &= \frac{\partial V}{\partial c}\frac{1}{(\partial c/\partial V)}|\hat{\nabla c}|^2 \\
&= \oiint_{c=c^*}\frac{1}{|\nabla c^*|}\,ds\;\;\frac{1}{(\partial c/\partial V)}\;\;\frac{\partial}{\partial V}\int_{c^*\geq c}\oiint_{c=c^*}\frac{|\nabla c^*|^2}{|\nabla c^*|}\,ds \\
&= \oiint_{c=c^*}\frac{1}{|\nabla c^*|}\,ds\;\;\frac{1}{(\partial c/\partial V)}\;\;\frac{\partial c}{\partial V}\;\;\frac{\partial}{\partial c}\int_{c^*\geq c}\oiint_{c=c^*}\frac{|\nabla c^*|^2}{|\nabla c^*|}\,ds \\
&= \oiint_{c=c^*}\frac{1}{|\nabla c^*|}\,ds\;\;\oiint_{c=c^*}\frac{|\nabla c^*|^2}{|\nabla c^*|}\,ds. && \text{(A.35)}
\end{aligned}$$

We then assume that $|\nabla c|$ is constant on the c-surface of interest and take it out of the integrals, giving

$$\begin{aligned}\frac{1}{(\partial c/\partial V)^2}|\hat{\nabla c}|^2 &= \frac{1}{|\nabla c^*|}\oiint_{c=c^*} ds \ \frac{|\nabla c^*|^2}{|\nabla c^*|}\oiint_{c=c^*} ds \\ &= \frac{|\nabla c^*|^2}{|\nabla c^*|^2}\oiint_{c=c^*} ds \oiint_{c=c^*} ds \\ &= \left[\oiint_{c=c^*} ds\right]^2 = A^2, \qquad \text{(A.36)}\end{aligned}$$

where A is the surface area. Thus, the diffusive flux depends upon the gradient across a surface, $\partial c/\partial V$, and the size of the surface, A, the terms one would expect.

A.3.2 Long-time Limit

In section 3.3 we describe the evolution of dye in our flow field under various parameters for the rotating cylinder flow. At long times, for the symmetric flow field, the dye contours resemble nested tori, although with cross-sections that are somewhat oval, between a circle and a square. Here, we show the derivation of the expected limit of $\int \kappa_{eff} dV$. We are assuming that the dye concentration at late times will depend only on distance from the central orbit the tori are nested around, meaning that the gradient of the dye concentration will be uniform along a torus and the effective diffusivity on each torus is exactly kA^2 as suggested by equation 18.

We can calculate $\int \kappa_{eff} dV$ for a standard circular tori, by taking the volume integral of kA^2, the background diffusivity multiplied by the squared surface area. Recall that the volume of a circular torus is

$$V_{ct} = 2\pi^2 r^2 R,$$

where r is the radius of the circular cross-section and R is the distance from the center of mass to the center of the cross-section. The surface area is

$$A_{ct} = 4\pi^2 r R.$$

Note that A is the derivative of V with respect to the half-width of the cross-section. Therefore, to do a volume integral of a function that changes only with that width, such as A^2, we can simplify the integration:

$$\iiint (\;) dV = \int (\;) A dr.$$

We can now calculate $\int \kappa_{eff} dV$ assuming the contours are nested circular tori. First, we rewrite the integral in terms of area:

$$\begin{aligned}\int \kappa_{eff} dV &= \iiint kA^2 dV \\ \int \kappa_{eff} dV &= k \int A^3 dr \\ &= k \int (A_{ct})^3 dr = k \int (A_{st})^3 dr.\end{aligned} \tag{A.37}$$

Then, we use the formula for area of a circular torus to complete the integration:

$$\begin{aligned}\int \kappa_{eff} dV &= k \int (A_{ct})^3 dr \\ &= k \int (4\pi^2 rR)^3 dr \\ &= 4^3 \pi^6 R^3 k \int r^3 dr \\ &= 4^2 \pi^6 R^3 k r^4 \Big|_{r_{min}}^{r_{max}}.\end{aligned} \tag{A.38}$$

For our cylinder, $R = 0.5$ and $r \in [0, 0.5]$, giving

$$\int \kappa_{eff} dV = k \int (A_{ct})^3 dr = 4^2 \pi^6 R^3 k r^4 \Big|_{r_{min}}^{r_{max}} = k\pi^6/8.$$

The circular torus result is a minimum, because there is still volume outside the largest torus that fits in the cylinder and the final cross-sections are somewhat oval, thus having a larger surface area per volume.

Appendix B

Eulerian Analysis Appendix

B.1 MITgcm Output Comparison to Climatology

Although truly validating any complex model output is not possible, demonstrating the approximate correctness of the output's behavior is desirable when relating modeled results to the natural system. Here, temperature, and salinity output from the MITgcm for a simulation of the Alboran Sea is compared to climatological temperature and salinity. The model has 1-3km resolution and is forced by ocean and atmospheric reanalysis data for November 2007 to December 2008. Monthly averages are shown; data is linearly interpolated to selected depths. The model run was performed by the author, and the climatological data is from the MEDAR/MEDATLAS II dataset, which is based on *in-situ* hydrographic observations (*http://www.ifremer.fr/medar/climatol.htm*). The mapping in climatology assumes a 100km correlation lengthscale.

Figures are presented for all 14 months with both Novembers and both Decembers adjacent; they are organized by depth (5, 100, 400, and 1000m), so the first 14 are for 5m depth. The salinity comparison shows fairly good matching at all depths and months. Temperatures show more separation. The model Atlantic is too warm below the surface, and at the 5m depth the seasonal cycle in the model is smaller than in climatology.

B.1.1 5m depth

Temperature images have a colorbar range of 14 (dark blue) to 22 (dark red), which is the potential temperature from the model and the *in-situ* temperature from climatology. Salinity images have a colorbar range of 35 (dark blue) to 38 (dark red) in practical salinity units.

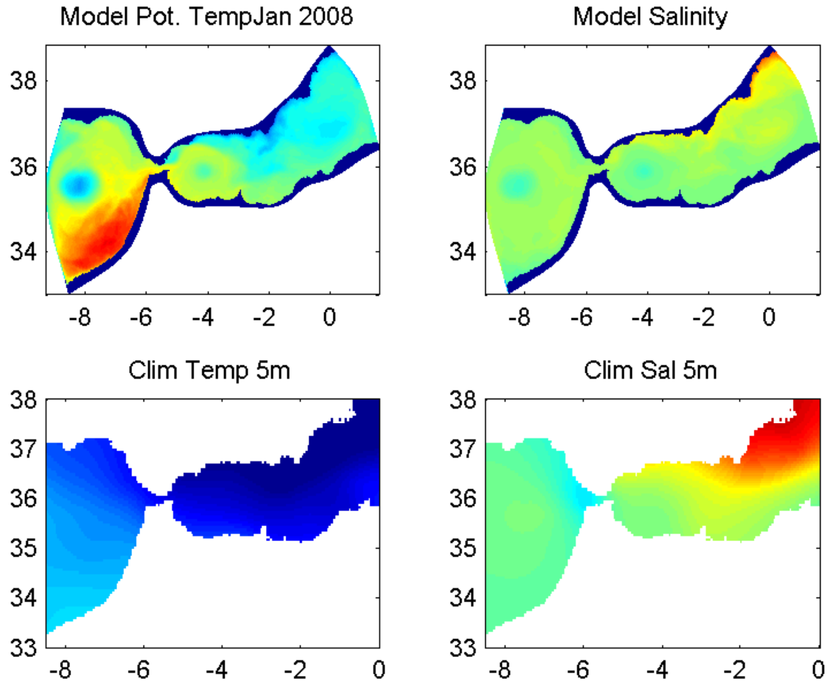
Model Pot. TempJan 2008
Model Salinity
Clim Temp 5m
Clim Sal 5m
38
36
34
-8
-6
-4
-2
0
38
37
36
35
34
33

(a) Jan

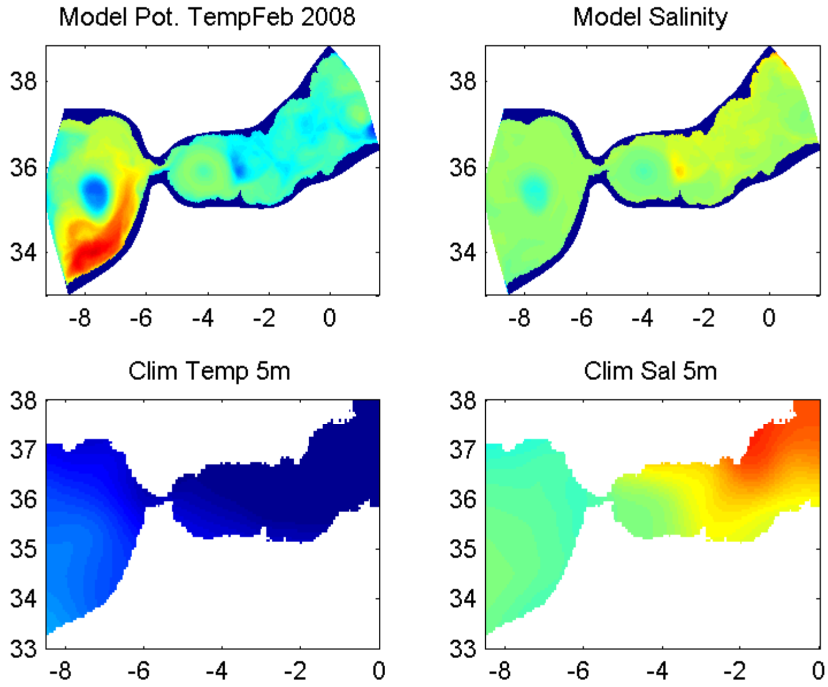
Model Pot. TempFeb 2008
Model Salinity
Clim Temp 5m
Clim Sal 5m
38
36
34
-8
-6
-4
-2
0
38
37
36
35
34
33

(b) Feb

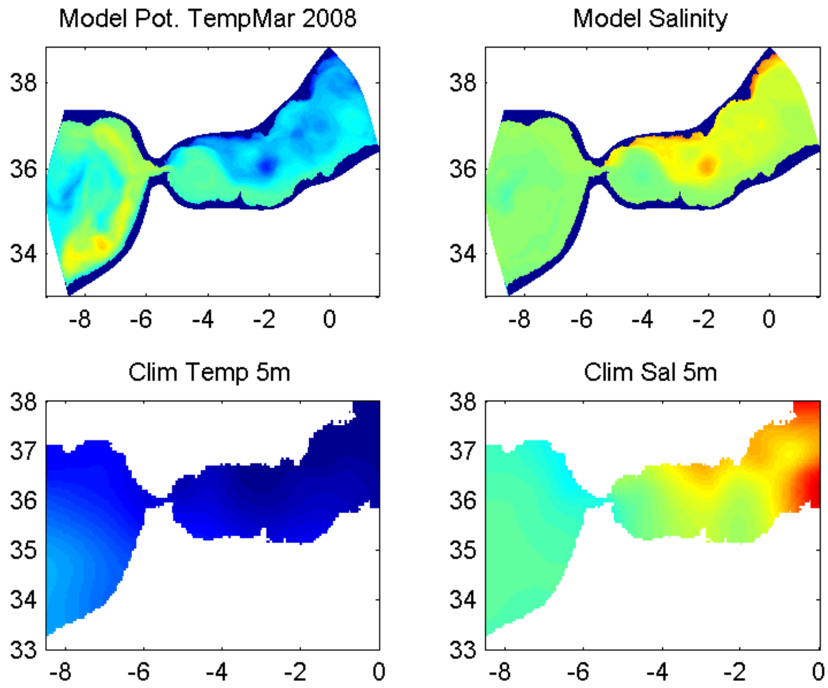
Model Pot. TempMar 2008
Model Salinity
Clim Temp 5m
Clim Sal 5m
38
36
34
-8
-6
-4
-2
0
38
37
36
35
34
33

(a) Mar

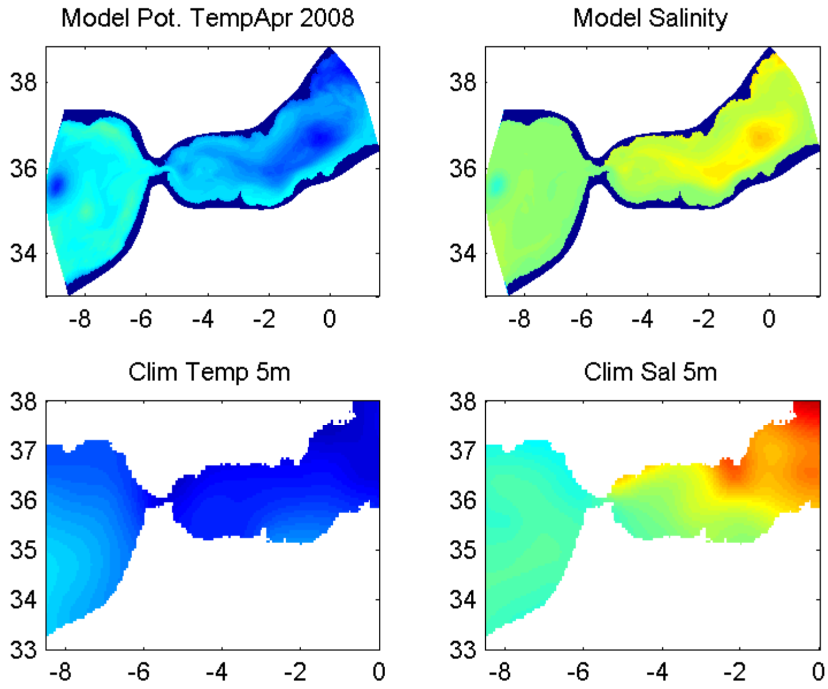
Model Pot. TempApr 2008
Model Salinity
Clim Temp 5m
Clim Sal 5m
38
36
34
-8
-6
-4
-2
0
38
37
36
35
34
33

(b) Apr

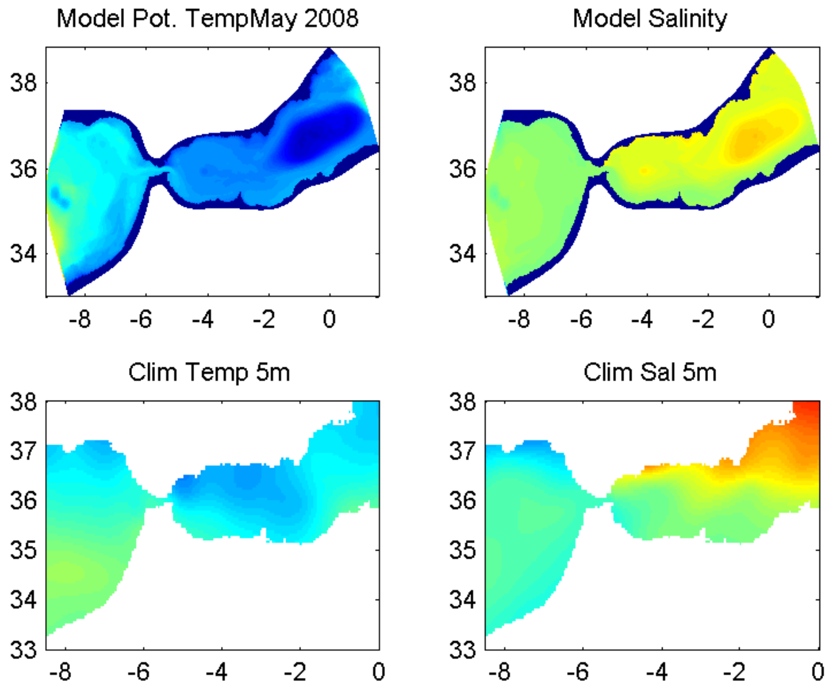
Model Pot. TempMay 2008
Model Salinity
Clim Temp 5m
Clim Sal 5m
38
36
34
-8
-6
-4
-2
0
38
37
36
35
34
33

(a) May

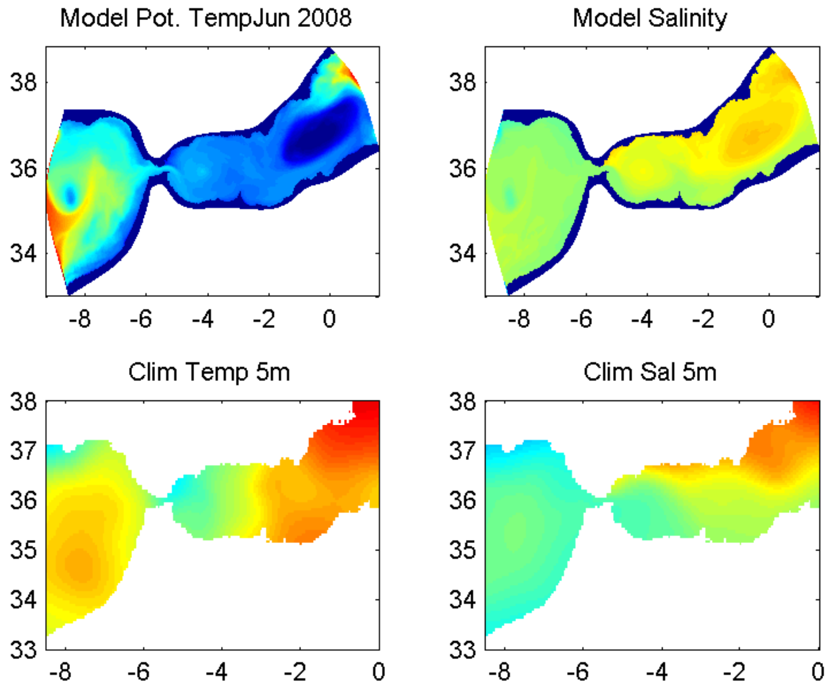
Model Pot. TempJun 2008
Model Salinity
Clim Temp 5m
Clim Sal 5m
38
36
34
-8
-6
-4
-2
0
38
37
36
35
34
33

(b) Jun

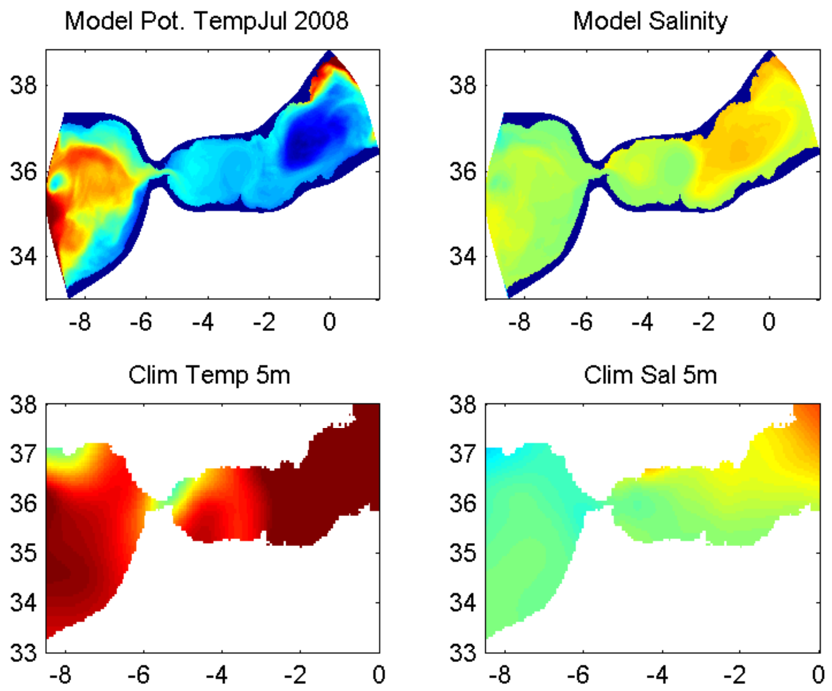
Model Pot. TempJul 2008

Model Salinity

Clim Temp 5m

Clim Sal 5m

(a) Jul

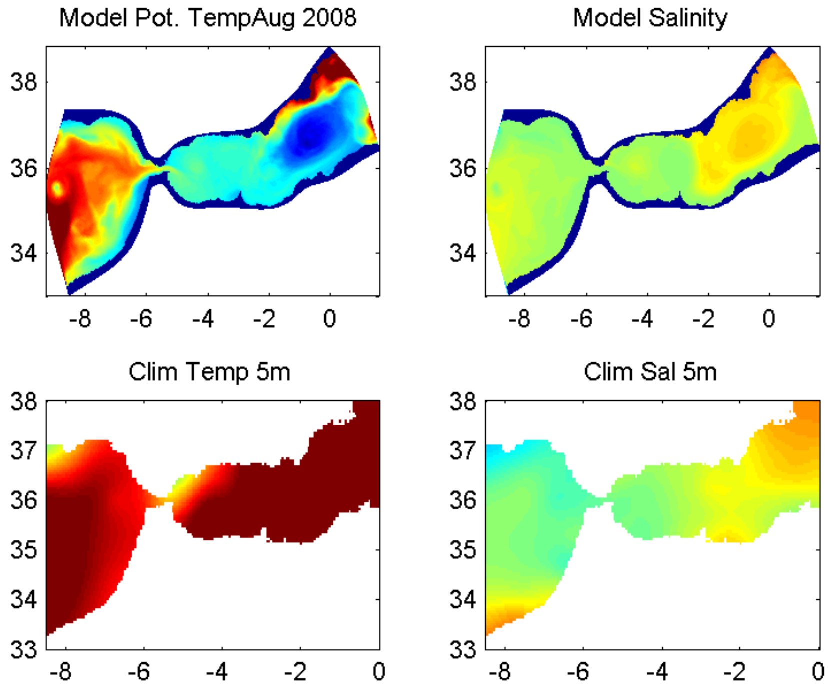
Model Pot. TempAug 2008

Model Salinity

Clim Temp 5m

Clim Sal 5m

(b) Aug

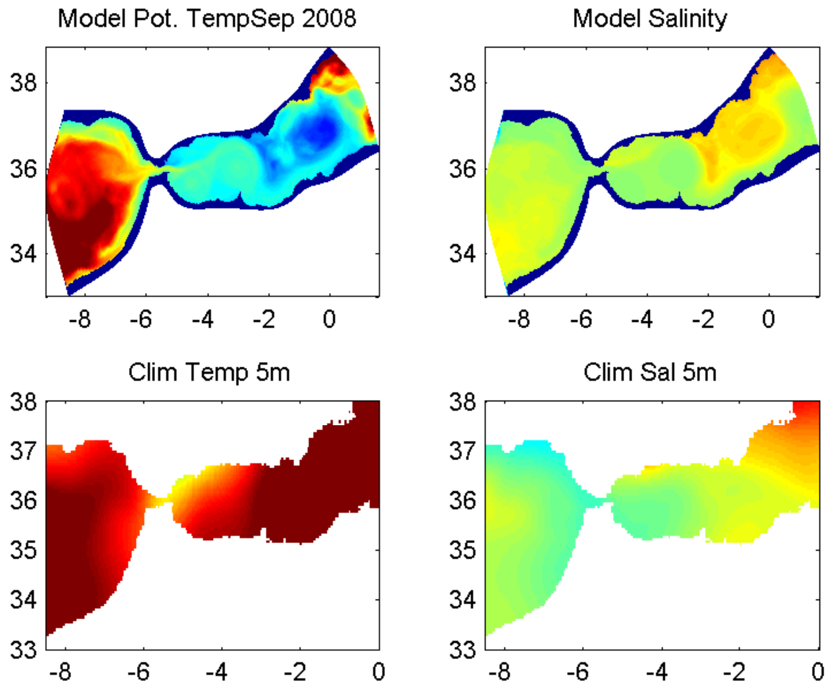
Model Pot. TempSep 2008
Model Salinity
Clim Temp 5m
Clim Sal 5m
38
36
34
-8
-6
-4
-2
0
37
35
33

(a) Sep

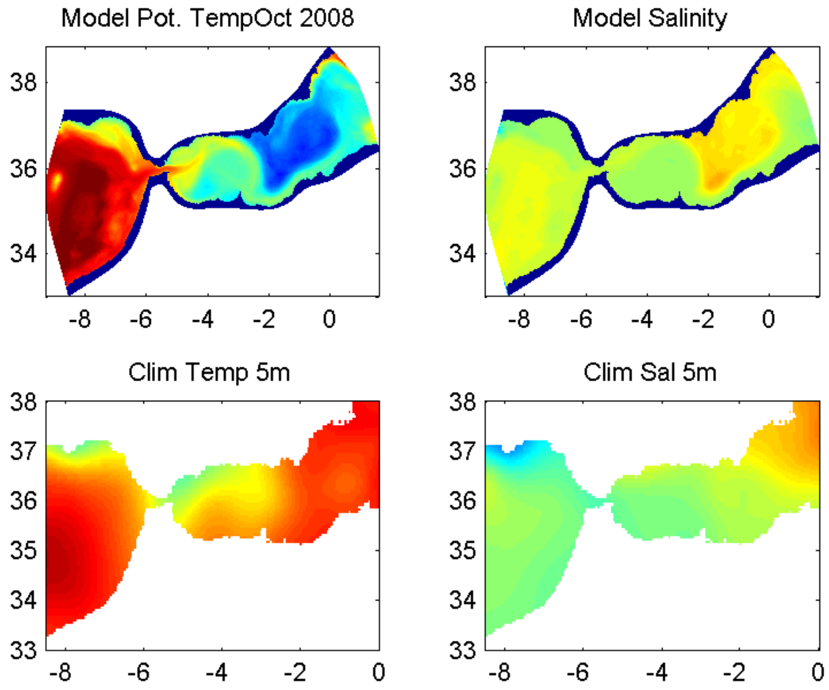
Model Pot. TempOct 2008
Model Salinity
Clim Temp 5m
Clim Sal 5m
38
36
34
-8
-6
-4
-2
0
37
35
33

(b) Oct

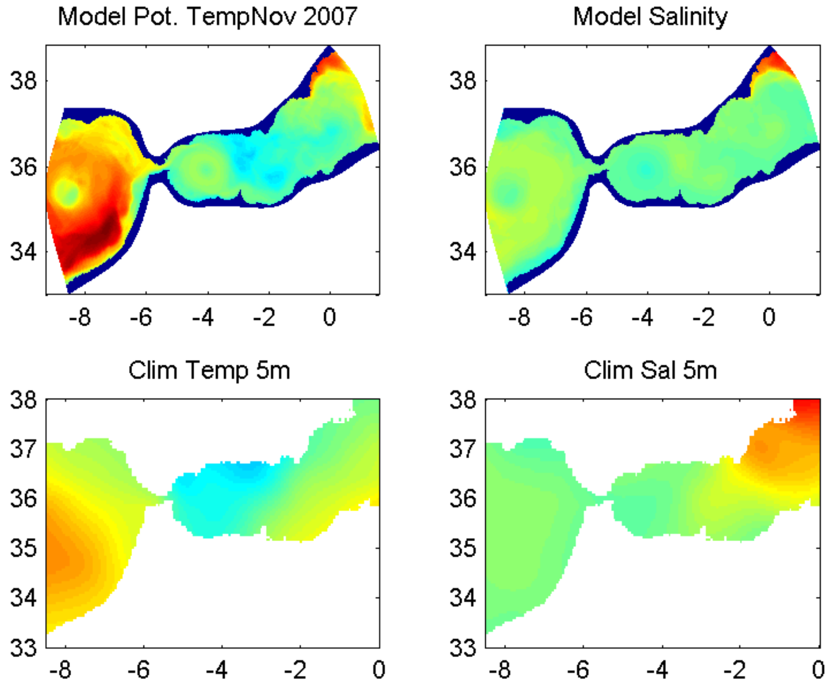

(a) Nov 2007

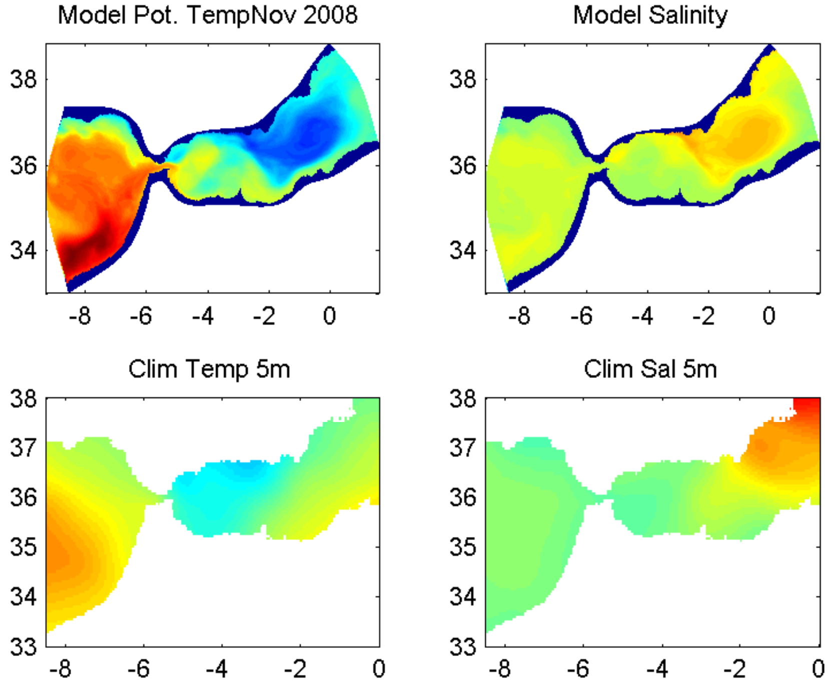

(b) Nov 2008

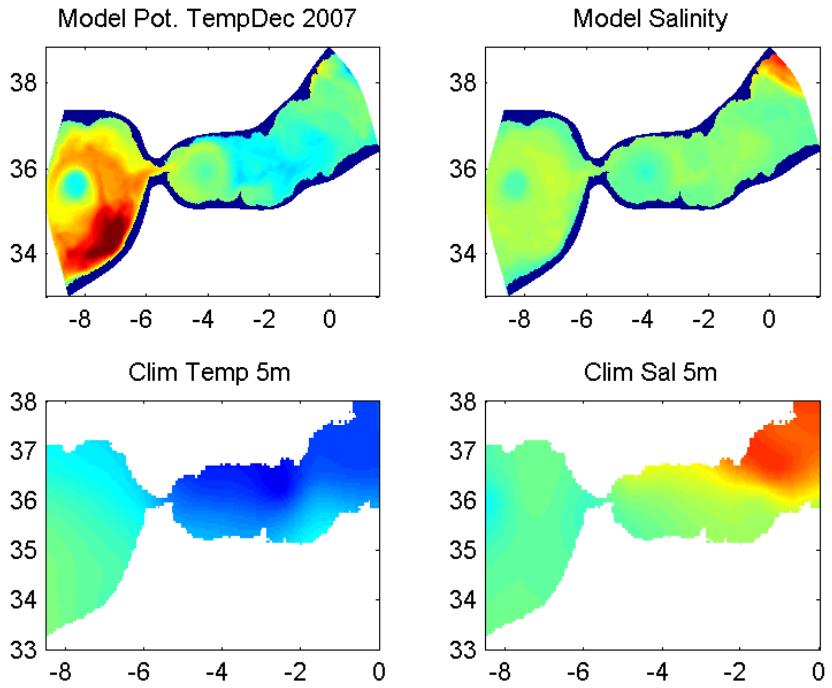

(a) Dec 2007

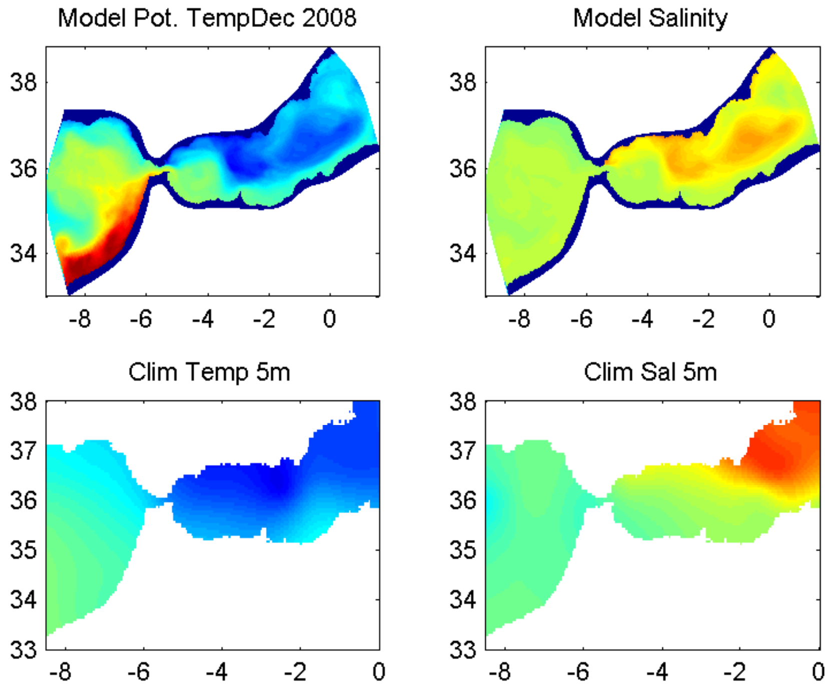

(b) Dec 2008

B.1.2 100m depth

Temperature images have a colorbar range of 10 (dark blue) to 15 (dark red), which is the potential temperature from the model and the *in-situ* temperature from climatology. Salinity images have a colorbar range of 35 (dark blue) to 39 (dark red) in practical salinity units.

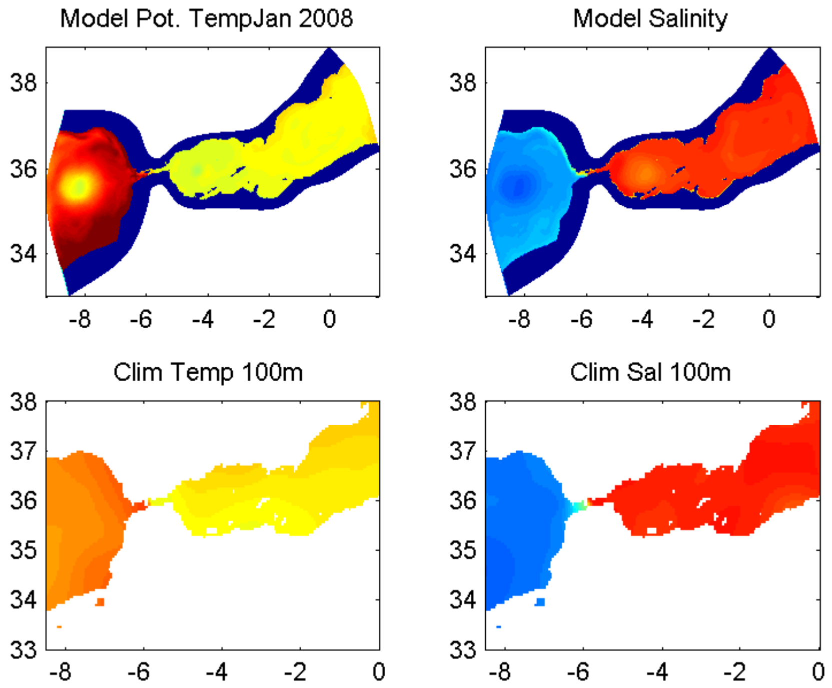
Model Pot. TempJan 2008
Model Salinity
Clim Temp 100m
Clim Sal 100m
38
36
34
-8
-6
-4
-2
0
38
37
36
35
34
33

(a) Jan

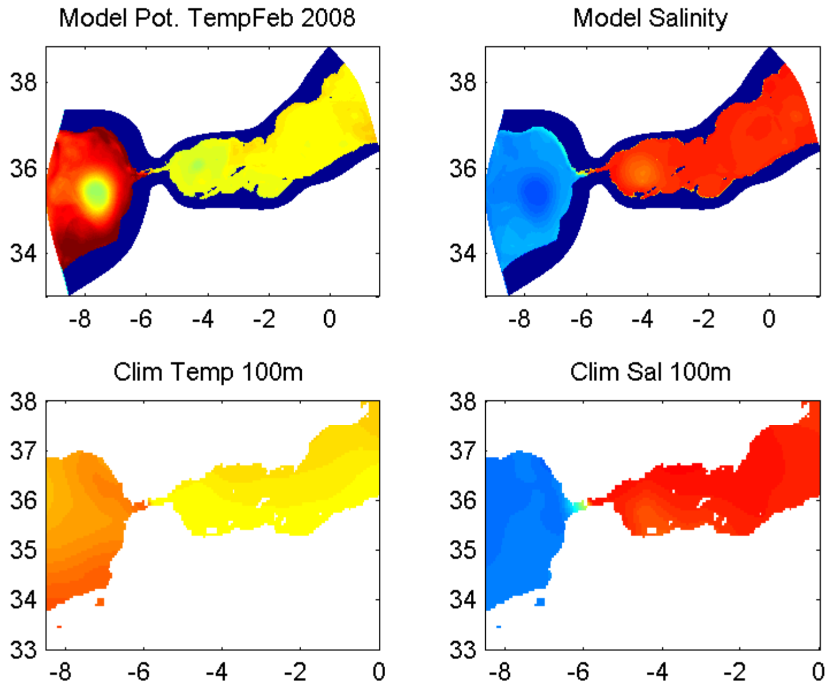
Model Pot. TempFeb 2008
Model Salinity
Clim Temp 100m
Clim Sal 100m
38
36
34
-8
-6
-4
-2
0
38
37
36
35
34
33

(b) Feb

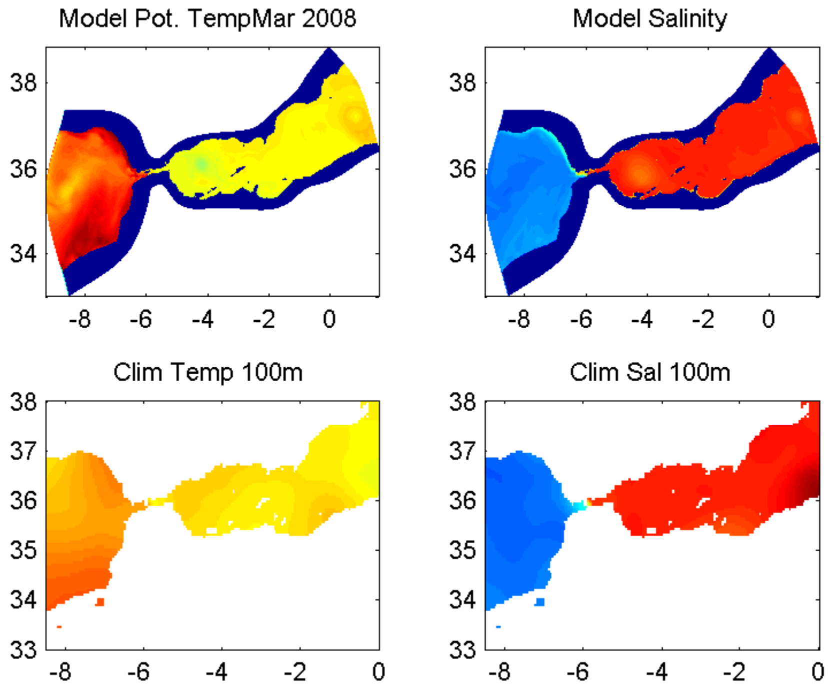
Model Pot. TempMar 2008
Model Salinity
Clim Temp 100m
Clim Sal 100m
38
36
34
-8
-6
-4
-2
0
38
37
36
35
34
33
-8
-6
-4
-2
0

(a) Mar

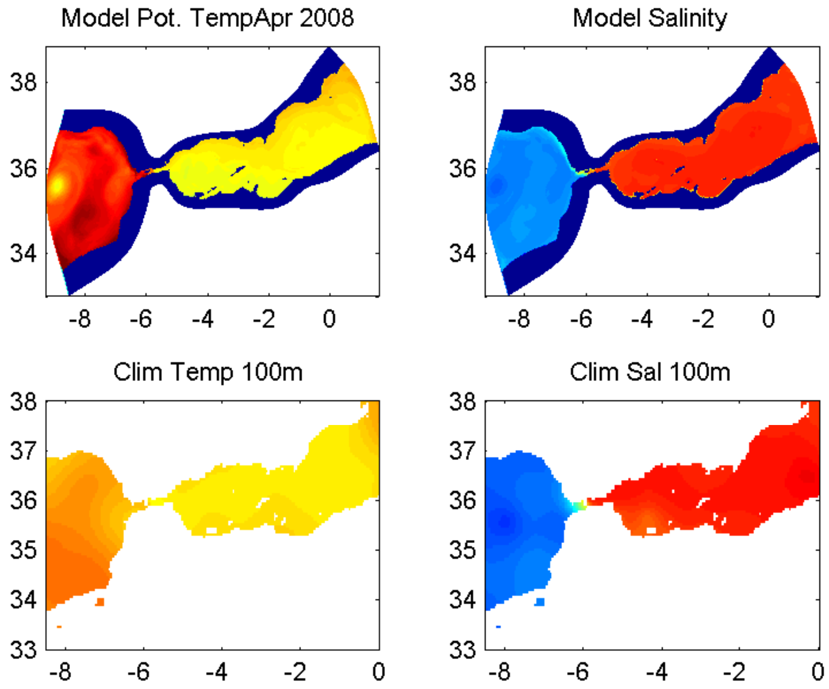
Model Pot. TempApr 2008
Model Salinity
Clim Temp 100m
Clim Sal 100m
38
36
34
-8
-6
-4
-2
0
38
37
36
35
34
33
-8
-6
-4
-2
0

(b) Apr

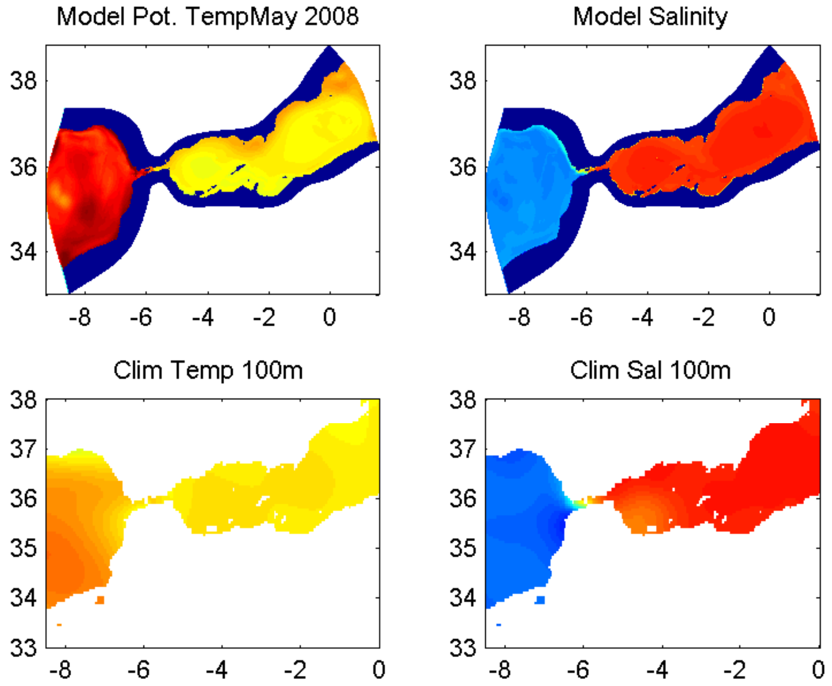
Model Pot. TempMay 2008
Model Salinity
Clim Temp 100m
Clim Sal 100m
38
36
34
-8
-6
-4
-2
0
38
37
36
35
34
33

(a) May

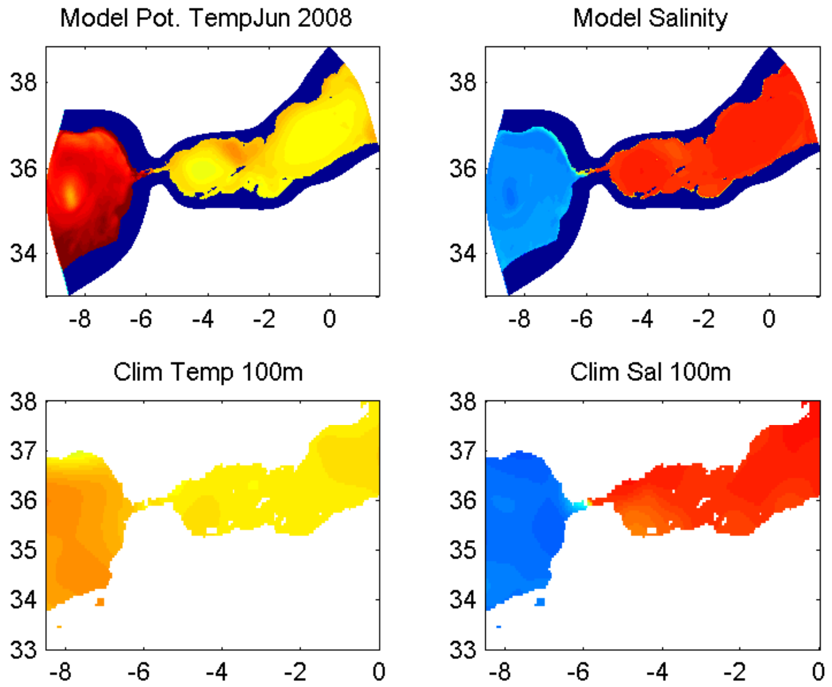
Model Pot. TempJun 2008
Model Salinity
Clim Temp 100m
Clim Sal 100m
38
36
34
-8
-6
-4
-2
0
38
37
36
35
34
33

(b) Jun

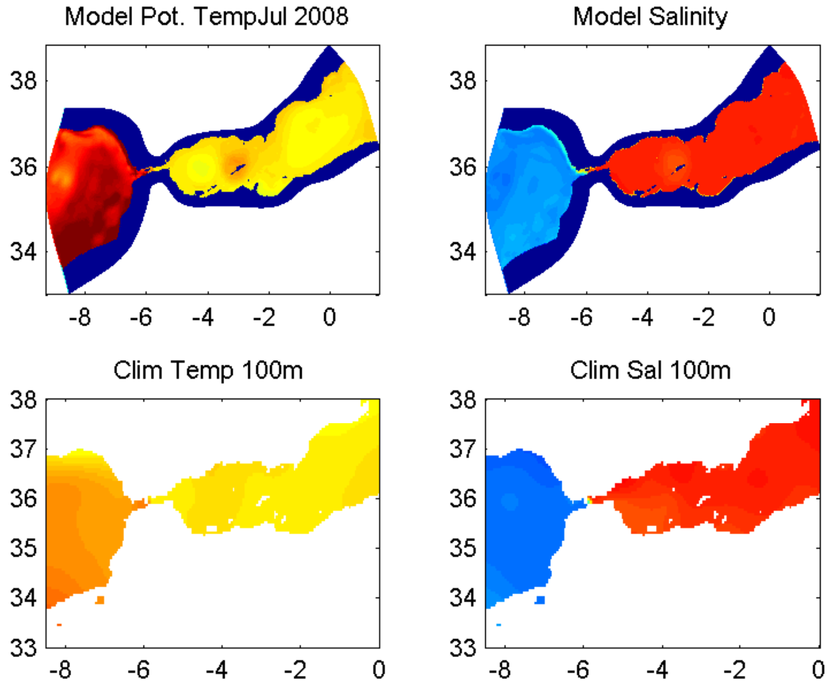
Model Pot. TempJul 2008
Model Salinity
Clim Temp 100m
Clim Sal 100m
38
36
34
-8
-6
-4
-2
0
37
35
33

(a) Jul

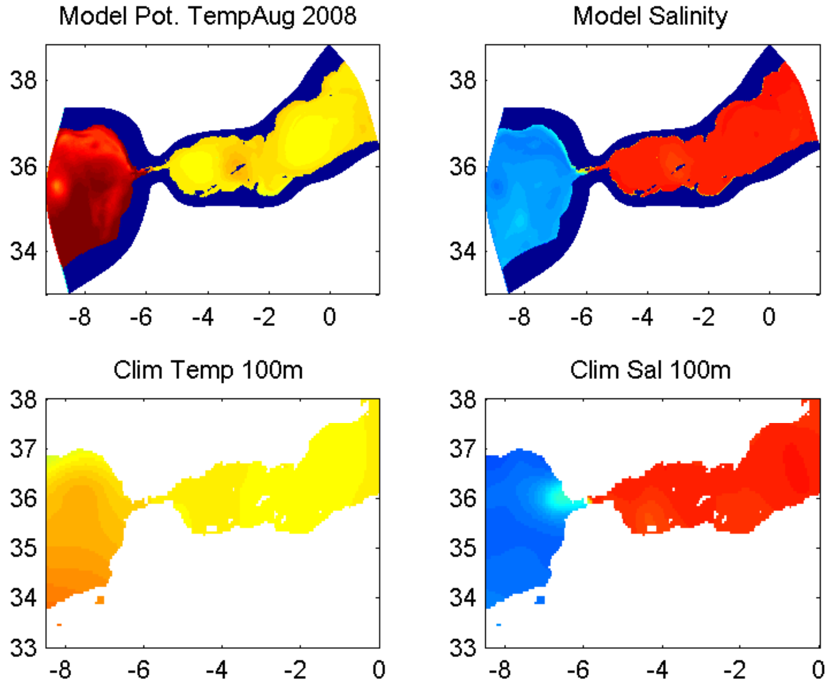
Model Pot. TempAug 2008
Model Salinity
Clim Temp 100m
Clim Sal 100m
38
36
34
-8
-6
-4
-2
0
37
35
33

(b) Aug

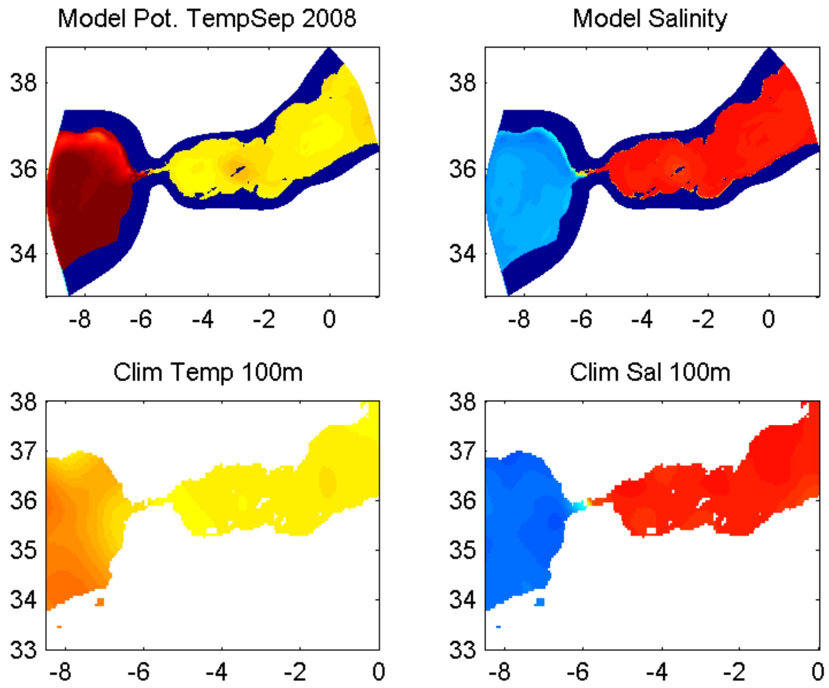
Model Pot. TempSep 2008
Model Salinity
Clim Temp 100m
Clim Sal 100m
38
36
34
-8
-6
-4
-2
0
38
37
36
35
34
33

(a) Sep

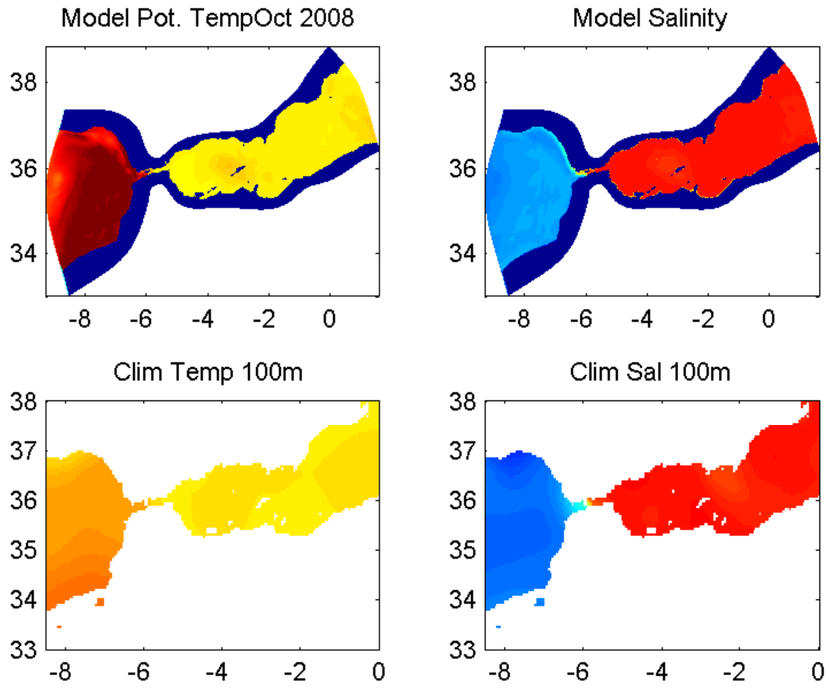
Model Pot. TempOct 2008
Model Salinity
Clim Temp 100m
Clim Sal 100m
38
36
34
-8
-6
-4
-2
0
38
37
36
35
34
33

(b) Oct

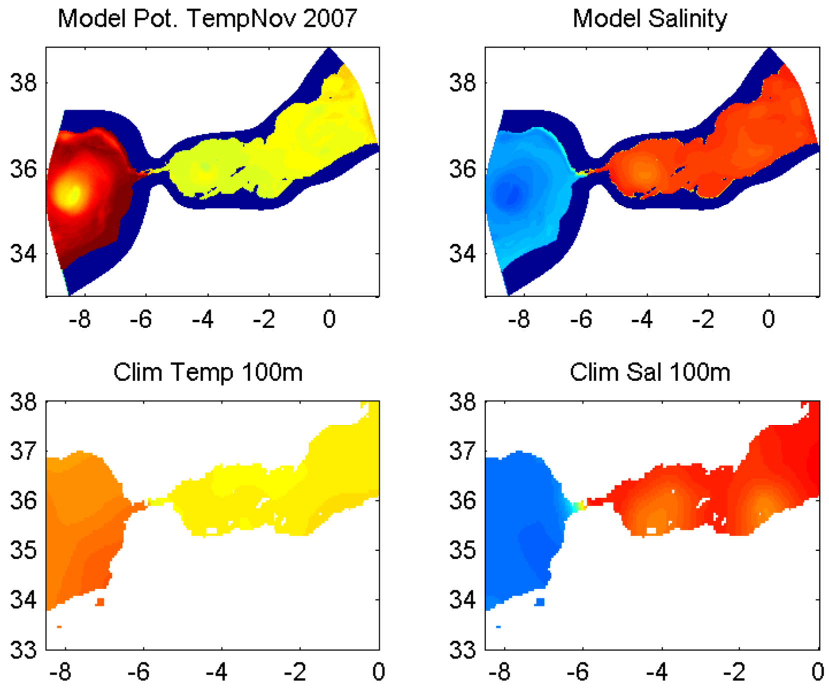

(a) Nov 2007

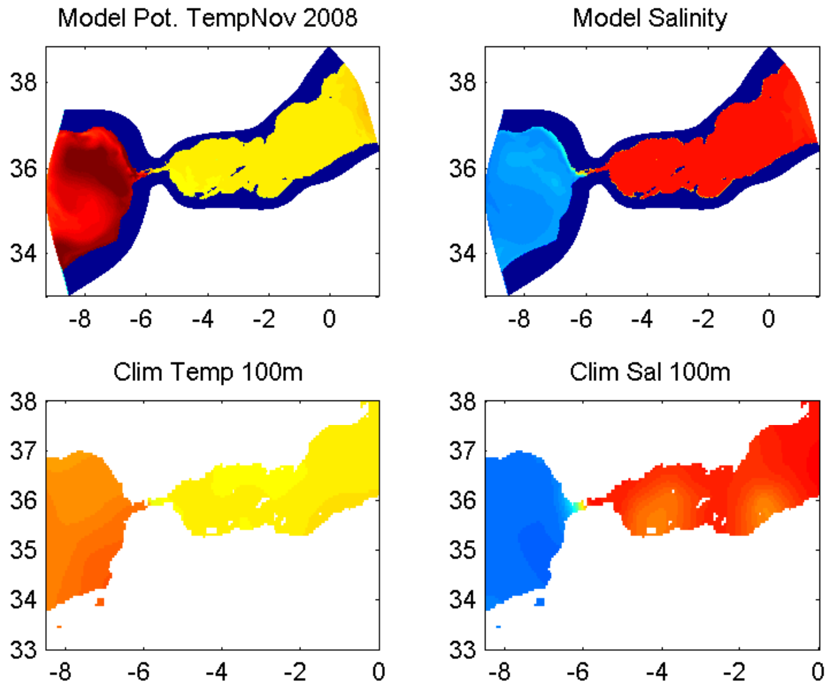

(b) Nov 2008

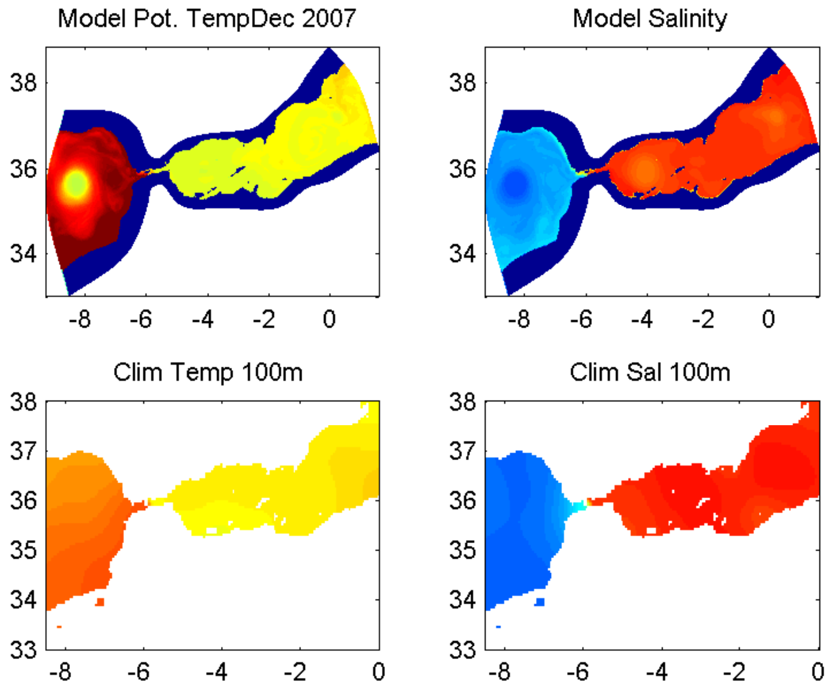

(a) Dec 2007

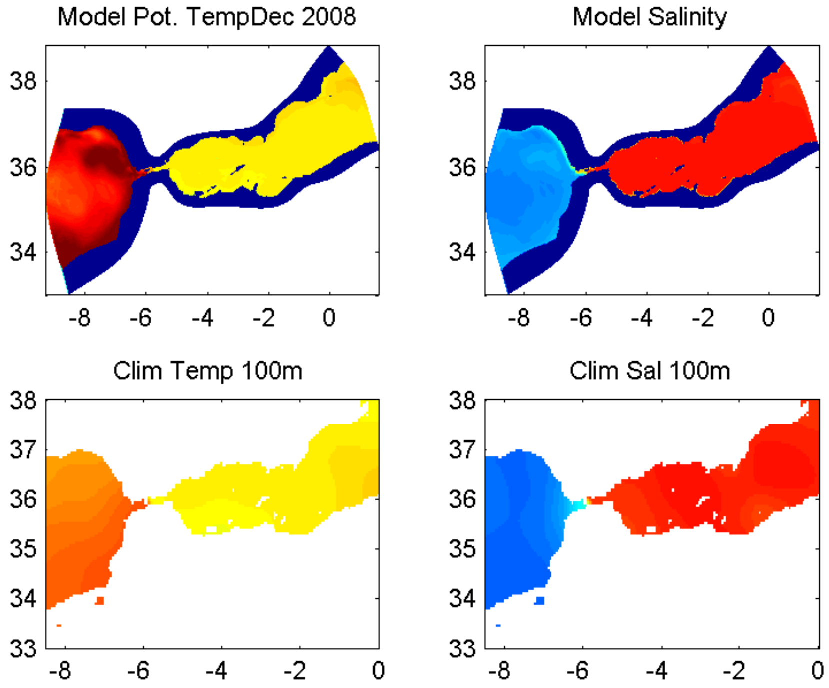

(b) Dec 2008

B.1.3 400m depth

Temperature images have a colorbar range of 9 (dark blue) to 14 (dark red), which is the potential temperature from the model and the *in-situ* temperature from climatology. Salinity images have a colorbar range of 35 (dark blue) to 39 (dark red) in practical salinity units.

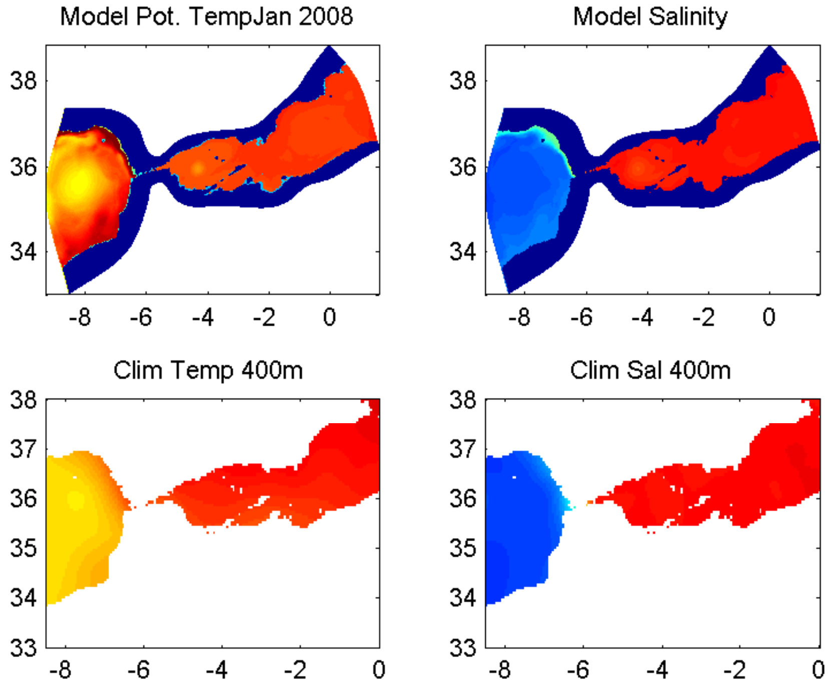
Model Pot. TempJan 2008
Model Salinity
Clim Temp 400m
Clim Sal 400m
38
36
34
-8
-6
-4
-2
0
38
37
36
35
34
33

(a) Jan

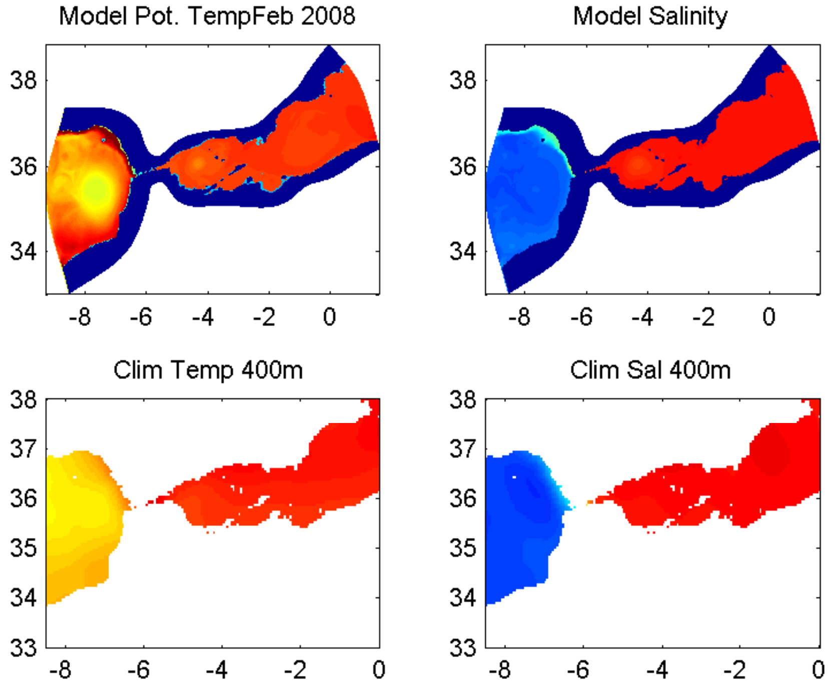
Model Pot. TempFeb 2008
Model Salinity
Clim Temp 400m
Clim Sal 400m
38
36
34
-8
-6
-4
-2
0
38
37
36
35
34
33

(b) Feb

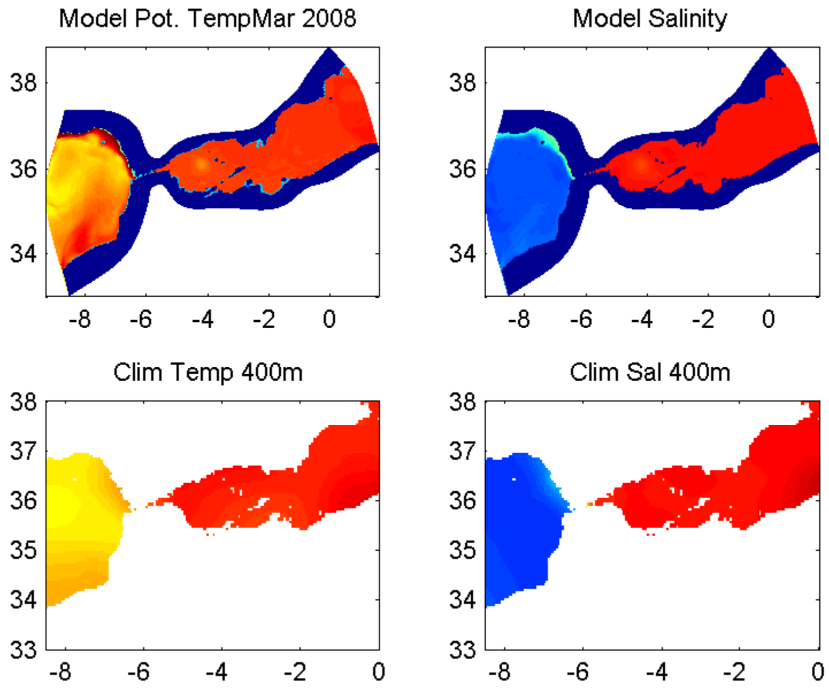
Model Pot. TempMar 2008
Model Salinity
38
36
34
-8
-6
-4
-2
0
Clim Temp 400m
Clim Sal 400m
38
37
36
35
34
33
-8
-6
-4
-2
0

(a) Mar

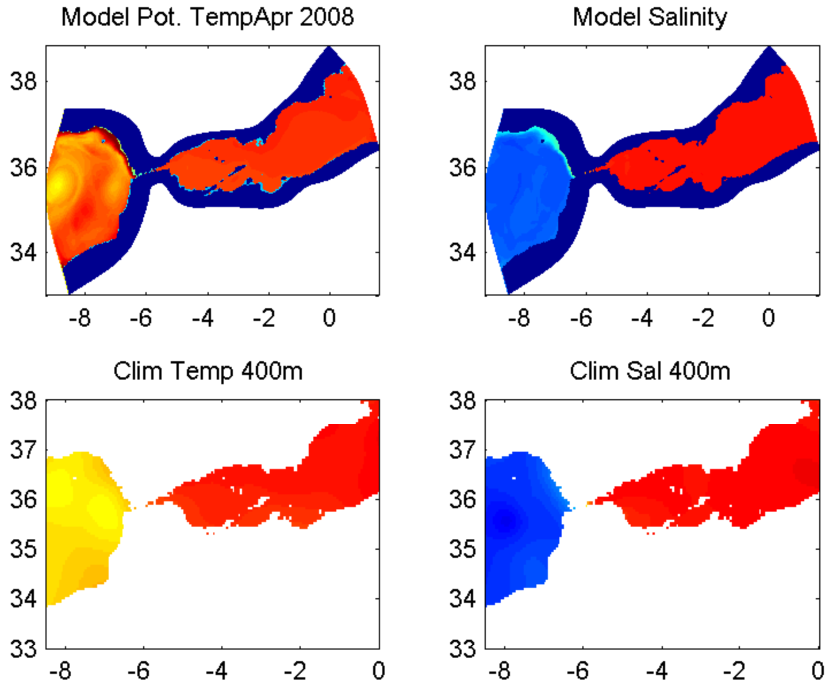
Model Pot. TempApr 2008
Model Salinity
38
36
34
-8
-6
-4
-2
0
Clim Temp 400m
Clim Sal 400m
38
37
36
35
34
33
-8
-6
-4
-2
0

(b) Apr

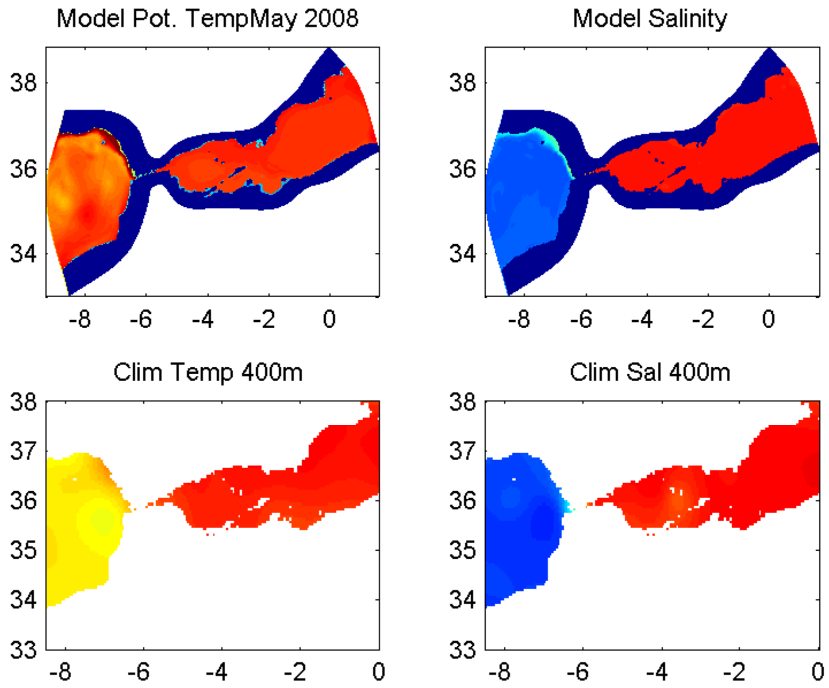
Model Pot. TempMay 2008
Model Salinity
Clim Temp 400m
Clim Sal 400m
38
36
34
-8
-6
-4
-2
0
38
37
36
35
34
33

(a) May

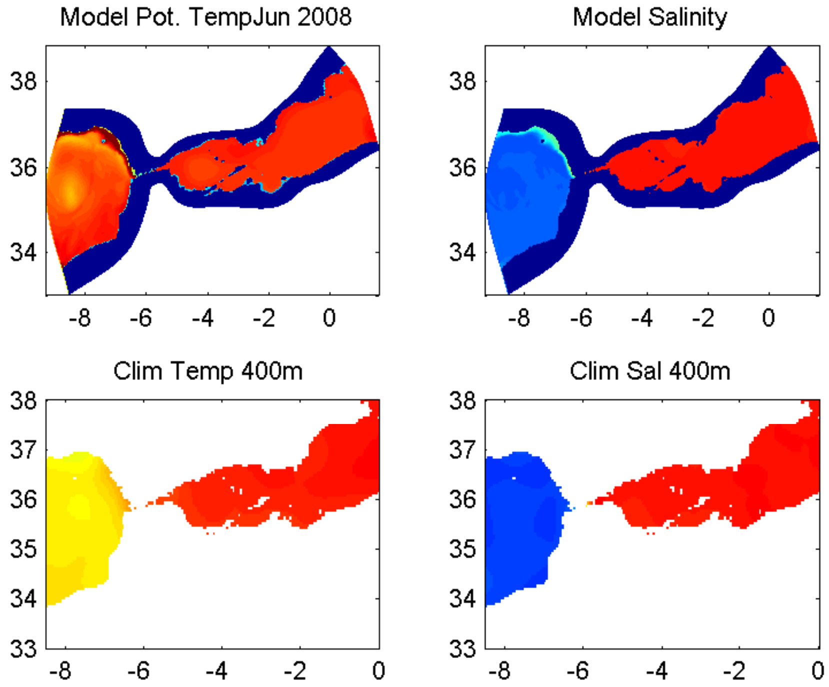
Model Pot. TempJun 2008
Model Salinity
Clim Temp 400m
Clim Sal 400m
38
36
34
-8
-6
-4
-2
0
38
37
36
35
34
33

(b) Jun

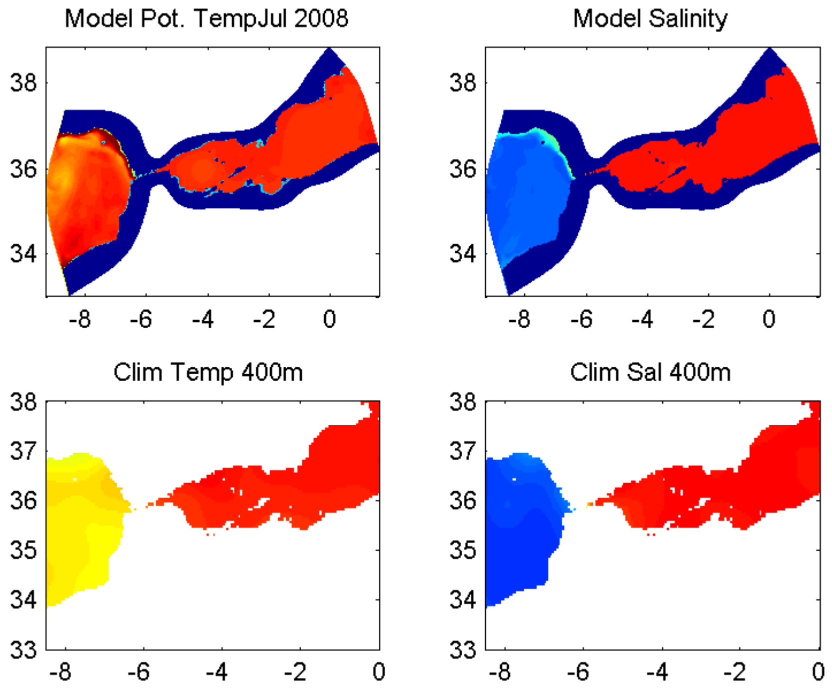
Model Pot. TempJul 2008
Model Salinity
Clim Temp 400m
Clim Sal 400m
38
36
34
-8
-6
-4
-2
0
38
37
36
35
34
33

(a) Jul

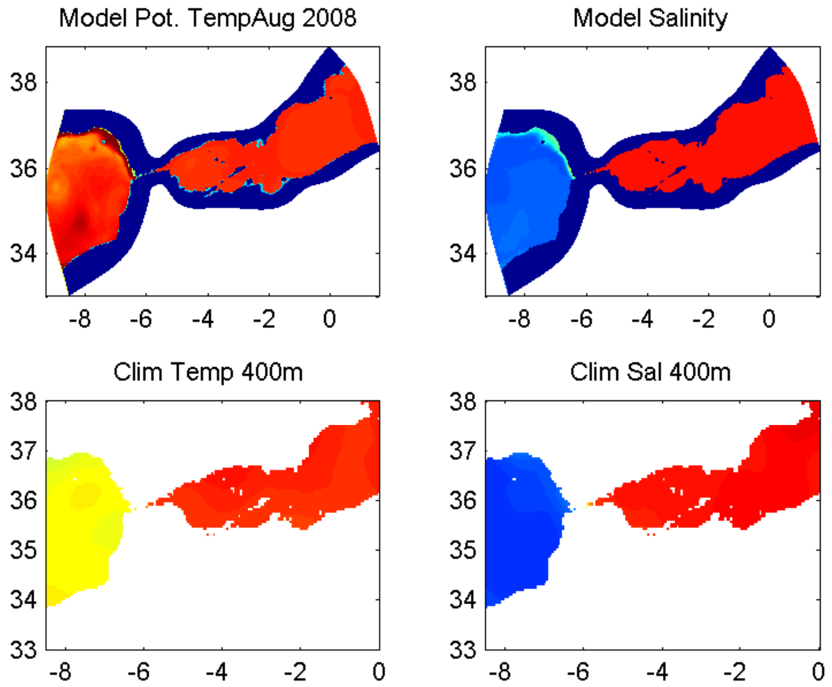
Model Pot. TempAug 2008
Model Salinity
Clim Temp 400m
Clim Sal 400m
38
36
34
-8
-6
-4
-2
0
38
37
36
35
34
33

(b) Aug

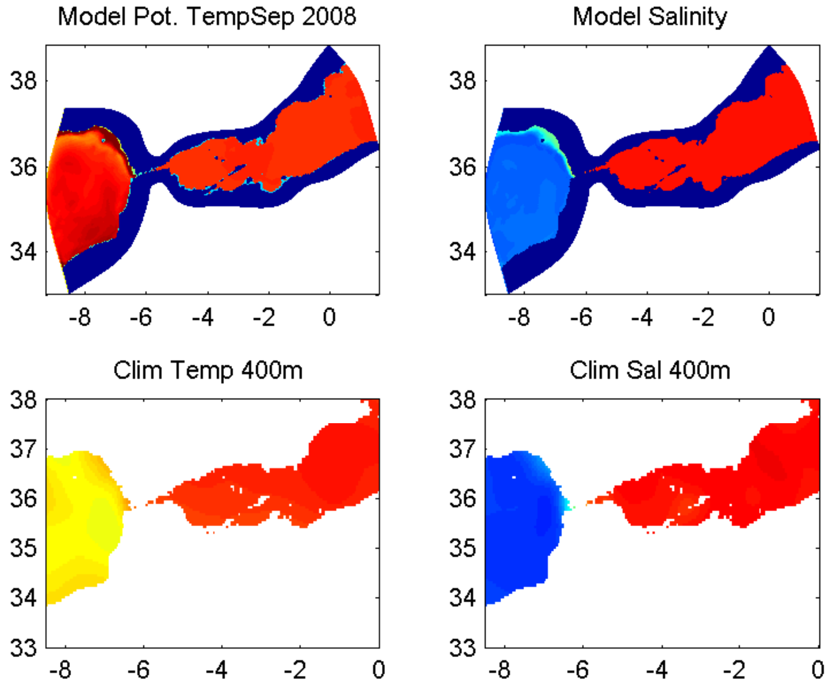
Model Pot. TempSep 2008
Model Salinity
Clim Temp 400m
Clim Sal 400m
38
36
34
-8
-6
-4
-2
0
33
34
35
36
37
38

(a) Sep

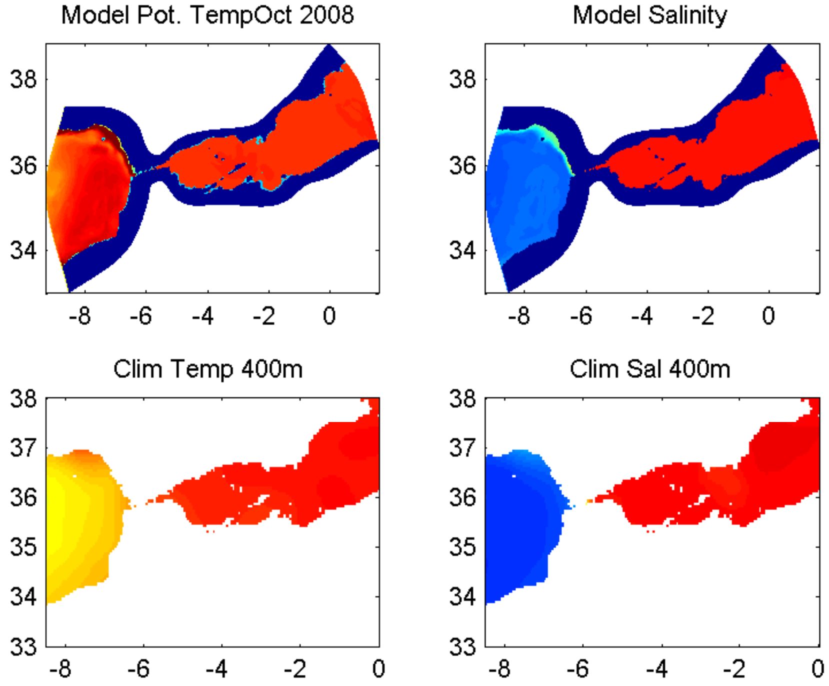
Model Pot. TempOct 2008
Model Salinity
Clim Temp 400m
Clim Sal 400m
38
36
34
-8
-6
-4
-2
0
33
34
35
36
37
38

(b) Oct

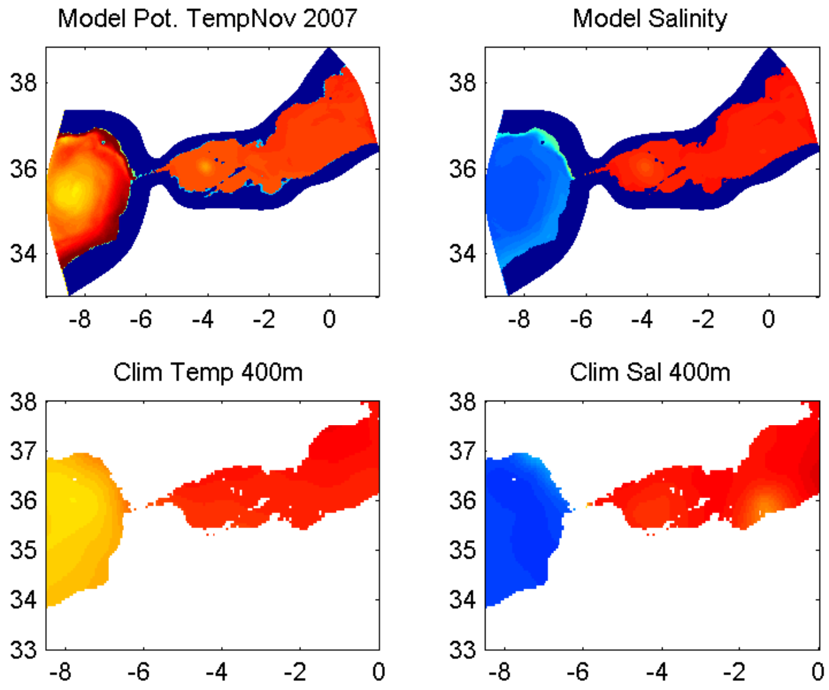

(a) Nov 2007

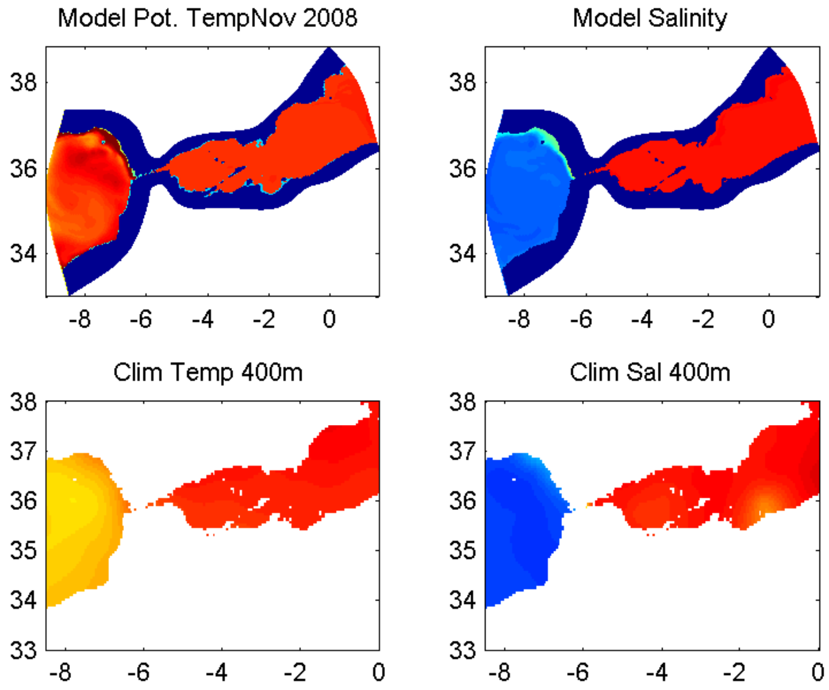

(b) Nov 2008

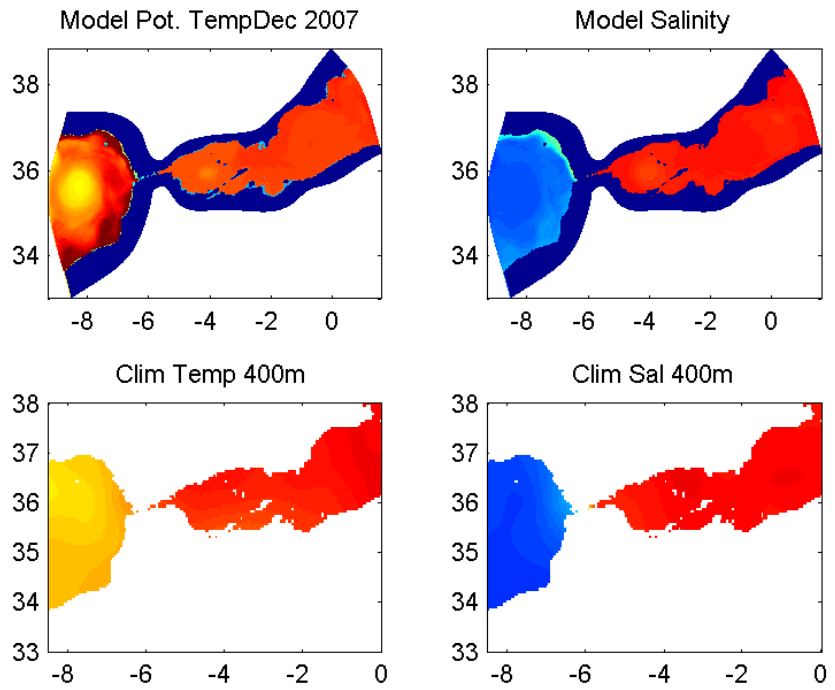

(a) Dec 2007

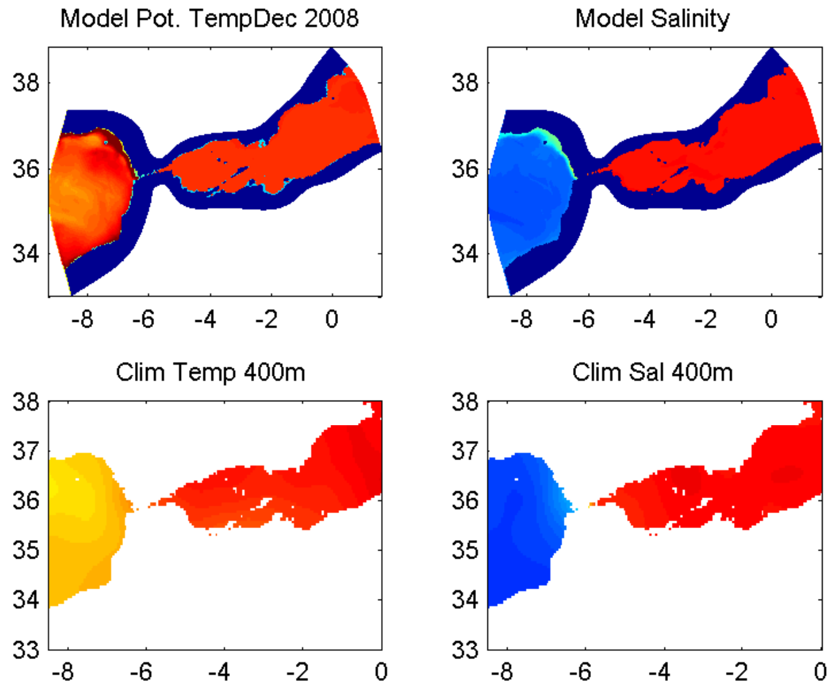

(b) Dec 2008

B.1.4 1000m depth

Temperature images have a colorbar range of 7 (dark blue) to 13.5 (dark red), which is the potential temperature from the model and the *in-situ* temperature from climatology. Salinity images have a colorbar range of 34 (dark blue) to 39.5 (dark red) in practical salinity units.

B.2 MITgcm Eulerian Budget Methods

B.2.1 Overview

The Massachusetts Institute of Technology general circulation model (MITgcm) allows for the output to include diagnostics necessary to close the volume, momentum, temperature, and salinity budgets of the model grid cells. In this section, I will list the necessary diagnostics and describe how I use them to examine the balance of terms in those budgets and a vorticity budget for the Western Alboran Gyre. Details of these budgets can change with the configuration of the MITgcm, but the following descriptions should be useful for those starting their own work. The information contained here is consolidated from the MITgcm documentation, archives of the MITgcm user listserv, and “Heat and salt budget in MITgcm" by Abisek Chakraborty and Jean-Michel Campin.

B.2.2 Diagnostics

My model configuration has a 10-second timestep, and I am analyzing the daily-averaged fluxes for my budgets. This averaging time is much larger than the timestep, so I am not including diagnostics needed to account for the Adams-Bashforth time-stepping (advection scheme 33 for heat and salt). My model run does include surface forcing (EXF package) but does not include relaxation to known fields; it is also a hydrostatic run. Other packages used include KPP (turbulence closure) and OBCS (open boundary forcing).

All diagnostics to be saved out must be specified before the model run begins. An example of the *data.diagnostics* file to request one of the diagnostics to be saved is:

```
frequency(3) = 86400.,
fields(1,3) = ’momVort3 ’,
filename(3) = ’VORTave’,
```

where *momVort3* is the vertical component of vorticity, and files *VORTave* will contain daily-

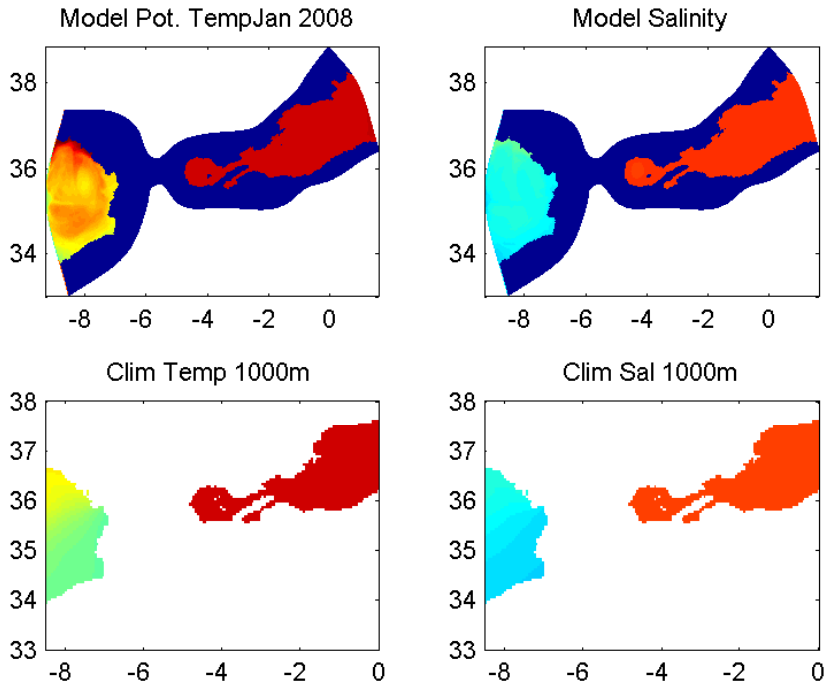
Model Pot. TempJan 2008

Model Salinity

Clim Temp 1000m

Clim Sal 1000m

(a) Jan

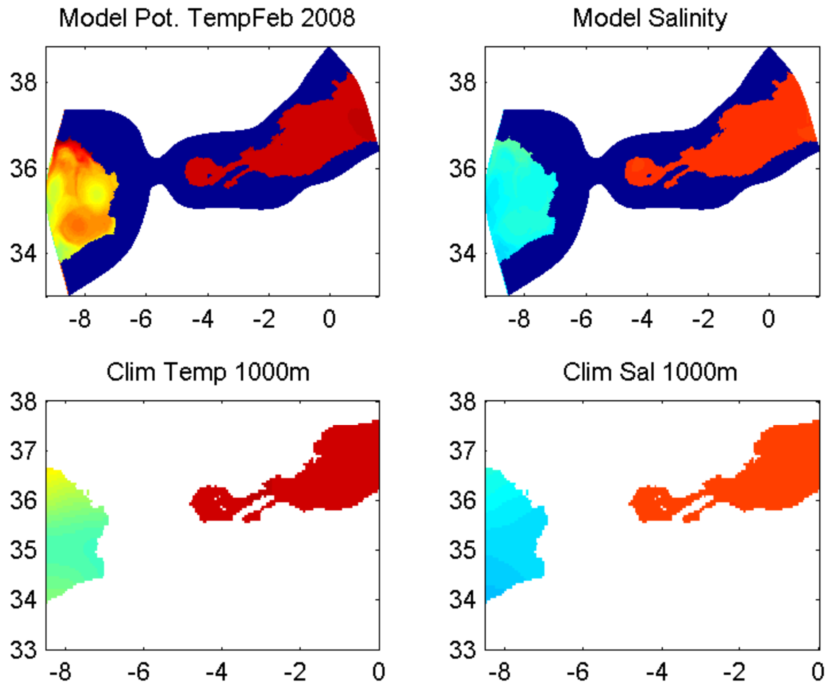
Model Pot. TempFeb 2008

Model Salinity

Clim Temp 1000m

Clim Sal 1000m

(b) Feb

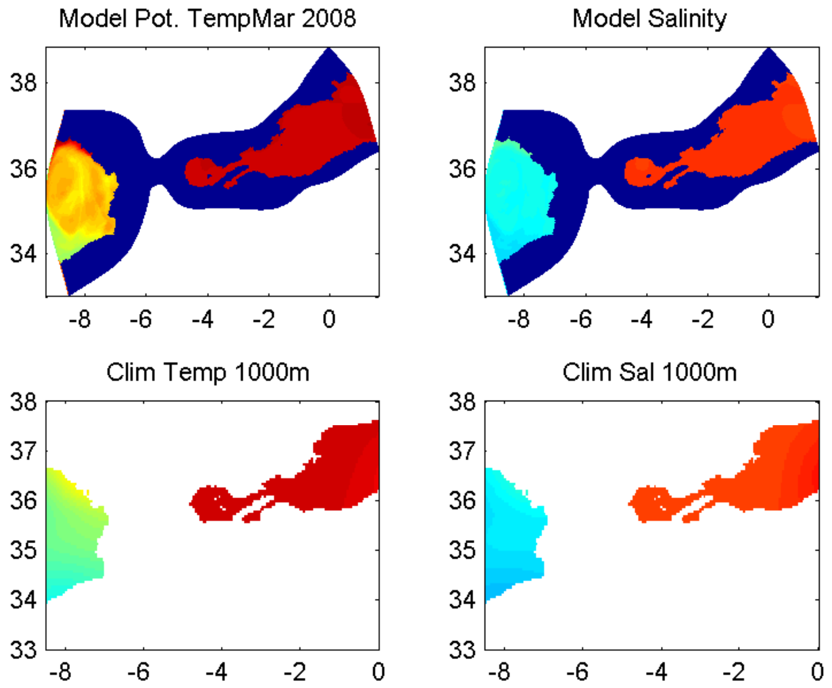
Model Pot. TempMar 2008
Model Salinity
Clim Temp 1000m
Clim Sal 1000m
38
36
34
-8
-6
-4
-2
0
38
37
36
35
34
33

(a) Mar

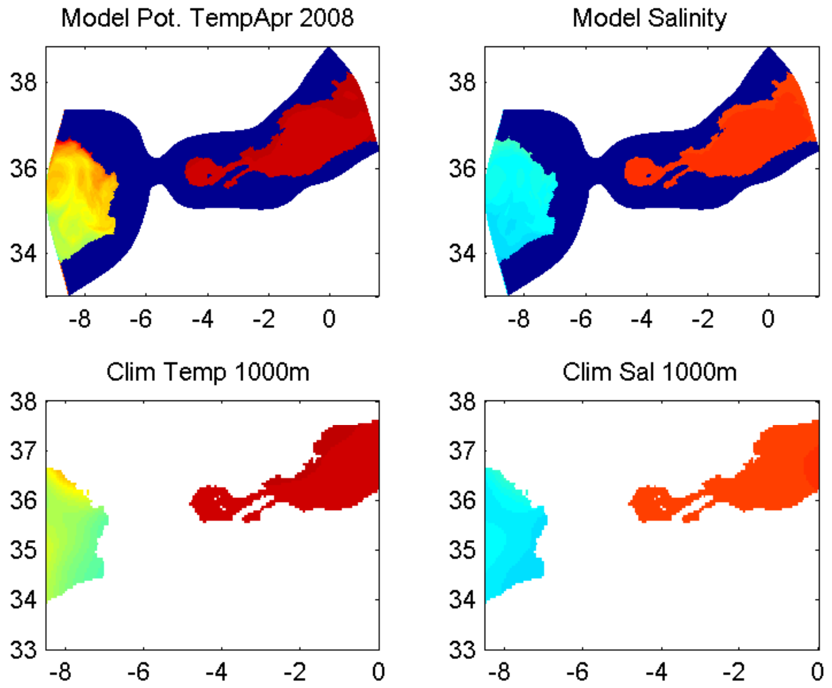
Model Pot. TempApr 2008
Model Salinity
Clim Temp 1000m
Clim Sal 1000m
38
36
34
-8
-6
-4
-2
0
38
37
36
35
34
33

(b) Apr

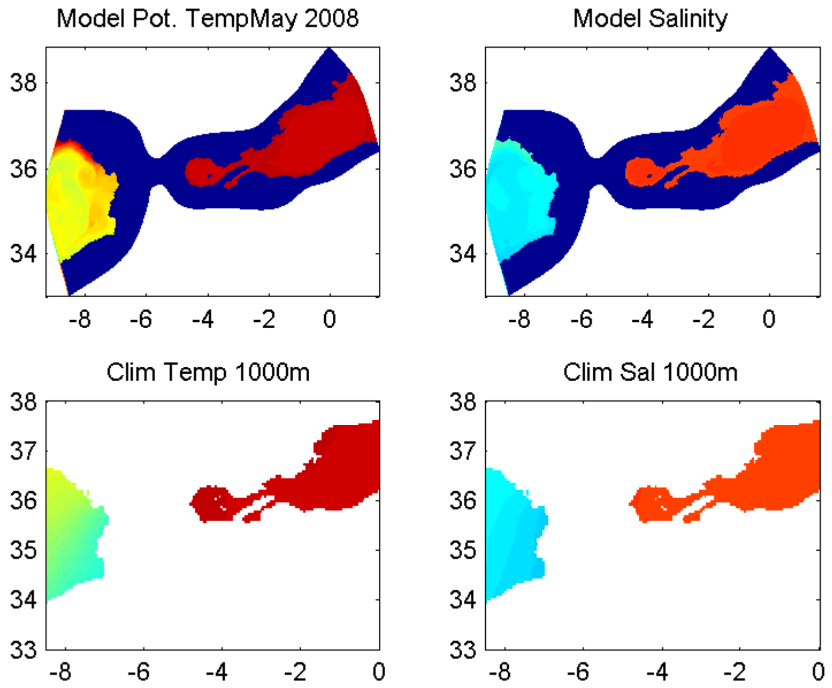
Model Pot. TempMay 2008
Model Salinity
Clim Temp 1000m
Clim Sal 1000m
38
36
34
-8
-6
-4
-2
0
38
37
36
35
34
33

(a) May

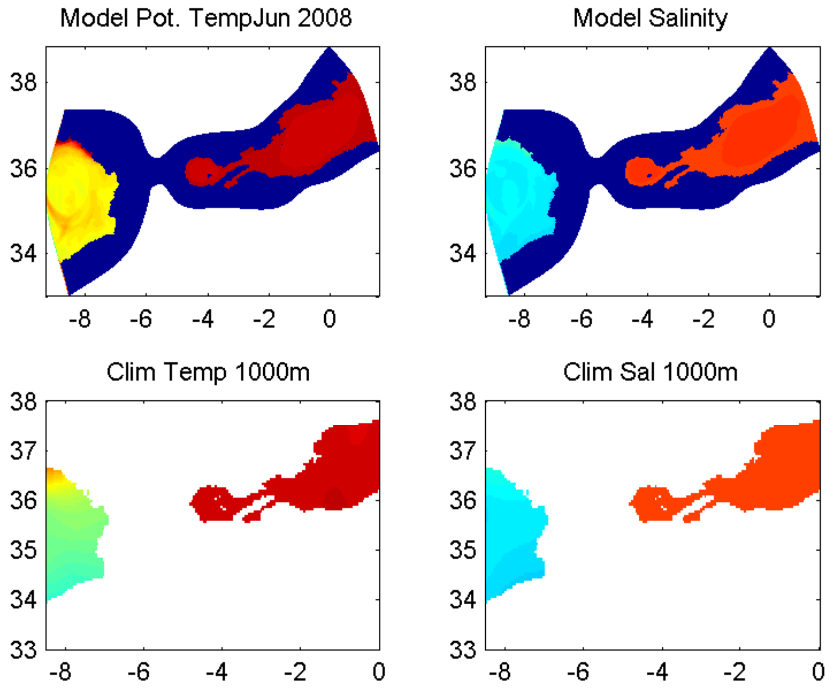
Model Pot. TempJun 2008
Model Salinity
Clim Temp 1000m
Clim Sal 1000m
38
36
34
-8
-6
-4
-2
0
38
37
36
35
34
33

(b) Jun

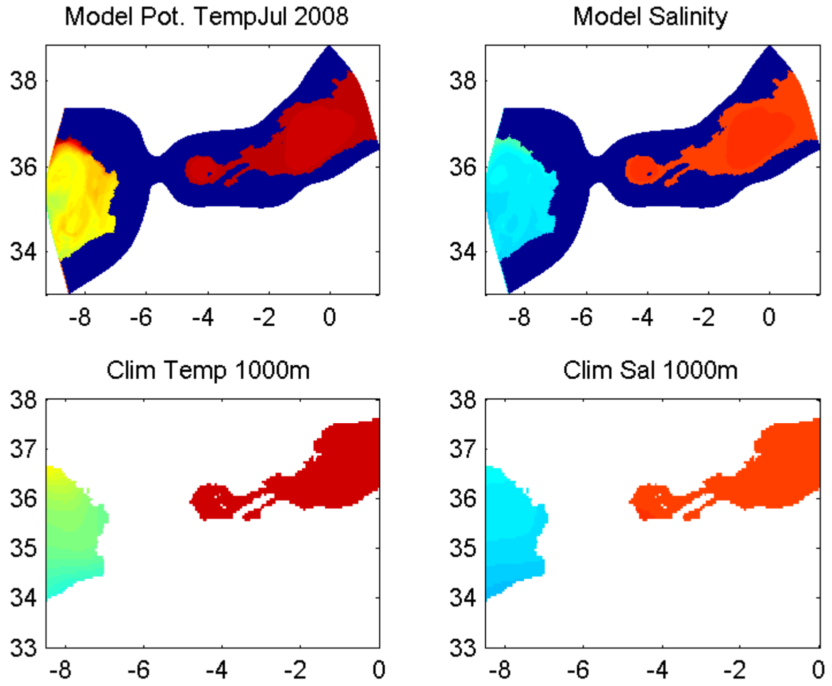
Model Pot. TempJul 2008
Model Salinity
Clim Temp 1000m
Clim Sal 1000m
38
36
34
-8
-6
-4
-2
0
38
37
36
35
34
33

(a) Jul

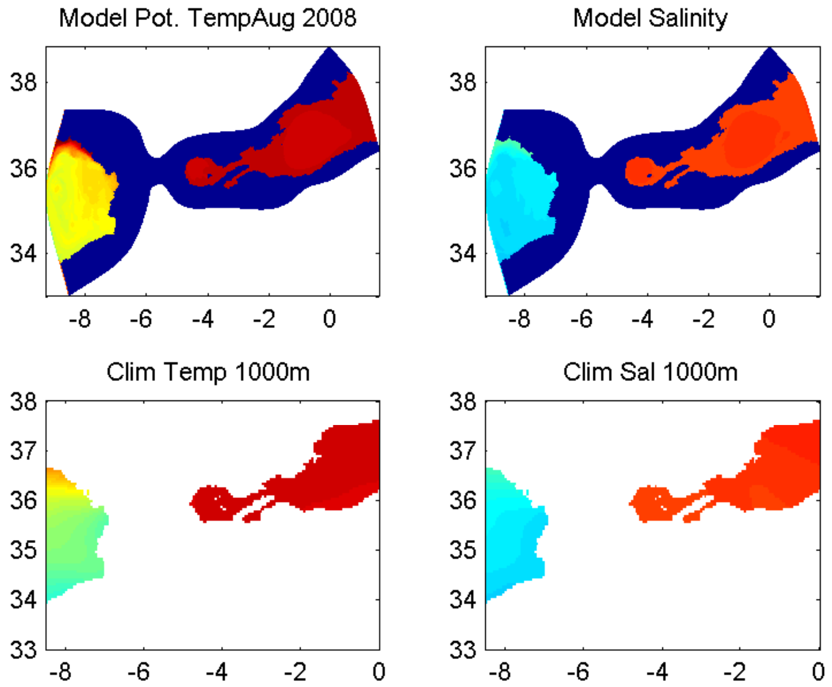
Model Pot. TempAug 2008
Model Salinity
Clim Temp 1000m
Clim Sal 1000m
38
36
34
-8
-6
-4
-2
0
38
37
36
35
34
33

(b) Aug

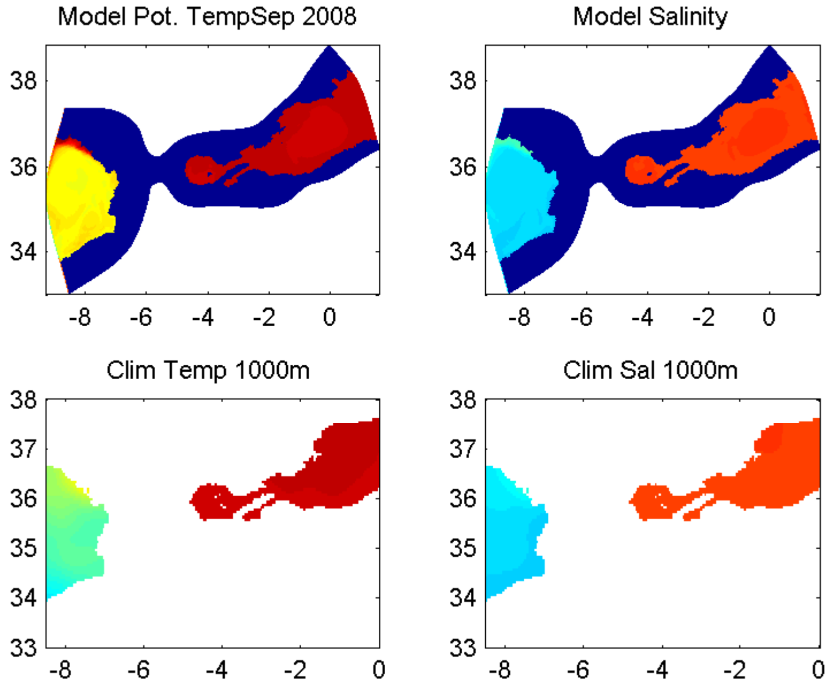
Model Pot. TempSep 2008
Model Salinity
Clim Temp 1000m
Clim Sal 1000m
38
36
34
-8
-6
-4
-2
0
38
37
36
35
34
33

(a) Sep

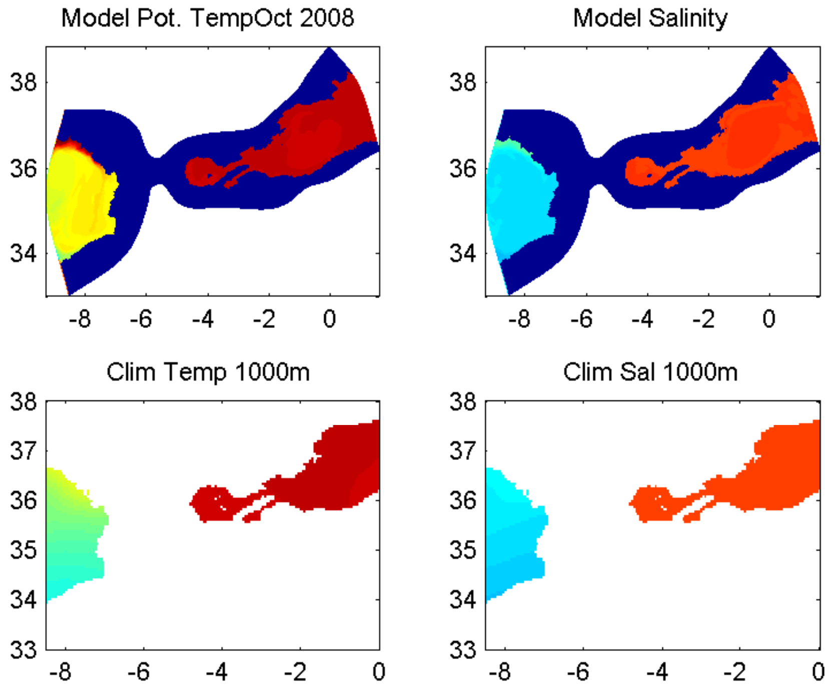
Model Pot. TempOct 2008
Model Salinity
Clim Temp 1000m
Clim Sal 1000m
38
36
34
-8
-6
-4
-2
0
38
37
36
35
34
33

(b) Oct

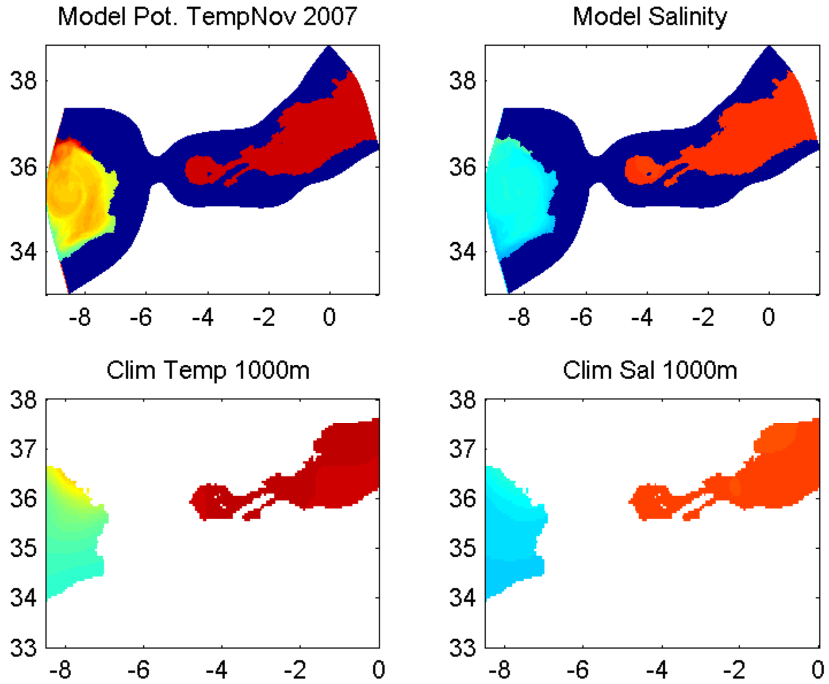

(a) Nov 2007

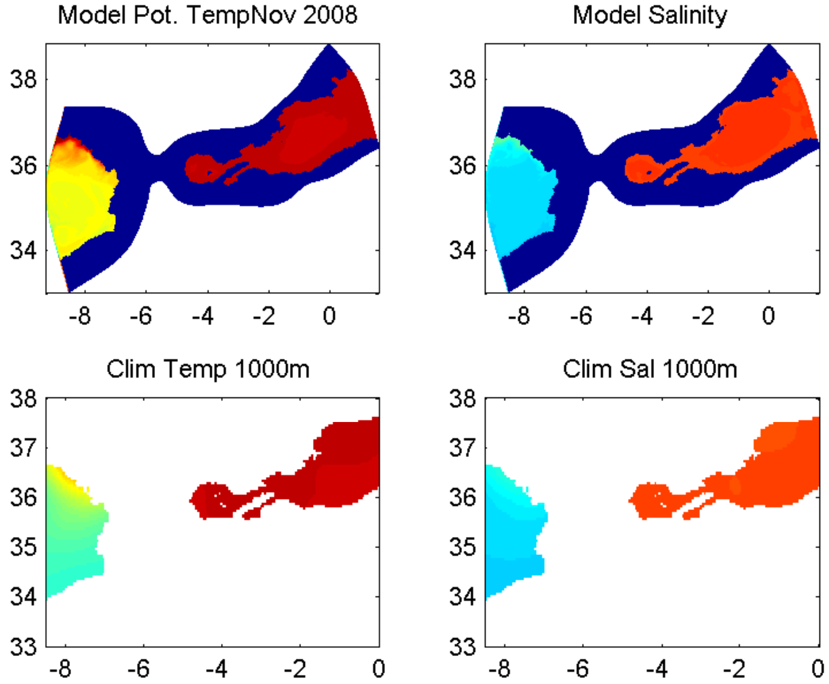

(b) Nov 2008

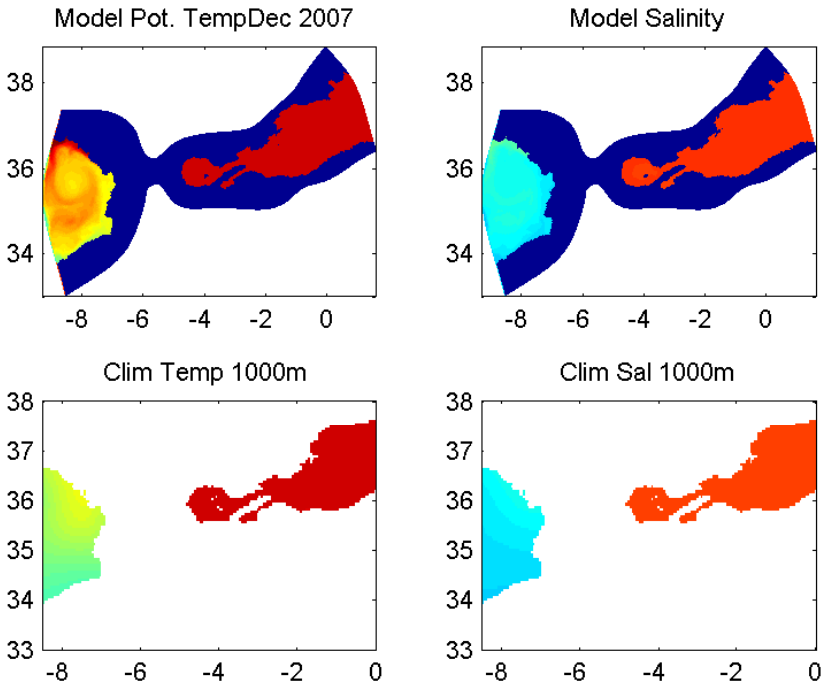

(a) Dec 2007

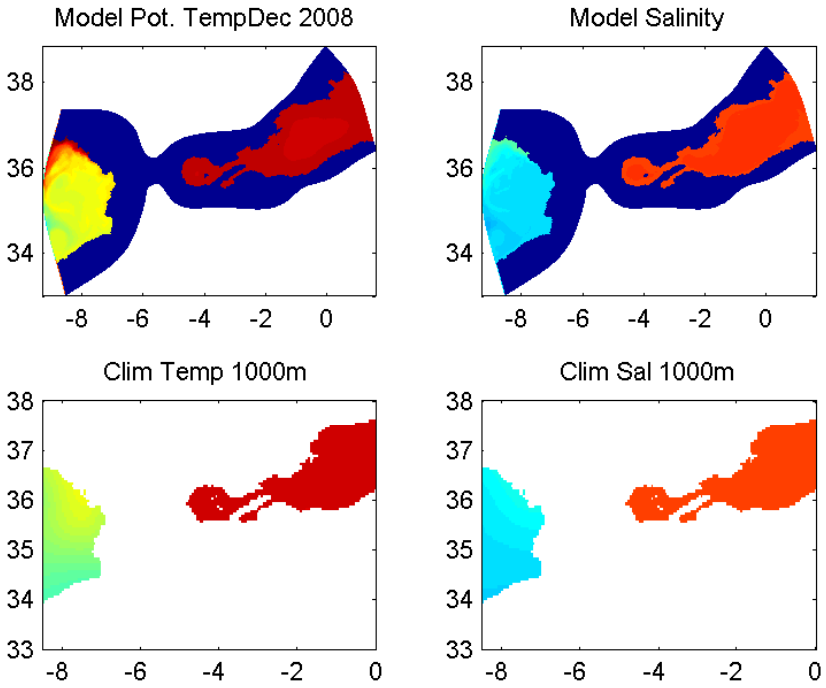

(b) Dec 2008

Table B.1: Table of diagnostic names and what they contain, plus grid measures needed for budgets and background stratifications.

Name	**Field**	**Units**
	Standard Diagnostics	
UVEL	Zonal velocity	m/s
VVEL	Meridional velocity	m/s
WVEL	Verical velocity	m/s
SALT	Salinity	psu
THETA	Potential Temperature	$\circ C$
RHOAnoma	Density Anomaly	kg/m^3
PHIHYD	Hydrostatic pressure potential anomaly	m^2/s^2
	Grid	
rAc	Temperature, salinity, vertical velocity (TSW) cell area	m^2
rAw	Zonal velocity cell area	m^2
rAs	Meridional velocity cell area	m^2
rAz	Vorticity cell areas	m^2
drF	Cell heights	m
hFacC	Portion of TSW cell height in water	m^2
hFacW	Portion of western edge of TSW cell height in water	m^2
hFacS	Portion of southern edge of TSW cell height in water	m^2
dxg	Zonal cell edge edge length	m
dyg	Meridional cell edge length	m
dxc	Zonal distance between TSW cell centers	m
dyc	Meridional distance between TSW cell centers	m
	Constants from *data* or *STDOUT*	
rhoConst	Background density	kg/m^3
CP	Specific heat	$J/kg \circ C$

average vorticity for each model cell.Table **??** lists the set of grid information and standard variables (e.g. temperature and salinity) that are needed for understanding the budgets. Table B.3 lists all the diagnostics needed to close the momentum (horizontal), vorticity (vertical), temperature, and salinity budgets.

Other useful diagnostics are UVEL, VVEL, WVEL, the velocity field; SALT, THETA, salinity and potential temperature; RHOAnoma, PHIHYD, density anomaly and pressure/density anomaly. A few other terms are needed: rhoConst and CP from your data file or STDOUT, and the grid distances and areas: rAc, rAw, rAs, drF, hFacC, hFacW, hFacS, dxg, dyg, dxc, dyc.

Table B.2: Table of diagnostic names and what they contain. This set of diagnostics can close the salinity and temperature budgets.

Name	**Field**	**Units**
	Change in Time	
TOTSTEND	Total salinity tendency	PSU/day
TOTTTEND	Total potential temperature tendency	$^\circ C/day$
	Advection	
ADVx_SLT	Zonal salinity advection	$PSUm^3/s$
ADVy_SLT	Meridional salinity advection	$PSUm^3/s$
ADVr_SLT	Vertical salinity advection	$PSUm^3/s$
ADVx_TH	Zonal potential temperature advection	$^\circ Cm^3/s$
ADVy_TH	Meridional potential temperature advection	$^\circ Cm^3/s$
ADVr_TH	Vertical potential temperature advection	$^\circ Cm^3/s$
WSLTMASS	Vertical velocity and salinity correlation	$PSUm/s$
WTHMASS	Vertical velocity and potential temperature correlation	$^\circ Cm/s$
	Mixing	
DFrI_SLT	Vertical implicit salinity diffusion	$PSUm^3/s$
DFrI_TH	Vertical implicit zonal potential temperature diffusion	$^\circ Cm^3/s$
DFrE_SLT	Vertical explicit salinity diffusion	$PSUm^3/s$
DFrE_TH	Vertical explicit zonal potential temperature diffusion	$^\circ Cm^3/s$
DFxE_SLT	Zonal salinity diffusion	$PSUm^3/s$
DFyE_SLT	Meridional salinity diffusion	$PSUm^3/s$
DFxE_TH	Zonal potential temperature diffusion	$^\circ Cm^3/s$
DFyE_TH	Meridional potential temperature diffusion	$^\circ Cm^3/s$
KPPg_SLT	Salinity flux due to vertical turbulence closure	$PSUm^3/s$
KPPg_TH	Potential temperature flux due to vertical turbulence closure	$^\circ Cm^3/s$
	Forcing	
oceFWflx	Surface freshwater flux	kg/m^2s
SFLUX	Surface salt flux, including effects of freshwater flux	gm^2/s
TFLUX	Surface heat flux	W/m^2
	Other	
SSH	Sea surface height	m
momHDiv	horizontal momentum divergence	s^{-1}

Table B.3: Table of diagnostic names and what they contain. This set of diagnostics can close the horizontal momentum and vertical vorticity budgets.

Name	**Field**	**Units**
	Change in Time	
TOTUTEND	Total zonal velocity tendency	$m/s/day$
TOTVTEND	Total meridional velocity tendency	$m/s/day$
	Advection	
Um_Advec	Zonal velocity tendency due to advection of momentum	m/s^2
Vm_Advec	Meridional velocity tendancy due to advection of momentum	m/s^2
	Mixing	
VISrI_Um	Vertical implicit zonal momentum diffusion	m^4/s^2
VISrI_Vm	Vertical implicit meridional momentum diffusion	m^4/s^2
Um_Diss	Horizontal diffusion and drag of zonal momentum	m/s^2
Vm_Diss	Horizontal diffusion and drag of meritional momentum	m/s^2
UBotDrag	Bottom drag of zonal momentum	m/s^2
VBotDrag	Bottom drag of meritional momentum	m/s^2
USidDrag	Side drag of zonal momentum	m/s^2
VSidDrag	Side drag of meritional momentum	m/s^2
	Forcing	
Um_Ext	Zonal velocity tendency due to wind	m/s^2
Vm_Ext	Meridional velocity tendency due to wind	m/s^2
	Other	
Um_Cori	Zonal velocity tendency due to Coriolis term	m/s^2
Vm_Cori	Meridional velocity tendency due to Coriolis term	m/s^2
Um_dPHdx	Zonal velocity tendency due to pressure gradient term	m/s^2
Vm_dPHdy	Meridional velocity tendency due to pressure gradient term	m/s^2
momVort3	Vertical component of vorticity	s^{-1}

B.2.3 Budget Terms

Volume Budget

The volume budget is the simplest of the budgets I discuss. The model grid is aligned such that velocities are defined at the centers of cell faces, allowing the velocity multiplied by the area of the face to be the total transport through that face. For a single cell, the volume budget is

$$\begin{aligned}\frac{dV(xi,yi,zi)}{dt} &= UVEL(xi-1,yi,zi)*hFacW(xi-1,yi,zi)*drF(zi)*dyg(xi-1,yi)\\ &- UVEL(xi,yi,zi)*hFacW(xi,yi,zi)*drF(zi)*dyg(xi,yi)\\ &+ VVEL(xi,yi-1,zi)*hFacS(xi,yi-1,zi)*drF(zi)*dxg(xi,yi-1)\\ &- VVEL(xi,yi,zi)*hFacS(xi,yi,zi)*drF(zi)*dxg(xi,yi)\\ &+ WVEL(xi,yi,zi-1)*rAc(xi,yi) - WVEL(xi,yi,zi)*rAc(xi,yi)\\ &+ oceFWflx*rAc(xi,yi,1)/rhoConst.\end{aligned}$$

The change in volume will be zero for all below-surface cells. At the surface, the change in volume is due to sea-surface height changes. The surface is also the only place where the fresh-water flux, $oceFWflx$, is defined. Depending on whether the surface is linear or nonlinear, at the surface, the horizontal fluxes may need to have SSH added to drF.

Horizontal Momentum

The physical horizontal momentum equations are:

$$\frac{\partial u}{\partial t} + \vec{u}\nabla u - fv = \frac{1}{\rho}\frac{\partial P}{\partial x} + \nu\nabla^2 u + F_x,$$

$$\frac{\partial v}{\partial t} + \vec{u}\nabla v + fu = \frac{1}{\rho}\frac{\partial P}{\partial y} + \nu\nabla^2 v + F_y,$$

where u and v are the eastward and northward velocities, $\vec{u}$ is the three-dimenstional velocity vector, t is time, f is the coriolis parameter, ρ is density, P is (hydrostatic) pressure, ν is viscosity, and $\vec{F}$

is forcing. Numerical budgets for horizontal momentum contain the same terms:

$$U\_tend = Um\_Advec + UPress\_tend + UDif\_tend + UDiss + Um\_Ext,$$

$$V\_tend = Vm\_Advec + VPress\_tend + VDif\_tend + VDiss + Vm\_Ext,$$

where each term is in the same order as the physical equation term. The advection term includes coriolis, but the coriolis alone is also a diagnostic, so the two can be separated if desired. The diffusion terms are vertical diffusion $UDif\_tend$ and dissipation, which includes horizontal diffusion as well as bottom and side drag. Bottom and side drag are available as separate diagnostics too, so these could be separated if desired. The first, fourth, and last terms on the right hand side are diagnostics. The $\_tend$ terms are calculated from diagnostics as follows:

$$\begin{aligned}
U\_tend &= TOTUTEND/86400,\\
V\_tend &= TOTVTEND/86400,\\
UPress\_tend &= Um\_dPHdx - g(SSH(xi+1, yi) - SSH(xi, yi))/dxc,\\
VPress\_tend &= Vm\_dPHdy - g(SSH(xi, yi+1) - SSH(xi, yi))/dyc,\\
UDif\_tend &= Um\_Diss + (VISrI\_Um(xi, yi, zi+1) - VISrI\_Um(xi, yi, zi))/(rAw * drF * hFacW),\\
VDif\_tend &= Vm\_Diss + (VISrI\_Vm(xi, yi, zi+1) - VISrI\_Vm(xi, yi, zi))/(rAs * drF * hFacS).
\end{aligned}$$

All zonal terms are defined at the center of the western edge of temperature/salinity/vertical velocity (TSW) cells. All meridional terms are defined at the center of the southern edge of TSW cells. To integrate momentum over a volume comprised of many TSW cells, multiply each term by the volume of the cell they are the center of. For zonal momentum terms, this is the western cell:

$$cellVolW = rAw * drF * hFacW,$$

while for meridional momentum terms, this is the southern cell:

$$cellVolS = rAs * drF * hFacS.$$

Vorticity

Vertical vorticity is the curl of the horizonal velocity, and the vertical vorticity equation can be derived from the curl of the horizontal momentum equations. The physical vertical vorticity equation is

$$\frac{\partial \zeta}{\partial t} + \vec{u} \cdot \nabla \zeta + f \nabla \cdot \vec{u}_h + \beta v = \frac{1}{\rho^2}(\nabla P \times \nabla \rho) + \nu \nabla^2 \zeta + \nabla \times \vec{F},$$

where ζ is relative vorticity and β is the meridional derivative of the coriolis parameter. The numerical budget is the curl of the horizontal momentum budgets, so it is defined at the corners of TSW cells. For a vorticity budget integrated over some volume of vorticity cells, Stoke's theorem means one can take an integral of the momentum components around the edge of cells rather than taking the curl of them and doing an area integral. The curl of the SSH component of $Press\_tend$ will be zero, but all other terms will persist. Forming the vertical relative vorticity budget requires using Stokes' theorem on each horizontal layer, being certain that only wet edges are used (check $hFacS$ and $hFacS$). For each layer of the volume, identify the edges of the area to be integrated over and create a logical that identifies them. I call these logicals *openN* for northern edges, *openE* for eastern edges, and the equivalent for southern and western. Then terms in the vorticity budget equivalent to those in the momentum budgets can be calculated in the same way as the tendency term,

$$\begin{aligned} \zeta\_tend =& U\_tend(openN) * dxc(openN) - U\_tend(openS) * dxc(openS) \\ &+ V\_tend(openE) * dyc(openE) - V\_tend(openW) * dxc(openW). \end{aligned}$$

Note that the pressure term can be calculated using Um_dPHdx and Vm_dPHdy without adding the SSH component, and will be the baroclinic pressure effect, the $\frac{1}{\rho^2}(\nabla P \times \nabla \rho)$ in the physical equation. The calculation is shown for a single layer, and the total over the volume requires each layer to be multiplied by drF before summing. Then the numerical budget will have terms

$$\zeta\_tend = \zeta\_Advec + \zeta\_Press + \zeta\_Dif\_tend + \zeta\_Diss + \zeta\_Ext.$$

As with the momentum budgets, it is possible to separate the coriolis from the advection term and the drags and horizontal diffusion from the dissipation term. To do so, one would calculate the listed terms, then perform the same calculation for the coriolis, bottom drag, and side drag, and subtract the timeseries found from the advection or dissipation term.

Salinity and Potential Temperature

The terms in the salinity and potential temperature, or salt and heat, budgets are the same. In the following, I will use C to represent SLT or TH in diagnostics names, and c for tracer concentration in equations. The physical tracer budget equation is:

$$\frac{\partial c}{\partial t} + \vec{u}\nabla c = \nabla \kappa \nabla c + \vec{F},$$

where $\vec{u}$ is velocity, κ is diffusivity, and $\vec{F}$ includes sources and sinks. The numerical tracer budget is:

$$C\_tend = Adv\_tend\_C + Dif\_tend\_C + Surf\_tend\_C,$$

where *tend* means tendency, and the terms adding up to the change in concentration of a cell are advection, diffusion (including mixing from turbulence closure), and surface forcing (including mass corrections due to a linear free surface approximation). The correspondence between the physical and numerical budgets is term-by-term, except that the mixing from the turbulence closure scheme in Dif_tend would be equivalent to a variable κ. Each of the terms in the numerical budget is calculated from the diagnostics in table B.3 as follows:

$$\begin{aligned}
C\_tend &= TOTCTEND/86400,\\
Adv\_tend\_C &= [(ADVr\_C(ix,iy,iz+1) - ADVr\_C(ix,iy,iz))/CellVol+\\
&\quad (ADVx\_C(ix+1,iy,iz) - ADVx\_C(ix,iy,iz))/CellVol+\\
&\quad (ADVy\_C(ix,iy+1,iz) - ADVy\_C(ix,iy,iz))/CellVol],\\
Dif\_tend\_C &= [(DFrE\_C(ix,iy,iz+1) - DFrE\_C(ix,iy,iz))/CellVol+\\
&\quad (DFrI\_C(ix,iy,iz+1) - DFrI\_C(ix,iy,iz))/CellVol+\\
&\quad (KPPg\_C(ix,iy,iz+1) - KPPg\_C(ix,iy,iz))/CellVol+\\
&\quad (DFxE\_C(ix+1,iy,iz) - DFxE\_C(ix,iy,iz))/CellVol+\\
&\quad (DFyE\_C(ix,iy+1,iz) - DFyE\_C(ix,iy,iz))/CellVol],\\
Surf\_tend\_C &= CFLUX(ix.iy)/(rhoConst * DRF(1) * hFacC(ix,iy,1)\\
&\quad - WCMASS(ix,iy,1)/(DRF(1) * hFacC(ix,iy,1),
\end{aligned}$$

where $CellVol$ is the tracer cell volume, $rAc * drF * hFacC$. A volume-integrated budget for a volume of interest would require numtiplying each term by its cell volume before adding; this generally is a simpler calculation, because the terms above require dividing by the cell volume.

It is important to know that the gradients of ADV terms are equivalent to

$$\partial(uc)/\partial x$$

and not

$$u\partial c/\partial x.$$

Thus the total advective tendency is equivalent to

$$\vec{u}\nabla c,$$

but if split into directional components, the divergence term must be subtracted:

$$u\partial c/\partial x = \partial(uc)/\partial x - c\partial u \partial x.$$

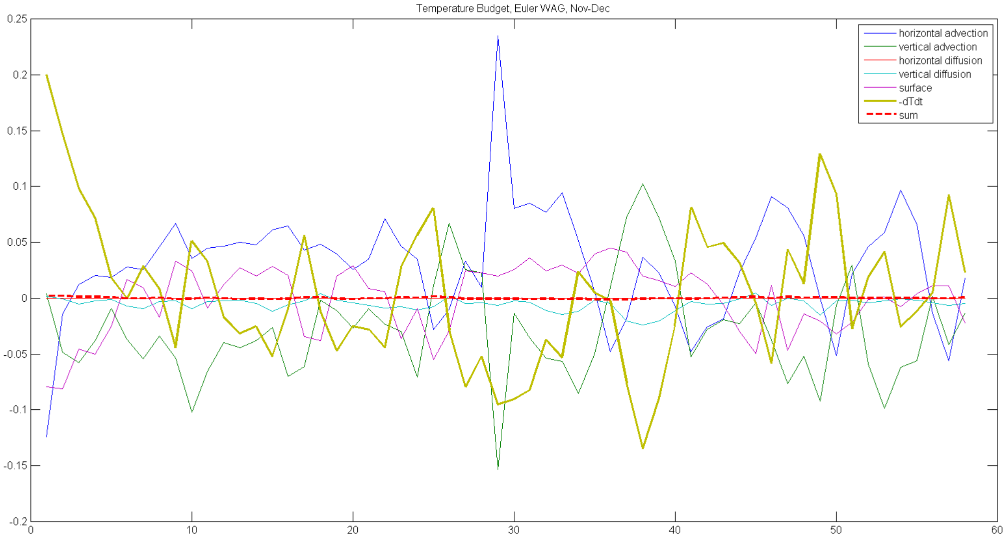

Figure B-1: Potential temperature budget with daily-averaged fields for two months. Fluxes are totals for the Eulerian Western Alboran Gyre. Red dashed line is the error.

The horizontal divergence diagnostic, momHDiv, can be used for splitting the advection tendency into horizontal and vertical components:

$$\begin{aligned} Adv\_tend\_C\_z &= [(ADVr\_C(ix,iy,iz+1) - ADVr\_C(ix,iy,iz))/CellVol + \\ &\quad C * momHDiv], Adv\_tend\_C\_h \\ &\quad = [(ADVx\_C(ix+1,iy,iz) - ADVx\_C(ix,iy,iz))/CellVol + \\ &\quad (ADVy\_C(ix,iy+1,iz) - ADVy\_C(ix,iy,iz))/CellVol - \\ &\quad C * momHDiv], \end{aligned}$$

The diffusion tendency can be easily split into vertical and horizontal by including the first 3 terms in the vertical and the last 2 in the horizontal. An example of this budget is in figure B-1; errors are at least an order of magnitude smaller than the fluxes.

Another option for careful division of advective terms is to consider the volume of interest as a control volume and calculate the fluxes through the edges. This can be done by identifying the edges and creating logicals for them as done for the vorticity budget. Then the advective terms of the volume-integrated budget can be calculated as

$$Adv\_tend\_C\_z = (ADVr\_C(openDown) - ADVr\_C(openUp)),$$

$$Adv\_tend\_C\_h = [(ADVx\_C(openW) - ADVx\_C(openE)) + (ADVy\_C(openS) - ADVy\_C(openN)).$$

These calculated terms are equivalent to those where every interior cell's divergence is also included.

B.3 Western Alboran Gyre Budget Examples

B.3.1 Overview

Using the methods of the previous section, Chapter 3 evaluated a number of budgets and used them to elucidate the processes controlling some of the features of the Western Alboran Gyre, WAG, from my model run. Salt and momentum budgets were evaluated but did not contribute well to the analyses. Those budgets are presented here, in case future researchers with different questions find them useful.

B.3.2 Full WAG salt budget

In the WAG, there is a subsurface salinity minimum. In Chapter 3, I presented a salt budget for just the area that contained the minimum in the mean. Here, I show a salt budget for the full WAG. This budget does not assist with an understanding of the minimum, but does demonstate how the different physical processes affect the salt content of the WAG.

Figure B-2 shows the full salt budget and a spatial representation of the mean advective transports. Advection through the sides and bottom of the volume are the dominant terms in the timeseries budget, as they were in the volume budget. The mean depth-integrated advective fluxes through the sides and mean advective flux through the bottom have spatial patterns quite similar to those for volume.

Because of how the MITgcm treats tracers, the positive upward volume flux through the bottom is moving positive amounts of salinity and potential temperature upward, but it is not directly clear if this is increasing or decreasing the total salt and heat in the gyre. Thus, in order to understand the effects of the salt transports, the volume transports of the mean gyre salinity (36.61) are removed, scaled with the means and the appropriate density and specific heat. Now positive salt transports

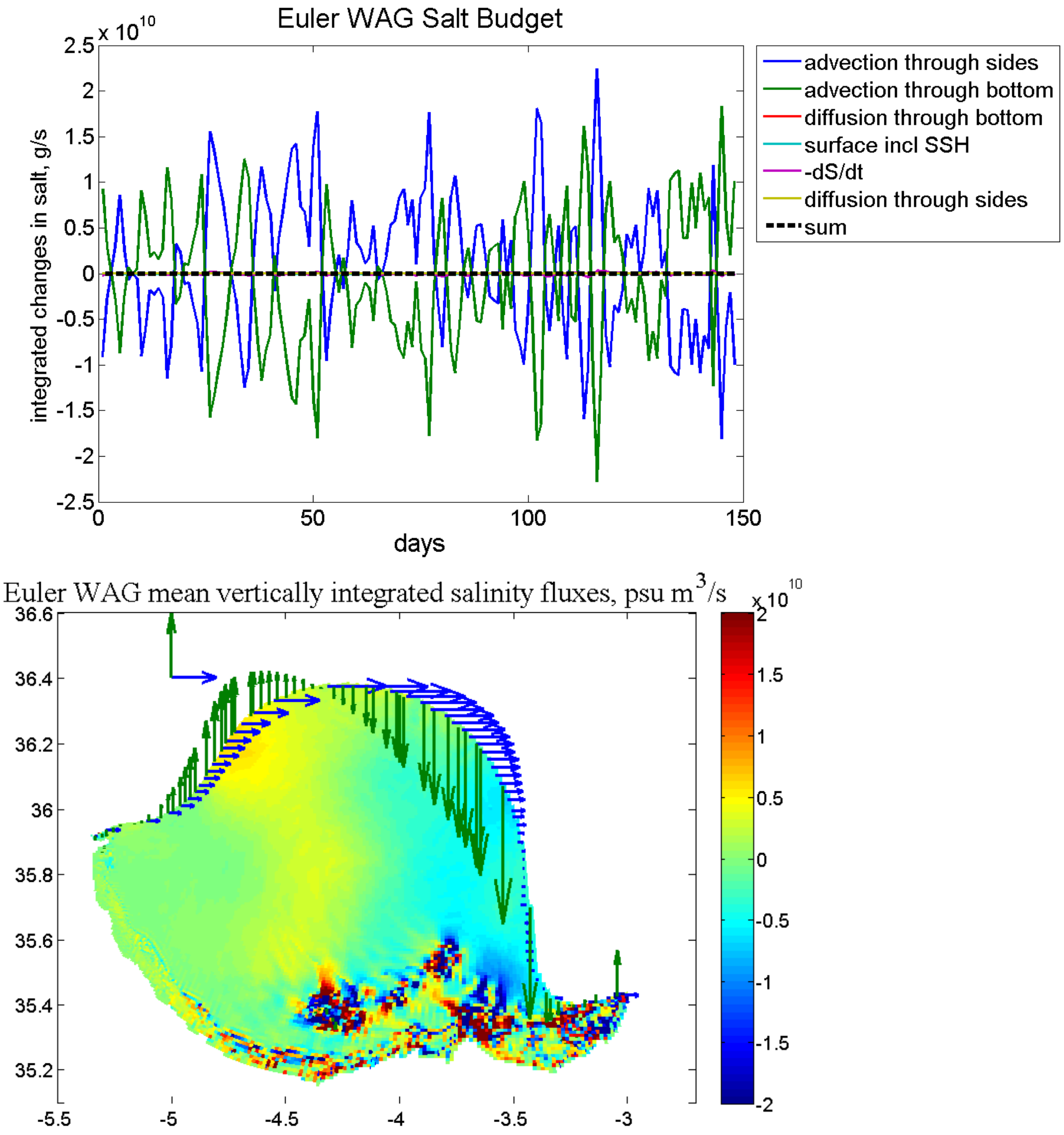

Figure B-2: Top, total Euler WAG salt budget, g/s. Bottom, mean vertically-integrated advective salinity fluxes for the Euler WAG. Colors show flux through the bottom, arrows show flux through the sides. Top left arrows show scale, $5 \cdot 10^{10} [c] m^3/s$, where $[c]$ is salinity units. Seamounts do not appear as empty space as they did for the mean volume fluxes because the flux across the bottom-most wet cell is used rather than the σ_θ surface.

indicate water with higher than average salinity moving into the gyre, or water with lower than average salinity moving out of the gyre. That budget, figure **??**, shows the transports through the sides and bottom and the changes in storage as the largest terms. In the mean-referenced salt budget, transport through the sides and bottom still oppose each other when they are largest, and diffusion and surface fluxes are still much smaller than the three large terms. The time-mean of these tranposts indicate that horizontal advection brings in fresher water, while advection through the bottom increases the salt content and drives a mean increase in salt over time.

To continue with the salt budget, when the dominant terms of advection across the sides and bottom are combined, it is clear they are nearly equal in size to the change in salt content. The surface forcing is an order of magnitude smaller and diffusion terms are smaller yet (figure B-4). The surface forcing fluxes' negative spikes indicate rain events. The relationship between total advection and changes in salinity content indicates that advection is the main driver in changes in salinity in the WAG. This is also clear in the mean of these transports (figure **??**), where advection of salt out through the sides and in through the bottom are the two terms on the order of the changes in salt. The surface forcing approximately balances the advection minus content change terms (see figure B-5). Bottom diffusion is an order of magnitude smaller, and much more constant in time, due to the consistent vertical gradient of salinity here (about $0.01psu/m$). Horizontal diffusion is not shown because it is extremely small, less than $1kg/s$, due to both small horizontal gradients of salinity (typically $0.01/km$) and the very small explicit numerical horizontal diffusivity, chosen due to the high resolution of the model.

B.3.3 Momentum Budgets

In order to understand the dynamics that maintain the WAG, I now examine the momentum and vorticity budgets. All necessary diagnostics to calculate the terms in the Navier-Stokes equations are available as outputs from the MITgcm except the barotropic portion of the pressure gradient term, which was calculated from SSH (details in the appendix). I will first discuss the zonal and meridional momentum budgets, followed by the vorticity budget.

The momentum budgets include the following terms:

$$\frac{dU}{dt} = \Delta U_{Advection} + \Delta U_{Coriolis} + \Delta U_{Pressure} + \Delta U_{Diffusion} + \Delta U_{Dissipation} + F_U + \Delta U_{AB}, \quad \text{(B.1)}$$

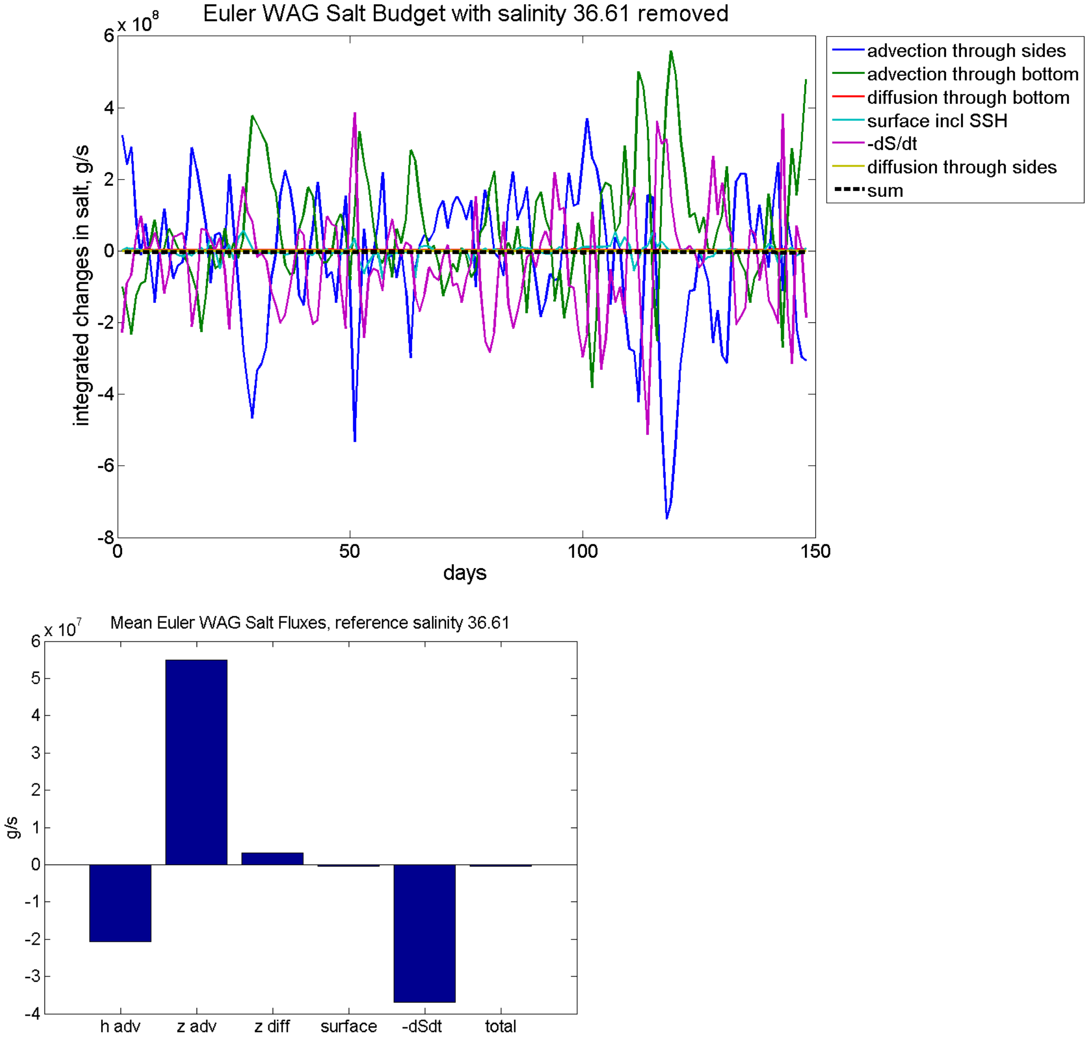

Figure B-3: Top, total Euler WAG salt budget with volume transport of water with mean WAG salinity, 36.61, removed. Bottom, time-mean transports of salt, g/s, with the transports of salt by the volume transports of the mean gyre salinity, 36.61, removed.

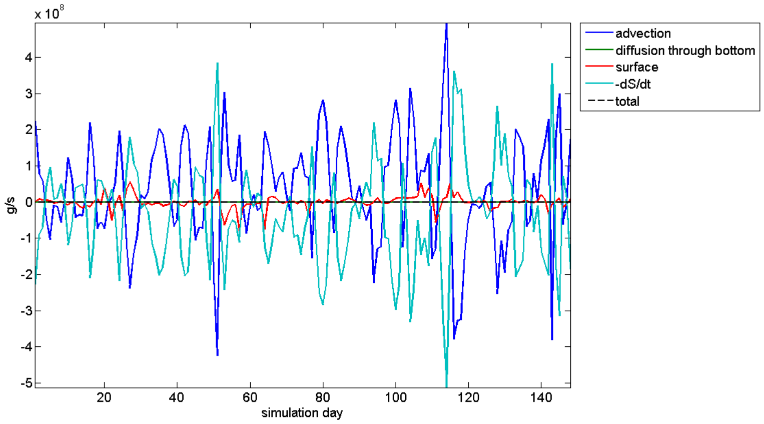

Figure B-4: Euler WAG salt budget, advection combined, g/s, with the transports of salt by the volume transports of the mean gyre salinity, 36.61, removed.

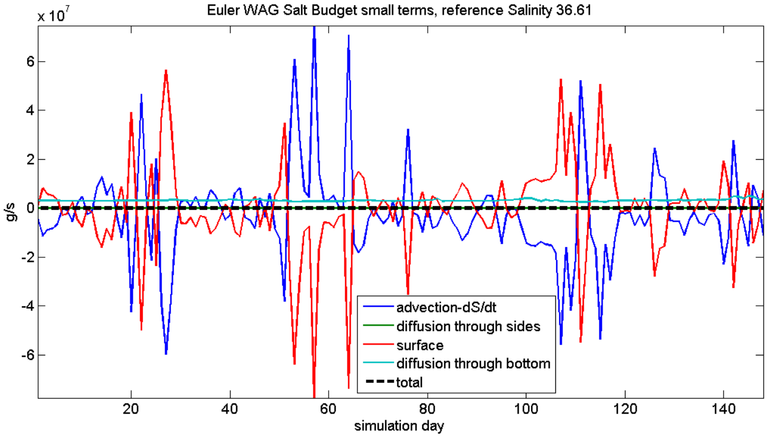

Figure B-5: Euler WAG salt budget, smaller terms, g/s, with the transports of salt by the volume transports of the mean gyre salinity, 36.61, removed. Negative peaks in the surface term are rain.

where the changes in the momentum due to advection, coriolis acceleration, pressure gradients, vertical diffusion, drag and horizontal diffusion (together called dissipation), surface forcing by windstress, and numerical timestepping details (AB) combine to the change in time of the momentum. The volume-integrated momentum budgets with all terms (figure B-6) show that the gyre is nearly in geostrophic balance, with the Coriolis and pressure gradient terms being the largest and opposing each other. The next-order terms include advection, windstress, and the topographic drag and horizontal viscous diffusion term. The smallest terms are the vertical viscous diffusion and the timestepping term, which is a correction due to half forward steps in the Adams-Bashforth advection scheme. The vertical viscous diffusion is small because it primarily redistributes momentum input by the surface windstress, rather than adding or removing momentum from the WAG; this will be explained with the vertical structure of the terms. Combining the Coriolis and pressure gradient terms removes the geostrophic part of the budget, and I call the remainder the ageostrophic term; it can be represented as the Coriolis acceleration of the ageostrophic velocities. This term and the next-order terms of the total budget show that the zonal and meridional budgets have different characteristics (figure B-7). In the zonal direction, the ageostrophic term is balanced by the surface windstress, while in the meridional direction it is balanced by advection. This difference is due, to the fact that the windstress is about twice as large in the zonal direction as meridional, whereas the advection terms are similarly sized. In the mean, the wind direction is mostly zonal (figure 3-23), confirming this difference in windstress.

The mean values of the momentum budget terms integrated over each vertical layer of the WAG gives additional insight into the physics (figure B-8). While the geostrophic balance is still dominant, and thus removed for readability to leave the ageostrophic term, the vertical viscous diffusion is larger than the dissipation at most depths, the opposite of in the integrated budget. The vertical viscous term includes the surface windstress in the top layer and shows how that momentum is redistributed downward over about $80m$. Again, the zonal momentum budget has a balance between the ageostrophic term and the windstress, but that now includes the vertical viscous diffusion and is true only in the top half of the gyre, with advection balancing the ageostrophic term below that. For the meridional momentum, in the top half the ageostrophic term, wind and vertical diffusion, and advection together form the main components, with the balance between the ageostrophic term and advection in the bottom half that was visible in the depth-integrated timeseries.

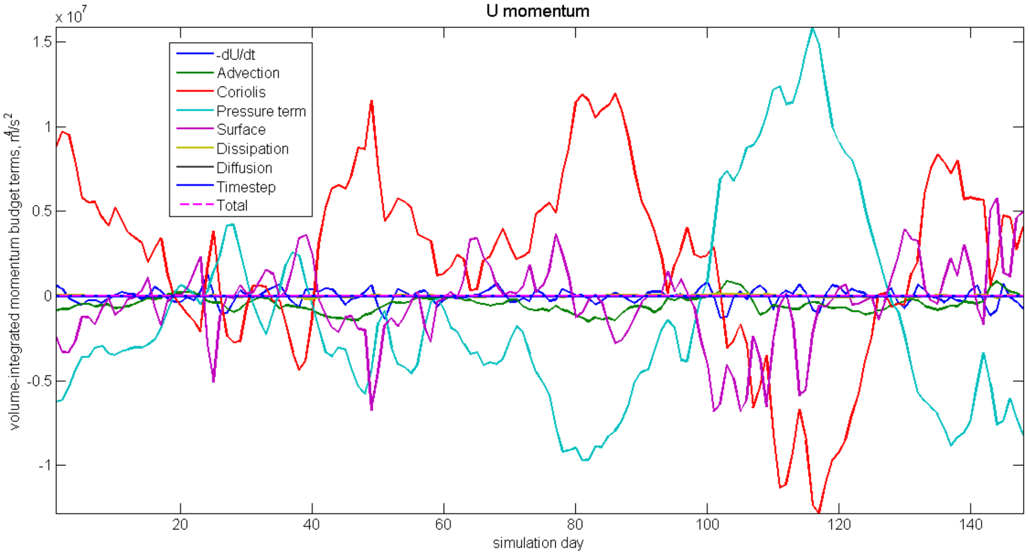

(a)

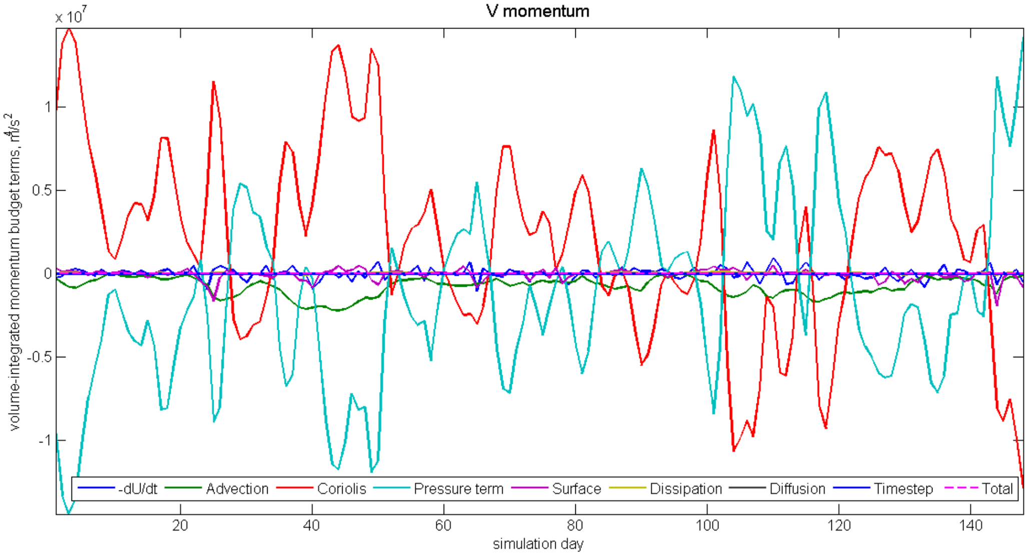

(b)

Figure B-6: Euler WAG volume-integrated momentum budget, all terms, m^4/s^2. Top, zonal; bottom, meridional.

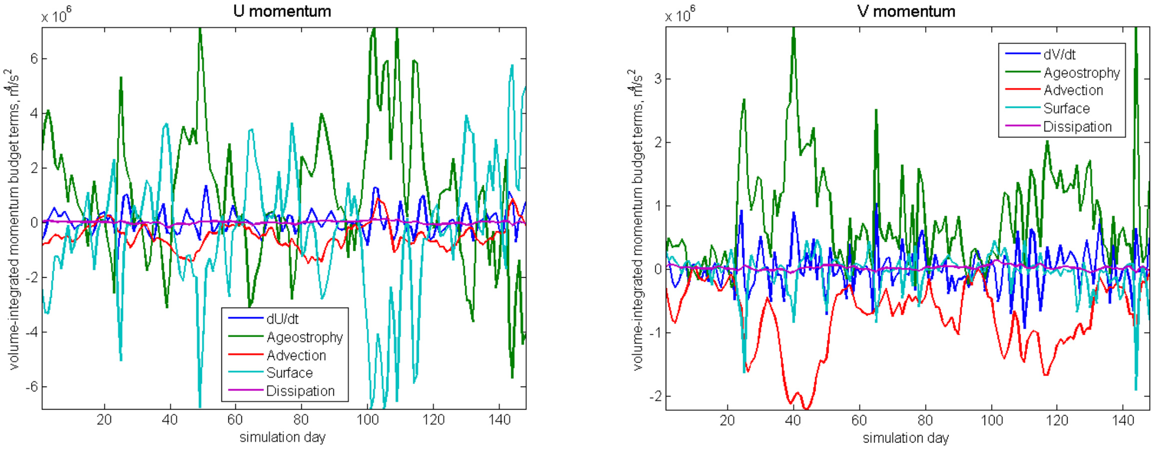

(a) (b)

Figure B-7: Euler WAG volume-integrated momentum budget, m^4/s^2, secondary terms (largest terms, Coriolis and pressure gradient force, are combined into the 'ageostrophic' term). Left, zonal; right, meridional

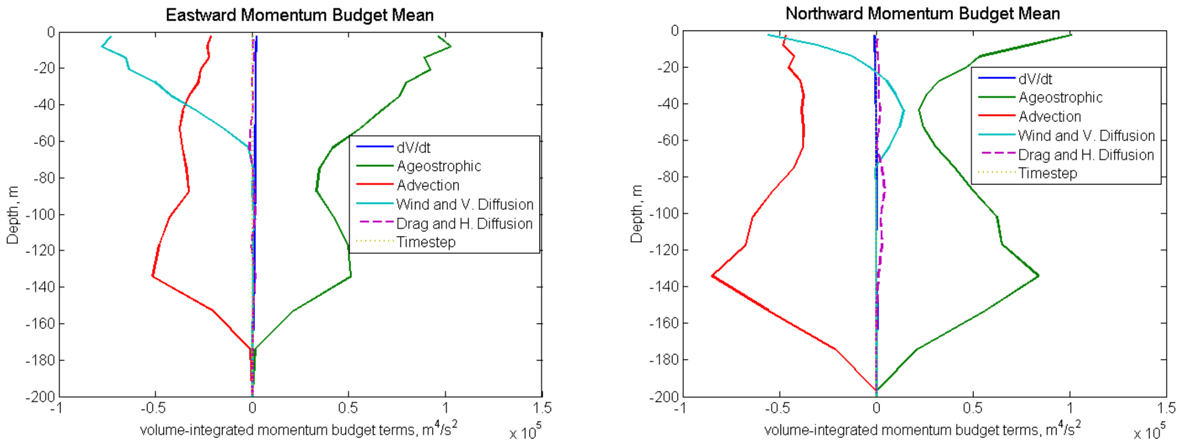

(a) (b)

Figure B-8: Euler WAG volume-integrated momentum budget in horizontal layers, mean of all terms vs. layer center depth, m^4/s^2. Left, zonal; right, meridional

Appendix C

Biological-Physical Interactions in the Alboran Sea

This appendix describes possible avenues for further research stemming from the work in chpaters 3 and 4. These projects were proposed as part of my thesis planning at various times, but were not completed due to challenges in the physical analysis. The physical analysis of the Alboran Sea and the Western Alboran Gyre (WAG) indicate that there is strong stirring around the edges of the WAG but not near the core. Also, the water from the Strait of Gibraltar inflow that becomes the Atlantic Jet (AJ) can be transported into the WAG on timescales of days to weeks. A similar connection to the northeastern part of the Alboran was found. Both the inflow waters and the northeastern area have enhanced nutrient loads. The first section below describes research considering how the different levels of stirring may affect competition and diversity in phytoplankton. The second section describes a research avenue to examine how the transport of high-nutrient-load water can impact productivity.

C.1 Phytoplankton in the Alboran Sea: Physical Interactions and Functional Types

This proposed work was submitted for a NASA Earth Science Student Fellowship grant and was rejected. Reviewers' and project managers' comments suggested that the questions were good and that this work should be done. However, connections to the larger scale needed to be further developed, and a better quantitative measure of diversity than the Shannon index was needed. This work would unfortunately not be possible with the model run of the physical system that I developed, because much of the year has a never-observed circulation. If a physical run of one full seasonal cycle that was reasonable existed, the following work would be possible.

C.1.1 Introduction and Background

Phytoplankton form the base of the marine ecosystem, produce most of the world's oxygen, and are a significant carbon pool. The region of the Mediterranean with the highest primary productivity is the Alboran Sea. This productivity supports a biologically diverse ecosystem that is home to several endangered and vulnerable vertebrates (Coll et al. 2010). As such, it is crucial to understand how ocean physics impacts phytoplankton productivity. The Alboran Sea is a favorable region to study interactions between phytoplankton and their physical environments because it is limited in extent and its circulation is controlled by a relatively small number of well-defined coherent structures, including a surface jet and several gyres and fronts that are thought to impact phytoplankton populations. The proposed work will explore the relationship between phytoplankton diversity and physics using a bio-physical model, dynamical systems analysis, and a recent advance in the interpretation of the Moderate Resolution Imaging Spectroradiometer (MODIS) data: PHYSAT-Med.

C.1.2 Physics

The Alboran is bounded by the Strait of Gibraltar where Atlantic Water enters in the Atlantic Jet (AJ) which is partially entrained into gyres and eddies along the African coast to become Modified Atlantic Water (MAW). Persistent features include the Northwestern Alboran Front (NWAF), the Almeria-Oran Front, and the Western Alboran Gyre (WAG); see Figure C-1. The WAG and other less-persistent gyres can shift and re-form within the sea with higher variability in the winter as described by Renault et al. (2013). Gyre motions were shown to be influenced by vorticity fluxes through the Strait of Gibraltar by Sánchez-Garrido et al. (2013). The transport in the Alboran has been shown to be spatially heterogeneous with enhanced mixing in some "chaotic" regions (d'Ovidio et al., 2004, Sayol et al. 2013). These regions, characterized by rapidly diverging fluid trajectories and elevated stirring, can be identified using Lagrangian analysis techniques developed within the

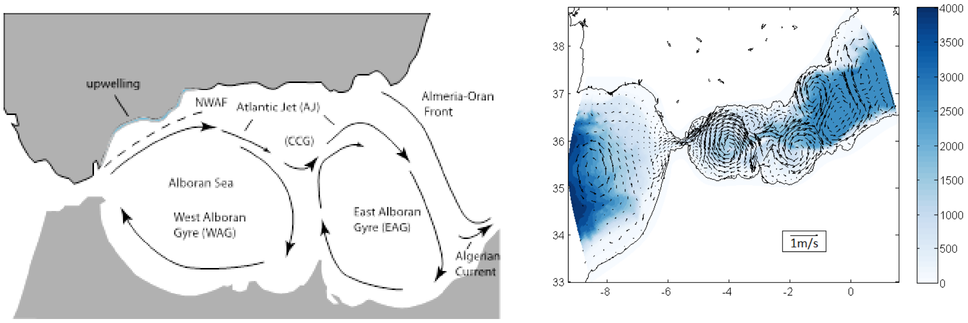

(a) Schematic

(b) Velocity

Figure C-1: (a)Schematic of the Alboran. This is one of several quasi-equilibrium states commonly observed. CCG is the Central Cyclonic Gyre. (b) An example MITgcm daily mean surface velocity plotted over bathymetry. Note the WAG at about $4°W$.

dynamical systems community over the past two decades. These techniques can provide a template that identifies transport pathways, barriers to transport, coherent material structures, and regions of strong or weak stirring and mixing (e.g. Rypina et al. 2009). Application is most straightforward when the flow field contains long-lived coherent features such as jets, fronts and gyres, making the Alboran Sea an ideal region to investigate. This study will explore the use of these methods in order to identify transport pathways and barriers, regions of strong and weak stirring, and the fluxes of relevant physical and biological properties, all with the purpose of clarifying the causes of phytoplankton community structure.

C.1.3 Biology

The Alboran's high animal biodiversity relates to diversity at the plankton level, but microbial diversity is difficult to document. Recent work has instead examined the functional types of phytoplankton present (Navarro et al. 2014, León et al. 2015) and the overall distribution (Siokou-Frangou et al. 2010). The density and relative frequency of phytoplankton functional types have mesoscale variability, an apparent “patchiness" that is similar to that of *chlorophyll-a* measurements. A recent study of *in-situ* phytoplankton measurements in the Alboran Sea by León et al. (2015) examined the mesoscale variation in density of pico and nanoplankton in relation to hydrodynamic features during three cruises, each sampling a different feature. For the NWAF, the physical process related to high phytoplankton densities was advection by the Atlantic Jet of waters mixed in the Strait of

Gibraltar. For the WAG, high-density patches of overall biomass and each plankton size formed in cold waters due to upwelling. For the Almeria-Oran Front, the distribution of prochlorococcus depended on the intrusion of Mediterranean Surface Water (MSW) from the basins to the east. Overall, this work showed that mesoscale advection causes biological responses, longer residence times relate to higher phytoplankton density, large changes occur on the timescale of days to weeks, and measurements of phytoplankton groups show greater spatial variability than *chlorophyll-a*.

While local studies focus on water mass advection and vertical velocities, idealized modeling work has examined the effects of transport barriers and chaotic stirring. Chaotic stirring caused a persistent high growth region in a study by Hernández-García and López (2004). A two-phytoplankton-type study of an idealized vortex street demonstrated that transport barriers between nutrient sources and the cores of eddies delineated regions of dominance for the two types (Bastine and Feudel 2010). Moving into a three-dimensional, time-varying flow with three phytoplankton types makes this work more realistic and allows comparison to both modeling and observation studies.

Remote measurements of ocean color allow scientists to study the near-surface phytoplankton across the world's ocean, but regional shipboard measurements of hydrography and biology are necessary to calibrate the satellite data. Navarro et al. (2014) have done this calibration for the Mediterranean to modify the PHYSAT algorithm for interpreting ocean color data from MODIS. The regional model, PHYSAT-Med, identifies the dominant phytoplankton functional type (PFT) for each pixel (about 4 km resolution) based on radiance anomalies at several wavelengths, allowing for the mapping and spatio-temporal study of phytoplankton throughout the Alboran Sea. The authors validated their results against *in-situ* data and found good agreement. Monthly climatologies of the most-seen dominant type are shown in Figure C-2. Two types are most common: nanoeukaryotes, a range of species of eukaryotes between 2 and 20 μm, and synechococcus, a picoplankton that grows well in low nutrient environs like the open ocean. In November through February some areas have a large presence of diatoms, a microplankton that grows in high nutrient environs and is often found near coasts. The proposed work will take advantage of this new PHYSAT-Med algorithm for comparison of the variation of community structure observed in the Alboran to that in the numerical model.

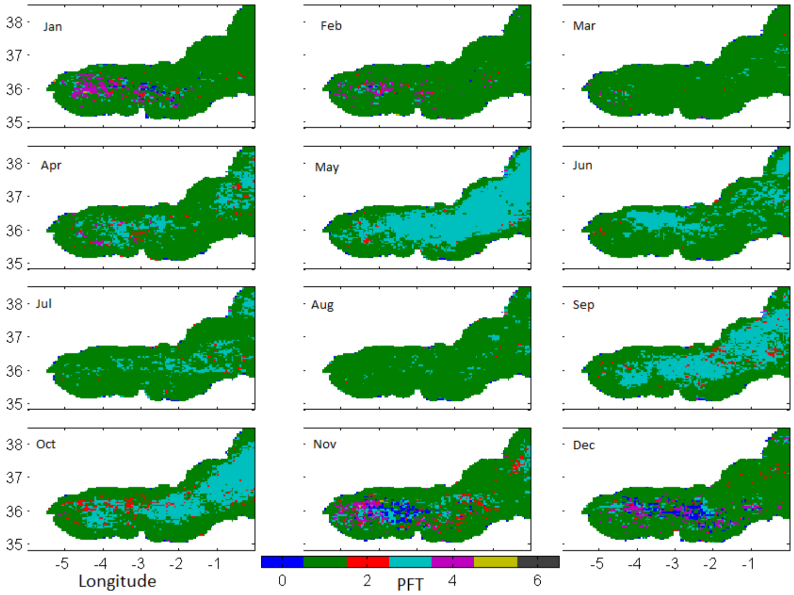

Figure C-2: PHYSAT-Med applied to MODIS data (2002 to 2013): monthly climatology of dominant PFT. Top row: Jan, Feb, Mar. Each pixel is marked as one of: 0 unidentified, 1 nanoeukaryote, 2 prochlorococcus, 3 synechococcus, 4 diatom, 5 phaeocystis, 6 coccolithophorid. The Alboran is dominated by nanoeukaryotes and synechococcus, with diatoms in Nov-Feb. (Adapted from Navarro et al. 2014.)

C.1.4 Proposed Work

C.1.5 Goal and Questions

This work will use MODIS data interpreted with PHYSAT-Med, previously published *in-situ* data, and a coupled physical-biological numerical model (MITgcm and Darwin) to investigate the relationship between phytoplankton diversity and physical oceanographic processes in the Alboran Sea. It will answer:

- What patterns of phytoplankton diversity and functional type dominance are seen in the physical-biological model? Specifically, how do the phytoplankton community structure and its spatio-temporal scales relate to major circulation features, their variability, and the associated fluxes?
- Given satellite observations of altimetry and functional types, what do relationships from the model tell us about the causes of the observed diversity patterns?

As part of answering these questions, I will apply dynamical systems methodology to compute fluxes between circulation features and identify regions of intense stirring. These measures will allow me to examine, for each region of the Alboran, which processes are most important; these processes include local growth and the fluxes of phytoplankton, nutrients, temperature, and salinity by horizontal and vertical advection, stirring, and mixing.

C.1.6 Approach

The proposed work will investigate the relationship between phytoplankton diversity and physical flow using a combination of physical-biological numerical modeling, dynamical systems analysis, and the recent advance in interpretation of Moderate Resolution Imaging Spectroradiometer (MODIS) data: PHYSAT-Med.

The physical model I will use is the Massachusetts Institute of Technology general circulation model (MITgcm) in hydrostatic mode (Marshall et al. 1997). The specific configuration is similar to that of Sánchez-Garrido et al. (2013), with resolution increased roughly by a factor of three in the eastern Alboran. This model solves the Boussinesq form of the Navier-Stokes equations for an incompressible fluid with a finite-volume spatial discretization on a curvilinear grid with horizontal resolution of 1 to 3 km. The vertical grid has 5m resolution at the surface, decreasing with depth, and 46 vertical levels. The model domain (see sample velocity field in Figure 1b) will include the Strait of Gibraltar and have open boundaries in the Atlantic and Mediterranean. Surface forcing will be provided by 6-hourly, 1/4-degree, 10m wind fields from the IFREMER CERSAT Global Blended Mean Wind Fields. This should provide adequate spatial and temporal resolution of wind fields to capture upwelling events. Surface heat and salt fluxes will be from the ERA-Interim reanalysis daily fields. Open east and west boundary forcing of velocity, salinity and temperature will be from the 1/12-degree, daily Atlantic-Iberian Biscay Irish-Ocean Physics Reanalysis. I have tested this set-up by running the model for 2008 (preceded by suitable spin-up period), a year with a large amount of available functional type data (Navarro et al. 2014). The model and satellite sea surface height (AVISO) are well correlated in the mean (Figure C-3).

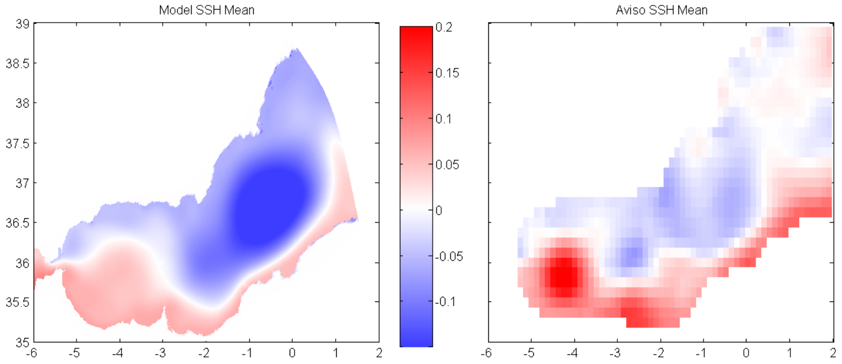

Figure C-3:
Mean SSH in the Alboran Sea for 2008 from the MITgcm (left) and AVISO (right).

I will use the Darwin model (Duktiewicz et al. 2009) as the biological model which will be coupled to the three-dimensional output of the MITgcm. The Darwin model is designed to reproduce the biology of multiple phytoplankton and zooplankton species. The phytoplankton prognostic equations represent growth as a function of light, temperature, and Monod functions for nutrient limitation. I will set up the model to represent just one nutrient and three functional types of phytoplankton (synechococcus, nanoeukaryotes, and diatoms) matching those observed most frequently by Navarro et al. (2014) and choose biological parameters based on Follows et al. (2007). For spatial or temporal patterns in the surface layer of the model that are similar to satellite-measured patterns, the model will be used to give insight into what physical oceanographic factors are important for phytoplankton dominance and diversity and the mechanisms involved. For a full year run, the monthly dominant type maps can be compared to the climatology shown earlier (Figure 2) and the individual months from 2008.

To examine diversity, I will look at variations in the community structure as quantified by the Shannon index, H:

$$H = \sum_i p_i / \log(p_i), \;\; p_i = P_i / \sum_i P_i, \;,$$

where P_i is a given functional type concentration (Shannon 1948, Spellerberg and Fedor 2003). When H is large, there are more species present in more equal fractions; thus, the diversity is large. The Shannon index can be computed for the model ouput at any scale from one grid cell and up. For direct comparison to satellite, the diversity of dominant types from each comparable surface point can be used for the Alboran as a whole or for sub-regions.

The model output can be compared to *in-situ* measurements by examining local variability. I can relate the overall biomass, converted from nitrogen units, and the relative abundance of different size classes by matching size classes with modeled types. Field measurements tend to be local, both in time and space. For studies with differentiation between sizes or phytoplankton taxa, the spatio-temporal scales of observed variation can be compared to those in the model. As an example, Figure C-4 from Arin et al. (2002) shows the variability of size-fractioned phytoplankton at three sites near the WAG, each visited every three days over two weeks.

To construct a story about the growth and decay of each particular functional type, I will take the Lagrangian perspective, following populations as they are advected by the near-surface circulation. The time history of nutrient fluxes is particularly important, both from local upwelling and AW inputs; barriers to transport may also explain oberved patterns. To examine fluxes of nutrients,

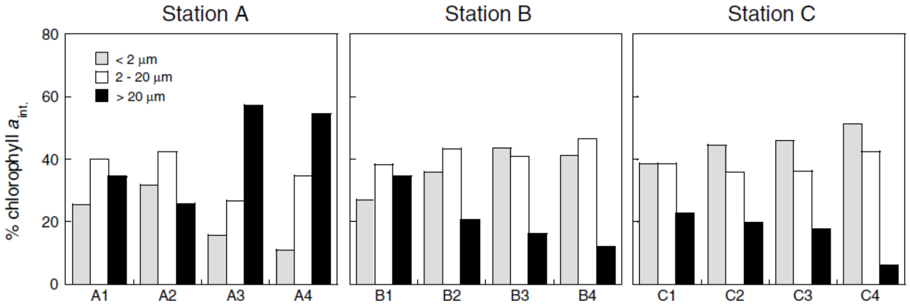

Figure C-4: Variability of the contribution of three size fractions of plankton to the total *chl-a*. Stations (A,B,C) were visited every 3 days (4 times total) during a cruise in May 1998. The location is in the northern portion of the WAG. (From Arin et al. 2002)

phytoplankton, temperature, and salinity between quasi-steady circulation features, I will apply lobe analysis (Samelson and Wiggins, 2006; Miller et al. 2002). When circulation features change quickly, I will trace water masses and populations through backwards trajectories. I will also use Finite-Time Lyapunov Exponents (FTLEs) to measure stirring, which is likely to increase homogeneity. I will experiment with these Lagrangian measures to see which correlate best with factors such as the Shannon index, as each measure gives information about the extent to which a particular water parcel is brought into close contact with parcels carrying different nutrients or phytoplankton types. I will also examine Eulerian fluxes between time-averaged circulation features for comparison.

C.2 Phytoplankton in the Alboran Sea: Can Nutrients Sources and Advection Explain Persistent Productivity?

Once it was clear that the existing physical model for the Alboran Sea would not allow the research proposed above, I sought a different option. Because I had about 5 months of physical circulation that I consider to be realistic and the timescales of the stirring and of phytoplankton blooms are a few weeks, I considered looking into just the effects of the nutrients being stirred into the WAG. This work did not occur because challenges with the physical analyses, particularly water property budgets, took much longer than anticipated. This work is possible using existing resources.

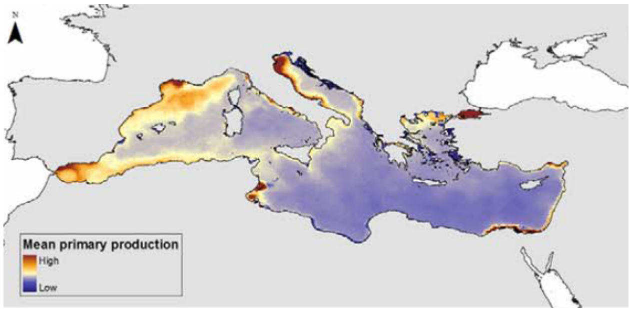

Figure C-5: Mean primary production across the Mediterranean. Generally productivity decreases from West to East and from coastal areas to deeper water. (Coll et al. 2010)

C.2.1 Motivation

The proposed work will use Lagrangian trajectories from a realistic simulation of the Alboran Sea to determine how much of the observed production patterns may be created by horizontal advection of nutrients from the westernmost parts of the basin. The reasons for choosing the Alboran Sea include its interesting flow structures, our existing knowledge of the system, and the existence of previous works, some supporting the alternate theory that high productivity is due to vertical motions in the basin interior, another supporting the SG source but without details of its contributions separated.

The Alboran Sea has the highest primary productivity of the Mediterranean; this is clear in mean primary production (figure C-5, Coll et al. 2010), which also shows enhanced values around the periphery of the WAG. As the base of the marine food web, phytoplankton growth is an intensely studied subject. Several physical processes contribute to the distribution of both nutrients and phytoplankton, leading to an interest in finding which are dominant under what circumstances. For instance, studies have looked at whether stirring rates in horizontal advection increase or decrease phytoplankton biomass (i.e. Hernandez-Garcia et al. 2004, Hernandez-Carrasco et al. 2014). Vertical fluxes of nutrients are also important, as shown by the mentioned Oguz et al. paper (2014). Most studies examining the physical controls of production have used a biological model of a single population of phytoplankton; this is a significant simplification of the biology at play, but one which will continue in my work.

C.2.2 Background

In the Alboran, there is addition of nutrients into surface waters from vertical tidal mixing in the Strait of Gibraltar, upwelling along the Northwest coast, and upwelling in cyclonic gyres or transient

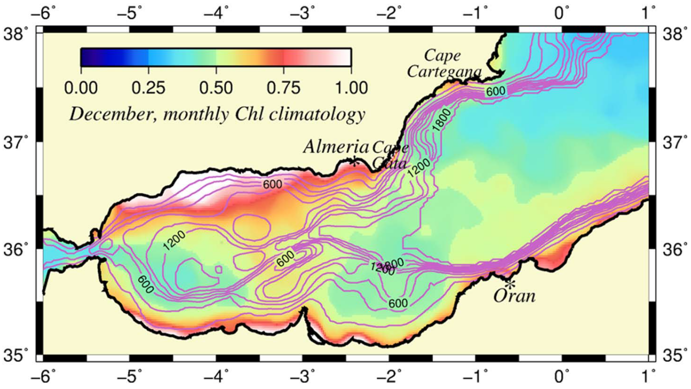

Figure C-6: Climatology of December *chl* from 9 km gridded monthly SeaWiFS in color. Magenta curves are isobaths. (Oguz et al. 2014)

cyclonic eddies. Peak chlorophyll-a (*chl-a*) values measured *in-situ* were subsurface values between 4 and $8 \mu g l^{-1}$, and primary production measurements range from 6 to $1300 mgCd^{-1}$ (Siokou-Frangou et al. 2010). Subsurface maxima, near 50m, tend to be present in the non-bloom spring and summer months (Oguz et al. 2013). A broad study of deep chlorophyll maxima in the Mediterranean, while not including the Alboran in the analysis, showed that in our period of November through March there is usually a surface maximum in both chlorophyll and primary production rate (Macias et al 2014).

Two areas with significant annual variation in chlorophyll measurements have been associated with patterns of absolute dynamic topography (ADT) by Navarro et al. (2011). The first is a high in the strait and the northwest coastal area, with peaks in the late summer and autumn. The second is highest along the northern edge of the WAG, where the AJ is typically located, with peaks in the late winter and early spring. These correlations imply that large-scale physical features force the large-scale plankton features. Given that our existing model run covers November 2007 to March 2008, fall to spring, we are likely to see variations associated with both patterns.

Satellite observations of ocean color allow for a quantification of the chlorophyll content of the near-surface water through analyzing the color spectrum. SeaWiFS products include $9km$ gridded monthly-averaged *chl-a*, which are publicly available. A common pattern in the Alboran is for the periphery of the WAG to have high *chl*, which may be wide enough to reach both coasts (figure C-6). This pattern can be explained by vertical velocities within the basin bringing nutrients into the surface layer, as demonstrated by Oguz et al. 2014.

C.2.3 Relevant Papers

The most relevant background for the work I am doing is four recent publications which all use models to describe phytoplankton spatial patterns in the Alboran. I will summarize each. All of the following works use limited biological models (one or a few each of nutrient, phytoplankton, zooplankton, and detrital categories) coupled to physical general circulation models. All are Eulerian and include multiple physical processes that affect the distribution of the biological fields, including horizontal and vertical advection and diffusion. The physical forcing varies, such as choosing whether to include tides and whether meteorological forcing is constant or realistic. Conclusions of which physical processes influence productivity are then drawn by comparison between either different regions of the flow or different realizations of the physical model.

Skliris et al. (2009) modeled the Alboran as a nested element in their Western Mediterranean model, examining how upwelling and advection affect nitrogen and phytoplankton. The modeled surface chlorophyll concentrations in the Alboran peaked in the northwest from the edge of the strait through the upwelling region, and the local maximum continued around the eastern side of the WAG. The authors find that the lifting of the nitracline at the north-eastern corner of the strait and in the north-west Alboran upwelling region are the main drivers of phytoplankton growth in the Alboran, and the continued maximum is due to advection by the AJ. The physical model is GHER with 1km resolution in the western Alboran as a nested grid within a broader Western Mediterranean grid of 5km resolution; open boundaries were relaxed to monthly climatological values; surface forcing was from an eight-year averaged ECMWF reanalysis to get one ‘climatological’ year. The biological model is NNPZDD, with initial and boundary conditions based on MEDAR climatology. The above-mentioned high-chlorophyll areas have the peak in the correct near-coast location, but have more broad spatial maxima; nonetheless the mean summer and winter surface patterns match satellite better than the MEDAR climatological maps do.

Oguz et al 2014 shows that the nonlinearity of the AJ leads to cross-frontal circulation that brings nutrients from depth into the euphotic zone. The jet becomes weaker to the east, and productivity also decreases to the east in the model and observations. No advection of the biological components is allowed in the SG, so this analysis does not include nutrients advected from the Atlantic or mixed into the surface in the SG. The biological model was NPZD. The physical model was POM with about 3km resolution, no surface forcing, and constant exchange in the Strait of Gibraltar. The highly productive areas are mostly along the jet, with higher subsurface production. The productive region does connect to the northern coast and decrease to the east, as seen in climatology, but both of these are less strong than in satellite observations of chlorphyll.

Sanchez-Garrido et al 2015 shows that including tides increases production in the Alboran by 40% overall, and more in the Western Alboran. This finding uses comparison between a model runs with and without tides. A third run shows that parameterizing the effects of the tides by greater vertical mixing of nutrients in the SG gives a good approximation of the production with tides, demonstrating that the propagating internal tides are less important than the mixing at the sill in the SG. The biological model was Darwin configured with four nutrients, two phytoplankton, and two zooplankton. The physical model is the MITgcm with 0.5-4km resolution with daily lateral forcing from the Iberia-Biscay-Ireland Regional Seas reanalysis, surface forcing from ASCAT winds and NCEP/NCAR reanalysis heat and freshwater fluxes. The highly productive areas are mostly in the western Alboran outside of the WAG; including tides increases productivity, total phytoplankton, and the east-west gradient of both. These productive areas match satellite observations of chlorphyll in general, with the tidal model doing a better job of matching the maxima and the east-west gradient. All model results show more phytoplankton in the WAG interior and along the southern coast than observed at the same time, but longer-time averages of observations do show southern-coast chlorophyll.

Oguz et al 2016 shows that the strength of the AJ controls the productivity: stronger cross-jet density gradients support frontenogenesis, creating the strong cross-frontal circulation shown to be important in the previous (2014) study. The authors also show that cyclonic eddies can create comparable levels of production through eddy pumping. The biological model was NPPZD. The physical model was POM with about 3km resolution, surface heat forcing from ERA40 reanalysis, no wind, no tides, and seasonally varying prescribed exchange in the Strait of Gibraltar. This study does not give any averaged maps of phytoplankton or productivity, as the authors were interested in changes over the course of the year as the Strait of Gibraltar exchange strength, and thus the AJ strength, varied. Individual depth-integrated biomass maps show higher values along the AJ in the western Alboran, but little extension to either coast, which is different from satellite observations of chlorophyll.

C.2.4 Proposed Work

- What regions of the Alboran are fed by nutrients from the Strait of Gibraltar? From the Northwest upwelling region?
- What patterns of phytoplankton concentration do we see when including only horizontal advection from one of these regions? How does this change with biological model parameters? Do these mirror satellite-observed patterns of *chl-a*?
- Since both horizontal and vertical velocities can move nutrients to give the observed phytoplankton growth, what is the relative size of nutrients in the initial conditions and accumulated from upwelling along trajectories? Can the Alboran be partitioned into regions where one or the other dominates?
- What are the (N,P) fluxes into the WAG?
- How do all of these compare in a mean vs time-varying flow?

I propose to use a nutrient-phytoplankton (NP) model coupled with the hydrodynamic flows from the MITgcm to study the spatial distribution of phytoplankton in the Alboran Sea. Physically, the surface and along-isopycnal horizontal flow will be used to create Lagrangian trajectories. The deepest isopycnal used will be determined based on the regional optical depth, to capture most of the photic zone and ease comparisons with satellite measurements; figure C-7 shows the climatological attenuation coefficient for the area from MODIS. The biological model will have one phytoplankton, representing chlorophyll concentration, and one nutrient, representing nitrate. Although much of the Mediterranean is phosphorus-limited, the Alboran is nitrate-limited (Lazzari et al. DSR-I Feb 2016).

The observed patterns of *chl* that I am interested in are where the periphery of the WAG has high *chl*, which may be wide enough to reach both coasts (figure C-6). The gradient in production between this high region and the relatively oligotrophic interior of the WAG may be a function of the vertical supply of nutrients, as previously shown by Oguz et al., since the anticyclonic WAG primarily downwells near the center. However, it could also be created by the limited exchange of water between the AJ and the WAG, which my previous work has shown to be intermittent but on the order of $10^5 m^3/s$ in an average over several months. The limited supply of nutrients, which will

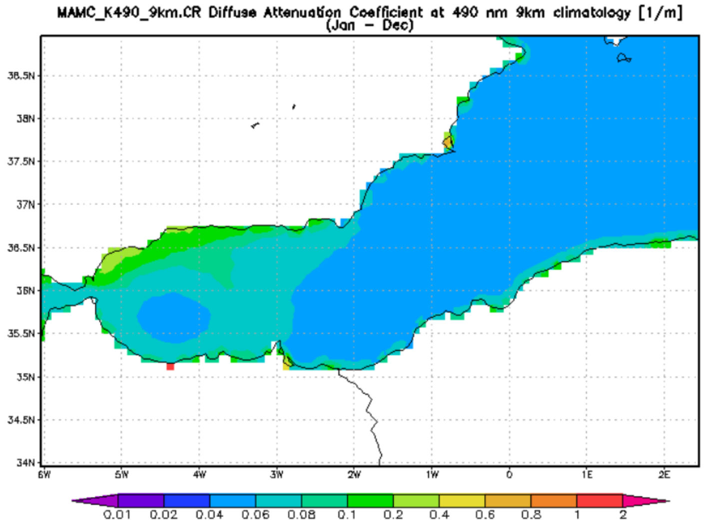

Figure C-7: Climatological diffuse attenuation coefficient (1/m) from MODIS 9km for 490nm. No appreciable difference is found using MODIS 4km. (MODIS data and Giovanni visualization by GES DISC, Acker and Leptoukh 2007)

be diminished from the initial values over about a week as they are advected into the gyre, may explain the lower production without any consideration of local vertical velocities.

The biological concentration equations are based on Modod kinetic models. The model equations are:

$$\frac{DN}{Dt} = -\mu_i \frac{N}{N+k} P + \epsilon \sigma P, \tag{C.1}$$

$$\frac{DP}{Dt} = \mu_i \frac{N}{N+k} P - \sigma P, \tag{C.2}$$

where D/Dt is the change in time (days) following a trajectory, P is chlorophyll concentration, N is nitrate concentration, μ is the maximum growth rate, k is the nitrate concentration for which phytoplankton growth is half the maximum rate, σ is the linear mortality of phytoplankton, and ϵ is the remineralization constant. This set of equations has a decay over time of total $N + P$, due to a fraction of dead phytoplankton being removed from the system, either from sinking or being consumed by higher trophic levels.

Our application of these equations will be along trajectories starting from the region of high surface nitrate in the western Alboran (figure C-8), which also has enhanced nitrate at depth, allowing us to follow the same procedure along sub-surface isopycnals to check whether production

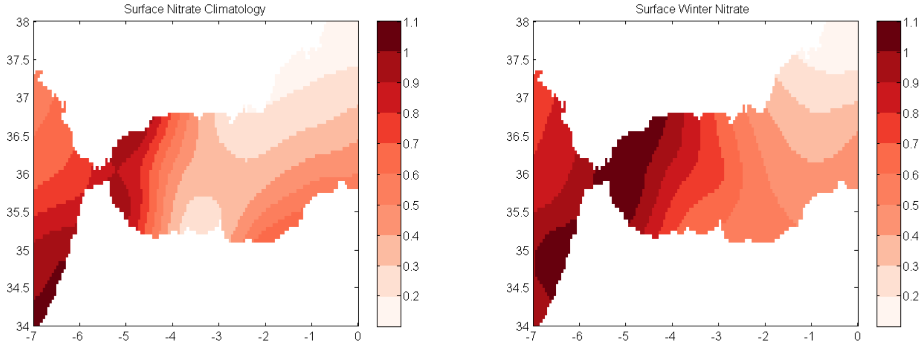

(a) (b)

Figure C-8: Climatological surface nitrate concentration ($mmol/m^3$) from MEDAR. (a) Full climatology (b) Winter only.

patterns in this simple case change with depth.

Variable	*range*	initial value
μ	0.4-2	1
k	0.1-0.5	0.5
σ	0.1-0.5	0.1
ϵ	0-1	0.1

Table C.1: Reasonable parameter values for nutrient-phytoplankton model.

I now perform an initial examination of the behavior of these equations. Table C.1 gives the expected range of the variables and the values I am using to begin with. Using the initial conditions of for $N = 1mmol/m^3$ (the high surface value) and a low $P = 0.01$, peak chlorophyll occurs after 10 days; increasing initial phytoplankton concentration to $0.1mg/m^3$ decreases the time to peak to 6 days (figure C-9). In the mean surface velocity of our model, with velocities up to $1m/s$, this peak would occur $200 - 1000km$ downstream of the Strait. Given sample trajectories, 11 days from the eastern Strait is at the eastern extent of the WAG or in its interior, depending on the initial position (figure C-10). As biological model parameters are varied, this distance will change, as will the path with the time-dependent velocities. However, this basic calculation of the reach suggests that the nutrients from Gibraltar may be able to cause enhanced chlorophyll throughout the area observed.

A larger demonstration, with different initial conditions, shows that the full pattern may be recoverable from this model/method. I start month-long trajectories throughout the region each

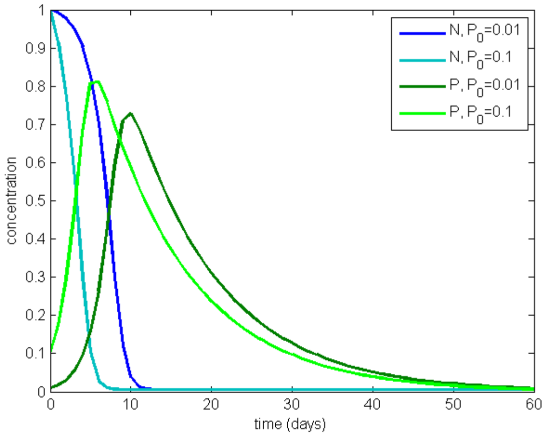

Figure C-9: Typical behavior of the NP model with time. Parameters as given as initial values in Table C.1, with initial $N = 1$, $P = 0.01$, 0.1.

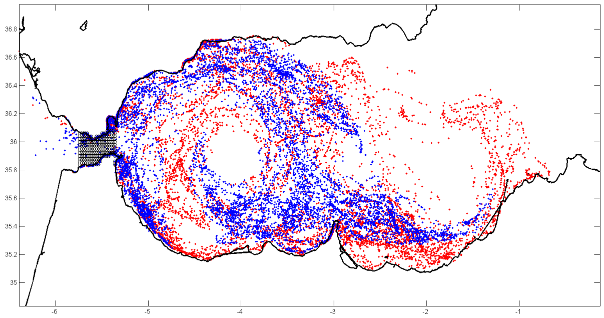

Figure C-10: Sample points from trajectories from surface MITgcm velocities. All initial points (black shading) are in the Strait of Gibraltar, east of the Camarinal Sill; daily releases for 45 days. Blue points are positions 6 days after release, red points are positions 10 days after release.

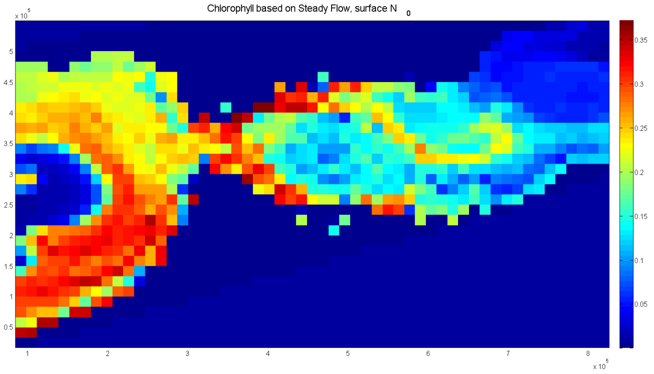

Figure C-11: Sample P field from one-month set of daily releases of trajectories throughout Alboran.

day for a month with the winter surface nitrate climatological values and constant $P = 0.01$. Then I bin the trajectories in space and average the NP values (the biological model has run for 0-28 days depending on which release day the trajectory is from). These binned fields (figure C-11) show the same type of high-periphery *chl* as the climatological SeaWifs (figure C-6).

C.3 References

- Acker, J. G. and G. Leptoukh, “Online Analysis Enhances Use of NASA Earth Science DataâĂİ, Eos, Trans. AGU, Vol. 88, No. 2 (9 January 2007), pages 14 and 17.
- Aref, Hassan. “Stirring by chaotic advection." Journal of fluid mechanics 143 (1984): 1-21.
- Arin, Laura, Xosé A.G. Morán, and Marta Estrada.Arin, Laura, XosÃľ Anxelu G. MorÃạn, and Marta Estrada. “Phytoplankton size distribution and growth rates in the Alboran Sea (SW Mediterranean): short term variability related to mesoscale hydrodynamics." Journal of Plankton Research 24.10 (2002): 1019-1033.
- Bastine, D., and U. Feudel. “Inhomogeneous dominance patterns of competing phytoplankton groups in the wake of an island." Nonlinear Processes in Geophysics 17.6 (2010): 715-731.
- Coll, Marta, et al. “The biodiversity of the Mediterranean Sea: estimates, patterns, and threats." PloS one 5.8 (2010): e11842.
- d’Ovidio, Francesco, et al. Geophysical Research Letters 31.17 (2004).
- Dutkiewicz, S., et al. Global Biogeochemical Cycles 23 (2009): GB4017.
- Follows, Michael J., et al. Science 315.5820 (2007): 1843-1846.

- Garcia-Gorriz, Elisa, and Mary-Elena Carr. “Physical control of phytoplankton distributions in the Alboran Sea: a numerical and satellite approach." Journal of Geophysical Research: Oceans (1978âĂŞ2012) 106.C8 (2001): 16795-16805.
- Gomez, Fernando, et al. “Microplankton distribution in the Strait of Gibraltar: coupling between organisms and hydrodynamic structures." Journal of plankton Research 22.4 (2000): 603-617.
- GRID-Arendal 2013, http://www.grida.no/graphicslib/detail/mediterranean-sea-water-masses-vertical-distribution_d84b#.
- Hernandez-Carrasco, Ismael, et al. “The reduction of plankton biomass induced by mesoscale stirring: A modeling study in the Benguela upwelling." Deep Sea Research Part I: Oceanographic Research Papers 83 (2014): 65-80.
- Hernandez-GarcÄśa, Emilio, Cristobal Lopez, and Zoltan Neufeld. “Small-scale structure of nonlinearly interacting species advected by chaotic flows." Chaos: An Interdisciplinary Journal of Nonlinear Science 12.2 (2002): 470-480.
- HernÃąndez-Garcia, Emilio, and Cristobal Lopez. “Sustained plankton blooms under open chaotic flows." Ecological Complexity 1.3 (2004): 253-259.
- León, P., et al. Journal of Marine Systems 143 (2015): 7-23.
- Lohrenz, Steven E., et al. “Interrelationships among primary production, chlorophyll, and environmental conditions in frontal regions of the western Mediterranean Sea." Deep Sea Research Part A. Oceanographic Research Papers 35.5 (1988): 793-810.
- MacÃŋas, Diego, Adolf Stips, and Elisa Garcia-Gorriz. “The relevance of deep chlorophyll maximum in the open Mediterranean Sea evaluated through 3D hydrodynamic-biogeochemical coupled simulations." Ecological Modelling 281 (2014): 26-37.
- MacÃŋas, D., et al. “Atmospheric-induced variability of hydrological and biogeochemical signatures in the NW Alboran Sea. Consequences for the spawning and nursery habitats of European anchovy." Deep Sea Research Part I: Oceanographic Research Papers 58.12 (2011): 1175-1188.
- MacÃŋas, D., et al. “Meteorologically-induced mesoscale variability of the North-western Alboran Sea (southern Spain) and related biological patterns." Estuarine, Coastal and Shelf Science 78.2 (2008): 250-266.

item Marshall, John et al. JGR: Oceans 102.C3 (1997): 5753-5766.

- May, Robert M. “Biological populations with nonoverlapping generations: stable points, stable cycles, and chaos." Science 186.4164 (1974): 645-647.
- May, Robert M., and Warren J. Leonard. “Nonlinear aspects of competition between three species." SIAM Journal on Applied Mathematics 29.2 (1975): 243-253.
- Mercado, JesÃžs M., Teodoro RamÃŋrez, and Dolores CortÃľs. “Changes in nutrient concentration induced by hydrological variability and its effect on light absorption by phytoplankton in the AlborÃąn Sea (Western Mediterranean Sea)." Journal of Marine Systems 71.1 (2008): 31-45.
- Miller, Patrick D., et al. “Chaotic transport of mass and potential vorticity for an island recirculation." Journal of physical oceanography 32.1 (2002): 80-102.
- Minas, Hans Joachim, et al. “Biological and geochemical signatures associated with the water circulation through the Strait of Gibraltar and in the western Alboran Sea." Journal of Geophysical Research: Oceans (1978âĂŞ2012) 96.C5 (1991): 8755-8771.
- Navarro, Gabriel et al. Remote Sensing of Environment 152 (2014): 557-575.
- Neufeld, Zoltan, Cristobal Lopez, and Peter H. Haynes. “Smooth-filamental transition of active tracer fields stirred by chaotic advection." Physical review letters 82.12 (1999): 2606.
- Oguz, Temel, et al. “Fueling Plankton Production by a Meandering Frontal Jet: A Case Study for the Alboran Sea (Western Mediterranean)." PloS one 9.11 (2014): e111482, doi:10.1371/journal.pone.01114
- Peliz, Alvaro, Dmitri Boutov, and Ana Teles-Machado. “The Alboran Sea mesoscale in a long term high resolution simulation: Statistical analysis." Ocean Modelling 72 (2013): 32-52.
- Renault, L., et al. “Surface circulation in the AlborÃąn Sea (western Mediterranean) inferred from remotely sensed data." Journal of Geophysical Research: Oceans (1978âĂŞ2012) 117.C8 (2012).
- Rypina, Irina I., Michael G. Brown, and Huseyin KoÃğak. “Transport in an idealized three-gyre system with application to the Adriatic Sea." Journal of Physical Oceanography 39.3 (2009): 675-690.
- Rypina, Irina I., et al. “Chaotic Advection in an Archipelago*." Journal of Physical Oceanography 40.9 (2010): 1988-2006.
- Samelson, R. M. and S. Wiggins. Lagrangian Transport in Geophysical Jets and Waves,

Springer, 2006, 147pp.

- Sanchez-Garrido, J. C., G. Sannino, L. Liberti, J. GarcÃŋa Lafuente, and L. Pratt (2011), “Numerical modeling of three-dimensional stratified tidal flow over Camarinal Sill, Strait of Gibraltar," J. Geophys. Res., 116, C12026.
- Sanchez-Garrido, Jose C., et al. “What does cause the collapse of the Western Alboran Gyre? Results of an operational ocean model." Progress in Oceanography 116 (2013): 142-153.
- Sandulescu, Mathias, et al. “Biological activity in the wake of an island close to a coastal upwelling." Ecological Complexity 5.3 (2008): 228-237.
- Sayol, J.M., et al. “Sea surface transport in the Western Mediterranean Sea: A Lagrangian perspective." Journal of Geophysical Research: Oceans 118.12 (2013): 6371-6384.
- Shannon, C.E. (1948) A mathematical theory of communication. Bell System Technical Journal, 27, 379âĂŞ 423.
- Siokou-Frangou, Ioanna, et al. “Plankton in the open Mediterranean Sea: a review." Biogeosciences 7.5 (2010): 1543-1586.
- Skliris, Nikolaos, and Jean-Marie Beckers. “Modelling the Gibraltar Strait/Western Alboran Sea ecohydrodynamics." Ocean Dynamics 59.3 (2009): 489-508.
- Spellerberg, Ian F., and Peter J. Fedor. “A tribute to Claude Shannon (1916âĂŞ2001) and a plea for more rigorous use of species richness, species diversity and the âĂŸShannonâĂŞWienerâĂŹIndex." Global Ecology and Biogeography 12.3 (2003): 177-179.
- Tel, Tamas, et al. “Chemical and biological activity in open flows: a dynamical system approach." Physics reports 413.2 (2005): 91-196.
- Velez-Belchi, P., Vargas-Yanez, M., Tintore, J., 2005. “Observation of a western AlborÃąn gyre migration event." Progress in Oceanography 66, 190âĂŞ210.
- Viudez, Alvaro, Joaquin Tintore, and Robert L. Haney. “Circulation in the Alboran Sea as determined by quasi-synoptic hydrographic observations. Part I: Three-dimensional structure of the two anticyclonic gyres." Journal of Physical Oceanography 26.5 (1996): 684-705.
- Whittaker, Robert J., Katherine J. Willis, and Richard Field. "Scale and species richness: towards a general, hierarchical theory of species diversity." Journal of Biogeography 28.4 (2001): 453-470.

Bibliography

[1] Abernathey, Ryan, and George Haller. “Transport by Lagrangian Vortices in the Eastern Pacific.” Journal of Physical Oceanography 48.3 (2018): 667-685.

[2] Acker, James G., and Gregory Leptoukh. “Online analysis enhances use of NASA earth science data.” Eos, Transactions American Geophysical Union 88.2 (2007): 14-17.

[3] Aref, H. (1984). “Stirring by chaotic advection.” Journal of fluid mechanics, 143, 1-21.

[4] Arin, Laura, Xosé A.G. Morán, and Marta Estrada. “Phytoplankton size distribution and growth rates in the Alboran Sea (SW Mediterranean): short term variability related to mesoscale hydrodynamics.” Journal of Plankton Research 24.10 (2002): 1019-1033.

[5] Bastine, D., and U. Feudel. “Inhomogeneous dominance patterns of competing phytoplankton groups in the wake of an island.” Nonlinear Processes in Geophysics 17.6 (2010): 715-731.

[6] Bormans, Myriam, and Chris Garrett. “A simple criterion for gyre formation by the surface outflow from a strait, with application to the Alboran Sea.” Journal of Geophysical Research: Oceans 94.C9 (1989): 12637-12644.

[7] Bower, Amy S., and Heather D. Hunt. “Lagrangian observations of the deep western boundary current in the North Atlantic Ocean. Part II: The Gulf StreamâĂŞdeep western boundary current crossover.” Journal of physical oceanography 30.5 (2000): 784-804.

[8] Bryden, Harry L., and Henry M. Stommel. “Origin of the Mediterranean outflow.” J. Mar. Res 40 (1982): 55-71.

[9] Branicki, M., and A. D. Kirwan Jr. “Stirring: the Eckart paradigm revisited.” International Journal of Engineering Science 48.11 (2010): 1027-1042.

[10] Abisek Chakraborty and Jean-Michel Campin “Heat and salt budget in MITgcm”, http://mitgcm.org/download/daily_snapshot/MITgcm/doc/Heat_Salt_Budget_MITgcm.pdf, December 2014.

[11] Chelton, Dudley B., Michael G. Schlax, and Roger M. Samelson. “Global observations of nonlinear mesoscale eddies.” Progress in Oceanography 91.2 (2011): 167-216.

[12] Coll, M., Piroddi, C., Steenbeek, J., Kaschner, K., Lasram, F.B.R., Aguzzi, J., Ballesteros, E., Bianchi, C.N., Corbera, J., Dailianis, T. and Danovaro, R. “The biodiversity of the Mediterranean Sea: estimates, patterns, and threats.” PloS one 5.8 (2010): e11842.

[13] Deese, Heather E., Larry J. Pratt, and Karl R. Helfrich. “A laboratory model of exchange and mixing between western boundary layers and subbasin recirculation gyres.” Journal of Physical Oceanography 32.6 (2002): 1870-1889.

[14] Dong, C., J. C. McWilliams, Y. Liu, and D. Chen. “Global heat and salt transports by eddy movement.” Nature communications 5 (2014): 3294.

[15] d’Ovidio, F., FernÃąndez, V., HernÃąndezâĂŘGarcÃŋa, E., & LÃşpez, C. “Mixing structures in the Mediterranean Sea from finiteâĂŘsize Lyapunov exponents.” Geophysical Research Letters 31.17 (2004).

[16] Dutkiewicz, Stephanie, Michael J. Follows, and Jason G. Bragg. “Modeling the coupling of ocean ecology and biogeochemistry.” Global Biogeochemical Cycles 23.4 (2009).

[17] Fereday, D. R., and P. H. Haynes. “Scalar decay in two-dimensional chaotic advection and Batchelor-regime turbulence.” Physics of Fluids 16.12 (2004): 4359-4370.

[18] Fine, Rana A. “Tracers, time scales, and the thermohaline circulation: The lower limb in the North Atlantic Ocean.” Reviews of Geophysics 33.S2 (1995): 1353-1365.

[19] Fischer, Paul F., James W. Lottes, and Stefan G. Kerkemeier. “nek5000 Web page." Web page: http://nek5000. mcs. anl. gov (2008).

[20] Fischer, Paul F. “An overlapping Schwarz method for spectral element solution of the incompressible NavierâĂŞStokes equations.” Journal of Computational Physics 133.1 (1997): 84-101.

[21] Flierl, Glenn R., and Nicholas W. Woods. “Copepod aggregations: influences of physics and collective behavior.” Journal of Statistical Physics 158.3 (2015): 665-698.

[22] Follows, M.J., S. Dutkiewicz, S. Grant and S.W. Chisholm. “Emergent biogeography of microbial communities in a model ocean.” Science 315.5820 (2007): 1843-1846.

[23] Fountain, G. O., Khakhar, D. V., MeziĂĞ, I., & Ottino, J. M. “Chaotic mixing in a bounded three-dimensional flow.” Journal of Fluid Mechanics, 417 (2000): 265-301.

[24] Froyland, G., Horenkamp, C., Rossi, V., Santitissadeekorn, N. and Gupta, A.S. “Three-dimensional characterization and tracking of an Agulhas Ring.” Ocean Modelling 52 (2012): 69-75.

[25] Garcia-Gorriz, Elisa, and Mary-Elena Carr. “Physical control of phytoplankton distributions in the Alboran Sea: a numerical and satellite approach.” Journal of Geophysical Research: Oceans (1978âĂŞ2012) 106.C8 (2001): 16795-16805.

[26] Gascard, J. C., & Richez, C. “Water masses and circulation in the Western Alboran Sea and in the Straits of Gibraltar.” Progress in Oceanography, 15.3 (1985): 157-216.

[27] Greenspan, H. P. 1969 The Theory of Rotating Fluids. Cambridge University Press.

[28] GRID-Arendal 2013, http://www.grida.no/graphicslib/detail/mediterranean-sea-water-masses-vertical-distribution_d84b#.

[29] Griffies, S.M., Winton, M., Anderson, W.G., Benson, R., Delworth, T.L., Dufour, C.O., Dunne, J.P., Goddard, P., Morrison, A.K., Rosati, A. and Wittenberg, A.T. “Impacts on ocean heat from transient mesoscale eddies in a hierarchy of climate models.” Journal of Climate, 28.3 (2015): 952-977.

[30] Gómez, F., Echevarria, F., Garcia, C.M., Prieto, L., Ruiz, J., Reul, A., Jiménez-Gómez, F. and Varela, M. “Microplankton distribution in the Strait of Gibraltar: coupling between organisms and hydrodynamic structures." Journal of plankton Research 22.4 (2000): 603-617.

[31] Hadjighasem, Alireza, et al. “A critical comparison of Lagrangian methods for coherent structure detection.” Chaos: An Interdisciplinary Journal of Nonlinear Science 27.5 (2017): 053104.

[32] Hallberg, R. “Using a resolution function to regulate parameterizations of oceanic mesoscale eddy effects.” Ocean Modelling, 72 (2013): 92-103.

[33] Haller, George. “Lagrangian coherent structures.” Annual Review of Fluid Mechanics 47 (2015): 137-162.

[34] Haller, George, and Francisco J. Beron-Vera. “Geodesic theory of transport barriers in two-dimensional flows.” Physica D: Nonlinear Phenomena 241.20 (2012): 1680-1702.

[35] Haller, George, and A. C. Poje. “Finite time transport in aperiodic flows.” Physica D: Nonlinear Phenomena 119.3-4 (1998): 352-380.

[36] Haynes, Peter, and Emily Shuckburgh. “Effective diffusivity as a diagnostic of atmospheric transport: 1. Stratosphere.” Journal of Geophysical Research: Atmospheres 105.D18 (2000): 22777-22794.

[37] Heburn, George W., and Paul E. La Violette. “Variations in the structure of the anticyclonic gyres found in the Alboran Sea.” Journal of Geophysical Research: Oceans 95.C2 (1990): 1599-1613.

[38] Hernández-Carrasco, I., Rossi, V., Hernández-Garcia, E., Garcon, V. and López, C. “The reduction of plankton biomass induced by mesoscale stirring: A modeling study in the Benguela upwelling.” Deep Sea Research Part I: Oceanographic Research Papers 83 (2014): 65-80.

[39] Hernandez-Garcia, Emilio, Cristobal Lopez, and Zoltan Neufeld. “Small-scale structure of nonlinearly interacting species advected by chaotic flows.” Chaos: An Interdisciplinary Journal of Nonlinear Science 12.2 (2002): 470-480.

[40] Hernández-Garcia, Emilio, and Cristobal Lopez. “Sustained plankton blooms under open chaotic flows.” Ecological Complexity 1.3 (2004): 253-259.

[41] Hill, D. F. “Simple Model for the Recirculation Velocity of Open-Channel Embayments.” Journal of Hydraulic Engineering 140.4 (2013): 06014004.

[42] Kolmogorov, Andrey Nikolaevich. “Dissipation of energy in locally isotropic turbulence.” Dokl. Akad. Nauk SSSR. Vol. 32. No. 1. 1941.

[43] Ledwell, James R., Andrew J. Watson, and Clifford S. Law. "Evidence for slow mixing across the pycnocline from an open-ocean tracer-release experiment." Nature 364.6439 (1993): 701.

[44] Ledwell, J. R., McGillicuddy, D. J., & Anderson, L. A. "Nutrient flux into an intense deep chlorophyll layer in a mode-water eddy." Deep Sea Research Part II: Topical Studies in Oceanography, 55.10 (2008): 1139-1160.

[45] Lenn, Y. D., & Chereskin, T. K. "Observations of Ekman currents in the Southern Ocean." Journal of Physical Oceanography, 39.3 (2009): 768-779.

[46] León, P., Blanco, J.M., Flexas, M.M., Gomis, D., Reul, A., Rodriguez, V., Jiménez-Gómez, F., Allen, J.T. and Rodriguez, J. "Surface mesoscale picoâĂŞnanoplankton patterns at the main fronts of the Alboran Sea." Journal of Marine Systems 143 (2015): 7-23.

[47] Lohrenz, S.E., Wiesenburg, D.A., DePalma, I.P., Johnson, K.S. and Gustafson Jr, D.E. "Interrelationships among primary production, chlorophyll, and environmental conditions in frontal regions of the western Mediterranean Sea." Deep Sea Research Part A. Oceanographic Research Papers 35.5 (1988): 793-810.

[48] Macias, D., Catalán, I.A., Solé, J., Morales-Nin, B. and Ruiz, J. "Atmospheric-induced variability of hydrological and biogeochemical signatures in the NW Alboran Sea. Consequences for the spawning and nursery habitats of European anchovy." Deep Sea Research Part I: Oceanographic Research Papers 58.12 (2011): 1175-1188.

[49] Macias, D., M. Bruno, F. Echevarria, A. Vázquez, and C. M. Garcia. "Meteorologically-induced mesoscale variability of the North-western Alboran Sea (southern Spain) and related biological patterns." Estuarine, Coastal and Shelf Science 78.2 (2008): 250-266.

[50] Macias, Diego, Adolf Stips, and Elisa Garcia-Gorriz. "The relevance of deep chlorophyll maximum in the open Mediterranean Sea evaluated through 3D hydrodynamic-biogeochemical coupled simulations." Ecological Modelling 281 (2014): 26-37.

[51] Mancho, A. M., D. Small, S. Wiggins, and K. Ide. "Computation of stable and unstable manifolds of hyperbolic trajectories in two-dimensional, aperiodically time-dependent vector fields." Physica D, 182 (2003): 188âĂŞ222.

[52] Marshall, J., Shuckburgh, E., Jones, H. and Hill, C. “Estimates and implications of surface eddy diffusivity in the Southern Ocean derived from tracer transport.” Journal of Physical Oceanography 36.9 (2006): 1806-1821.

[53] Marshall, J., A. Adcroft, C. Hill, L. Perelman, and C. Heisey “A finite-volume, incompressible Navier Stokes model for studies of the ocean on parallel computers.” Journal of Geophysical Research, 102.C3 (1997): 5753-5766.

[54] May, Robert M. “Biological populations with nonoverlapping generations: stable points, stable cycles, and chaos.” Science 186.4164 (1974): 645-647.

[55] May, Robert M., and Warren J. Leonard. “Nonlinear aspects of competition between three species.” SIAM Journal on Applied Mathematics 29.2 (1975): 243-253.

[56] McDougall, T.J. and P.M. Barker, 2011: Getting started with TEOS-10 and the Gibbs Seawater (GSW) Oceanographic Toolbox, 28pp., SCOR/IAPSO WG127, ISBN 978-0-646-55621-5.

[57] Mercado, Jesús M., Teodoro Ramirez, and Dolores Cortés. “Changes in nutrient concentration induced by hydrological variability and its effect on light absorption by phytoplankton in the Alboran Sea (Western Mediterranean Sea).” Journal of Marine Systems 71.1 (2008): 31-45.

[58] Miller, Patrick D., Lawrence J. Pratt, Karl R. Helfrich, and Christopher KRT Jones. “Chaotic transport of mass and potential vorticity for an island recirculation.” Journal of physical oceanography 32.1 (2002): 80-102.

[59] Minas, Hans Joachim, Bernard Coste, Pierre Le Corre, Monique Minas, and Patrick Raimbault. “Biological and geochemical signatures associated with the water circulation through the Strait of Gibraltar and in the western Alboran Sea.” Journal of Geophysical Research: Oceans (1978âĂŞ2012) 96.C5 (1991): 8755-8771.

[60] Nakamura, N., “Two dimensional mixing, edge formation, and permeability diagnosed in area coordinates.” Journal of the Atmospheric Sciences, 53 (1996): 1524âĂŞ1537.

[61] Nakamura, N., J. Ma, “Modified LagrangianâĂŘmean diagnostics of the stratospheric polar vortices, 2, Nitrous oxide and seasonal barrier migration in the CLAES and SKYHI GCM.” Journal of Geophysical Research, 102 (1997): 25712âĂŞ25735.

[62] Navarro, Gabriel, Agueda Vázquez, Diego Macias, Miguel Bruno, and Javier Ruiz. "Understanding the patterns of biological response to physical forcing in the Alboran Sea (western Mediterranean)." Geophysical Research Letters 38.23 (2011).

[63] Navarro, Gabriel, SÃĩverine Alvain, Vincent Vantrepotte, and I. E. Huertas. "Identification of dominant phytoplankton functional types in the Mediterranean Sea based on a regionalized remote sensing approach." Remote sensing of environment 152 (2014): 557-575.

[64] Neufeld, Zoltan, Cristobal Lopez, and Peter H. Haynes. "Smooth-filamental transition of active tracer fields stirred by chaotic advection." Physical review letters 82.12 (1999): 2606.

[65] Oguz, Temel, Diego Macias, Jesus Garcia-Lafuente, Ananda Pascual, and Joaquin Tintore. "Fueling Plankton Production by a Meandering Frontal Jet: A Case Study for the Alboran Sea (Western Mediterranean)." PloS one 9.11 (2014): e111482.

[66] Okubo, Akira. "Oceanic diffusion diagrams." Deep sea research and oceanographic abstracts. Vol. 18. No. 8. Elsevier, 1971.

[67] Olascoaga, M. J., & Haller, G. "Forecasting sudden changes in environmental pollution patterns." Proceedings of the National Academy of Sciences, 109.13 (2012): 4738-4743.

[68] Pattanayak, Arjendu K. "Characterizing the metastable balance between chaos and diffusion." Physica D: Nonlinear Phenomena 148.1-2 (2001): 1-19.

[69] Pratt, L. J., Rypina, I. I., Ozgokmen, T. M., Wang, P., Childs, H., & Bebieva, Y. "Chaotic advection in a steady, three-dimensional, Ekman-driven eddy." Journal of Fluid Mechanics, 738 (2013): 143-183.

[70] Peliz, Alvaro, Dmitri Boutov, and Ana Teles-Machado. "The Alboran Sea mesoscale in a long term high resolution simulation: Statistical analysis." Ocean Modelling 72 (2013): 32-52.

[71] Perkins, H., Kinder, T., & Violette, P. L. "The Atlantic inflow in the western Alboran Sea." Journal of Physical Oceanography, 20.2 (1990), 242-263.

[72] Preller, R. H. "A numerical model study of the Alboran Sea gyre." Progress in Oceanography, 16.3 (1986), 113-146.

[73] Renault, L., T. Oguz, A. Pascual, G. Vizoso, and J. Tintore. “Surface circulation in the AlborÃąn Sea (western Mediterranean) inferred from remotely sensed data.” Journal of Geophysical Research: Oceans (1978âĂŞ2012) 117.C8 (2012).

[74] Rypina, I.I.; Brown, M.G.; Beron-Vera, F.J.; Kocak, H.; Olascoaga, M.J.; Udovydchenkov, I.A. “Robust transport barriers resulting from strong Kolmogorov-Arnold-Moser stability.” Physical Review Letters 2007, 98, 104102.

[75] Rypina, I. I., Brown, M. G., Beron-Vera, F. J., Kocak, H., Olascoaga, M. J., & Udovydchenkov, I. A. “On the Lagrangian dynamics of atmospheric zonal jets and the permeability of the stratospheric polar vortex.” Journal of the Atmospheric Sciences, 64.10 (2007): 3595-3610.

[76] Rypina, Irina I., Lawrence J. Pratt, Julie Pullen, Julia Levin, and Arnold L. Gordon. “Chaotic advection in an archipelago." Journal of Physical Oceanography 40.9 (2010): 1988-2006.

[77] Rypina, I. I., Pratt, L. J., Wang, P., Ozgokmen, T. M., & Mezic, I. “Resonance phenomena in a time-dependent, three-dimensional model of an idealized eddy.” Chaos: An Interdisciplinary Journal of Nonlinear Science, 25.8 (2015): 087401.

[78] Samelson, R. M. and S. Wiggins. “Lagrangian Transport in Geophysical Jets and Waves: The dynamical systems approach.” Vol. 31. Springer, 2006.

[79] Sammartino, Simone, Jesús Garcia Lafuente, C. Naranjo, José Carlos Sánchez Garrido, Ricardo Sánchez Leal, and A. Sánchez Román. “Ten years of marine current measurements in Espartel Sill, Strait of Gibraltar.” Journal of Geophysical Research: Oceans 120.9 (2015): 6309-6328.

[80] Sanchez-Garrido, J. C., G. Sannino, L. Liberti, J. GarcÃŋa Lafuente, and L. Pratt. “Numerical modeling of three-dimensional stratified tidal flow over Camarinal Sill, Strait of Gibraltar.” Journal Geophysical Research, 116 (2011): C12026.

[81] Sánchez-Garrido, José C., Jesús Garcia Lafuente, Enrique Alvarez Fanjul, Marcos Garcia Sotillo, and J. Francisco. “What does cause the collapse of the Western Alboran Gyre? Results of an operational ocean model.” Progress in Oceanography 116 (2013): 142-153.

[82] Sandulescu, Mathias, Cristóbal López, Emilio Hernández-Garcia, and Ulrike Feudel. “Biological activity in the wake of an island close to a coastal upwelling.” Ecological Complexity 5.3 (2008): 228-237.

[83] Sayol, J-M., A. Orfila, G. Simarro, C. López, L. Renault, A. Galán, and D. Conti. “Sea surface transport in the Western Mediterranean Sea: A Lagrangian perspective.” Journal of Geophysical Research: Oceans 118.12 (2013): 6371-6384.

[84] Shannon, C.E. “A mathematical theory of communication.” Bell System Technical Journal, 27 (1948): 379âĂŞ 423.

[85] Siokou-Frangou, Ioanna, Urania Christaki, M. G. Mazzocchi, Marina Montresor, Maurizio Ribera d’Alcalá, Dolors Vaqué, and A. Zingone. “Plankton in the open Mediterranean Sea: a review.” Biogeosciences 7.5 (2010): 1543-1586.

[86] Skliris, Nikolaos, and Jean-Marie Beckers. “Modelling the Gibraltar Strait/Western Alboran Sea ecohydrodynamics.” Ocean Dynamics 59.3 (2009): 489-508.

[87] Son, D. T. “Turbulent decay of a passive scalar in the Batchelor limit: Exact results from a quantum-mechanical approach.” Physical Review E 59.4 (1999): R3811.

[88] Spellerberg, Ian F., and Peter J. Fedor. “A tribute to Claude Shannon (1916âĂŞ2001) and a plea for more rigorous use of species richness, species diversity and the ‘Shannon-Wiener’ Index.” Global Ecology and Biogeography 12.3 (2003): 177-179.

[89] Tél, Tamás, Alessandro de Moura, Celso Grebogi, and Gyorgy Károlyi. “Chemical and biological activity in open flows: a dynamical system approach." Physics reports 413.2 (2005): 91-196.

[90] Thiffeault, J-L. “Scalar decay in chaotic mixing.” Transport and Mixing in Geophysical Flows. Springer, Berlin, Heidelberg, 2008. 3-36.

[91] Velez-Belchi, P., Vargas-Yanez, M., Tintore, J. “Observation of a western Alboran gyre migration event.” Progress in Oceanography 66 (2005): 190âĂŞ210.

[92] Viudez, Alvaro, Joaquin Tintore, and Robert L. Haney. “Circulation in the Alboran Sea as determined by quasi-synoptic hydrographic observations. Part I: Three-dimensional structure of the two anticyclonic gyres.” Journal of Physical Oceanography 26.5 (1996): 684-705.

[93] Whitehead, J. A., & Miller, A. R. “Laboratory simulation of the gyre in the Alboran Sea.” Journal of Geophysical Research: Oceans, 84.C7 (1979): 3733-3742.

[94] Whittaker, Robert J., Katherine J. Willis, and Richard Field. “Scale and species richness: towards a general, hierarchical theory of species diversity.” Journal of Biogeography 28.4 (2001): 453-470.

[95] Wiggins, Stephen. Introduction to applied nonlinear dynamical systems and chaos. Vol. 2. Springer Science & Business Media, 2003.

[96] Zambianchi, Enrico, and Annalisa Griffa. “Effects of finite scales of turbulence on dispersion estimates.” Journal of marine research 52.1 (1994): 129-148.